



BRNO UNIVERSITY OF TECHNOLOGY

VYSOKÉ UČENÍ TECHNICKÉ V BRNĚ

CENTRAL EUROPEAN INSTITUTE OF TECHNOLOGY BUT

STŘEDOEVROPSKÝ TECHNOLOGICKÝ INSTITUT VUT

FABRICATION AND CHARACTERIS. OF NANOSTR.

PŘÍPRAVA A CHARAKTERIZACE NANOSTRUKTUR

**ADVANCED PLASMONIC MATERIALS FOR
METASURFACES AND PHOTOCHEMISTRY**

POKROČILÉ PLAZMONICKÉ MATERIÁLY PRO METAPOVRCHY A FOTOCHEMII

DOCTORAL THESIS

DIZERTAČNÍ PRÁCE

AUTHOR

AUTOR PRÁCE

Ing. Filip Ligmajer

SUPERVISOR

ŠKOLITEL

prof. RNDr. Tomáš Šikola, CSc.

BRNO 2018

CONTENTS

Acknowledgements	v
Preface	vii
Introduction	1
1 Plasmonics	3
1.1 Maxwell's equations	4
1.2 Models of dielectric function	5
1.3 Surface plasmon polaritons	10
1.4 Localized surface plasmons	17
1.5 Conclusions	22
2 Applications of plasmonics	25
2.1 Fabrication of plasmonic nanostructures	25
2.2 Plasmonic antennas	30
2.3 Plasmonic sensing	33
2.4 Metamaterials and metasurfaces	35
2.5 Hot electrons	40
2.6 Conclusions	45
3 Plasmonics for control of light	47
3.1 Experimental techniques in plasmonics	47
3.2 Plasmonics for polarization control	52
3.3 Plasmonics for phase control	57
3.4 Conclusions	61
4 Tunability in plasmonics	63
4.1 Tunable metasurfaces	63
4.2 Vanadium dioxide	64
4.3 VO ₂ for optical modulation	72
4.4 Epitaxial VO ₂ metasurface	76
4.5 Conclusions	82
5 Plasmonics and electrochemistry	83
5.1 Fundamentals of electrochemistry	84
5.2 Studies combining plasmonics and electrochemistry	89
5.3 Hot-electron photochemistry on WS ₂ nanotubes decorated with gold nanoparticles	91
5.4 Conclusions	106
6 Conclusions and future directions	109
List of Abbreviations	113
Bibliography	115
List of Publications	141

ACKNOWLEDGEMENTS

My sincere gratitude goes first to Prof. Tomáš Šikola, who is the key person behind the wonderful academic environment that has surrounded me since I have stepped into my alma mater. His enthusiasm, endless support for the scientific ideas of our group, and especially his kindness, all obliged me to be as hard-working and humble as he is. It is not a coincidence that people of similar qualities were surrounding me also at my workplace: at IPE FME BUT and at CEITEC BUT. Although many of them gave lectures to me and marked my assessments in the early days, they later became my good friends and inspiring colleagues. I thank Jiří Spousta for his lessons and suggestions, not only academic but also from day-to-day life. I am also grateful to Radek Kalousek, Vlastimil Křápek, Jan Čechal, and Stanislav Průša, who taught me by their own actions that proper scientists should never be satisfied with a superficial knowledge or evidence, and that one should always aim for deep understanding of any given problem. I thank to my students too, for their energy and enthusiasm which motivated me to keep learning and to come up with new research ideas. Many thanks also go to my colleagues and friends from the plasmonic group at IPE — Petr Dvořák, Zoltán Édes, Martin Hrtoň, Martin Konečný, Lukáš Kejík, Michal Kvapil, Tomáš Šamořil, Jiří Babocký and others. Each of them with his own strength, they all turned out to be excellent team players and it was a pleasure for me to tackle our common research goals together. I would also like to thank Lukáš Flajšman for not only his technical advices but also for the practical help with building of optical setups. Finally, a special “thank you” goes to Miroslav Kolíbal, who has been my mentor throughout the great part of my studies and who is for me an embodiment of the great scientific virtues like curiosity and honesty.

The results in this thesis also reflect several collaborations I have been lucky to take part in. My concern with VO_2 has started at Imperial College London — thanks to the opportunity by Prof. Stefan Maier I got a chance to learn, among others, from Yannick Sonnfraud, Alice Orsi, and Dang Yuan Lei. With the last one we still keep collaborating and I was even fortunate enough to spend some time within his group at Hong Kong PolyU. There, I got a chance not only to push forward the VO_2 -related work but also to dwell into new research projects like the one devoted to upconverting nanocrystals together with a brilliant and humble student Jijun He. Another big piece of collaborative effort was the work on the plasmonic phase measurements together with our colleagues from the biophotonics group of Radim Chmelík: Lenka Štrbková, Aneta Křížová, Jana Čolláková, Petr Bouchal, and Zbyněk Dostál all proved to be patient, flexible and creative partners

for our project, which eventually ended up as successful one after all. The last important cooperation has been going on with the group of Assoc. Prof. Miroslav Fojta at IBP AS CR. Together with Luděk Havran, and especially Aleš Daňhel, they turned out to be our guides into the world of biochemistry and electrochemistry.

I also thank the funding agencies who supported this work. It was especially the European Union through its programme Erasmus, European Regional Development Fund, and Horizon 2020. My research internship in the group of Dangyuan Lei was supported by the Hong Kong Polytechnic University under its Research Student Attachment Programme for Incoming Visiting Ph.D. students. On the national level, several parts of this thesis were done with the support of Grant Agency of the Czech Republic, Technological Agency of the Czech Republic, and Ministry of Education, Youth and Sports (Project No. LQ1601 – CEITEC 2020). This work was also carried out with the support of CEITEC Nano Research Infrastructure (MEYS CR, 2016–2019).

I would like to thank my friends for their pleasant distractions from my studies, for enriching my life, and for showing me that one can find joy also outside science and academia. The biggest thanks surely go to my parents, to my wife, and to our closest families. Without their unconditional love, trust, and support I would never be able to get this far.

PREFACE

This dissertation is a summary of the research done mainly in the laboratories of CEITEC BUT, but several parts were done during my research stays abroad or within other scientific collaborations, as specified below. The aim of the extensive introduction to plasmonics and its applications in the first two chapters is twofold: To serve as a primer for anyone who wants to get involved in that wonderful discipline at the boundary between optics and solid-state physics, but also to unite the diverse research findings of this thesis within a single theme of challenges and research avenues of contemporary nanophotonics and plasmonics. Although the three chapters that come after those opening ones will be devoted mostly to the experimental and theoretical results, each of them contains several introductory sections too. In the process of writing, I did my best to frequently reference to the proverbial “giants” on whose shoulders all my knowledge stands. My intend was to primarily select the textbooks and articles which do the best job in explaining all those complicated topics to the inexperienced audience.

Some parts of the research presented in the second half of this dissertation have been already published. They are indexed in the [List of publications](#), together with my contribution to each of them, as they are all results of a broad, collaborative, and often also international effort. In more details, section 3.2 is based on the publication [A2] , section 3.3 on the publication [A3], section 4.3 on the publication [A4], and section 4.4 on the publication [A1]. So far unpublished results shown in section 5.3 were measured in close cooperation with my colleague Ing. Lukáš Kejík. Part of the data shown in Fig. 57 were measured by Ing. Zita Salajková under my supervision. Note that many of the figures from the published results were not reproduced as they are but rather adapted with some further modifications to better suit the style and especially the purpose of this thesis. My goal was to present the results in such a way that the reader does not have to refer to the original publications, but more details can be found in them if needed.

INTRODUCTION

“When I’m back in Zurich, the first thing we’ll do is climb the Ütliberg,” Einstein writes to Mileva, referring to a local hill. “I can already imagine the fun we’ll have ... And then we’ll start it on Helmholtz’s electromagnetic theory of light, which I still haven’t read — first, because I’m afraid to, and second, because I didn’t have it.”

The Love Letters

ALBERT EINSTEIN, MILEVA MARIĆ

The ability to control and utilize the flow of light have attracted mankind practically from its origins. It is also the cornerstone of many fields of the contemporary sciences. Early scholarly explorations, for example, led to the formation of classical optics, which is behind a great deal of phenomena we encounter and use every day. Optical experiments were also the key ones which nurtured the quantum-mechanical description of the world around us. In other words, light-matter interactions enable us to probe and understand the laws of nature in more and more intricate ways. By pushing our ability to control optical interactions towards the nanometer scale, we can open up new perspectives and take advantage of them. But since the 19th century it has been recognized that there is a natural and fundamental limitation which prohibits focusing of free-space light into an area of size smaller than the wavelength. Fortunately, with the aid of nanoscience and nanotechnology, this limit has been bypassed and the multidisciplinary fields of nano-optics and nanophotonics emerged. The key to this development was plasmonics — the science of light which interacts with metals.

The main goal of this dissertation is to introduce plasmonics from several points of view. To gradually build up the knowledge necessary for understanding all the important concepts of that field and then present how these concepts can be utilized to create useful devices or to discover novel phenomena. Chapter 1 starts with a description of the physics of light (electromagnetism), which is united with the physics of metals (solid-state physics). From this combination, the unique properties of plasmons gradually emerge and we then elaborate on their dispersion relation, confined nature, and on the enhanced scattering and absorption processes, which accompany the excitation of plasmons in nanostructured metals.

Chapter 2 is devoted to applications of plasmonics. We will first introduce the most common approaches to fabrication of plasmonic nanostructures. Then, the concept of plasmonic antennas will be brought in and scientific disciplines where it is

used will be presented. The domain of sensing will be briefly mentioned, for example, as plasmonics have been a stable source of promising devices with unprecedented properties there. A special focus will be placed also on the field of metasurfaces and metamaterials, where plasmonic nanoantennas play a role of the indispensable building blocks. The last section of this chapter then deals with plasmonically generated hot electrons, which have been recently a subject of renewed interest due to their great potential for photochemistry and photovoltaics.

In the next three chapters, we will introduce three separate studies where the unique properties of plasmonic nanostructures are put to use. Chapter 3 will elucidate how gold nanorods, having their plasmonic response tailored to match the emission bands of nearby upconversion nanocrystals, influence the polarization state of the emitted light. It also contains a section concerning an important aspect of metasurface development, namely, the quantitative measurements of the phase distribution of the electric fields altered by a metasurface. This is all supplemented by a brief survey of experimental techniques which are commonly used in plasmonics.

Chapter 4 is centred around the concept of active tunability in plasmonics. It starts with a short classification of various types of tunable metasurfaces, including those based on integration of phase-change materials. Vanadium dioxide, an archetypal tunable phase-change material, is then described in greater detail. An emphasis is placed especially on the relationships among structural, electronic, and optical properties. Then, two studies employing the VO_2 as an active component of a metasurface will be presented. In the first one, gold disc nanoantennas are interfaced with a VO_2 film and their plasmonic resonances is actively tuned by ultraviolet light pulses. In the second one, epitaxially grown VO_2 nanobeams themselves act as the nanostructured plasmonic element. The resulting metasurface can be operated as light modulator or even as a switchable quarter-wave plate in the telecommunication wavelength range.

In chapter 5, we consider the possibility of using nanotechnology and plasmonics to endow photochemistry or electrochemistry with new prospects. The fundamentals of electrochemistry are described first, with emphasis on its connection to the solid-state physics and explanation of the most relevant voltammetric techniques and experimental setups. What follows is a detailed study of hot-electron effects on photochemistry at semiconductor–metal interfaces of electrochemical electrodes. The presented findings confirm that plasmonic effects can be detected using electrochemical methods and that rational engineering of the nanostructured electrodes can lead to unusual charge-separating effects in the plasmonically active system. The whole thesis is then closed with a chapter filled with concluding remarks and ideas for future work, which have naturally emerged from all the findings presented here.

1 PLASMONICS

It is often said that Faraday and Maxwell provided the bridge between Newton and Einstein. While true, this statement is incomplete. Newton was known to have attributed his achievements to “standing on the shoulders of giants,” and when Einstein visited Britain it was natural for the press to ask him if he had stood on the shoulders of Newton. Einstein replied: “That statement is not quite right; I stood on Maxwell’s shoulders.” Maxwell would have pointed out that he, in turn, had Faraday’s shoulders to stand on. Their partnership made a contribution to physical science, indeed to human knowledge, comparable with those of Newton and Einstein

Faraday, Maxwell, and the Electromagnetic Field

NANCY FORBES

When an electromagnetic wave is incident on matter with free charge carriers it forces them to oscillate. This seemingly trivial fact leads to coupled light-matter oscillations called plasmon polaritons, or shortly plasmons, which are the primary cause of many amazing phenomena like concentration of light below diffraction limit or existence of artificial materials with negative refractive index. All these processes are studied in the field of plasmonics, which is, in essence, electrodynamics of metals. Plasmonics naturally connects the physics of electromagnetism with the physics of solid state in order to reveal and utilize the extraordinary properties of the plasmons. In this chapter, we will introduce the essential components necessary for formation of plasmons and we will also describe their main properties. In order to do so, Maxwell’s equations (which represent the physics of electromagnetism) must be brought in and connected with some model of the optical properties of matter (representing the physics of solid state). From this combination, the enhancement of the electromagnetic field around illuminated metals, its tight confinement, and propagation constants of plasmons will emerge. Following the explanation of the propagating form of plasmons, a detailed account on their localized counterpart will be also presented. Localized plasmons are associated with nanostructured metals, which are the main building blocks of metasurfaces and are also important in other applications, as will be explained later in the text.

1.1 Maxwell's equations

It is a great wonder of nature that classical electromagnetism, optics, and electric circuits are all governed by a set of just four fundamental Maxwell's equations:

$$\nabla \cdot \mathbf{D} = \rho_{\text{ext}}, \quad (1a)$$

$$\nabla \cdot \mathbf{B} = 0, \quad (1b)$$

$$\nabla \times \mathbf{E} = -\frac{\partial \mathbf{B}}{\partial t}, \quad (1c)$$

$$\nabla \times \mathbf{H} = \mathbf{J}_{\text{ext}} + \frac{\partial \mathbf{D}}{\partial t}. \quad (1d)$$

These differential equations describe how macroscopic electromagnetic fields (represented by the electric displacement field \mathbf{D} , the magnetic induction \mathbf{B} , the electric field \mathbf{E} , and the magnetizing field \mathbf{H}) are generated by changes of each other (represented by the partial time derivatives) and also by the presence and motion of external charges (represented by the charge density ρ_{ext} and the current density \mathbf{J}_{ext} , respectively). Maxwell's equations can be written in many forms [1]. The one chosen here — so-called “macroscopic” or “in-matter” formulation — is useful for description of electromagnetism within media containing charges. The problem with these media is that the spatial distributions of their charges (either free or bound) will be modified upon presence of electromagnetic fields and this will give rise to some additional polarization field $\mathbf{P} = \varepsilon_0 \chi_e \mathbf{E}$ or magnetization field $\mathbf{M} = \chi_m \mathbf{H}$, where ε_0 is the vacuum permittivity. These fields are related to the density of permanent or induced electric/magnetic dipole moments, and they are proportional to the respective driving fields (the coefficients of proportionality χ_e and χ_m) are called the electric and magnetic susceptibility, respectively. With the formulation used above, however, one does not have to deal with all these charges and fields because the material response is incorporated into the equations through constitutive relations using (relative) permittivity ε_r and (relative) permeability μ_r :

$$\mathbf{D} = \varepsilon_0 \mathbf{E} + \mathbf{P} = \varepsilon_0 (1 + \chi_e) \mathbf{E} = \varepsilon_0 \varepsilon_r \mathbf{E} = \varepsilon \mathbf{E}, \quad (2a)$$

$$\mathbf{H} = \frac{1}{\mu_0} \mathbf{B} - \mathbf{M} = \frac{1}{\mu_0 (1 + \chi_m)} \mathbf{B} = \frac{1}{\mu_0 \mu_r} \mathbf{B} = \frac{1}{\mu} \mathbf{B}, \quad (2b)$$

where μ_0 is the vacuum permeability. The ε_r and μ_r are not constants, though. They are complex functions whose form depends on the structural and material properties of a particular medium: For nonlinear media, for example, they depend on the fields \mathbf{E} and \mathbf{B} . For anisotropic media, they become tensors. And due to non-locality in space and time, they are also functions of the wave vectors \mathbf{k} and frequencies ω of the driving fields [2].

In other words, from the point of view of electromagnetism, every material is fully characterized by the form of its permittivity and permeability. The challenge is, however, to find a suitable and correct model of ε and μ of the particular sample in question. In plasmonics, we will mainly deal with the linear, isotropic, and nonmagnetic ($\mu_r = 1$) media. We thus need to concern ourselves only with the permittivity, which will be solely frequency-dependent, and we will follow the convention of calling it the complex dielectric function $\varepsilon(\omega) \equiv \varepsilon_1(\omega) + i\varepsilon_2(\omega)$, with the real part $\varepsilon_1(\omega)$ and the imaginary part $\varepsilon_2(\omega)$. In the next section, we will explain how the dielectric functions of metals and dielectrics can be modelled. We are then going to plug these models into the equations that were introduced above and we will watch how plasmon polaritons naturally emerge as the possible solutions. Note that later in this thesis, we will see how this problem can be inverted when nanotechnology is used for fabrication of so-called metamaterials that possess customized or even unnatural values of ε and μ .

1.2 Models of dielectric function

In the previous section, the complex dielectric function was established as the single entity that describes the response of nonmagnetic materials towards electromagnetic fields. The most straightforward method how to obtain the dielectric function of a particular material should be a spectroscopic measurement in reflection or transmission configuration. Indeed, in some special cases, even a simple reflectance measurement will give very accurate and correct results. In general, however, the complex nature of the dielectric function requires much more sophisticated ellipsometric measurements [3].

Theoretical calculations are therefore an important and useful complement, as they provide not only the values of $\varepsilon(\omega)$ but also insights into the physical mechanisms behind its form. In principle, the dielectric function is theoretically determined by calculating how the charge distribution inside the medium changes when its atoms or molecules respond to the local fields (influenced not only by the driving field but also by the polarized matter around). These interactions can be modelled on many levels of approximation. The most sophisticated approach includes many-body calculations of current-current correlation functions within quantum field theory using so-called Kubo formula [4]. Although this method can provide insights into the unique optical properties of some unusual materials, it requires large computational resources and produces meaningful results only when provided with correct input parameters that are often very hard to estimate. Fortunately, classical models are more than appropriate in most situations. In these models, the atoms or molecules

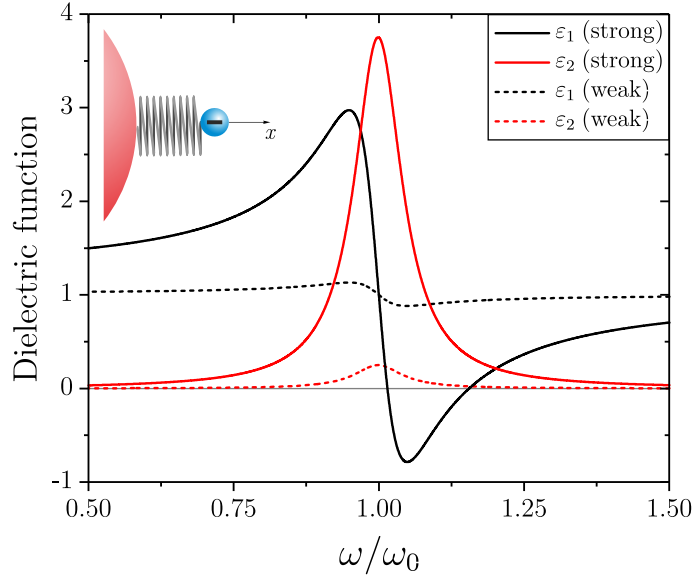


Fig. 1: Real $\varepsilon_1(\omega)$ and imaginary $\varepsilon_2(\omega)$ parts of dielectric functions calculated according to the Lorentz model (schematically shown in the inset). Parameters: $\omega_0 = 6 \times 10^{15} \text{ rad s}^{-1}$ ($E = \hbar\omega_0 = 4 \text{ eV}$), $\Gamma = \omega_0/10$, and $n_e = 4.4 \times 10^{20} \text{ cm}^{-3}$ (strong, solid lines) or $n_e = 3 \times 10^{19} \text{ cm}^{-3}$ (weak, dashed lines).

in a medium are represented by classical harmonic oscillators that are driven by an incident electromagnetic wave. As there are many types of solid state matter, there are also many types of dielectric polarizations and naturally also many types of classical models that can represent them (Sellmeier, Cauchy, Tauc-Lorentz, Gaussian etc.) [3]. But two oscillator models stand out as the most widely used. Drude model describes polarization of materials containing free carriers and it is widely used to explain optical properties of metals. The Lorentz model, on the other hand, describes the response of semiconductors and dielectrics, i.e., materials with bounded charge carriers. Furthermore, slightly modified Lorentz model can be used to describe the intricate details of the response of metal particles and thus it is very relevant also in the field of plasmonics [5–9].

The Lorentz model is schematically shown in the inset of Fig. 1. A negatively charged electron with the charge $q = -e$ and mass m_e is bound to a positively charged and much heavier atomic nucleus. Their bond is represented by a spring with the spring constant k_F that follows Hook’s law and produces the restoring force $\mathbf{F}_r = -k_F \mathbf{x}$ proportional to the electron displacement \mathbf{x} . Consequently, the electron will behave like a harmonic oscillator with the resonant frequency $\omega_0 = \sqrt{k_F/m_e}$. Damping of its motion is represented by a viscous force $\mathbf{F}_d = -m_e \Gamma \dot{\mathbf{x}}$ proportional to its mass, speed $\dot{\mathbf{x}}$, and damping frequency Γ . The physical origin of this damping is scattering of electrons by other electrons, phonons, grain boundaries, impurities

or defects [10]. Finally, we let the harmonically oscillating external electric field $\mathbf{E} = \mathbf{E}_0 \exp(-i\omega t)$ with the amplitude \mathbf{E}_0 drive this oscillator by the electrostatic force $\mathbf{F} = q\mathbf{E} = -e\mathbf{E}$. Using Newton's second law, we can write the equation of motion for such a one-dimensional system as

$$m_e \ddot{\mathbf{x}} = -m_e \Gamma \dot{\mathbf{x}} - m_e \omega_0^2 \mathbf{x} - e\mathbf{E}. \quad (3)$$

We then assume that the electron displacement follows the frequency of the alternating electric field, that is, $\mathbf{x}(t) = \mathbf{x}_0 \exp(-i\omega t)$, and solve for \mathbf{x}_0 :

$$\mathbf{x}_0 = -\frac{e\mathbf{E}_0}{m_e} \frac{1}{\omega_0^2 - \omega^2 - i\Gamma\omega}. \quad (4)$$

The dielectric polarization field \mathbf{P} is defined as the electric dipole moment induced per unit volume. In other words, it is proportional to the product of the charge carrier density n_e , charge, and charge displacement: $\mathbf{P} = -n_e e \mathbf{x}$. We can thus plug the calculated displacement into Eq. (2a) to finally obtain the complex Lorentz dielectric function:

$$\varepsilon_{\text{r,Lorentz}}(\omega) = 1 + \chi_e = 1 + \frac{\mathbf{P}}{\varepsilon_0 \mathbf{E}} = 1 + \frac{n_e e^2}{\varepsilon_0 m_e} \frac{1}{\omega_0^2 - \omega^2 - i\Gamma\omega} \equiv \varepsilon_1 + i\varepsilon_2. \quad (5)$$

To discuss its shape, both real $\varepsilon_1(\omega)$ and imaginary $\varepsilon_2(\omega)$ parts of two model Lorentz dielectric functions (strong and weak) are plotted in Fig. 1. The resonant behaviour is obvious from the shape of the imaginary part, with its position at ω_0 and full width at half maximum (FWHM) equal to Γ . The resonance broadening is therefore directly proportional to the damping frequency. Regarding the real part, two things are noteworthy: First, unlike the imaginary part, $\varepsilon_1(\omega)$ is strongly influenced by the oscillator even surprisingly far from its resonant frequency. This stems from the causality principle (i.e., the light cannot be absorbed before it enters the medium), which is represented by the Kramers–Kronig integral relations [4]. Consequently, when modelling real materials, the contribution of all seemingly unimportant frequency-distant resonances must be included into the model to generate the correct value of ε_1 at the particular frequency. Second, it is the fact that ε_1 can drop to negative values on the high-frequency side of a resonance, given it is strong enough (compare the solid and dashed lines in Fig. 1). This fact is very relevant to plasmonics because the negative values of ε_1 are linked with presence of frequency band gaps and polaritonic states, which will be discussed below.

Now we will focus on a description of materials that contain free charge carriers. For them, a model representing the oscillations of unbounded electrons must be used. The equation of motion of this so-called Drude model can be obtained by omitting the restoring force factor from Eq. (3):

$$m_e \ddot{\mathbf{x}} = -m_e \Gamma \dot{\mathbf{x}} - e\mathbf{E}. \quad (6)$$

Using the same approach as above, we can get the desired dielectric function associated with the free electron oscillations

$$\varepsilon_{\text{r,Drude}}(\omega) = 1 - \frac{\omega_{\text{p}}^2}{\omega^2 + i\Gamma\omega} \equiv \varepsilon_1 + i\varepsilon_2, \quad (7)$$

where $\omega_{\text{p}}^2 = (n_{\text{e}}e^2) / (\varepsilon_0 m_{\text{e}})$ is so-called plasma frequency. When compared with the Lorentz oscillator, it is obvious that Drude's model is in fact its special case for $\omega_0 = 0$. Accordingly, ε_1 is negative at all frequencies from zero up to ω_{p} , where it goes through zero and monotonically increases to a positive limit. From reasons that will become obvious in the next section, plasma frequency is a major attribute of all metals with respect to their response to the electromagnetic waves. Moreover, the fact that it depends on the charge carrier density can be used to tune the optical properties of e.g. highly doped semiconductors. Note that in some cases, m_{e} is sometimes replaced by the modified effective mass m_{e}^* to account for the interactions of electrons with the lattice, phonons, and other charge carriers [10].

It has been already established on page 6 that in real materials there is often more than one type of dielectric polarization present. To accurately model their realistic dielectric functions, one therefore needs to sum up the contributions of various polarizations with appropriate type, frequency, damping, and strength. This process is sketched in Fig. 2, where the dielectric polarizations of various origins are summed up throughout the whole spectrum of frequencies. Note that every material behaves like a vacuum with $\varepsilon_1 = 1$ at sufficiently high frequencies beyond electronic polarization. On the other side of the spectrum, the value of (static) dielectric function $\varepsilon_1(0) = \varepsilon_{\text{s}}$ is given by the cumulative contribution of all sources of the dielectric polarization across the whole spectrum. People in practice often work within a limited band of frequencies and they therefore deal only with a small subset of all resonances in the medium. The contribution of oscillators outside this band is then incorporated into the model by replacing the number one in equations (3) or (7) by an arbitrary constant ε_{∞} (see Fig. 2 for a visual representation). One example of summing up the individual oscillator contributions in order to accurately model a measured dielectric function of gold is shown in Fig. 3. Although the dielectric function of gold can be well approximated by a sole Drude term at energies below 2 eV, the appearance of interband transitions at higher energies [12] requires to add another five more oscillators in order to match the experimental data with acceptable accuracy.

In this section, we have shown why the dielectric function is the principal attribute of all materials with respect to their electromagnetic response and how this dielectric function can be sufficiently modelled by a sum of classic harmonic oscillators. We will now use this knowledge to describe how exactly the electromagnetic

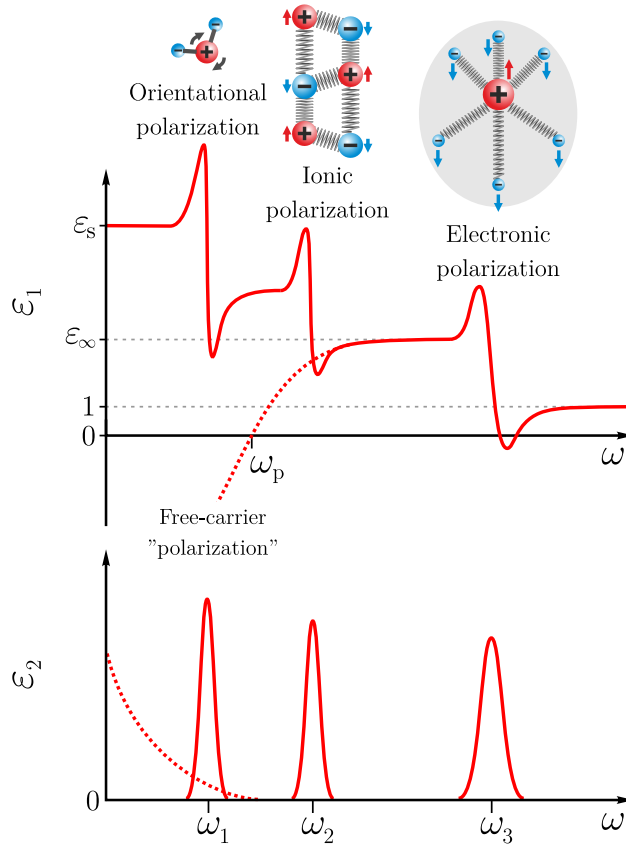


Fig. 2: Schematic representation of real $\varepsilon_1(\omega)$ and imaginary $\varepsilon_2(\omega)$ parts of a hypothetical complex dielectric function. Contributions of electronic, ionic, and orientational polarizations (inset) are represented by three resonances in the imaginary part and the corresponding line shapes in the real part. The contribution of free carriers in metals and semiconductors (the Drude model) is represented by the dotted lines.

waves behave when they interact with media that can be electromagnetically polarized. In such cases, light can be considered as “dressed” in the material excitations that are associated with the electric or magnetic dipoles, “dragging” them along as it propagates through the medium. The specific elementary excitations in solids (with their corresponding quasiparticles) involve lattice vibrations (phonons), electron-hole pairs (excitons), free electrons (plasmons), or even spins of electrons (magnons) [13]. The collective excitations that result from this coupling are called polaritons [14, 15]. Polaritons have their energy density distributed between electromagnetic energy (associated with the radiation field) and mechanical or electrical energy (associated with the elementary excitation). When the coupling is absent or weak, electromagnetic waves propagate freely through the material and their group velocity is only slightly modified. But as the coupling gets stronger, both the light dispersion and elementary excitation dispersion are substantially altered due to their avoided crossing in the energy-momentum space, the group velocity is strongly

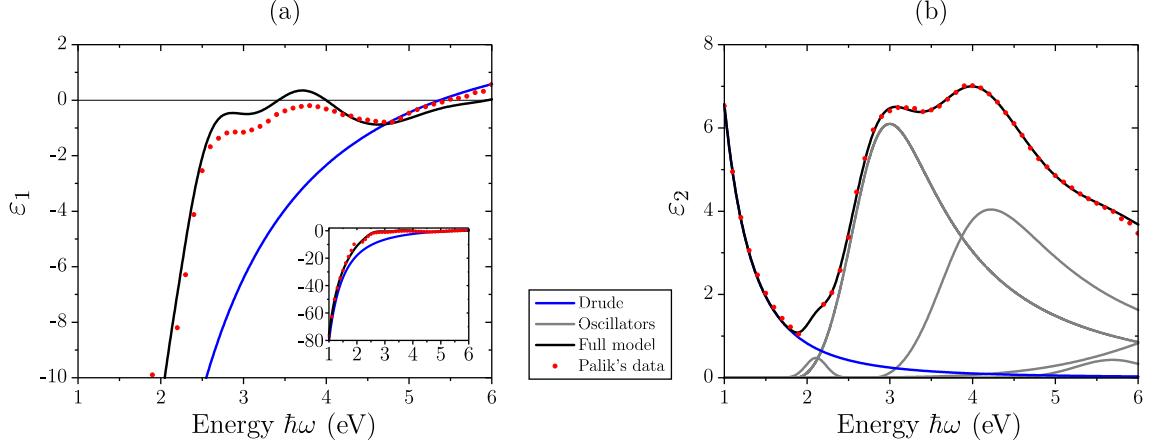


Fig. 3: Measured (a) real and (b) imaginary parts of the dielectric function of gold (red dots, data from Ref. [11]) fitted by the Drude–Lorentz model. The pure Drude’s model (blue line) fits well up to energies close to 2 eV, where interband transitions appear and drastically influence the optical response. Five more oscillators of the Gaussian or the Tauc–Lorentz type (grey lines) have to be added so that the total model dielectric function (black line) fits. The inset in (a) shows the wider picture of the same $\varepsilon_1(\omega)$ data as in the main picture.

frequency dependent, and polaritonic picture must be employed [16, 17]. We will now proceed to introduce polaritons that are the most relevant for this work — the surface plasmon polaritons.

1.3 Surface plasmon polaritons

Surface plasmon polaritons (SPPs) are oscillations of free electrons coupled to a light wave at the boundary between metals and dielectrics. The main features of these waves are large wave vectors along the boundary and also large confinement in the perpendicular direction. Many remarkable phenomena are connected with SPPs and the whole field of nanophotonics emerged from their investigations. To discover their properties — namely to determine their spatial E - and H -field profiles and their dispersion relation — we will gradually apply all the possible constraints placed upon them by the combination of Maxwell’s equations and the dielectric function of free electrons.

First, the geometry of the problem must be established. The most convenient one corresponds to a system of two homogeneous semi-infinite media with the interface at $z = 0$ plane: a dielectric with $\varepsilon_{r,d}$ located above ($z > 0$) and a metal with $\varepsilon_{r,m}$ located below ($z < 0$), see Fig. 4. Because we look for waves that are propagating along the interface, we will investigate only harmonic solutions that correspond to

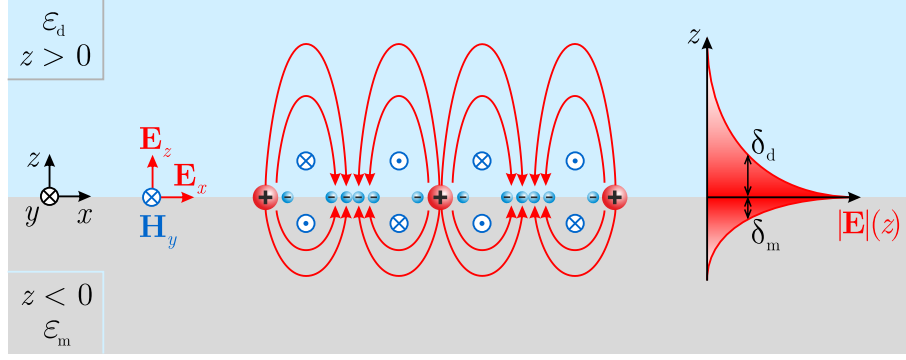


Fig. 4: The geometry used for derivation of properties of SPPs and a sketch of their electromagnetic fields. Coherent oscillations of free electrons (blue spheres) on the background of positive ion cores (red spheres) give rise to surface-confined electric fields in the xz plane (red lines) and also to perpendicular magnetic fields (blue vectors). The surface confinement is represented by the exponential dependence of the electric field magnitude $|\mathbf{E}|$ on the z coordinate, as characterized by two penetration depths $\delta_{d/m}$.

plane waves along x axis:

$$\begin{Bmatrix} \mathbf{E}(\mathbf{r}, t) \\ \mathbf{H}(\mathbf{r}, t) \end{Bmatrix} \equiv \begin{Bmatrix} \mathbf{E}(z) \\ \mathbf{H}(z) \end{Bmatrix} \exp[-i(\omega t - \beta x)], \quad (8)$$

where β is so-called *propagation constant*, the wave vector in the direction of propagation along x axis. Now we have to verify that the proposed waves are indeed solutions of the problem at hand. In order to do so, we will take an advantage of working with homogeneous nonmagnetic media without external charges and currents, and combine Maxwell's equations (1) to yield two so-called *wave equations* for both \mathbf{E} and \mathbf{H} [2]:

$$\left(\nabla^2 - \varepsilon \mu_0 \frac{\partial^2}{\partial t^2} \right) \begin{Bmatrix} \mathbf{E}(\mathbf{r}, t) \\ \mathbf{H}(\mathbf{r}, t) \end{Bmatrix} = 0. \quad (9)$$

The proposed solutions, represented by Eq. (8), can be now inserted into the wave equations (9) to get a new form of wave equations suitable for description of guided electromagnetic waves:

$$\left[\frac{d^2}{dz^2} + (k_0^2 \varepsilon_r - \beta^2) \right] \begin{Bmatrix} \mathbf{E}(z) \\ \mathbf{H}(z) \end{Bmatrix} = 0, \quad (10)$$

where $k_0 = \sqrt{\varepsilon_0 \mu_0} \omega$ is the wave vector of the propagating wave in a vacuum.

Next step is to further constrain the six field components of $\mathbf{E}(z)$ and $\mathbf{H}(z)$ by inserting the proposed solution directly into Maxwell's equations [2]. This action reveals that only two sets of three nonzero field components can exist in this situation:

a transverse magnetic (TM or p-) mode with the components (E_x, E_z, H_y) and a transverse electric (TE or s-) mode with the components (E_y, H_x, H_z) . Next step is to write down the solutions at each side of the boundary (i.e., for wave vectors in the two media $k_{d/m}$ perpendicular to the interface) and couple them using the continuity conditions for H_y and $D_z = \varepsilon E_z$ (TM mode) and for H_x and E_y (TE mode) [1]. Application of these conditions leads to a rather surprising finding that the TE mode is incompatible with solutions bounded to the interface. The only possible polarization of the surface waves is therefore the TM mode with the one set of field amplitudes at the dielectric side ($z > 0$, the $-k_d z$ term, in blue) and another set at the metallic side ($z < 0$, the $+k_m z$ term, in red):

$$E_{x,d/m}(z) = \pm i \frac{k_{d/m}}{\omega \varepsilon_0 \varepsilon_{r,d/m}} \exp(i\beta x) \exp(\mp k_{d/m} z), \quad (11a)$$

$$E_{z,d/m}(z) = -\frac{\beta}{\omega \varepsilon_0 \varepsilon_{r,d/m}} \exp(i\beta x) \exp(\mp k_{d/m} z), \quad (11b)$$

$$H_{y,d/m}(z) = \exp(i\beta x) \exp(\mp k_{d/m} z). \quad (11c)$$

The waves with such polarization are exactly the aforementioned SPPs, which are the central topic of this thesis. We will now explain them in more detail as we will bring out yet another restriction on their properties. This time it will be relations between the individual components of the total wave vector, which can be derived from the continuity conditions and Maxwell's equations, as follows:

$$\frac{k_d}{k_m} = -\frac{\varepsilon_{r,d}}{\varepsilon_{r,m}}, \quad (12a)$$

$$k_{d/m}^2 = \beta^2 - k_0^2 \varepsilon_{r,d/m}. \quad (12b)$$

If we recall that we are looking for solutions that are confined to the interface, i.e., with the evanescent decay in the perpendicular z -direction in our geometry, we arrive to the conclusion that according to Eq. (11) this restricts the real parts of wave vectors $k_{d/m}$ to only positive values. If we neglect the losses in the environment (i.e., if we consider only real permittivities and wave vectors), the condition represented by Eq. (12a) can be fulfilled only if $\varepsilon_{r,d}$ and $\varepsilon_{r,m}$ have opposite signs. And because dielectrics have in general positive dielectric function, we have finally established the single reason why materials with the negative real part of the dielectric function are essential for plasmonics. The largest class of materials with this property are naturally metals. Preferentially noble metals with high charge carrier density and therefore high plasma frequency that allows SPP formation even at optical frequencies (see Fig. 3). But even materials with bound charge carriers can sometimes have negative ε_1 . This is illustrated by the high-frequency side of the resonance modelled by a Lorentz oscillator in Fig. 1. The Lorentz model is used to represent many sources of dielectric polarization like, e.g., lattice vibrations or excitons. Accordingly,

also in those cases, the physics related to negative ε_1 leads to the coupled light-matter excitations. They are called surface phonon polaritons or surface exciton polaritons and they have qualitatively very similar properties as the SPPs discussed here, but their description is beyond the scope of this thesis [18, 19].

We will now proceed further and by combining equations (12a) and (12b) we will get the major result of this section, a very important characteristic of SPPs — the dispersion relation that links their propagation constant and frequency:

$$\beta(\omega) = k_0(\omega) \sqrt{\frac{\varepsilon_{r,d}(\omega)\varepsilon_{r,m}(\omega)}{\varepsilon_{r,d}(\omega) + \varepsilon_{r,m}(\omega)}}. \quad (13)$$

To better understand the dispersion relation of SPPs it is useful to revise the dispersion relation of electromagnetic waves in a homogeneous bulk medium: From Maxwell’s equations it follows that two types of generic dispersion relations can exist based on the polarization of the electric field vector. Transverse waves, where the electric field is perpendicular to the wave vector ($\mathbf{k} \cdot \mathbf{E} = 0$), must obey the dispersion relation $k^2 = \varepsilon_0 \mu_0 \varepsilon_r(\omega) \omega^2$. The longitudinal waves ($\mathbf{k} \cdot \mathbf{E} = kE$), on the other hand, can exist only when $\varepsilon_r(\omega) = 0$ [2]. Inside conventional dielectric media, away from resonances of their dielectric polarization, $\varepsilon_{r,d}(\omega)$ can be well approximated by a positive constant so the dispersion relation for the transverse waves $\omega = (\varepsilon_0 \mu_0 \varepsilon_r)^{-1/2} k$ is a simple linear function (so-called *light line*). Note that because $\varepsilon_{r,1} \neq 0$, the longitudinal waves cannot even exist in such a medium. To see how this situation changes inside bulk metals, we will now insert into Eq. (12b) the realistic Drude component of the dielectric function of gold with negligible damping (blue curve in Fig. 3a, Eq. (7) with $\Gamma = 0$). The result is shown in Fig. 5a and a significant departure from the light line can be observed. For $\omega > \omega_p$, $\varepsilon_{r,m}$ is positive and real, the bulk wave vector k is also real (we do not need to stick to the in-plane wave vector β in this case), and the metal supports propagation of transverse waves with a group velocity $v_g = d\omega/dk < c$. As the frequency decreases, the waves “slow down” until the point of $\omega = \omega_p$ is reached and collective ($k = 0$) longitudinal ($\varepsilon_{r,m} = 0$) oscillations called *volume plasmons* occur. Volume plasmons represent the free electrons oscillating at their natural frequency ω_p . They are, however, presented mainly for completeness here, as they are not very relevant to applications because they do not couple to transverse electromagnetic waves. The remaining region of the dispersion relation of light inside bulk metals corresponds to frequencies below ω_p , where ε_r is negative and real, the wave vector k is purely imaginary (its magnitude is represented by the grey area in Fig. 5a) and the electromagnetic waves cannot propagate inside but only exponentially decay within the metal.

Similar considerations as for the dispersion relations of bulk materials can be applied for the dispersion relations of SPPs that are supported on a metal–dielectric

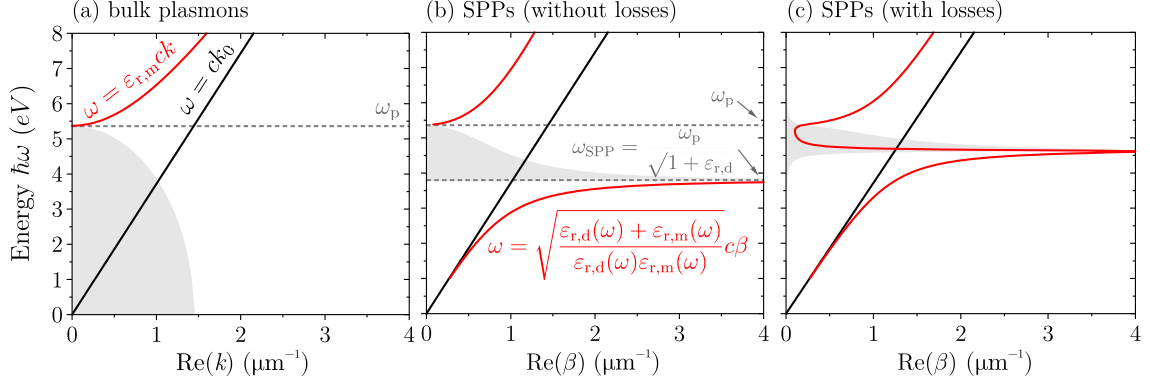


Fig. 5: Dispersion relations of plasmons (red lines). The magnitudes of the imaginary parts of the wave vectors are represented by the grey-filled curves. Dispersion relations of waves propagating in vacuum (light lines) are also plotted for reference (black lines). (a) Dispersion relation of bulk plasmons in a metal, which is represented by a lossless Drude oscillator with plasma energy $\hbar\omega_p = 5.37$ eV (which closely corresponds to gold). (b) Dispersion relation of SPPs at the interface between a vacuum and the same Drude material as in (a). (c) SPP dispersion relation for a Drude material with the same $\hbar\omega_p$ as in (a) and (b) but with the additional damping ($\hbar\Gamma = 0.08$ eV).

interface. Dielectric functions of both materials just have to be fed into Eq. (13). The results of such calculations for an interface between vacuum and the same lossless Drude model of gold as above and are shown in Fig. 5b. The SPP dispersion is very similar to that of bulk metals at frequencies above ω_p , where the radiation penetrates into the metal. Below ω_p , there is a frequency band gap region where wave vector β is again purely imaginary and propagation of electromagnetic waves inside the metal is forbidden. But at even smaller frequencies below this band gap, there is a region where SPPs can exist: In the limit of low frequencies, β is close to the light line and SPPs have a form of a conventional light wave under grazing incidence angle. The nature of these so-called *Sommerfeld-Zenneck waves* is illustrated by their calculated electric field profile shown in Fig. 6a. The fields of this sort of SPPs are almost exclusively distributed inside the dielectric and they are therefore only weakly attenuated and have very large propagation lengths $L_x \equiv [2\text{Im}(\beta)]^{-1}$. On the other hand, Sommerfeld-Zenneck waves are only weakly confined to the interface and thus extend significantly into the dielectric, as governed by Eq. (12b). On the other side of the SPP band, the SPP dispersion diverges from the light line and β goes to infinity as the frequency approaches the characteristic SPP frequency $\omega_{\text{SPP}} = \omega_p / \sqrt{1 + \epsilon_{r,d}}$. The group velocity of SPPs goes to zero (as in the case of volume plasmons) and the field acquires a quasistatic character with the characteristic field profiles, which are sketched in Fig. 4 and calculated in Fig. 6b. The losses in real metals slightly alter this ideal picture, as can be seen in Fig. 5c. Adding realistic

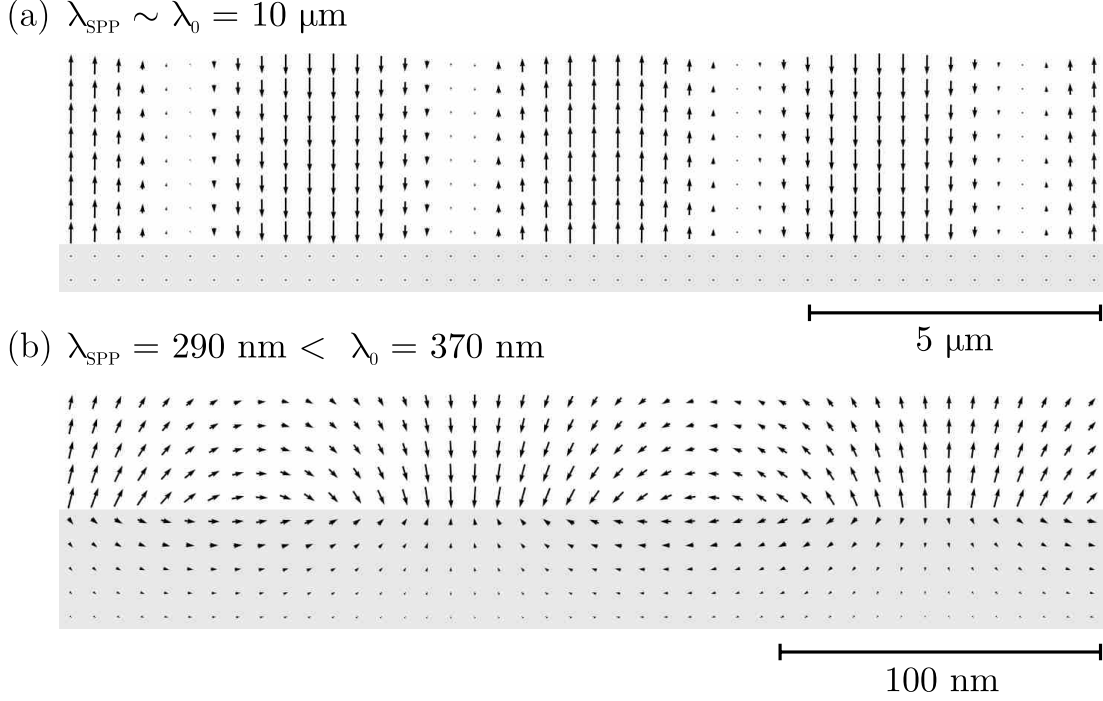


Fig. 6: Electric field profiles of SPPs at a silver–air interface calculated at two free-space wavelengths: (a) $10 \mu\text{m}$ (0.12 eV), corresponding to Sommerfeld–Zenneck waves with only a slightly smaller wavelength and low confinement, which do not penetrate into the metal, and (b) 370 nm (3.35 eV), corresponding to SPPs with much smaller wavelength that are confined to the interface from both sides. A derivative of an animation by Steven Byrnes [20].

losses $\Gamma > 0$ while keeping the same ω_p leads to damping of the SPP resonance and it places an upper limit on the achievable propagation length L_x . Losses in the metal also put a lower bound both on the SPP wavelength $\lambda_{\text{SPP}} = 2\pi/\text{Re}(\beta)$ and on the penetration depth $\delta_{\text{d/m}} = 1/|k_{\text{d/m}}|$, which characterizes SPP’s confinement towards the interface. At the same time, the impenetrable band gap between ω_{SPP} and ω_p vanishes because β becomes complex in this region and SPPs can leak into free space. The relationship between the confinement and attenuation of SPPs is demonstrated in Fig. 7. As the wave energy $\hbar\omega$ approaches SPP resonance from both low- and high-frequency sides, the propagation length L_x is drastically decreased due to losses. This process is accompanied by a simultaneous decrease of the penetration depth $\delta_{\text{d/m}}$ at both sides of the interface. In resonance, the SPP is confined even below the wavelength of the corresponding light wave propagating in a vacuum [21]. This inevitable trade-off between losses and confinement is a natural complication for many plasmonic applications where the highest possible confinement is more than desirable [22]. The last important feature of the dispersion relation of SPPs is the wave vector mismatch between the light line and the SPP line (see Fig. 5b).

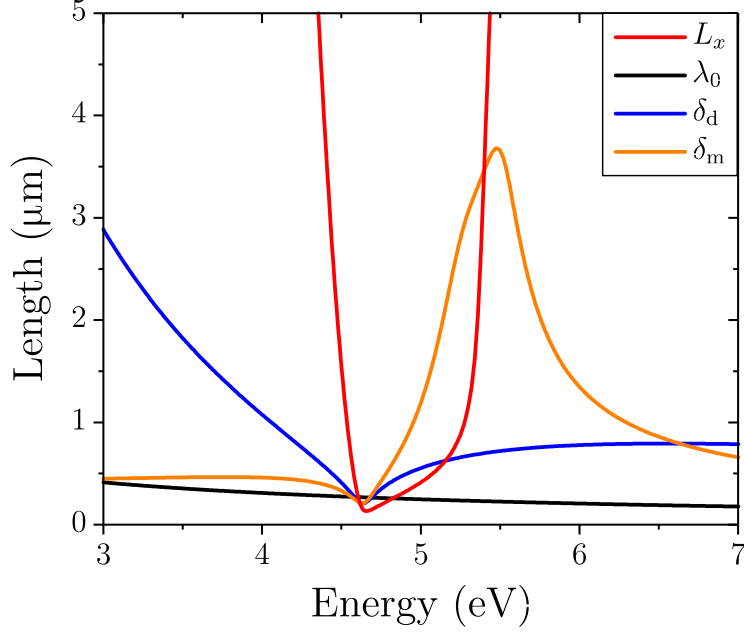


Fig. 7: Important measures of SPP confinement and damping calculated according to the model of Fig. 5c. Propagation constant L_x is related to the attenuation during propagation along the interface. Penetration depth $\delta_{d/m}$ characterizes the exponential decay in the perpendicular direction, i.e., into the dielectric or metal, respectively. Free-space wavelength λ_0 is naturally the characteristic length of propagating electromagnetic waves in vacuum.

Because of it, excitation of SPPs is impossible using propagating transverse waves. There are basically only two kinds of coupling schemes that facilitate the required continuity of the wave vector [23]. The first one relies on the use of evanescent waves that are associated with near-field optical microscopy probes (sharp tips) or total internal reflection (prisms). The latter scheme is now heavily used especially in the field of biosensing (see Fig. 17), where it became a firmly established method for label-free analysis of biomolecules and their interactions, as will be discussed in the next chapter. The second class of coupling schemes is based on diffraction and scattering effects, and it includes excitation of SPPs by gratings or by some other types of surface corrugations.

In this section, we have introduced all the main properties of SPPs: How their existence emerges from equations of electromagnetism combined with models of solid-state matter, how their fields look like, what are the peculiarities of their dispersion relation, and how this translates into their confinement and attenuation. Knowledge of the propagating form of SPPs is essential for understanding almost all topics of nanophotonics. Moreover, from the practical side, SPPs have become mature and even commercialized technology in the field of biosensing. There is, however, yet

another fundamental form of plasmons that manifests itself in a very large spectrum of phenomena — the localized surface plasmon.

1.4 Localized surface plasmons

We have seen that SPPs are two-dimensional, dispersive electromagnetic waves propagating at the interface between a conductor and a dielectric. When the resonance condition is fulfilled, a special kind of SPPs is formed — non-propagating collective oscillations of electron plasma along the interface called surface plasmons. But if the interface is spatially restricted in the lateral direction, like in the case of metallic nanostructures, another class of non-propagating excitations of electron plasma can be formed. In the following paragraphs, we will show how these so-called *localized* surface plasmons (LSPs) arise on the surface of nanostructured metals and how their presence strongly influences the resulting optical properties of the whole system.

We will start our derivation in the same manner as with SPPs, by setting up a simple geometry suitable for an analytical treatment — a spherical particle made of material with dielectric function $\varepsilon(\omega)$, with radius R , immersed in the medium with dielectric function ε_d and illuminated by an electromagnetic plane wave. If the particle dimensions are much smaller than the wavelength of light in the surrounding medium ($R \ll \lambda$), retardation effects are negligible (i.e., the phase of the harmonically oscillating incident electromagnetic field is practically constant over the whole particle). Calculation of the fields inside and outside the particle can then be simplified into finding a solution to the quasi-static problem of a particle in a homogeneous field and only appending the harmonic time dependence to that solution at the end. The situation is sketched in Fig. 8, where the electric field \mathbf{E} of an incident electromagnetic wave induces polarization of free electrons and the attraction coming from much heavier — and therefore motionless — ionic cores then

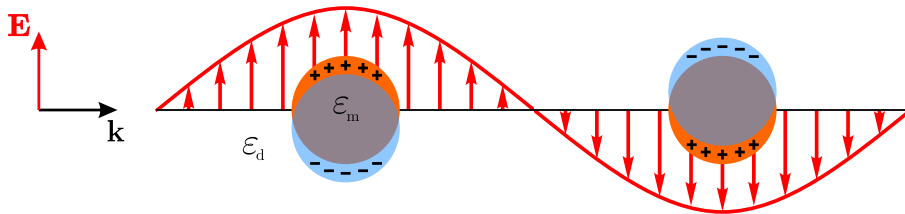


Fig. 8: Schematic illustration of two metallic particles illuminated by an electromagnetic wave with wave vector \mathbf{k} . Oscillating electric field \mathbf{E} forces the electron “cloud” (light blue) to move, whereas the much heavier ionic cores (orange) are virtually unaffected. When the size of a particle is much smaller than the wavelength of light, it is reasonable to reckon the field as homogeneous on the scale of the particle dimensions.

Tab. 1.1: Summary of the resonance conditions and resonance frequencies for the three fundamental plasmon-supporting geometries.

Geometry	Resonance condition	Resonance frequency
Bulk metal	$\varepsilon_1(\omega) = 0$	$\omega_0 = \omega_p = \sqrt{(n_e e^2) / (\varepsilon_0 m_e)}$
Planar metal surface	$\varepsilon_1(\omega) = -1$	$\omega_0 = \omega_p / \sqrt{2}$
Subwavelength sphere	$\varepsilon_1(\omega) = -2$	$\omega_0 = \omega_p / \sqrt{3}$

gives rise to a restoring force. Such behaviour is very similar to the model of Lorentz oscillator (see Fig. 1 and related discussion on p. 6). In the present case, the problem can be solved using Maxwell's equations, which give us the induced dipole moment inside the particle as [2]

$$\mathbf{p} = \varepsilon_0 \varepsilon_d 4\pi R^3 \frac{\varepsilon(\omega) - \varepsilon_d}{\varepsilon(\omega) + 2\varepsilon_d} \mathbf{E} = \varepsilon_0 \varepsilon_d \alpha \mathbf{E}. \quad (14)$$

Note that up to now, we have always considered the dipole moment *density*, defined with the aid of electric susceptibility as $\mathbf{P} = \varepsilon_0 \chi_e \mathbf{E}$. Here we try to describe a single isolated particle, so we use a description based on a single dipole moment $\mathbf{p} = \varepsilon_0 \varepsilon_d \alpha \mathbf{E}$, where the proportionality constant α , the analogue of χ_e , is called polarizability. To establish a connection between P and p , i.e., between the material description (using susceptibility or relative permittivity) and the description of the individual material's constituents (using polarizability), one has to find a self-consistent solution based on their arrangement in the medium (using so-called Clausius–Mossotti relation [10]). In any case, it follows from Eq. (14) that α is resonantly enhanced whenever the term $\varepsilon(\omega) + 2\varepsilon_d$ goes to zero. We have thus arrived to the same conclusion as in the case of SPPs: LSPs can be supported only when the particle has a negative dielectric function. In other words, the particle must be metallic. For particles described by the Drude dielectric function (7) and located in air, this condition is met at the resonant frequency $\omega_0 = \omega_p / \sqrt{3}$ (see Tab. 1.1).

Apart from the polarizability, which was used for demonstration of the resonant nature of LSPs, one can also use Maxwell's equations to obtain the distribution of the electric field inside and outside the sphere [2]

$$\mathbf{E}_{\text{in}} = \frac{3\varepsilon_d}{\varepsilon(\omega) + 2\varepsilon_d} \mathbf{E}, \quad (15a)$$

$$\mathbf{E}_{\text{out}} = \mathbf{E} + \frac{3\hat{\mathbf{n}}(\hat{\mathbf{n}} \cdot \mathbf{p}) - \mathbf{p}}{4\pi\varepsilon_0\varepsilon_d} \frac{1}{r^3} \equiv \mathbf{E} + \mathbf{E}_{\text{sca}}, \quad (15b)$$

where $\hat{\mathbf{n}}$ is the unit vector and r the distance in the direction towards the point of interest, where the fields are evaluated. The resonance in the dipole moment \mathbf{p} ,

represented by Eq. (14), thus implies also the resonant enhancement of both the internal field and the field outside the particle \mathbf{E}_{out} , which can be separated to the incident field \mathbf{E} and the scattered field \mathbf{E}_{sca} . Moreover, the factor $3\hat{\mathbf{n}}(\hat{\mathbf{n}} \cdot \mathbf{p}) - \mathbf{p}$ suggests that the field profile has a character of a simple electric dipole [1]. These properties are illustrated with the aid of numerical calculations in Fig. 9a, which shows a map of electric field enhancement $|\mathbf{E}_{\text{in/out}}|/|\mathbf{E}_0|$ calculated in the vicinity of a silver nanoparticle (NP) illuminated close to its resonant wavelength. When translated into intensity enhancement, values above 50 can be observed in the deeply subwavelength regions. Such nanofocusing ability is one of the most important and useful attributes of metallic nanostructures with many practical applications, as will be shown in the next chapter.

Closely connected with the large field enhancement is yet another attractive feature of metal NPs — enhanced efficiency with which they scatter and absorb incident light. To characterize this process, so-called scattering and absorption cross sections $C_{\text{sca/abs}}$ can be defined as fractions of the total power $P_{\text{sca/abs}}$ [W] scattered or absorbed by a particle and the incident source intensity I_{inc} [W m^{-2}]. In quasi-static approximation, these characteristics can be calculated using specific energy fluxes corresponding to the electromagnetic fields associated with an oscillating dipole [24]:

$$C_{\text{sca}} \equiv \frac{P_{\text{sca}}}{I_{\text{inc}}} = \frac{k^4}{6\pi} |\alpha|^2 = \frac{8\pi}{3} k^4 R^6 \left| \frac{\varepsilon(\omega) - \varepsilon_d}{\varepsilon(\omega) + 2\varepsilon_d} \right|^2, \quad (16a)$$

$$C_{\text{abs}} \equiv \frac{P_{\text{abs}}}{I_{\text{inc}}} = k \text{Im}(\alpha) = 4\pi k R^3 \text{Im} \left| \frac{\varepsilon(\omega) - \varepsilon_d}{\varepsilon(\omega) + 2\varepsilon_d} \right|. \quad (16b)$$

Two important aspects can be observed: First, both processes are strongly enhanced whenever the plasmon resonance condition is fulfilled, in the same manner as the electric field and polarizability. Second, there is a significant difference between scattering and absorption processes in terms of scaling with the NP radius: For very small NPs, the major part of the incident power is absorbed in their volume, whereas for larger particles, electromagnetic waves are mostly scattered. In Fig. 9b is demonstrated how the scattering cross-section resonance of 50 nm silver NP at 410 nm coincides with the enhanced dipolar electric fields at its poles. The absorption cross-section, on the other hand, is much smaller and it spectrally coincides with the penetration of the electromagnetic fields into the NP around $\lambda_0 = 350$ nm.

So far, LSPs were analyzed in the limit of the quasi-static approximation, which is valid only for very small metal NP. Fortunately, in the majority of application-relevant situations, NPs with dimensions below 100 nm and light with wavelengths much larger than that are used, and so this approximation is very useful. Nevertheless, there are some important aspects of LSPs that are not captured by this model.

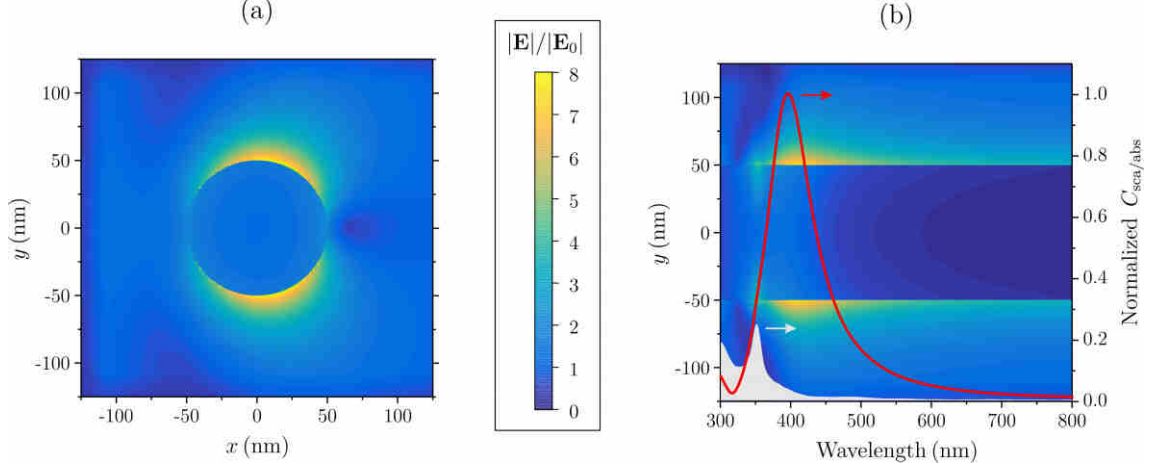


Fig. 9: (a) Electric field enhancement in the vicinity of a silver NP with ($R = 50$ nm), with the characteristic dipolar shape. The map was calculated by finite-difference time-domain solver Lumerical for y -polarized wave propagating along x -axis with $\lambda_0 = 410$ nm. The dielectric function of silver was taken from Ref. [25]. The slight asymmetry of the field is a characteristic of a system beyond quasi-static regime. (b) Spectral dependence of the electric field enhancement along y -axis (at $x = 0$) for the same NP. Normalized scattering (red line) and absorption (grey-shaded area) cross-sections from the same simulation are overlaid over the spectral map as well.

One example is the spectral position of the dipole resonance, which, in reality, broadens and red-shifts with the increasing particle size — an effect that quasi-static approximation does not predict. In Fig. 9a we can also observe a slight deviation from the ideal symmetric dipole fields caused by non-negligible retardation of the incident wave. To account for such effects when dealing with particles of larger sizes, a rigorous electrodynamic approach is needed. This corresponds to solving Maxwell’s equations in a spherical geometry (so-called Mie solution). The resulting fields are then represented by an infinite series of vector spherical harmonics (multipoles) that constitute a set of normal modes [24]. Naturally, the lowest-order approximation of this expansion corresponds to the quasi-static dipole term introduced above. Figure 10a displays predictions of both quasi-static and Mie solution in the form of extinction cross-section $C_{\text{ext}} = C_{\text{sca}} + C_{\text{abs}}$ for a set of gold particles with varying diameters. In both theories, the magnitude of C_{ext} grows with the increasing NP size, as expected from Eq. (16). The changes of the spectral position and width of the LSP resonance, which have been observed in experiments [26], are, however, captured only by the Mie theory. The significant red-shift can be ascribed mainly to retardation effects between the excitation and the depolarization field [27]. The broadening and weakening of the LSP resonance with increasing particle size is caused mainly by the radiation damping (i.e., by the direct radiative decay of the coherent

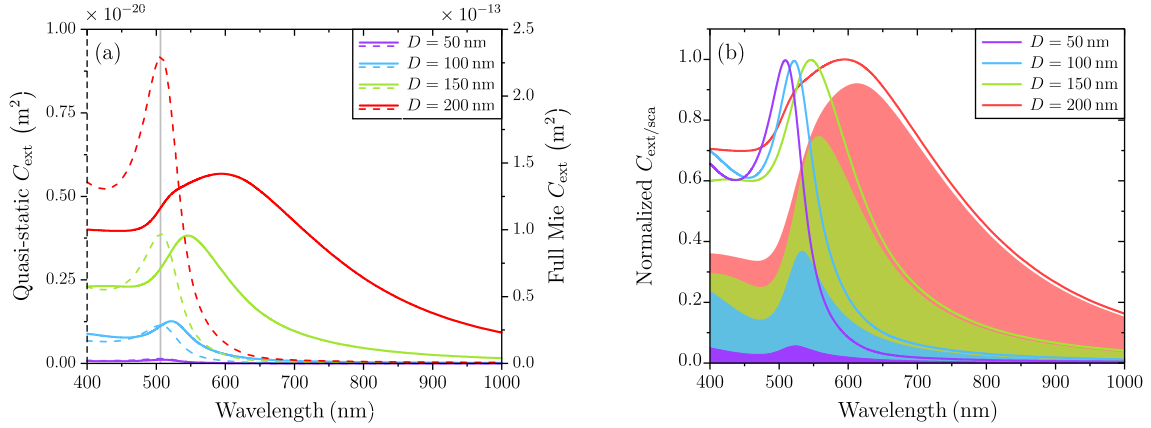


Fig. 10: (a) Extinction coefficient C_{ext} for gold particles with varying diameter D calculated within quasi-static approximation (dashed lines) and using Mie solution (solid lines). The vertical grey line indicates the quasi-static LSP resonance wavelength. The dielectric function of gold was taken from Ref. [11]. (b) Normalized Mie theory C_{ext} (lines) together with the corresponding scattering coefficients C_{sca} (filled areas), which were divided by the corresponding extinction maxima in order to visualize the scattering contribution.

electron oscillation into photons) [28]. To better visualize these features, the normalized C_{ext} spectra are plotted in Fig. 10b together with the corresponding C_{sca} (filled areas). From such a plot it is evident that in the limit of small particles, scattering is very weak and absorption thus dominates extinction. For larger particles, on the other hand, especially at longer wavelengths, scattering is the dominant decay channel.

It should be pointed out that Mie’s analytical solution discussed here is available only for spheres and spheroids [29]. To describe other geometries, one must usually resort to solving Maxwell’s equations using numerical methods. The examples include discrete dipole approximation (DDA), finite-difference time-domain (FDTD) or finite element methods (FEM), where the particular nanostructure of interest is represented by a set of finite polarizable elements whose mutual interactions with applied electric field are self-consistently calculated in the frequency or time domain [30–32]. Development of these methods, together with the increased computational power, resulted in many studies analysing LSP spectra of NPs with various shapes, including triangular prisms, discs, wires, cubes, etc. [33]. Extinction spectra of gold nanorods in Fig. 11 are a typical example. Gold nanorods possess a weak transverse band in the visible (VIS) region, corresponding to the electron oscillations along the short axis, but also a strong longitudinal band in the near-infrared (NIR) region, corresponding to oscillations along the long axis. The latter resonance is very sensitive to the nanorod shape and it experiences a red-shift with increasing aspect ratio. When comparing this red-shift to that of spherical NPs with

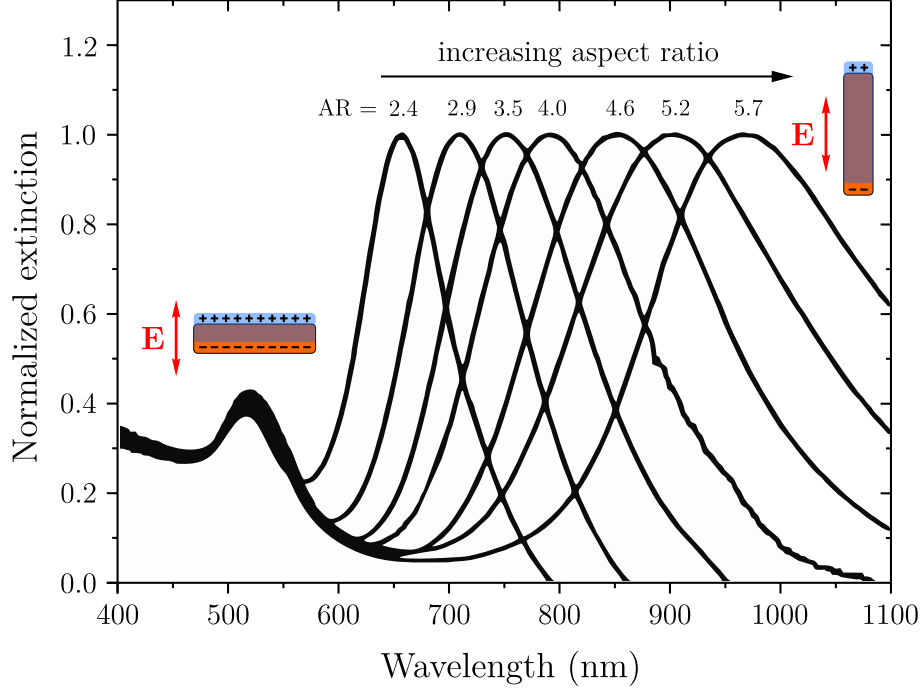


Fig. 11: Measured extinction spectra of gold nanorods with varying aspect ratio. Two modes of electron oscillations driven by the electric field \mathbf{E} (schematically shown) result in two modes of LSP resonance — a weak transverse mode insensitive to the shape of nanorods and a strong longitudinal mode experiencing large red-shift with the increasing aspect ratio. The data were taken from Ref. [26].

varying diameter (Fig. 10), it is obvious that the LSP is much more sensitive to the aspect ratio than to the lateral size. This nicely demonstrates how understanding and controlling the mechanisms of anisotropic growth of NP can result in precise tuning of the LSP resonance through a spectral region spanning several hundreds of nanometres.

1.5 Conclusions

In this chapter, we have described the fundamentals of plasmonics. We began with a comprehensive introduction to Maxwell’s equations and to various representations of optical properties of solid-state materials in terms of their dielectric functions. We then coupled a model of metal–dielectric interface (represented by their dielectric functions) with Maxwell’s equations and we saw how the main properties of propagating SPPs emerged from such a conjunction. In particular, we thoroughly studied their dispersion relation and we highlighted the confined nature of their electric and magnetic fields. The localized counterpart of the propagating plasmons was then introduced, having its origin in laterally confined metallic structures. We explai-

ned the formation of multipolar electromagnetic fields near metal spheres and we described the three resonantly enhanced entities: scattering, absorption, and field magnitudes. One of the main points was that the properties of SPPs and LSPs can be tuned by varying both the constituting dielectric functions and the geometry of the constituents (their size and shape). This fact has recently gained importance with emergence of nanotechnology, which resulted in virtually unrestricted freedom in the possible shapes and the choice of materials that can be used to design plasmonic elements. As a result, many new interesting phenomena were discovered and plasmonics even entered some new fields of study. The next chapter will introduce the essential nanofabrication methods and will summarize the most important applications of plasmonics with a special emphasis on the three most relevant fields for this work: sensing, metasurfaces, and hot electrons.

2 APPLICATIONS OF PLASMONICS

I would like to describe a field, in which little has been done, but in which an enormous amount can be done in principle. This field is not quite the same as the others in that it will not tell us much of fundamental physics — in the sense of, “What are the strange particles?” — but it is more like solid-state physics in the sense that it might tell us much of great interest about the strange phenomena that occur in complex situations. Furthermore, a point that is most important is that it would have an enormous number of technical applications. What we want to talk about is the problem of manipulating and controlling things on a small scale.

There’s Plenty of Room at the Bottom
RICHARD P. FEYNMAN

The theory of plasmonics predicts the extraordinary light-concentrating ability of nanostructured metals. Without nanotechnology, however, the unique features of SPPs and LSPs would lack the practical relevance. In this chapter, we will therefore first introduce the techniques that can be used to prepare metal nanostructures. We will focus on the top-down strategy, which resides in selective removal of material from bulk (lithography or milling), but also on the bottom-up methods, where the nanostructure building blocks are assembled one by one under external or internal stimuli. Then we will introduce the concept of metal nanostructures acting as optical antennas and overview the most important applications of the related unique plasmonic effects.

2.1 Fabrication of plasmonic nanostructures

A typical nanoengineering workflow consists of three key processes: theoretical description, nanofabrication, and experimental characterization. The production cycle usually starts with an idea that is followed by theoretical calculations or numerical simulations in order to find an initial guess for the nanostructure shape and dimensions. Once the device has been fabricated, its performance can be then tested experimentally, and the results can be used in the next optimization cycle. To exploit the most advanced concepts in plasmonics and to be able to proceed through several rounds of optimization, one must be able to reliably produce high-quality nanostructures with good repeatability. Fortunately, the nanofabrication tools have experienced a rapid development in the past decades, driven primarily by the semiconductor industry.

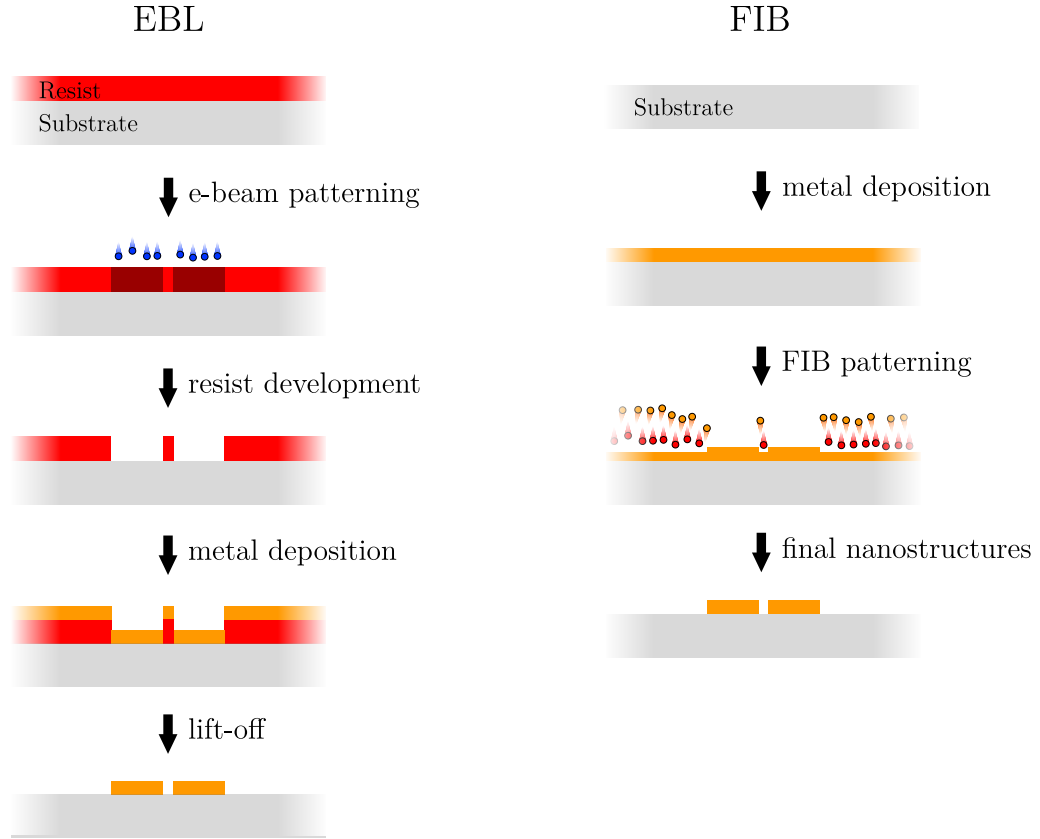


Fig. 12: Sketch of the main steps of standard EBL and FIB nanofabrication. After [34].

Electron beam lithography (EBL) is the workhorse of nanofabrication. It makes use of an electron-sensitive polymer layer (resist) that is spin coated onto a sample and which is then selectively irradiated by a sharply focused electron beam to accurately define the desired geometry (see Fig. 12a). After the resist development, deposition of a plasmonic film, and the final lift-off process, nanostructures with sub-10 nm features can be produced [35]. Although powerful and very popular, this method has several drawbacks. First, EBL is unsuitable for fabrication on large scales ($>1\text{ cm}^2$) because of its serial nature and low throughput (on the order of $10^{-10}\text{ m}^2\text{ s}^{-1}$) [36]. Other challenges are associated with the lift-off process, which does not allow production of nanostructures with large height-to-width ratio, or challenges related to the necessity of working only on conductive substrates.

Focused ion beam (FIB) milling is a technique that can be considered the inverse of EBL. Instead of depositing plasmonic material only on the pre-patterned locations, it is based on local sputtering of metal films by a tightly focused beam of Ga^+ or He^+ ions scanning over it. FIB is the ideal technique for production of very narrow slits inside optically thick metal films [37]. Moreover, it can be used for nanostructuring of single-crystalline metal flakes and thus for producing high-quality

nanostructures [38]. The major disadvantage of FIB milling is even lower throughput than in the case of EBL (on the order of $10^{-13} \text{ m}^2 \text{ s}^{-1}$), which precludes this technique only for prototyping tasks [39]. Although some of the limitations of EBL and FIB have been partially overcome by soft lithography [40], nanoimprint lithography [41], nanoskiving [36], or template stripping [42], new methods are still investigated in order to find faster or more versatile ones [43].

An alternative to the aforementioned top-down methods is naturally the bottom-up approach [44]. On the smallest scale, it is represented by colloidal NP synthesis, where the atoms themselves can be the building blocks. Due to its versatility and scalability, colloidal synthesis is an essential method for production of metal NPs with controllable size, shape, material composition, or surface termination [45]. A survey of NP shapes that can be produced are shown in Fig. 13.

Although free NPs in their native colloidal solutions have found their use in biosensing [46, 47], water treatment [48], or drug delivery [49], there are many applications which require immobilized and precisely placed NPs. In this respect, unfortunately, the bottom-up methods are still no substitute for the precisely controlled top-down techniques. Nevertheless, several concepts for guided self-assembly of NPs have been developed. Arguably the most important are the combined methods, which take the best of the two worlds — the high quality and versatility of colloidal NPs, and the high level of control and precision of the top-down patterning. In principle, they rely on guided self-assembly of the colloidal NPs onto substrates that are pre-patterned by some sort of a lithographic process. This leads to spatial organization of NPs with controlled interparticle distances and mutual orientations (see Fig. 14a). The driving stimuli can be chemical ones (based on spatially modified surface groups or attached molecules [50, 51]), electrostatic ones (based on spatially charged insulating layers [52–54]), or topographic ones (based on modified surface topography and utilization of capillary forces during the solvent evaporation [55–57]). When the precise spatial positioning of NPs is not that important, but their mutual orientations are, so-called hierarchical self-assembly methods usually come into play (see Fig. 14b). These are based on self-assembly not onto the substrate, but on some sort of guiding scaffolds like DNAs, proteins, or block copolymers [58–60]. The last method we will mention here is optical printing, where optical gradient forces acting upon NPs result in the mechanical manipulation of dielectric particles and their subsequent stable optical trapping [61–63]. Recently, after the trapping of not only dielectric, but also metal NPs was demonstrated, this technique was quickly adapted for fabrication in the field of nano-optics (see Fig. 14c).

The current section provided a brief overview of the most common techniques used for fabrication of plasmonic nanostructures. Of course, more information can be found in the dedicated reviews [64, 65]. The list of the reported methods is by no

means exhaustive, as this field is rapidly developing and new innovative approaches are frequently reported. Because the fabrication is not the central point of this work, we will now focus more on a description how plasmonic nanostructures act as light concentrators and optical nanoantennas.

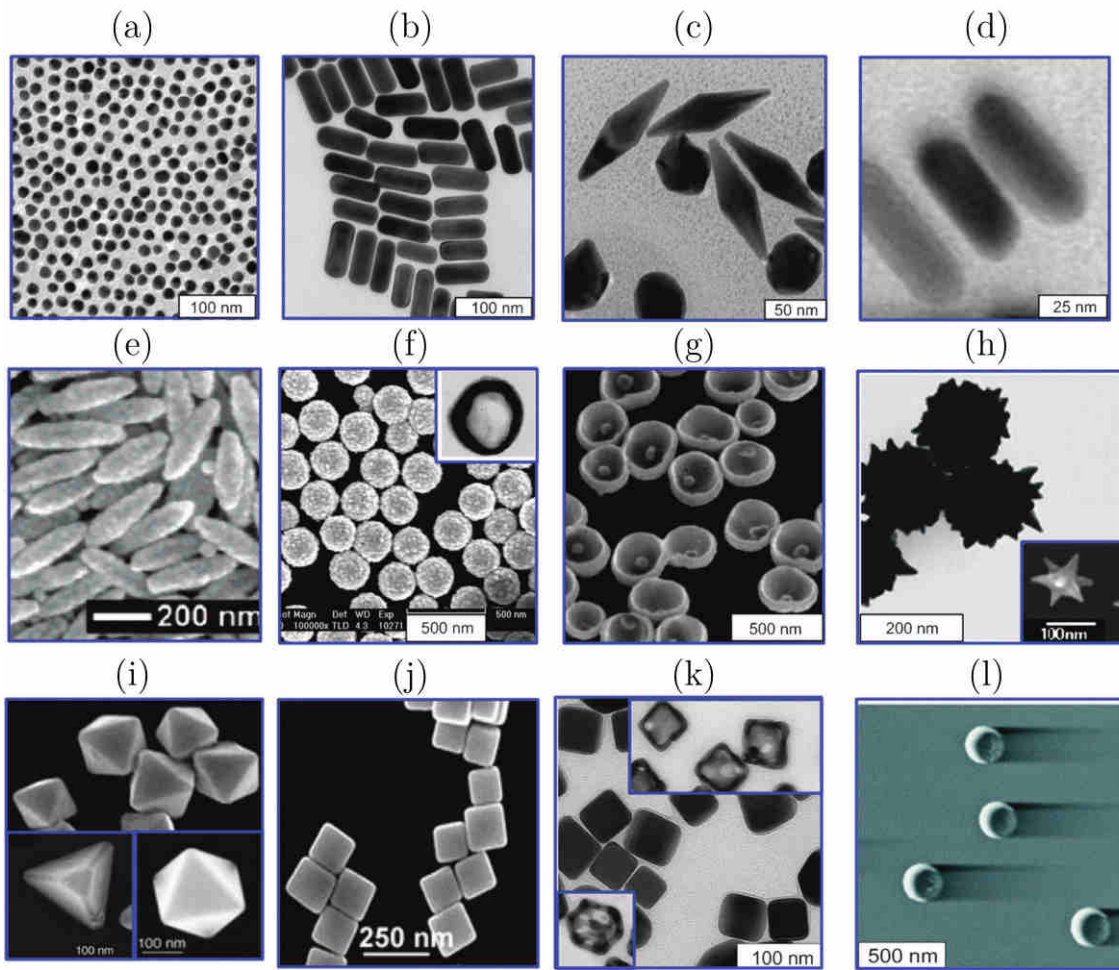
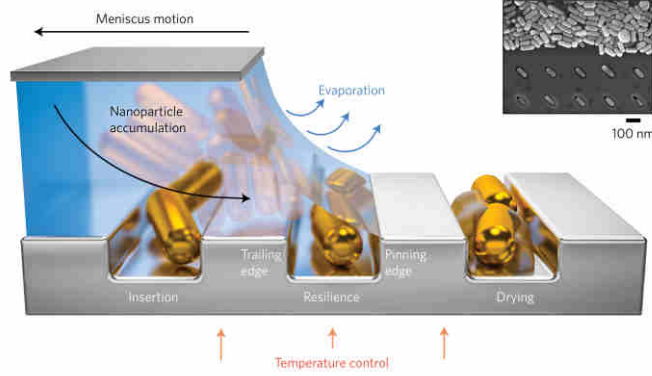
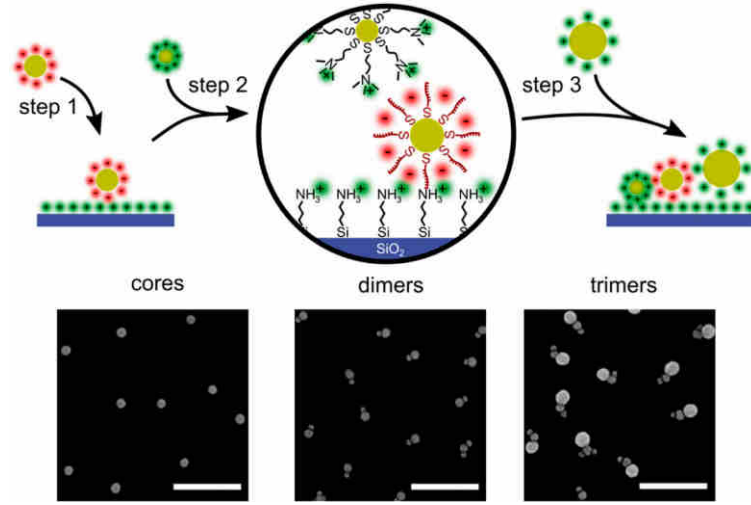


Fig. 13: Various types of plasmonic NPs. (a) 15 nm colloidal Au nanospheres; (b) 70 nm×30 nm Au nanorods; (c) Au bipyramids; (d) Ag@Au nanorods; (e) Au@Fe₂O₃ “nanorice”; (f) 17 nm@160 nm nanoshells, the inset shows a hollow nanoshell; (g) 250 nm Au nanobowls with 55 nm seeds inside; (h) spiky Au@SiO₂ nanoshells, the inset shows a Au nanostar; (i) Au tetrahedra, octahedra, and cubooctahedra; (j) Au nanocubes; (k) Ag nanocubes and Au-Ag nanocages (in the insets) obtained from them; (l) Au nanocrescents. Reproduced from [66].

(a) Combined



(b) Hierarchical



(c) Optical

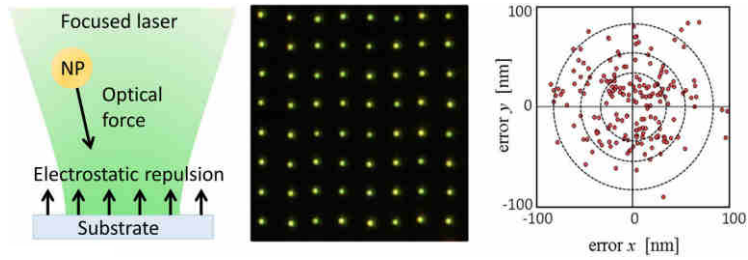


Fig. 14: Selected methods for guided self-assembly of plasmonic NPs. (a) Capillary assembly of NPs onto topographical traps of a low-wetting substrate. Reproduced from [57]. (b) Hierarchic assembly based on electrostatic forces between alternating negatively (red) and positively (green) charged particles on top of a positively charged substrate. Scale bar: 250 nm. Reproduced from [59]. (c) Optical printing process based on optical forces acting on NPs. The dark-field microscope image shows two (10×10) arrays of optically printed 60 nm Au NPs; the 2D scatter plot illustrates the measured printing error. Reproduced from [63].

2.2 Plasmonic antennas

All light–matter interactions at nanoscale suffer from a large mismatch between the wavelength of light and size of the quantum objects that can absorb or emit light (atoms, molecules, quantum dots, etc.), as illustrated in Fig. 15. Because of that, the interaction of light with nanoscale objects is very weak and the absorption/emission rates are very low. Plasmonics can be used to circumvent this issue with the aid of strong local fields around metal nanostructures that facilitate efficient coupling of radiation to and from the quantum objects (see Fig. 9). Radio-frequency (RF) engineering had to deal with the similar mismatch problem in order to achieve the wireless transmission of signals. In that particular context, it meant to overcome a mismatch between the size of a macroscopic electrical circuit and the free-space wavelength corresponding to the signal frequency. This was achieved by connecting

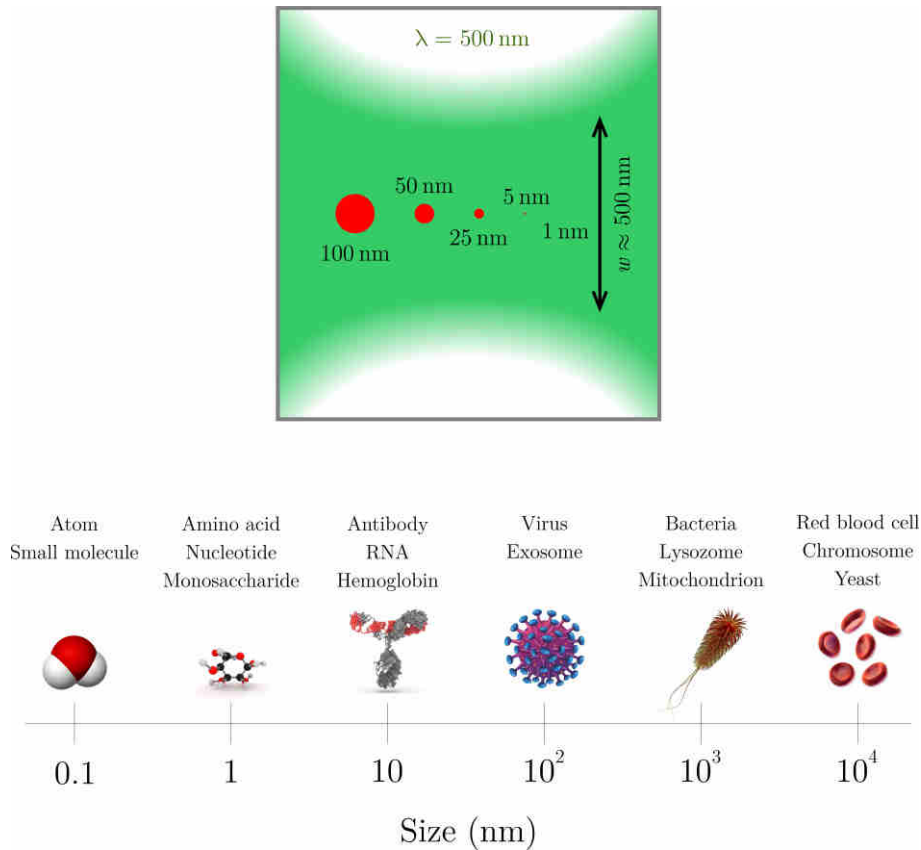


Fig. 15: Top: Schematic illustration of the mismatch between a diffraction-limited focal spot (spot size w is approximately equivalent to the free-space wavelength λ) and sizes of various nanoscale objects (represented by red circles drawn in scale). Bottom: Illustration of nanoscale dimensions including ordered depictions of important biomolecules and organisms. Inspired by [67].

a resonant LC circuit to a wavelength-sized antenna, designed to effectively convert electrical signals into radiation and vice versa. In optics, the same concept can be applied — the role of the optical nanoantennas is then played by plasmonic nanostructures [68].

In section 1.4, we have already established the nanofocusing ability of metal nanostructures, and we illustrated it by the electric field intensity enhancement in deeply subwavelength regions around a silver NP (Fig. 9a). To describe and quantify their optical properties, we then used the classic rigorous Mie theory. But plasmonic nanostructures can be intuitively described also in a different way — as Fabry–Perot resonators for SPPs [69–71]. Note that optical antennas are in fact conceptually very similar to photonic microcavities, but they are specific in their small size, conductivity, and near-field mode of operation [72]. In the resonant cavity model, SPPs that were previously propagating along a boundless interface (Fig. 4) are now laterally confined to represent the nanorod geometry. The SPP waves are then expected to be reflected at the nanorod ends and to interfere. This way, the resonant cavity modes emerge whenever the nanorod length L fits exactly a half-integer number n of the effective wavelength λ_{eff}

$$L = \frac{n}{2} \lambda_{\text{eff}}. \quad (17)$$

An illustrative example of this behaviour is shown in Fig. 16a, where electric field intensity enhancements at three LSP resonances of a silver nanorod are calculated. In the classical RF antenna theory, λ_{eff} would be equal to the free-space wavelength λ , because electromagnetic radiation does not penetrate into the metal, which thus behaves like a perfect electric conductor. But this idealistic description breaks down for metal nanoantennas at optical frequencies, where SPPs with much shorter λ_{SPP} are excited and therefore λ_{eff} must be also significantly shorter. To account for these intrinsic plasmonic effects, for the realistic geometry of the nanoantennas, and for the dielectric properties of the whole system, more sophisticated scaling laws have been developed [73, 74]. In Fig. 16b, the results of so-called “effective wavelength scaling” law are shown for three diameters D of gold cylindrical nanorod antennas. When compared with the perfect conductor case, it is obvious that λ_{eff} is roughly 2–6 times shorter than the free space wavelength and that it also depends on the aspect ratio of the nanostructure.

Large absorption and scattering cross-sections enable nanoantennas to collect electromagnetic energy from the incident radiation with very high-efficiency. The near-field enhancement allows the transfer of most of that energy into small volumes in the vicinity of the nanoantenna. This is a key point for applications of nanoantennas: Focusing light into nanoscale volumes can be used in energy harvesting schemes, like in photovoltaics [76–79] and in photodetection [80–82]. Intense electromagnetic

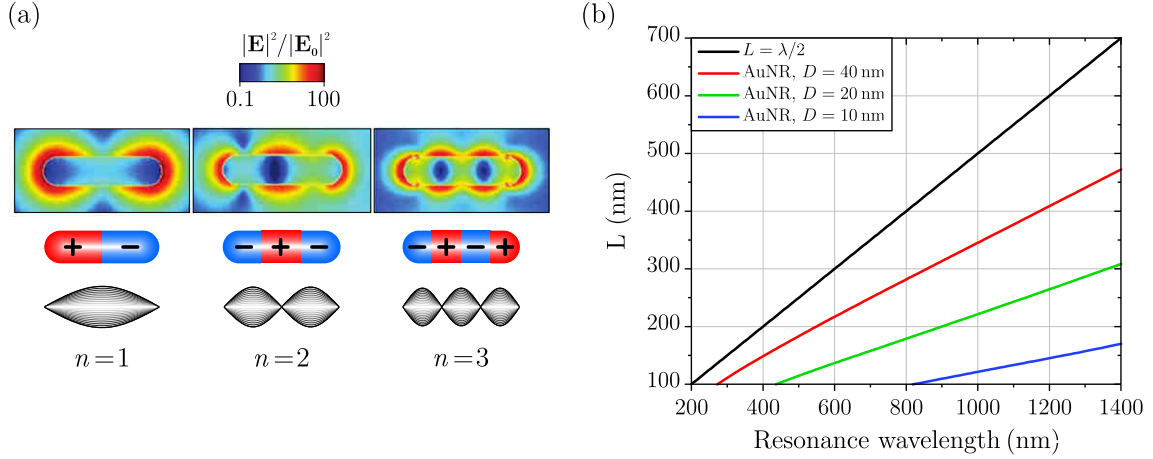


Fig. 16: (a) Numerically calculated electric field intensity enhancement corresponding to the three lowest longitudinal LSP modes ($\lambda_1 = 1380$ nm, $\lambda_2 = 765$ nm, $\lambda_3 = 632$ nm) supported by a silver nanorod with dimension $400 \text{ nm} \times 100 \text{ nm} \times 50 \text{ nm}$ deposited on a glass substrate. The sketches below the field maps show instantaneous charge distributions for the three resonances. Adapted from [75]. (b) $\lambda/2$ antenna length L in the RF limit (black) and calculated using the effective wavelength scaling method for three gold cylindrical nanorods (AuNRs) with varying diameter D located in the vacuum. Data extracted from [73].

fields are also necessary for nonlinear light generation [83–85] and for heat generation [86–88], a simple yet powerful feature connected with metal NPs which has vastly improved magnetic storage technology [89]. Plasmonic nanoantennas have also been established as nanophotonic building blocks — funnelling energy into waveguides [90–92] or controlling the flow of light while acting as modulators [93–95]. As illustrated in Fig. 15, plasmonic nanostructures can be used to enhance interactions of light with matter, both on the emission and the absorption side. This has been utilized in plasmonic lasers [96–98] and also in detection of molecular vibrations via surface-enhanced Raman scattering (SERS) [99] or surface-enhanced infrared absorption (SEIRA) [100, 101].

While certainly not exhaustive, this list of applications of plasmonic nanoantennas shows how utilization of the physics of metal nanostructures, introduced in Chapter 1, transformed many sorts of scientific and technological disciplines. We will now elaborate on three specific topics that have not been mentioned so far, although they are possibly even more influential: plasmonic sensing, metasurfaces, and hot electrons.

2.3 Plasmonic sensing

Sensing is a topic that is in the spotlight of contemporary research in plasmonics and it is also the field where plasmonic nanostructures have proven themselves to be a ground-breaking element. Since its first appearance in 1982 [102], biosensing based on the *propagating* form of SPPs has become a firmly established method for label-free quantitative real-time analysis of biomolecules and their interactions [103–105]. The main principle of SPP biosensing resides in the resonant excitation of SPP at a metal–dielectric interface, while the inherent wave vector mismatch is overcome using prism coupling (see Fig. 17). As the resonant condition for this setup strongly depends on the optical properties of the medium above the interface, we can monitor intensity of the reflected light as a function of time and that way detect the changes of the refractive index caused by adsorption of the investigated analyte. Since the electromagnetic field of SPPs decays exponentially with the distance from the surface and is therefore confined to it, the refractive index changes are therefore probed only in a limited sensing region. Recently, several conceptual improvements for surface plasmon resonance (SPR) sensing have been proposed, including monitoring of the reflected-light phase [106, 107], utilization of long-range SPPs [108], and detection using a spectrometer-less setup [109, 110].

SPR sensors had already become a mature and commercialized technology when the first biosensors based on *localized* SPR (LSPR) appeared around the turn of the millennium [112, 113]. Since then, it has been argued that LSPR sensing, with either NPs or nanoholes [114], could constitute a promising alternative to the classical SPR sensing. Surprisingly, both concepts (LSPR and SPR) exhibit very similar sensing performance in terms of signal-to-noise and wavelength shifts for realistic biosensing [115], although SPR sensors remain unmatched in terms of detection limits of surface coverage [116]. The most significant advantage of LSPR over SPR is almost ten times higher field confinement [117]. This has several important consequences, e.g., better robustness towards temperature fluctuations, which represent a serious problem in SPR sensing [118]. Moreover, as the LSPR sensing does not require bulky and expensive instrumentation to excite SPP, it is much more suitable for ready-made biosensors and point-of-care applications in general [119, 120]. Although the aforementioned benefits can be sometimes outbalanced by higher costs related to nanostructuring processes, together with a vast amount of additional degrees of freedom in biosensing design they represent the main reasons for high application potential of LSPR sensing. This is being constantly proven by advances in this field, recently represented, for example, by a multiplex LSPR detection scheme [121] or by colorimetric sensing based on plasmon coupling. In colorimetric sensing, metallic NPs themselves act as scattering transducers and thus enable de-

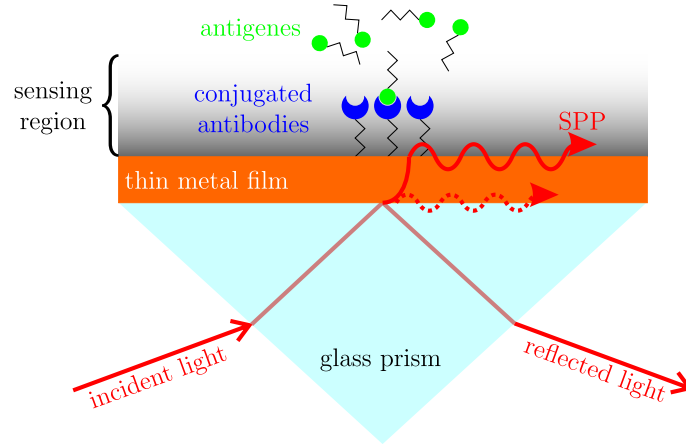


Fig. 17: Plasmonic biosensing with SPPs. A collimated incident light beam is totally reflected at the prism-metal interface, while it excites a SPP at the outer boundary of the metal by an evanescent wave pass through the thin film. The incident angle and wavelength at which the resonance occurs depend on the refractive index of the material located in the sensing region, within the field penetration depth. To achieve the required selectivity of the biosensor, the surface is often functionalized by some chemical recognition elements (antibodies) which represent the chemical counterparts for the pre-selected target molecules (antigens). The binding event then causes a change of resonance condition, which can be detected as a shift of the resonance angle (for a given wavelength) or the resonance wavelength (for a given angle). Adapted from [111].

tection of proteins [122] or nucleic acid imperfections down to a single-base level [123]. Naked-eye detection is even enabled in colorimetric-assay [124] or lateral-flow [125] sensing schemes, the latter being a perfect example of utilization of plasmonics for point-of-care analysis [120].

The SPR and LSPR sensing schemes described above undoubtedly dominate the field of plasmonic biosensing. But despite their undisputable success, they approach limits inherent from their fundamental principles, namely, that they rely essentially on changes of the refractive index in the vicinity of plasmonic materials. This fact renders all above-mentioned variants of plasmonic biosensing inherently non-selective towards specific molecules. They must therefore rely on some sort of chemical functionalization of the sensing surfaces which ensure that only preselected analytes covalently bind to them. These conjugate molecules must be sufficiently specific in order to prevent false signals from interfering substances present in real-world samples, often in higher concentrations than the target analytes [126]. This problem is common to many other label-free detection systems and represents a necessary trade-off between the sensor simplicity and its specificity. It nevertheless renders the evaluation of the (L)SPR-transduced signals problematic, and great efforts must be taken to carefully design associated functionalization protocols [127].

Because of that, other “non-refractometric” methods of sensing, which also utilize plasmonic nanostructures have been explored:

For example, plasmon-enhanced fluorescence, making use of the optical antenna effect described in section 2.2, found quickly its place in sensing [128, 129]. SERS [130] and SEIRA [131], which are based on the similar nanoantenna effect [132], have both become indispensable in chemical (and later biochemical) analysis, enabling sensitivities down to a single molecule level [133, 134]. As a matter of fact, plasmonic refractometric sensing was actually preceded by utilization of nanostructured metals in vibrational spectroscopies of molecules [135, 136]. The major advantage of these two methods dwells in their molecular specificity inherited from their primary (non-enhanced) versions, which is based on detection of specific extinction bands of molecular vibrational modes. As frequencies of these vibrations lay in the mid-infrared (MIR) part of the spectrum, where they can overlap with plasmonic resonances of μm -sized metallic antennas, research into interactions between molecules and nanoantennas and into their impact on optical characteristics is still ongoing [137–139].

We have now introduced the main concepts of plasmonic sensing and also identified the current challenges in this field. It is worth noting that strategies how to overcome the current limitations are a subject of intense research activity. Although only the increased specificity has been discussed in this section, there are many more improvements that are currently investigated. These include mainly utilization of novel materials (dielectrics, conductive oxides or 2D materials [140]), combined use with other read-out methods [141], or identification of spectral signatures of molecules without using spectrometers and laser sources [142].

In the next section, we will briefly describe another interesting area of nanotechnology where plasmonic nanostructures are the indispensable elements — the field of metasurfaces and metamaterials.

2.4 Metamaterials and metasurfaces

In Chapter 1 we have shown how by engineering the shape and size of nanostructures we can control their optical properties, which can then significantly differ from the optical properties of the constituent bulk metal. This practice is taken one step further in the field of metamaterials. A metamaterial is an artificially structured material which attains the desired optical properties from its subwavelength building blocks (meta-atoms) rather than from the constituent material [143]. The metamaterial is therefore inhomogeneous on the nanoscale but its electromagnetic response can be expressed in a homogenized way.

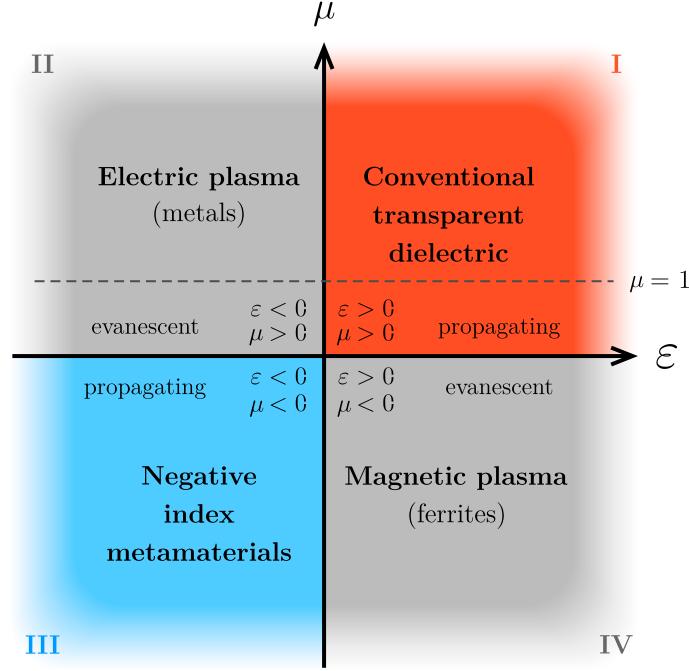


Fig. 18: “Phase diagram” of electromagnetic media. Based on the two fundamental parameters of electromagnetism — electric permittivity ϵ and magnetic permeability μ — all materials can be divided into four categories, each located in a particular quadrant of the parameter space. Inspired by [143].

We have already established that from the point of view of electromagnetism, every material is fully characterized by the form of its response functions — permittivity and permeability — which are dictated by the inner structure and interactions of a particular medium. Based on these two characteristics we can classify materials in a two-dimensional parameter space (see Fig. 18). Conventional dielectric materials, located in the first quadrant corresponding to the positive values of both ϵ and μ , are the most common and also ordinary in the sense that electromagnetic waves can freely propagate through them. The second quadrant represents materials with negative ϵ , typically metals, which have been already extensively discussed in this work with regard to the existence of non-propagating evanescent waves in such media due to presence of electric plasma. In contrast to materials from this quadrant, magnetic materials with negative μ and positive ϵ (fourth quadrant), which would support magnetic plasma oscillations, are far less common. Moreover, beyond GHz frequencies, magnetic polarization currents cannot follow the fast oscillating fields and permeability of all materials is limited to a very narrow region around the non-magnetic $\mu = 1$ line [144]. All metamaterial research is in fact the effort to move material properties away from the non-magnetic lane, into regions where no conventional materials appear, like the third quadrant of Fig. 18, where so-called negative

index metamaterials are located. Originally, metamaterials were almost exclusively equivalent to negative index media [145], which are often associated with perfect lensing [146]. But in the recent years, all sorts of other optical functions were investigated, which allow to tailor the flow of light in unprecedented ways [147]. Due to the fundamental requirement on the subwavelength size of the meta-atoms, it is very challenging to fabricate completely three-dimensional metamaterials working at optical frequencies. But devices based on their two-dimensional equivalents — metasurfaces — have already proven the immense potential of this concept.

In conventional optics, focusing or polarization control are achieved via light propagation through bulk optical elements like lenses or polarizers. In lenses, for example, the focusing ability is based on the fact that incident plane wave acquires spatially varying propagation phase due to spatially varying optical thickness of the glass which forms the lens. In metasurfaces, on the contrary, the same functionalities are achieved by abrupt light phase discontinuities caused by the presence of a subwavelength array of nanoantennas with spatially varying geometric parameters. Each nanoantenna then acts as a tiny resonant source of a spherical wavelet with the specified amplitude, phase, and polarization. Interference of these wavelets then, in line with Huygens' principle, forms a new wavefront with the pre-designed shape. [148]

But how can one control the phase of the light scattered by nanoantennas? First, it is essential to recall that the phase response to the driving field of any resonant system goes through a phase shift of π between the low- and high-frequency side of the resonance [3]. Take, for example, the nanorod antenna in the perfect conductor regime. When the antenna length is smaller than the optimal $\lambda/2$, the induced electric current leads ahead of the incident electromagnetic field. Conversely, when the antenna length is larger, the current lags behind. In any case, the oscillating antenna current then leads to radiation of electromagnetic waves — nanoantenna scatters the incident light. By choosing different antenna lengths, we can control the phase of the induced currents and accordingly also the phase of the scattered waves (see Fig. 19a). To gain full control over optical wavefronts, the meta-atoms should offer the scattered phase that spans a whole 2π region, while ideally having a uniform (and large) scattering amplitude. The single resonators like the nanorod antennas obviously do not fulfil such requirements, but other elements with at least two independent or coupled resonances were found to be adequate for this task [149]. The model example are V-shaped antennas that support two orthogonal plasmonic modes (Fig. 19b) [150]. Because of that, the phase of the scattered cross-polarized light can be tuned over the whole 2π range by adjusting the arm lengths and their opening angles (Fig. 19c). Another type of the metasurface building block is represented by so-called patch antennas, which consist of rod-shaped antennas separated

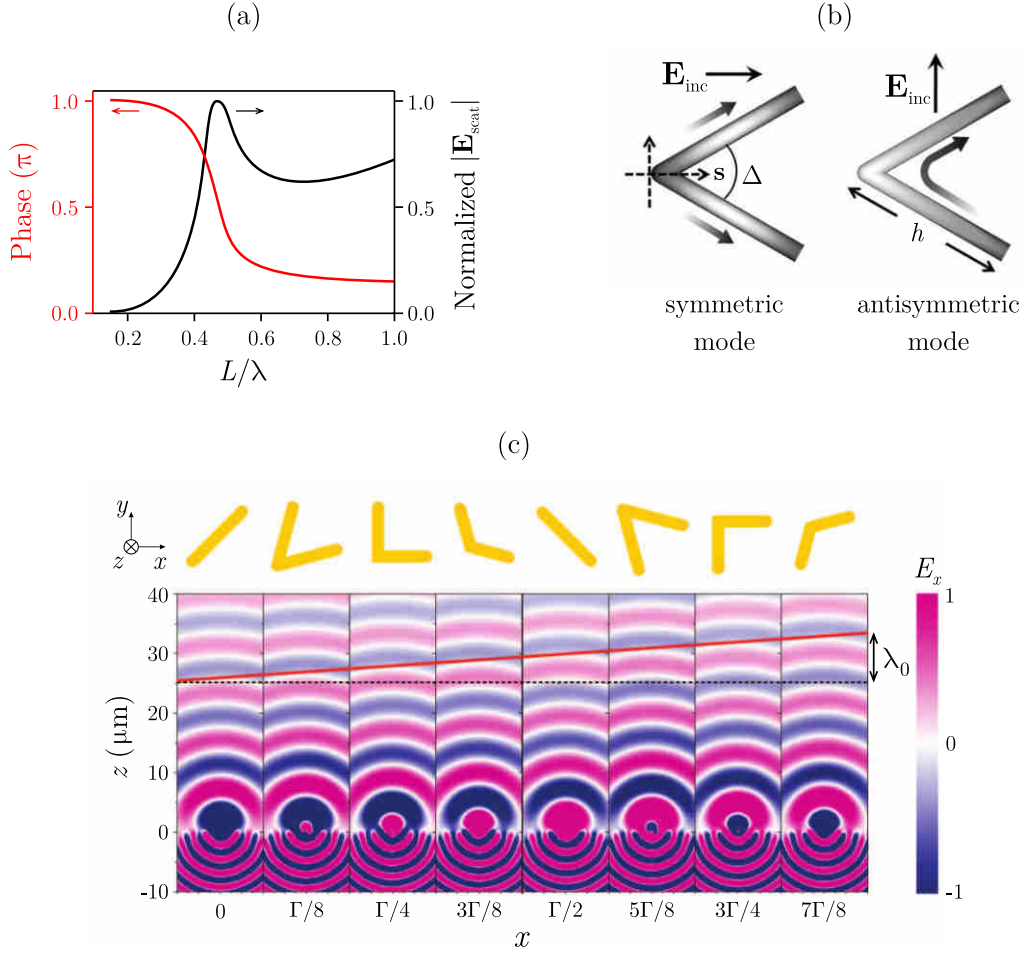


Fig. 19: (a) Analytically calculated amplitude and phase of the scattered light from a straight rod antenna with variable length L made of a perfect electric conductor. Normally incident monochromatic light \mathbf{E}_{inc} with wavelength λ is polarized along the antenna. The scattered light is monitored in the far-field and its phase is calculated relative to that of the excitation. (b) V-shaped antenna is an example of a plasmonic meta-atom with two orthogonal resonant modes — a symmetric one and an antisymmetric one — corresponding to the \mathbf{E}_{inc} parallel and perpendicular to the antenna symmetry axis \mathbf{s} , respectively. The grey scale colour represents the current distribution on the antenna with lighter tones indicating larger current density. The instantaneous direction of the current flow is indicated by arrows with gradient. (c) FDTD simulations of scattered electric fields from the V-shaped antenna array in a metasurface beam deflector. The arm lengths and opening angles of the antennas are designed so that all the antennas have equal scattering amplitudes and the phase of the scattered light accumulated over the whole unit cell in eight steps is equal to 2π . The plots show x -polarized scattered fields for y -polarized plane wave excitation at normal incidence from the silicon substrate located at $z \leq 0$. The antennas are equally spaced at a subwavelength separation $\Gamma/8$, where Γ is the unit cell length. The tilted red straight line is an envelope of projections of the spherical waves scattered by the antennas onto the x - z plane. Adapted from [148].

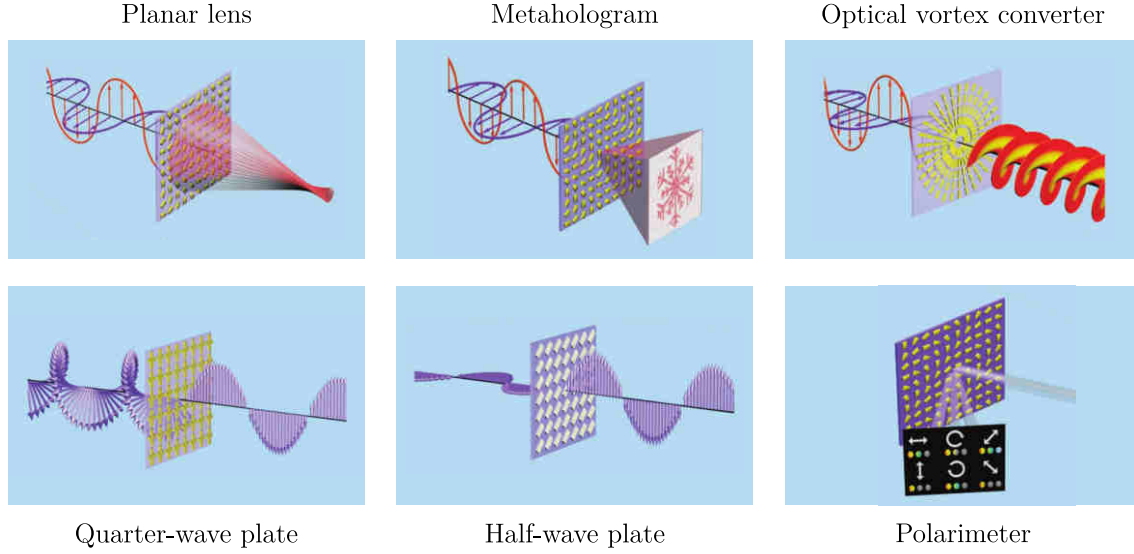


Fig. 20: An overview of metasurface-based applications related to wavefront shaping (top row) and those related to polarization control and detection (bottom row). Adapted from [149].

by a thin layer of insulator from a flat metal plane behind them. Their dipolar plasmonic resonances are then coupled with the corresponding mirror images in the back plane and the full 2π phase modulation of reflectivity can be achieved with very high efficiency just by adjusting the nanoantenna lengths [151, 152]. The phase control can be achieved not only by varying the geometry of the individual elements within a unit cell but also by utilization of rather exotic concept of so-called geometric or Pancharatnam-Berry phase [153, 154]. The phase modulation is then directly associated with the polarization modulation, which can be achieved only by varying the orientation of a single type of anisotropic meta-atom. Recently, an effort to mitigate dissipative losses associated with plasmonic meta-atoms made of noble metals led to utilization of virtually lossless dielectric scatterers, where the phase is altered due to presence of two spectrally overlapping electric and magnetic resonances [155]. Excellent results were achieved also by use of meta-atoms formed by truncated waveguides from dielectric with very high refractive index [156].

Meta-atoms categorized above were used in many optical devices that could potentially replace their conventional bulk counterparts (see the overview in Fig. 20). The most significant progress has been made in the field of metalenses [157], which is now getting close to the industrial production of ultrathin achromatic lenses with exceptional properties [158]. Another important class of metasurfaces is represented by metaholograms, which provide reconstructed holographic images with supreme resolution, field of view, and colour depth [159–161]. Finally, metasurfaces are used for creation of optical vortices [162–164], which gained significant interest due to

their potential applications in optical communications [165]. Apart from the wavefront manipulations introduced so far, metasurfaces can be used also as ultrathin optical components for polarization control and detection, such as quarter-wave plates [166, 167], half-wave plates [168], or polarimeters [169].

In the previous paragraphs we introduced several classes of nanostructured surfaces that can control the amplitude, phase, polarization, or orbital momentum of electromagnetic waves propagating in free space. Many technical and scientific challenges have been already solved in this field, as demonstrated by the fully functional optical components with potentially revolutionary properties [158]. Several challenges remain, however. It is especially the issue of efficiency, which has been partially addressed by utilization of dielectric meta-atoms with significantly reduced losses [156]. Broadband and achromatic operation is also in great demand, yet it is still limited even when the state-of-the-art metasurfaces are considered [170]. Also, to have a significant industrial impact in high-volume applications like, e.g., mobile phone camera modules or wearable displays, the manufacturing process must be also further optimized for the existing foundry technology [171] and, ideally, made tunable using mechanical, electrical, or optical control [172]. The aspect of tunability is especially relevant to this work. We will elaborate on it in the next chapter, where we will describe how the dynamic metasurfaces can be produced with the aid of phase-change materials like VO_2 . But before that, we are going to finish this chapter by a brief overview of an interesting phenomenon related to plasmonic resonances, which has recently gained a renewed interest due to its promises for fundamental research and applications — we are going to discuss plasmon-induced hot carrier generation.

2.5 Hot electrons

After the surface plasmons are excited in metals, they have essentially two decay pathways: the radiative or the nonradiative one. The former corresponds to emission of elastically scattered photons and it is represented by the scattering cross-section C_{sca} , which was discussed on page 19. The latter is associated with creation of electron-hole pairs and it is correspondingly described by the absorption cross-section C_{abs} . As predicted by the Mie theory (Fig. 10), the ratio between these two cross-sections, and accordingly, between the two decay channels is a function of the geometry and composition of the nanostructures. In particular, the smaller the nanostructure and the larger the ratio between the imaginary and the real part of its dielectric function, the larger the nonradiative contribution will be. For some applications, the nonradiative losses are very undesired, as is the case of metasurfaces for

wavefront manipulations, where the highest efficiency of conversion into scattered light is in great demand [156, 173, 174]. On the other hand, there are also applications where the highest possible losses and absorption are desired. To understand why, it is useful to review the mechanism of the nonradiative decay [175, 176].

The processes involved in the decay of plasmons are sketched in Fig. 21: After excitation, the initially coherent plasmons dephase into individual charge carriers (electrons and holes) on a time scale ranging from 1 fs to a few tens of femtoseconds. The initial thermal distribution of charge carriers around Fermi level E_F thus transforms into a highly non-thermal distribution of “hot” electrons and holes. Later, within several hundreds of femtoseconds, electron–electron scattering interactions lead to redistribution of the excess energy among many lower-energy electrons. The charge carriers therefore reach a Fermi–Dirac-like distribution that corresponds to some elevated effective electron temperature. The subsequent equilibration with the lattice (via electron–phonon interactions) occurs over a longer timescale of several picoseconds. Note that the mean free path of electrons in noble metals is on the order of tens of nanometres [177]. With the Fermi velocity of $\approx 10^{15} \text{ nm s}^{-1}$ [178] this means they can random-walk thousands of nanometres within the first picoseconds after excitation. They can thus encounter a vast number of interactions with other electrons, phonons, or with the surface. Finally, after all the excess energy of electrons is inevitably transferred to the lattice, the lattice energy gradually dissipates to the environment in the form of heat. This process can take from 100 ps to 10 ns, depending on the material, the particle size, and the thermal conduction properties of the environment. Note that since the dissipation time is sometimes only slightly longer than the thermalization time, these two timescales are often not fully separable.

The exact electron energy distribution and its time evolution strongly depend on the electronic structure of the material and its surroundings. Take, for example, the band structure of a typical noble metal such as gold (Fig. 22a). From the quantum mechanical point of view, the photon absorption can only involve transitions from the occupied states (below E_F) to the unoccupied states (above E_F), which are separated by the energy $\hbar\omega_{\text{phot}}$ of the absorbed photon. Given the typical noble metal band structure landscape, two kinds of absorption processes can take place, determined by the photon energy: For low photon energies, the absorption process is governed by the dispersion of the partially occupied sp-band (see Fig. 22b). Consequently, there is a large momentum mismatch between the initial and the final state of the electron, and the required momentum must be supplied by some sort of scattering process involving other electrons or phonons [180]. In nanostructured metals, the scattering on their surface can also help to fulfil the momentum conservation law, and it leads to so-called Landau damping of plasmons [181]. For small NPs, this

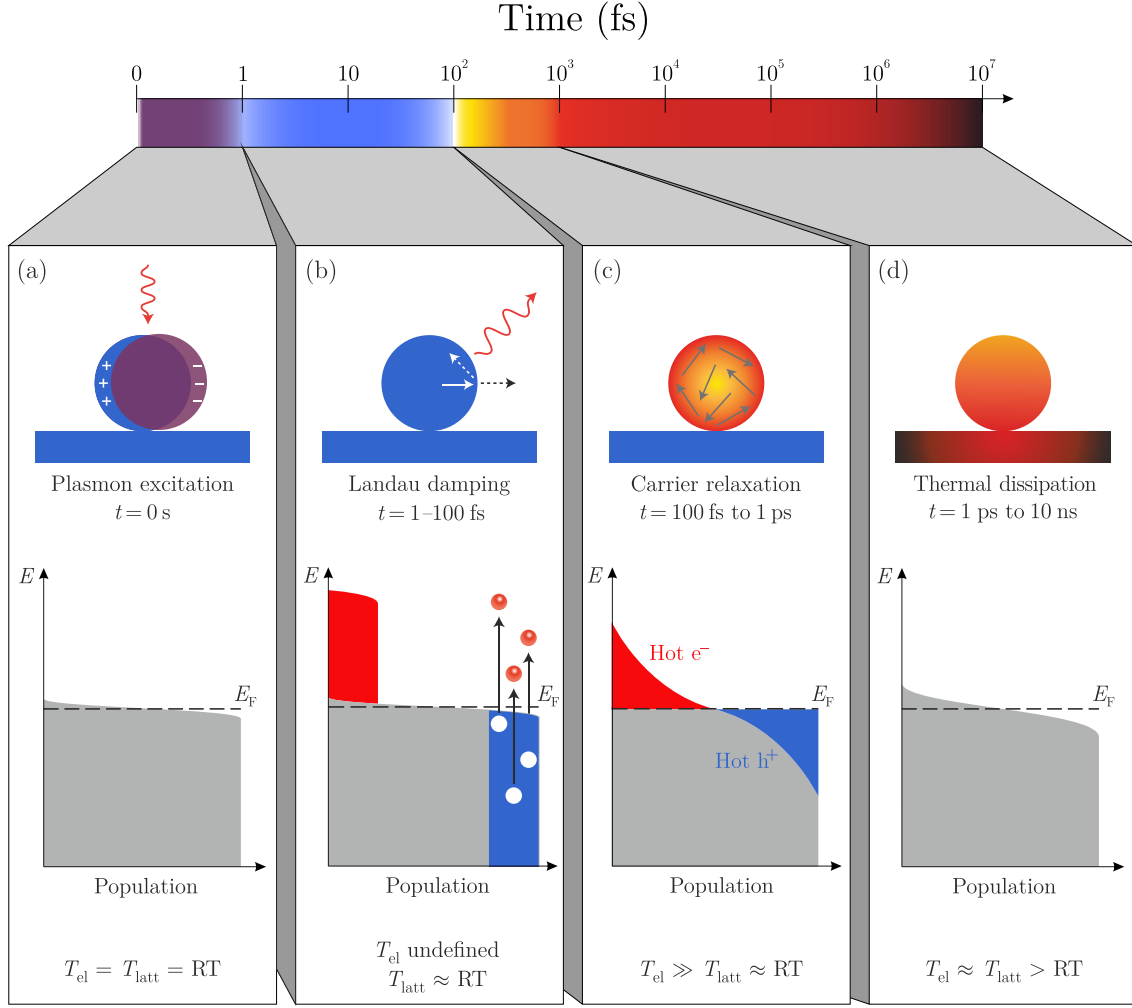


Fig. 21: Photoexcitation and subsequent relaxation processes following the illumination of a metal NP with a laser pulse, and the characteristic timescales. Schematic representations of the population of the electronic states (grey) following plasmon excitation. Hot electrons are represented by the red areas above the Fermi energy E_F and hot hole distributions are represented by the blue areas below E_F . (a) First, the excitation of a LSP redirects the flow of light towards and into the NP, while the effective electron temperature (T_{el}) is in equilibrium with the lattice (T_{latt}) and also with the environment (RT). (b) In the first 1 fs to 100 fs after the excitation, during Landau damping, the excited electron—hole pairs decay either through re-emission of photons or through carrier multiplication caused by electron—electron interactions. During this very short time interval, the hot carrier distribution is highly non-thermal. (c) The generated hot carriers will redistribute their energy by electron—electron scattering processes on a timescale ranging from 100 fs to 1 ps. (d) Finally, the energy is transferred to the lattice and it is dissipated as heat into the surroundings of the metal nanostructure on a longer timescale ranging from 100 ps to 10 ns via thermal conduction. Adapted from [175].

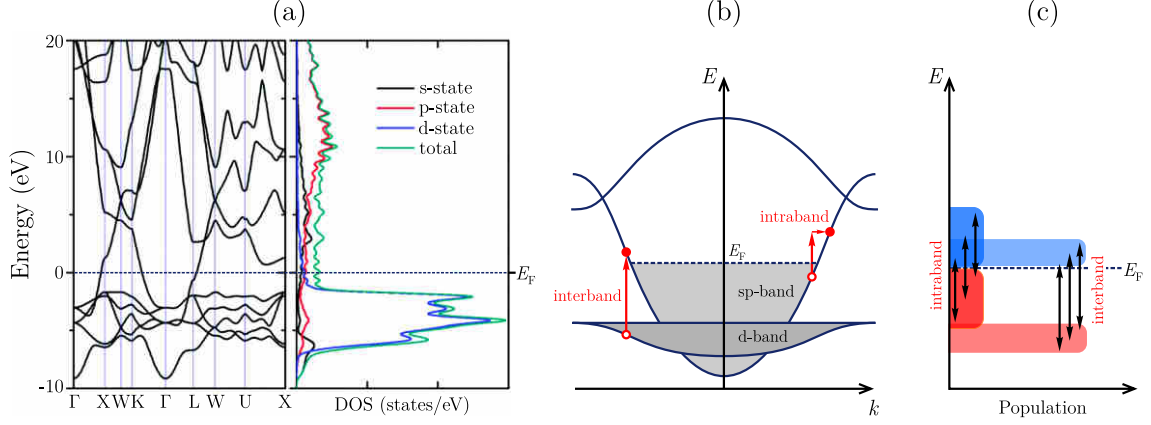


Fig. 22: (a) Electronic band structure of gold (left) and the corresponding projected density of states (right) calculated using density functional theory. Adapted from [179]. (b) Simplified band diagram of gold with two types of absorption processes denoted by red arrows. Intraband transitions (right) require additional momentum from some sort of scattering process. For interband transitions (left), the momenta of initial and final states are equal and no additional scattering is required. (c) Schematic energy distribution of charge carriers created after nonradiative decay of plasmons. The intraband pathway leads to broad energy distributions of hot electrons (dark blue) and hot holes (dark red). The interband pathway leads to narrow distributions of low-energy electrons (light blue) and hot d-band holes (light red).

process is actually the dominant pathway for generation of hot charge carriers [182]. The second scenario is applicable for absorption of photons with higher energies that exceed a certain interband energy threshold (e.g. ≈ 2 eV for Au). In that situation, the deeper d-band states can get involved in the absorption process, the momentum conservation holds even without any external scattering contributions, and direct (vertical) transitions take place. Based on these two described absorption pathways, two distinct regimes of hot carrier generation exist (Fig. 22c): Intraband transitions lead to a broad energy distribution of electrons and holes with moderate energies up to 2 eV and relatively long mean free path up to 40 nm. Interband transitions, on the other hand, are much stronger because the d-band is relatively narrow and has large density of states (DOS; see Fig. 22a). But the energy is transferred mostly to the hot d-band holes, which have very short mean free path (≈ 1 nm), while the electrons can acquire only low energies above the Fermi level.

As outlined above, hot charge carriers can be created at various energy levels based on the electronic structure of the metal, the frequency of the incident light, or the geometry of the whole system [183]. The initial distribution then evolves as the electrons interact among themselves, with the lattice, and also with the environment. The goal of hot carrier science and technology is to control and utilize

these interactions for various purposes. This involves creation of plasmon-induced excitonic states on nearby molecules or semiconductors at very fast timescales in a process called plasmon-induced resonance energy transfer (PIRET, by analogy with Förster resonance energy transfer) [184]. Hot electrons can be also transferred into unoccupied levels of nearby acceptor molecules and induce photochemical transformations [185]. The associated spatial and temporal control over chemical reactions transformed the field of photochemistry, where the most significant were especially the discoveries of unique reaction pathways related to the excitation of hot charge carriers [186–188]. The essence of hot carrier chemical catalysis lies in the excitation of electronic or vibrational transitions inside molecules near the plasmonic nanostructures by the hot electrons in their transient high-energy states [189, 190]. Of particular significance is also utilization of plasmon-induced hot carriers for solar water splitting and artificial photosynthesis [191–193]. Last but not least, the hot carriers can give rise to non-chemical transformations like, for example, plasmon-induced hot-electron injection, which was associated with ultrafast doping [194] or material phase transitions [195, 196]. The usefulness of plasmonic nanoantennas in the fields of photovoltaics and photodetection has been already pointed out with respect to their nanofocusing ability. But it is worth noting that these devices are fundamentally based on the photoexcitation and subsequent separation of electron–hole pairs in semiconductors. And as such, they suffer from very low efficiencies for photons with energies below the semiconductor band gap, which cannot be detected or harvested. But when the semiconductor is in contact with a metal nanostructure, so-called Schottky junction is formed and the hot electrons are naturally separated at this interface [197]. This feature has been employed in several types of solar cells [198–201] and photodetectors [80, 202, 203]. The ultimate product of the nonradiative plasmon decay, the heat, can be put to good use as well. The local heating associated with plasmonic NPs has been utilized in many biological, chemical, or technological applications [86, 88, 204].

To sum up, various effects associated with hot charge carriers have found many applications in all sorts of scientific and technological disciplines. The detailed mechanisms of Landau damping, electron–electron scattering, or PIRET are still not known to a full degree [205, 206]. In this section we provided just a brief overview of the most important processes that are necessary for understanding the main concepts of hot carrier science. In section 5.3, we will build on this knowledge in a study focused on the utilization of charge carriers in electrochemical experiments involving semiconducting inorganic nanotubes coupled with gold nanoparticles.

2.6 Conclusions

In this chapter, we have described the selected applications of plasmonic nanostructures. We started with a quick description of the most important nanofabrication techniques. We then introduced the concept of optical nanoantennas, which is very useful for description of nanofocusing ability of metal nanostructures in the context of light–matter interactions. A multitude of reported applications of nanoantennas, which stem from their extraordinary features, was also overviewed. The three most relevant to this work were explained in greater detail. First, sensing based on SPPs and LSPs was described and critically evaluated. Then, the concept of optical metamaterials and metasurfaces was introduced, together with several examples of metasurface-based equivalents of conventional optical components. The last section was devoted to the physics of hot carriers, which are a product of non-radiative decay of plasmons, and which have received significant attention in the recent years due to their promises for improvements in photovoltaics and especially in photochemistry.

The first two chapters of this thesis were supposed to introduce the reader into its most relevant topics. The goal was to gradually build up the fundamentals of plasmonics and put them into the context of solid state physics and electrodynamics. The broad overview of applications was supposed to help the reader to identify the vast amount of contemporary technological challenges where plasmonics can be of use. Three of these challenges will be thoroughly studied in the following chapters. Namely, the effect of plasmonic nanostructures on the polarization and phase of light, the concept of tunability in plasmonics, and the impact of plasmonic effects on electrochemistry.

3 PLASMONICS FOR CONTROL OF LIGHT

“Science is spectral analysis. Art is light synthesis.”

Pro Domo et Mundo
KARL KRAUSS

In the previous chapter we have established that the plasmonic resonances can be identified in the optical spectra by the features corresponding to enhanced scattering or absorption. Although there is a great variety of experimental techniques suitable for this task, the goal of this section will be to provide a brief overview only of the most important and relevant of them. Then, we will investigate the influence of gold nanorods on upconversion luminescence. At single nanoparticle level, we will show that the plasmon-modulated upconversion emission is very sensitive to the geometry of the whole system and also to the spectral alignment of the plasmon resonance modes and upconversion emission bands. We will also present a novel technique for 3D quantitative phase imaging and demonstrate its unique features by visualization of phase-altering plasmonic metasurfaces.

3.1 Experimental techniques in plasmonics

The simplest way how to detect the “fingerprints” of plasmonic resonances is to simply measure the spectrum of light either transmitted or reflected by a plasmonically active sample. In that case, the enhanced extinction due to plasmon excitation is translated into dips in the transmittance or peaks in the reflectance spectra of the sample. This measurement can be performed either with a simple collimated beam of light or with the help of a more complex microscopic apparatus. Similar variability is available within the domain of spectral decomposition methods. Probably the most common is to use spectrometers — integrated devices with a dispersive element (grating or prism) and a corresponding detector or camera to quantify the spectral distribution of light intensity. The second alternative is to use the Fourier-transform (FT) spectrometers, which are based on a different principle. Whereas in the dispersive spectrometer only a single frequency can reach each individual pixel of the detector, the detector in a FT spectrometer “sees” all the frequencies present in the light beam simultaneously. In more detail, the light from a broadband light source is directed to the Michelson interferometer with one fixed and one moving

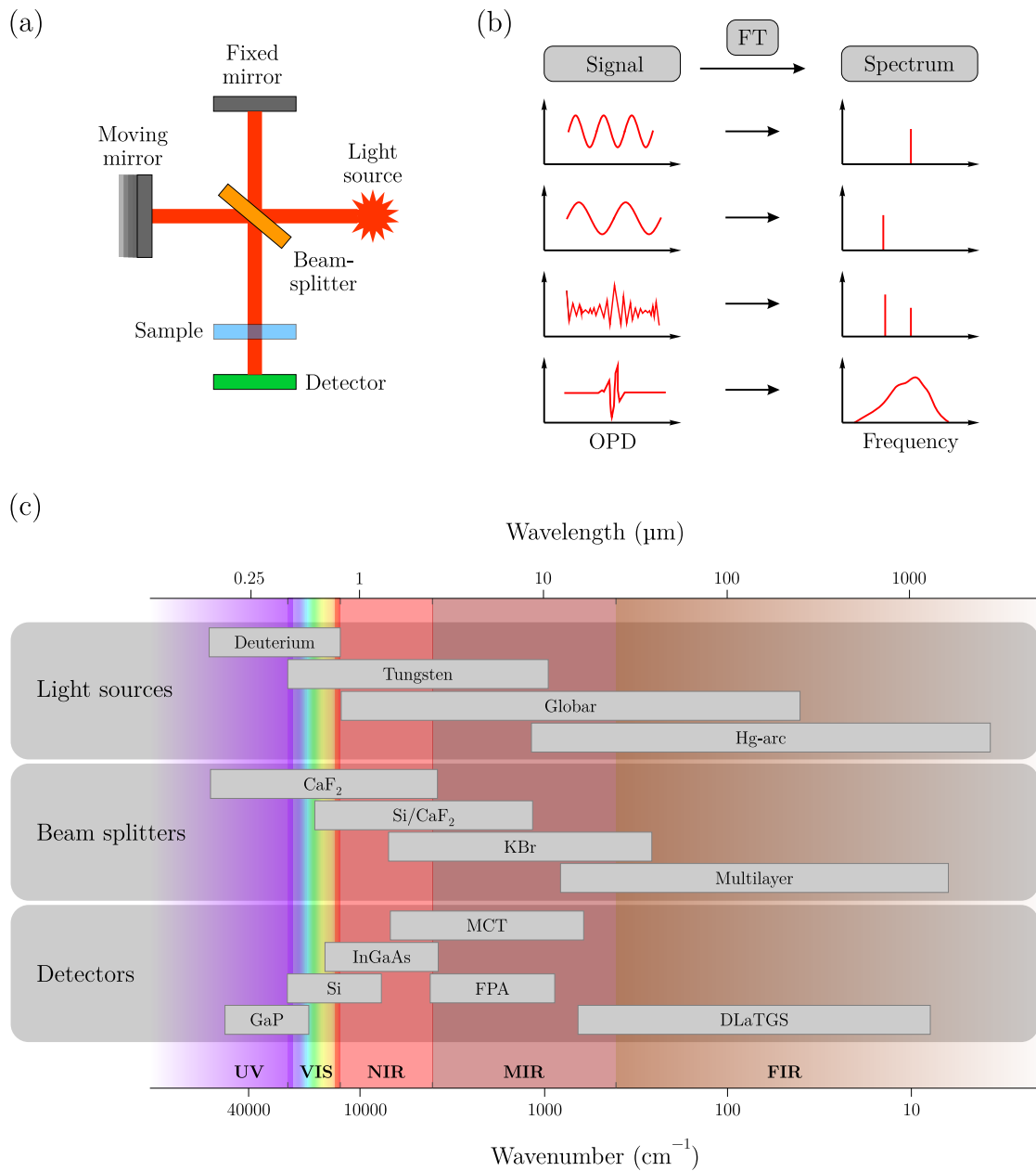


Fig. 23: (a) Schematic diagram of a Fourier-transform spectrometer. (b) Schematic relationships between the detected interferograms (light intensity vs. optical path difference) and corresponding light spectra calculated using the Fourier transform. (c) Overview of the operating ranges of the main components of the Fourier-transform spectrometers.

mirror (see Fig. 23a). The interfering beams are then reflected or transmitted by the sample and reach the detector, which records the light intensity as a function of the position of the moving mirror (i.e., of the optical path difference, OPD). The biggest advantage of the FT spectrometer is that the frequency spectrum of the light beam can then be calculated from the detected signal in a single step using the mathematical operation of the FT. This process is visualized by the examples shown in Fig. 23b. If there is only a single frequency present in the light beam, a sinusoidal signal will be detected with the maxima and minima corresponding to the constructive and destructive interference, respectively. Because the real light sources usually emit a wide range of frequencies, the typical detector output is a sum of all the single-frequency contributions leading to a complicated interferograms with a characteristic central peak around the value of zero OPD. This is not a complication, however, as the light spectrum is still calculated using the same single mathematical transformation. By comparing the transmittance/reflectance of the sample with a blank reference, its plasmonic response can then be easily identified. Although conventionally used in the IR range and termed Fourier-transform infrared spectrometers (FTIRs), these devices can cover a great part of the electromagnetic spectrum when a suitable combination of the light source, beam splitter, and detector is used (Fig. 23c).

The methods introduced in the beginning of the previous paragraph can be categorized as so-called bright-field microscopy techniques, often considered as the simplest of all optical microscopies. A more advanced approach, very often used in plasmonics, is the dark-field microscopy. Recall that the plasmonic effects often manifest themselves very strongly in the form of light scattering (see Fig. 24a, cf. Fig. 10 on p. 21). The dark-field microscopy separates this scattering contribution out by preventing the directly transmitted or specularly reflected light to reach the detector (Fig. 24b). This significantly enhances the image contrast because all the scattering elements like, e.g., the plasmonic NPs then appear on the black background [207]. This is an indispensable feature especially when the individual nanoparticles have to be analyzed, as their spectral signatures would be otherwise buried under the bright primary illumination [208–210].

The bright-field and dark-field (micro)spectroscopies discussed here are by far the most often used methods for analysis of plasmonic effects, but there of course many more, which will be just listed here for completeness. Absorption contribution to the total extinction can be probed by photothermal imaging [211, 212] or by spatial modulation spectroscopy [213]. Directivity of plasmonic nanoantennas is very often probed by so-called Fourier imaging (back focal plane imaging), which provides quantitative information about the angular spectrum radiated by a microscopic sample [214–216]. Properties of the near fields of plasmonic na-

nostructures can be investigated as well, using scanning near-field optical microscopy (SNOM) [217, 218], photoelectron emission microscopy (PEEM) [219–221], cathodoluminescence (CL) [222, 223], or electron energy loss spectroscopy (EELS) [224–227]. Recently, super-resolution techniques, which are widespread in biological imaging, were also applied to plasmonic nanostructures, producing some very promising outcomes [228–230].

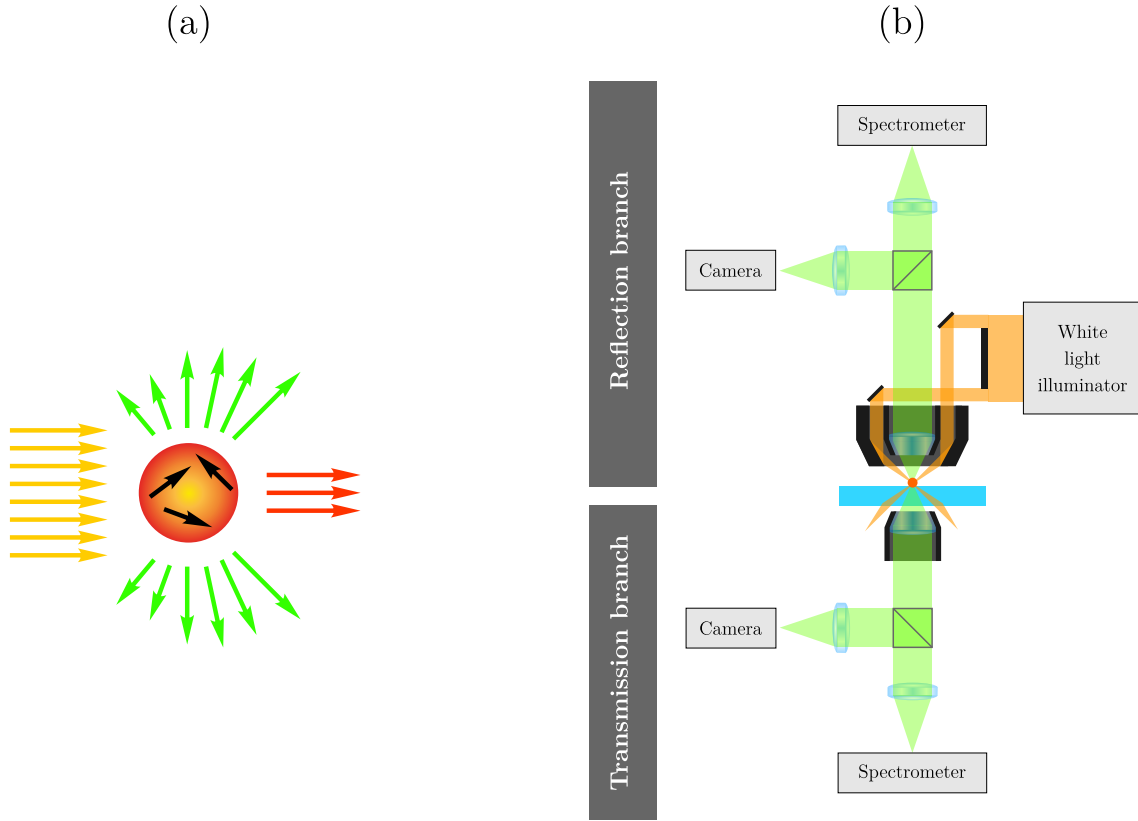


Fig. 24: (a) Schematic of the energy flow of the scattering (green arrows) and absorption (black arrows) processes accompanying the excitation of a localized plasmon in a metal nanoparticle. These two processes combined constitute the extinction, i.e., a significant part of the incident beam (yellow arrows) vanishes and does not contribute to the transmitted intensity (red arrows). (b) Diagram illustrating the light path through a dark-field microscope. The central part of the light beam from a white light source is blocked by a patch stop to create a hollow cone of light focused on the sample by a dark-field objective or a condenser lens. Only the scattered light then enters the objective lens either in the transmission or in the reflection branch, while the directly transmitted or specularly reflected light is discarded, respectively. The collected light can then constitute a dark-field image detected by a camera or be spectrally decomposed in the spectrometer.

3.2 Plasmonics for polarization control

One of the important applications of plasmonics is its use to enhance and control light emission from nanoscale sources (see section 2.2). Lanthanide-doped upconversion nanocrystals (UCNCs), which can absorb NIR light and emit VIS light via an anti-Stokes process, are the perfect examples of such nanoscale light sources [231]. Due to their tunable spectral characteristics and exceptional photostability, UCNCs have become a popular fluorescence material in applications like biosensing [232], bioimaging [233], or photovoltaics [234]. However, UCNCs often suffer from low emission efficiency and strong luminescence quenching. Although many chemical and physical methods have been developed to overcome these weaknesses, one of the most effective approaches is to couple UCNCs with plasmonic materials supporting localized surface plasmon resonances. Moreover, plasmonic nanostructures can strongly influence also the polarization state of the upconversion (UC) fluorescence [235]. This effect could enable polarized fluorescence imaging and thus greatly enhance its sensitivity and detection limits.

To study the polarization of plasmonically modulated UC luminescence we used core-shell-satellite hybrid nanostructures made of gold nanorod (GNR) core, SiO_2 shell, and Yb^{3+} and Er^{3+} doped CaF_2 satellite nanocrystals, which can be seen in Fig. 25a. The UCNCs were synthesized via a sodium co-doping co-precipitation route and had an average diameter of 7.5 nm [237]. GNRs were grown in an aqueous solution via seed-mediated route [238]. Their dimensions were finely tuned by anisotropic oxidation, resulting in the nominal length and diameter of approximately 82 nm and 32 nm, in order to align their longitudinal and transverse plasmonic resonance wavelengths with the red (660 nm) and green (540 nm) emission bands of the UCNCs, respectively (see Fig. 25b). If the UCNCs were attached in direct contact with the GNRs, the excited activators (Er^{3+} ions) could undergo nonradiative decay due to energy or charge transfer to the metal NPs. This could diminish the luminescence enhancement or even quench it. To systematically investigate this effect, the UCNCs were attached on the surface of GNRs covered with dielectric SiO_2 spacers of varying thicknesses ranging from 9 nm to 35 nm, which were prepared via modified Stöber method [239]. The UCNCs were later attached to them simply via electrostatic attraction to form the hybrid nanostructures. Their emission intensity was then measured in the solution phase using fluorescence spectrometer (Edinburgh Instruments FLS900), as shown in Fig. 25c. The maximum intensity enhancement factor for green UC emission was threefold (for silica spacers about 20 nm thick), while for the red UC emission it was even almost sevenfold (Fig. 25d).

Once the plasmonic enhancement was verified by the measurements, the polarization state of the plasmonically enhanced UC emission was studied on a single-particle

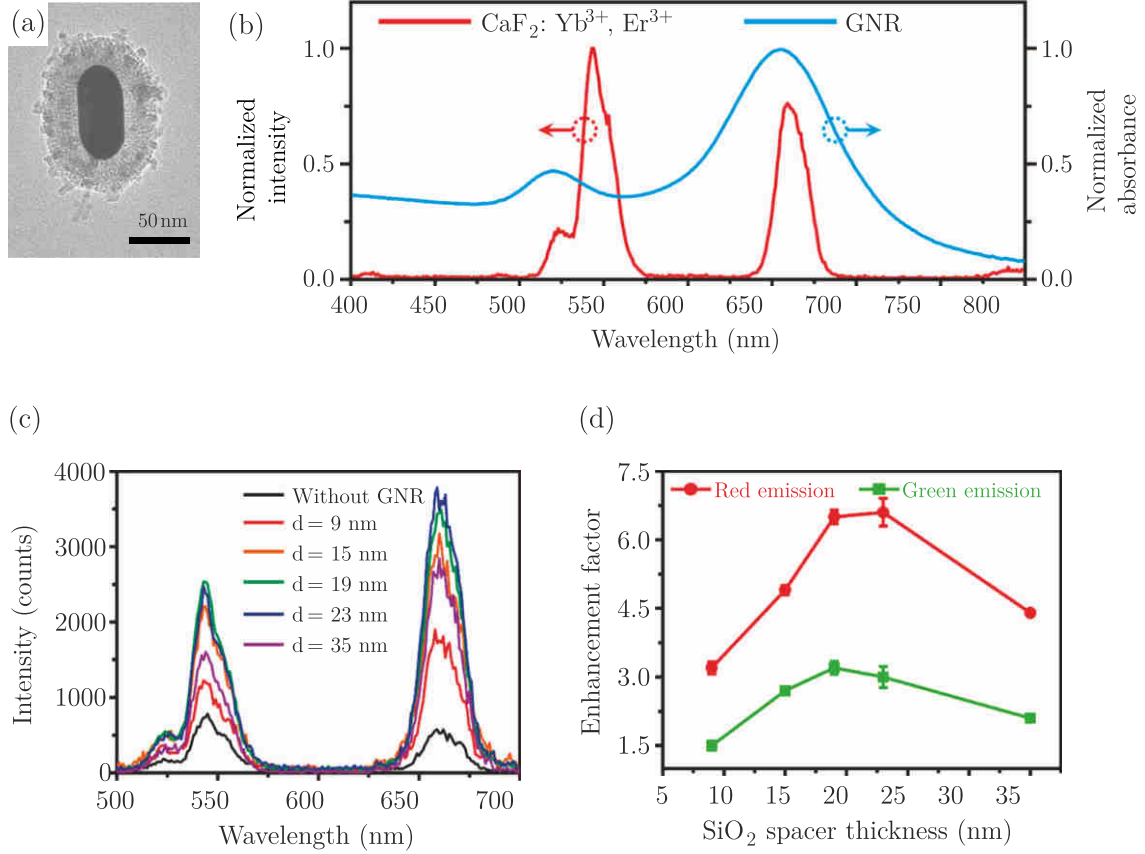


Fig. 25: (a) Transmission electron microscope image of GNR core, SiO₂ shell, and Yb³⁺ and Er³⁺ doped CaF₂ satellite nanocrystals. (b) Ensemble emission spectrum of bare CaF₂:Yb³⁺, Er³⁺ nanocrystals (red) and ensemble absorbance spectrum of bare GNRs in water (blue). (c) Emission spectra of bare UCNC nanocrystals without GNR together with the spectra of hybrid nanostructures with varying silica spacer thickness d . The concentration of UCNCs in all samples was fixed at 0.32 mg/mL. (d) Luminescence enhancement factors extracted from (c) for both green and red emission bands as a function of the silica spacer thickness. Adapted from [236].

level using dark-field microscopy. First, the hybrid nanostructures with 19 nm silica spacer were drop-casted onto a glass slide. The scattering measurements were carried out with a conventional 100 W tungsten lamp as a white-light source and with an imaging spectrometer as a detector. A broadband polarizer (so-called analyzer) was placed in front of the spectrometer input slit and rotated in 30° steps to determine the polarization state of the scattered light. After the polarized single-particle spectra of several NPs were acquired, the sample was subsequently imaged by a

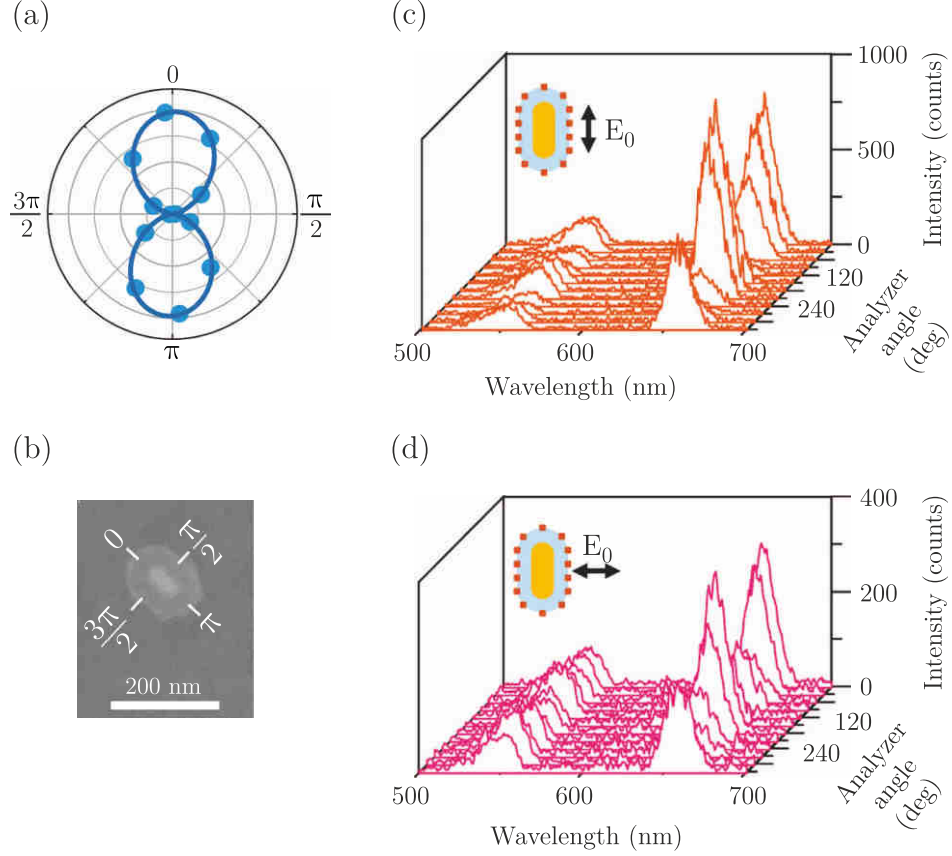


Fig. 26: (a) Polar plot of scattering intensity of the hybrid nanostructure as a function of the analyzer angle. (b) Selected SEM image of a single hybrid nanostructure that was used in the experiments with the labelled axes for orientation of light polarization. (c,d) UC emission spectra obtained as the analyzer angle was varied from 0 to 2π under the excitation polarization (c) *parallel* or (d) *perpendicular* to the long axis of the hybrid nanostructure. Adapted from [236].

scanning electron microscope (SEM) to exclude any clustered nanostructures and to verify their orientation. The results confirmed the typical dipolar scattering pattern with very high degree of polarization (DOP) corresponding to the longitudinal plasmonic mode of the GNR, which can be regarded as an oscillating electric dipole parallel with the long axis of the GNR (see Fig. 26a,b). With this information at hand, a 980 nm laser was introduced through a dichroic mirror into the light path of the microscope and its polarization was aligned either parallel or perpendicular to the long axis of the hybrid nanostructure, based on their previously acquired scattering pattern. The polarization state of both red and green UC emissions was then investigated using a rotating analyzer (Fig. 26c,d). From these polarization-resolved spectra, the polar intensity plots were extracted for the green and red emission band (Fig. 27). The results clearly show that the interplay between the two emission bands

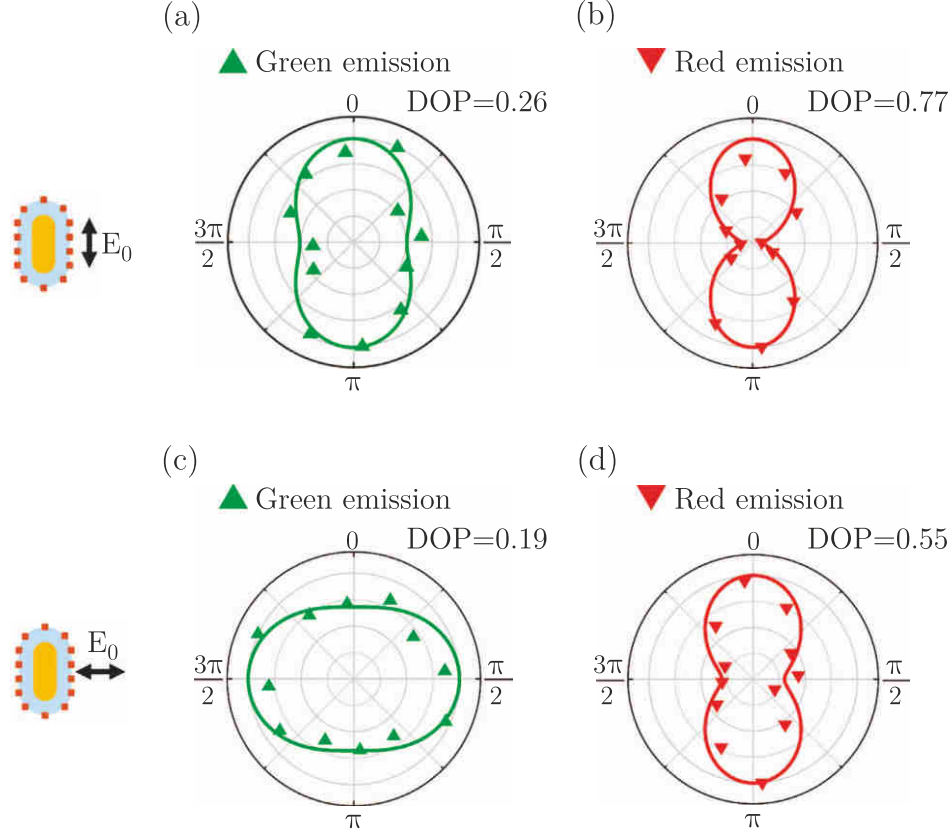


Fig. 27: Polar intensity plots extracted from the UC emission spectra in Fig. 26. (a, b) Excitation polarization parallel with the hybrid nanostructure — (a) green and (b) red emission band. (c, d) Excitation polarization perpendicular to the hybrid nanostructure — (c) green and (d) red emission band. The lines in the polar plots are cosine-squared fits of the experimental data. The calculated DOPs are shown in the top right corner of each polar plot. Adapted from [236].

of UCNCs and the two orthogonal plasmonic modes of the GNR strongly influences the polarization state of the emitted light. Under *parallel* excitation, both green and red emissions follow the polarization pattern of the scattering by the bare GNR itself, albeit the DOP of the green emission is slightly reduced. Under *perpendicular* excitation, the red emission is still polarized along the long axis of the GNR like in the previous case, but surprisingly, the green emission pattern (again with somehow lowered DOP) is now oriented in the direction perpendicular to the GNR long axis. Although the polarized laser used for excitation could, in principle, impose its polarization on the UC emission, it was verified, that such an effect alone cannot account for the observed DOP. Because the UC emission comes predominantly from the NCs located in the regions of high electric fields, and because the position of these regions is determined by the mutual orientation of the nanorod axis and the excitation polarization, it is logical to presume that this will be the dominant factor in the

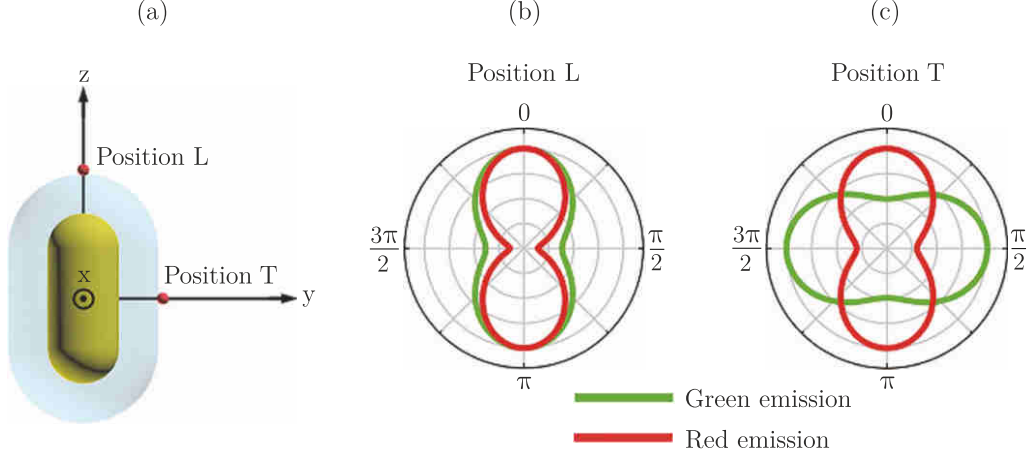


Fig. 28: (a) FDTD simulation geometry with a GNR with silica spacer and two dipole sources placed at the intersection of the silica surface either with the z -axis or the y -axis, denoted as L- or T-position, respectively. (b,c) Polar plots of normalized calculated emission intensity of dipole sources with green (540 nm) and red (660 nm) emission located at L- or T-positions. Adapted from [236].

polarized emission. To verify this assumption, a series of FDTD simulations was carried out using a commercial solver (Lumerical).

In the simulations, the silica-coated GNR was modelled as a hemispherically capped cylindrical body with dimensions corresponding to the mean values obtained from SEM imaging. The UCNCs were represented by Hertzian dipoles with the emission wavelength set at 540 nm (green emission) or 660 nm (red emission), according to the experimental values. These dipoles were placed either at the tip of the GNR with the silica spacer (L-position) or along its side (T-position) — see the schematic in Fig. 28a. Since we expect the activator ions in our hybrid nanostructures to be randomly oriented, it is safe to assume their emissions to be a linear combination of three dipoles oriented along the x , y , and z axis, respectively. Emulating the experiments, the angular dependencies of the calculated emission intensities were evaluated with respect to the polarization state in the far-field yz plane (corresponding to the light collection by a microscope objective). The results, which are presented in Fig. 28b in the form of normalized polar plots, show that when the dipole is located in the L-position, both green and red emissions are highly polarized along the long axis of the GNR (cf. Fig. 27a,b). For the dipole in the T-position, the simulated polar plot confirms that the radiation patterns of the green and red emission are perpendicular to each other and have a decreased degree of polarization (cf. Fig. 27c,d). These results of numerical simulations provide an excellent support for the experiments, and they are also in line with a theoretical description within the framework of Förster resonance transfer theory, that was also

developed in our work, but which goes beyond the scope of this thesis (for details, refer to [236]).

The results presented in this section demonstrate how interactions between the emission dipoles of the UCNCs and the plasmonic dipoles of the GNRs determine the polarization state of the UC emission in various situations. This effect was elucidated using both numerical simulations and theoretical description. Because the concept of plasmonic polarization control is universal for a range of emitter–enhancer combinations, it can be used for accurate control of polarization of light emitted from all sorts of nanoscale light sources, as demonstrated in the studies which followed [240, 241].

3.3 Plasmonics for phase control

In the previous section it was shown how plasmonic nanostructures facilitate the control over polarization of light emanating from nanoscale emitters in their vicinity. But plasmonic nanoantennas can also mould the flow of light due to their phase-altering properties, as described in section 2.4 devoted to metasurfaces. To assess the performance of metasurfaces and compare their characteristics to predictions coming from numerical simulations, it is useful to have an ability to quantitatively assess the phase distribution of the electric field in the sample plane. This process is usually referred to as quantitative phase imaging. There are, however, only few methods adequate to this task – ellipsometry [242], scattering-type scanning near-field optical microscopy [243], or spectroscopic interferometry with either continuous [244–246] or pulsed light sources [247–249]. Each of them has their own drawbacks and limitations — some are slow, some work only in limited spectral windows, and almost all are restricted in their ability to measure the light phase from large sample areas at rates that would match the switching speeds of tunable metamaterials. Within this project, we have utilized coherence-controlled holographic microscopy (CCHM) for quantitative phase-imaging of plasmonic metasurfaces. CCHM, which is based on the technique of off-axis holography, provides unambiguous phase information from the whole field of view and thus overcomes the necessity for lateral sample scanning. It is also fast and can be applied even in diffuse environments [250–252]. Although it is conventionally used for fast monochromatic imaging of live biological samples using incoherent light sources, when equipped with a tunable laser it is able to perform spectrally resolved imaging of plasmonic nanostructures.

The ideal way how to demonstrate the capabilities of any new method is to use it for analysis of some well-known benchmark sample. Simple plasmonic nanoantennas with a single dipolar resonance are the excellent candidate for this role as the light

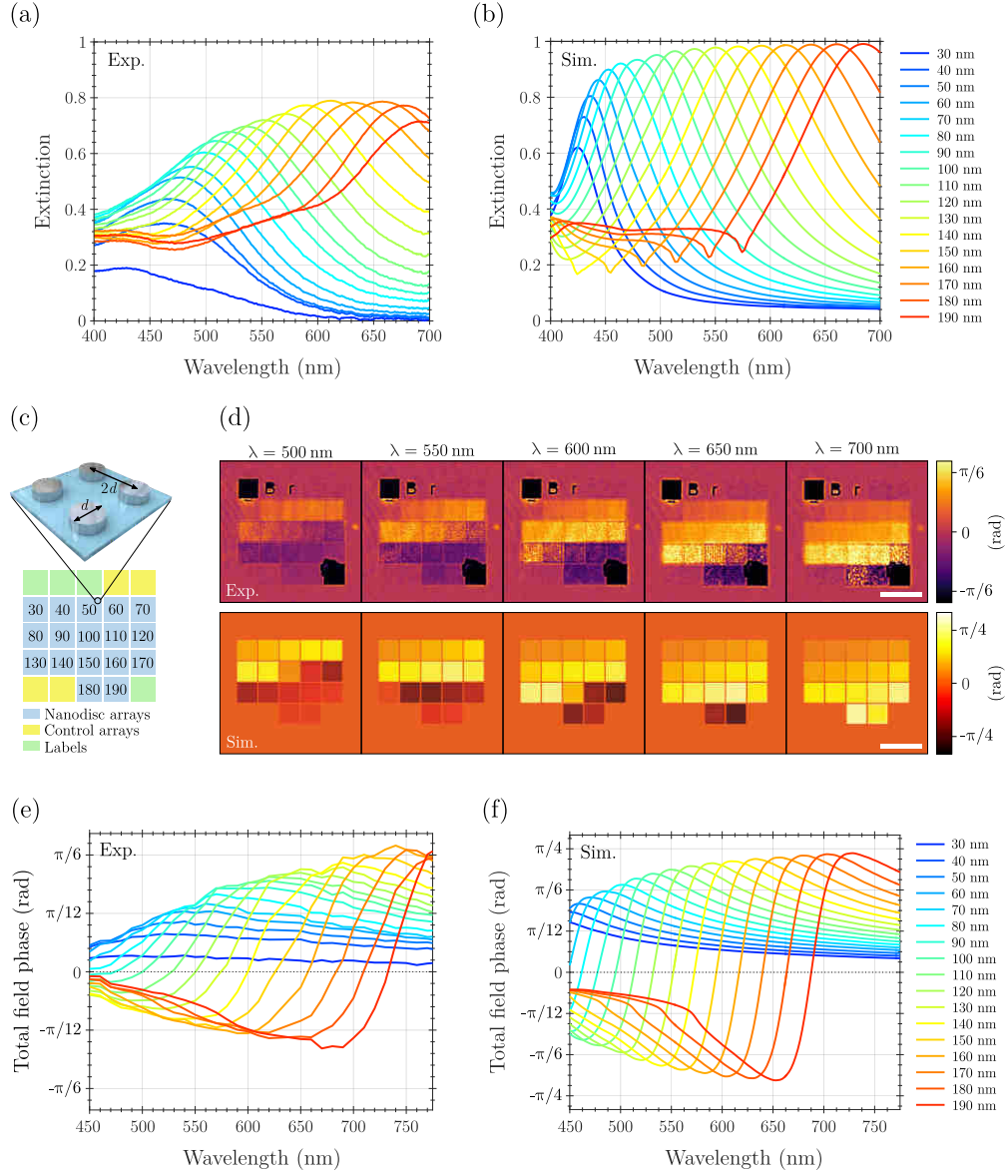


Fig. 29: (a) Experimental and (b) FDTD-calculated extinction spectra of silver nanodisc arrays on glass. Both show characteristic plasmon resonances that red-shift with increasing disc diameter (indicated by line colours). The experimental extinction in (a) has been calculated by the formula $1 - T/T_{\text{REF}}$, where T is the transmission through the nanodisc array and T_{REF} is the transmission through the bare substrate. (c) The sample consisted of silver nanodisc arrays (blue squares), control arrays made of off-resonance nanostructures (yellow squares), labels and alignment markers (green squares). Diameter d of nanodiscs (in nm) is denoted in each blue square; pitch of all arrays was fixed as $2d$. (d) Quantitative phase images of silver nanodisc arrays at a selected subset of illumination wavelengths, measured in CCHM (top) and theoretically calculated (bottom). Scale bars are $20 \mu\text{m}$. (e, f) Spectra of the total field phase at nanodisc arrays of various dimensions extracted from the full set of measured CCHM images (e) and from numerical simulations (f). Adapted from [253].

scattered by them exhibits a phase shift of π between the low- and high-frequency side of the resonance (see Fig. 19a and related discussion on p. 37). Therefore, a set of arrays of silver disc-shaped antennas with diameters ranging from 50 nm to 200 nm were fabricated using a conventional EBL (see Fig. 29c). The strong dipolar plasmonic resonance modes of the nanodiscs were identified in the measured VIS and NIR extinction spectra (Fig. 29a). The experimental data were also verified by the complementary FDTD numerical simulations, which were in very good agreement, concerning the inevitable fabrication imperfections and inherent minute oxidation of silver (Fig. 29b).

The central result of this study is a set of CCHM images of the amplitude and phase distribution in the sample plane, acquired while the illumination wavelength was swept in the 10 nm steps across the whole accessible spectral range of the holographic microscope. Several examples of the resulting phase images are shown in Fig. 29d (top), where one can observe a rapid phase flip which moves toward arrays filled with larger discs (and with resonances at higher wavelengths) as the illumination wavelength increases. To better visualize the information contained in the phase images, we have extracted the average phase value for each array at all measured wavelengths and plotted the resulting spectra in Fig. 29e (while compensating for a small background signal by subtracting the phase outside the arrays). Apparently, the phase measured by CCHM exhibits an S-shaped flip from positive (above resonance) to negative values (below resonance) and goes to zero in both regions far from the resonance. That is in contrast with considerations based on a classical model of simple resonant systems, where the scattered phase changes monotonically from 0 to π (with $\pi/2$ at the resonance) [9]. This seeming discrepancy has two main reasons. First, it is the additional phase acquired due to propagation of the scattered waves through the microscope. Second, it is the fact that CCHM works with a superposition of the scattered fields with the original reference wave. The resulting total phase image thus depends on the relative amplitudes and phases between these two fields. When both these aspects are incorporated into the theoretical description of the CCHM image formation, the experimental data can be fully reproduced, as it is shown in Fig. 29d (for more details see Ref. [253]). Note that the only external input of our model is the optical response of the individual metasurface building blocks calculated by the FDTD method. To make a quantitative comparison with the experiment, the average phase from each array in our calculated images was extracted and the resulting spectra were plotted in Fig. 29f. Although there are slight discrepancies in terms of amplitudes and spectral positions of the phase spectra, overall, our model satisfactorily reproduces the experimental data, with their characteristic S-shaped phase flips in the vicinity of the disc resonances. The capacity of our theoretical model to reliably predict and interpret the

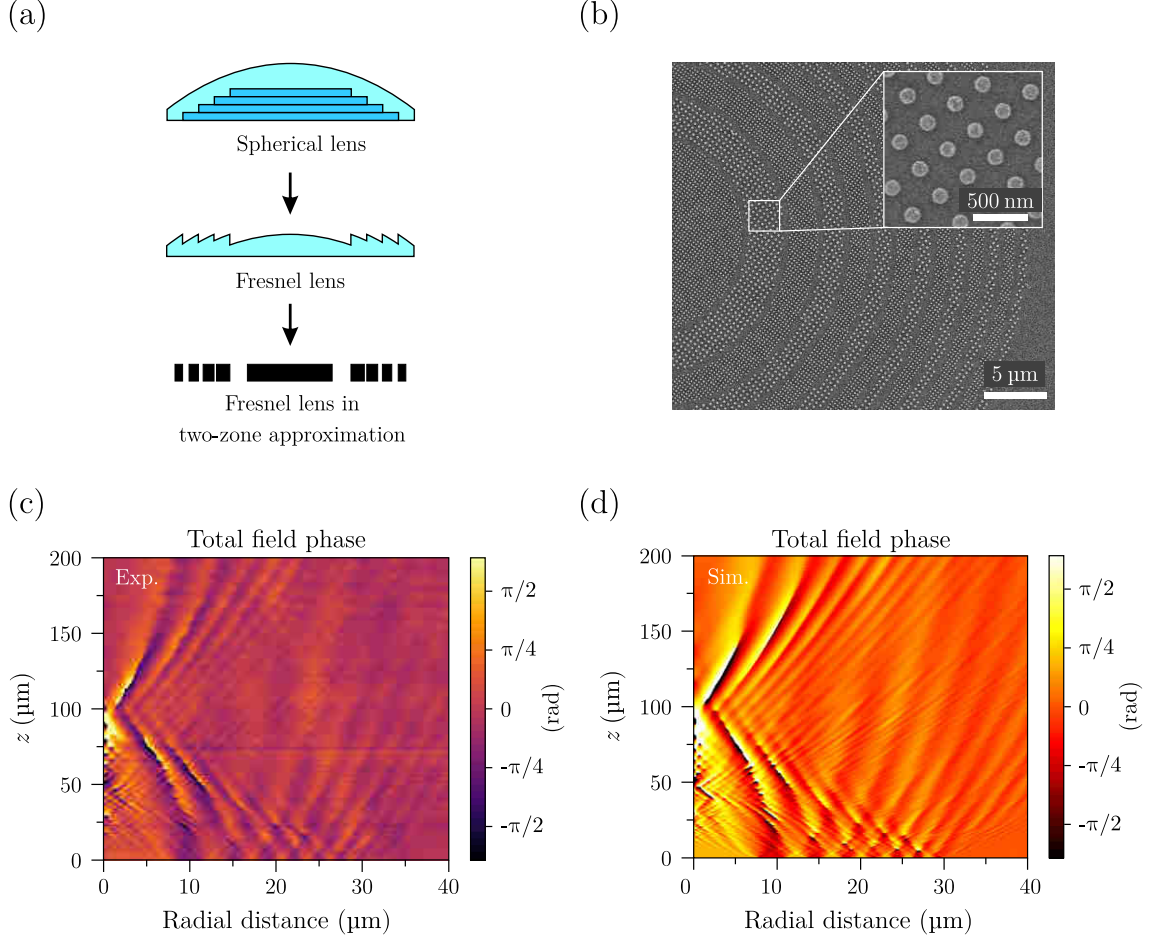


Fig. 30: (a) SEM image of the fabricated zone plate where individual zones are formed by silver nanodiscs (130 and 190 nm). (b) 3D visualization of the measured total phase distribution in the half-space above the plasmonic zone-plate. Measured (c) and simulated (d) phase map in the xz -plane above the zone plate where the main ($z \approx 100 \mu\text{m}$) and subsidiary ($z \approx 50 \mu\text{m}$, $z \approx 25 \mu\text{m}$) focal points are clearly distinguishable close to the zero radial distance. Adapted from [253].

outcomes of the measurements facilitates the use of CCHM for design of plasmonic devices with complex functionality, namely for direct inspection and verification of inner workings of metasurfaces based on new and unexplored concepts.

Another major benefit of CCHM is its ability to produce 3D phase maps by z -stacking images taken at different defocus levels. To demonstrate this feature for characterization of plasmonic metamaterials, we performed 3D phase imaging of the electric field produced by a focusing plasmonic metasurface (see Fig. 30a) [254, 255]. The theory behind these flat optical elements (often also termed zone plates or Fresnel lenses) is based on a simple, yet powerful, idea of scraping all the unnecessary elements of the conventional lenses which produce the redundant phase differences equal to multiples of 2π . The resulting echelette-like phase profile can then be

reproduced at many degrees of approximation, the lowest one being just a two-level structure with a π phase difference between the annular areas (Fig. 30b). With our system of silver nanodiscs, the largest achievable phase difference at the selected operating wavelength of 630 nm can be achieved using the zones filled with 130 nm and 190 nm nanodiscs ($\approx \pi/5$, based on the experimental results shown in Fig. 29e). Although such phase contrast is significantly smaller than what the theory prescribes, the fabricated Fresnel lens has still a decent focusing ability. This is verified not only by the measured light intensity distribution behind the lens but especially by the 3D quantitative phase map of wavefronts propagating from the metasurface lens. Using a precise sample positioning system, the CCHM images were acquired in 1 μm steps and then z -stacked in order to produce the resulting phase map of the xz -plane (Fig. 29c). Converging stripes of constant phase originating at the sample are clearly visible, leading to a pre-designed focal point at $z \approx 100 \mu\text{m}$. Furthermore, by feeding the real spatial distribution of the nanodiscs into our theoretical description of CHHM imaging, the validity of this theory was confirmed by its remarkable agreement with the experimental data (Fig. 29d).

To sum up, we have established CCHM as a real-time, wide-field, and quantitative light-microscopy technique which enables 3D imaging of electromagnetic fields. Its ability to provide complete information about both intensity and phase renders it a powerful tool for performance assessment of all kinds of phase-altering metasurfaces. After we presented the current state-of-the-art methods for light phase imaging, we demonstrated the use of CCHM in analysis of a sample made of well-known plasmonic disc-shaped nanoantennas, where the phase of transmitted light can be easily predicted and controlled. We then showed that the obtained phase images can be directly related to the optical properties of the metamaterial building blocks. The proposed theory constitutes a general framework for the use of holographic microscopy in metamaterial phase analysis. As a proof of concept, we demonstrated 3D phase mapping of wavefronts behind a plasmonic focusing metasurface based on the principle of the Fresnel lens.

3.4 Conclusions

In this chapter, we have dwelled on the subject of utilization of plasmonic nanostructures for control of light. After a brief introduction to the most important experimental techniques in plasmonics, it was shown how gold nanorods influence the intensity and polarization state of light emitted from the nearby upconversion luminescence nanocrystals. Then, a detailed account of the quantitative phase measurements of the plasmonic metasurfaces was provided. We have demonstrated how off-axis di-

digital holography enables wide-field, single-shot measurements of the phase of light which was scattered from plasmonic nanostructures. We have also shown the ability of this technique to perform measurements in 3D and thus analyze the working principles of the metasurface optical components. Together with the fast acquisition speed this makes the digital holography a valuable tool for design and characterization of many sorts of metasurfaces and metamaterials. In the following chapter, we will remain in the field of metasurfaces and we will take a closer look on the aspect of tunability. That is, we will try to answer the question how can be the optical function of metasurfaces actively controlled via external stimuli.

4 TUNABILITY IN PLASMONICS

“If the Easter pilgrims in Piazza San Pietro were to represent the carriers in a metal, then an insulator would resemble the Antarctic with one solitary traveller. In the abundance of carriers there is an enormous gap between conductors and insulators.”

Opening speech for the 1956 Nobel Prize in Physics

E. G. RUDBERG

4.1 Tunable metasurfaces

In section 2.4, which is devoted to metamaterials and metasurfaces, we have shown how nanostructured media can be used for engineering of the electromagnetic space and controlling the propagation of light in unprecedented ways. We have also indicated several challenges that remain in this field, including the issue of metamaterials’ tunability and switching. Because the nature of plasmonic resonances strongly depends on the shape and mutual orientations of the individual meta-atoms, the primary approach how to incorporate tunability into metasurfaces is the one based on mechanical reconfigurability [256]. The corresponding technological solutions involve manipulations with the substrate (e.g., stretching) [257, 258], microfluidic injection of a conductive liquid into a network of meta-atoms [259], electrostatic actuation [260, 261] or pure mechanical modifications of nano- and micro-electro-mechanical systems (MEMS) [262, 263]. Infiltration of a metamaterial with liquid crystals, while controlling their orientation via electric field, can also be used for effective refractive index modulation. Although these techniques offer robust and low-voltage operation, they often suffer from low bandwidths and long switching times [264].

The second large class of tunable metasurfaces is based on modulation of charge-carrier density either in the substrate or in the meta-atoms themselves. A substantial change in the dielectric properties can be achieved through injection of free carriers into semiconductors like gallium arsenide or into conductive oxides like indium tin oxide [265–267]. Another material offering electro-optical tunability is graphene, particularly at infrared (IR) and terahertz frequencies [268–270].

The third method how to achieve nanoscale optical and plasmonic switching is to employ materials that can undergo a radical change in the atomic or electronic structure — so-called phase transition or phase change. A typical example of such

materials are chalcogenide glasses, which can be repeatedly switched between their amorphous and crystalline states, in a process which is accompanied by a rapid change of their optical and electrical properties. This functionality allows storage of information and it has been used for a long time in rewritable optical discs and phase-change memory devices [271]. Another important example of a phase-change medium is vanadium dioxide (VO_2), which exhibits a metal–insulator transition that renders it an attractive material for tunable metamaterial structures.

There are basically two ways how can be a phase-change material incorporated into a metasurface. The more facile way is to employ it as a substrate with tunable properties and to fabricate the meta-atoms on top of it. Tunable perfect absorbers [272, 273], tunable polarizing elements [274], and metamaterials with on-demand reflection and transmission resonances [275] have been produced this way. The more direct approach consists in nanostructuring the tunable material itself by some sort of a top-down nanofabrication process [276–278]. In that case, the optical properties can be controlled in a direct manner, reducing the delays and inefficiencies caused by the heterogeneity of the metasurface [279, 280]. In the following, we will show examples of both these types of metasurfaces. First, a hybrid system of plasmonic nanodisc arrays on top of a VO_2 substrate will be used to demonstrate all-optical control of a persistent nanoscale memory effect. Second, we will introduce a new class of tunable plasmonic/dielectric metasurfaces that are based on epitaxially grown VO_2 nanobeams, where the nanostructured tunable material is produced with no need for time-intensive nanofabrication process. But before that, we will elaborate on the VO_2 itself, which represents an archetypal tunable phase-change material, and describe it in more details in the following section.

4.2 Vanadium dioxide

Oxides exhibit probably the widest range of electrical behaviour of any class of materials (see Fig. 31). They include some of the very best insulators, but at the same time some genuinely metallic conductors or even superconductors. The room-temperature electrical conductivities of oxides range from values comparable to very good conductors like copper and silver ($10^6 \Omega^{-1} \text{cm}^{-1}$ for metallic RuO_2 or ReO_2) to values twenty orders of magnitude lower (like $10^{-14} \Omega^{-1} \text{cm}^{-1}$ for insulating SiO_2). A large class of oxide materials also exhibits an intriguing phenomenon of metal–insulator transitions (MIT), in which even minute changes of physical or chemical variables produce abrupt transitions between the metallic and insulating states of matter. It has been observed almost 60 years ago by Morin [283], for example, that VO and V_2O_3 undergo a jump in their electrical conductivities of almost eight or-

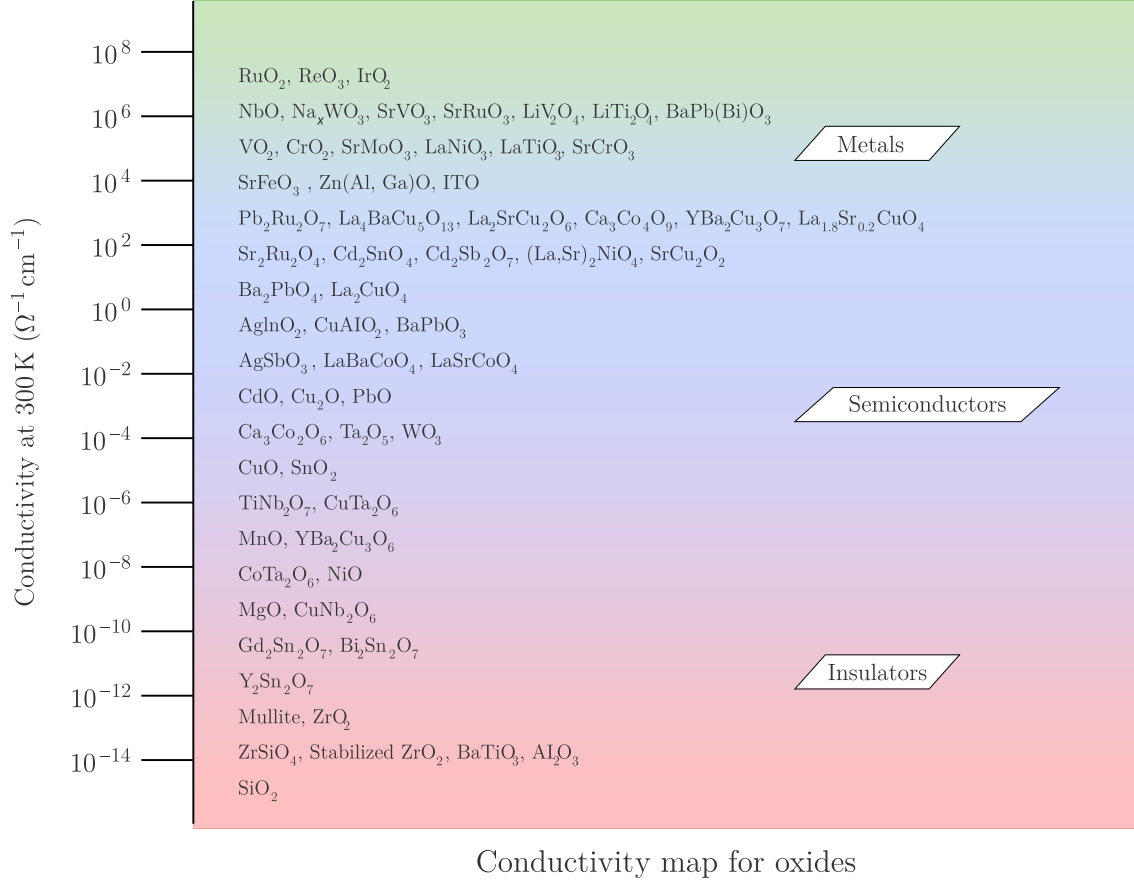


Fig. 31: Room-temperature electrical conductivities of oxides. The figure illustrates the enormous range encountered for this fundamental property of matter and also the heterogeneity of oxides, which can exhibit either metallic, semiconducting, or insulating behaviour. Adapted from [281].

ders of magnitude at transition temperatures around 125 K and 150 K, respectively (see Fig. 32). As C. Rao put it, it is as if “wood have become copper at the transition temperature” [284]. The elementary mechanisms leading to the conductivity transition, as well as its magnitude, depend on the intricate interplay between the structural and electronic properties of the material in question. Figure 33 shows a map of transition temperatures T_{MIT} of various oxides, for which the transition is triggered by temperature. Among them, VO_2 stands out as being the closest one to the room temperature (RT), with the MIT at approximately 340 K (67 °C) for its bulk crystals. This unique property made VO_2 the flagship MIT material and predestined it to be the active component of various device concepts utilizing MIT, such as electronic switch devices, optical devices, metasurfaces, or sensors. To understand the intriguing electrical properties of MIT materials, it is necessary to recall the theory of solid state physics:

Originally, the theoretical description of metals was represented by Drude’s free-

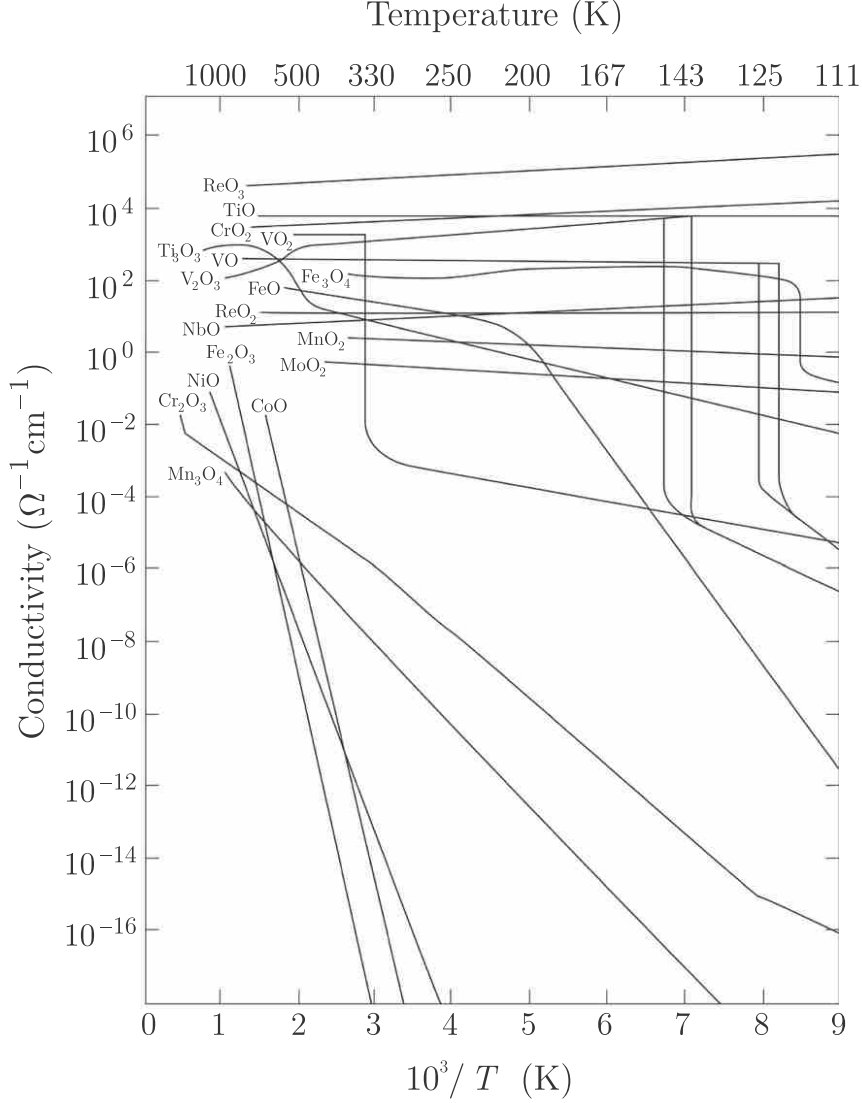


Fig. 32: Temperature dependence of the electrical conductivity of selected binary transition metal oxides. Some oxides that contain vanadium or titanium atoms can undergo metal-insulator transition. Adapted from [281].

electron model, which we have already encountered in section 1.2 in the context of dielectric functions. In this model, the electrons, ionized from their “parent” atoms, are free to move throughout the metal and they behave like an ideal gas of elementary particles. Although this simple concept neglects interactions of electrons both with the ions and also among themselves, it successfully explains the heat capacity, thermal conductivity, and electrical conductivity of metals. However, there is an equally large class of insulating materials, for which the electrons appear to be bound rather than free. To describe also insulators and semiconductors, the free-electron model must be extended to take into account also interactions with positive ions arranged in the periodic lattice of the solid. This is done by introducing

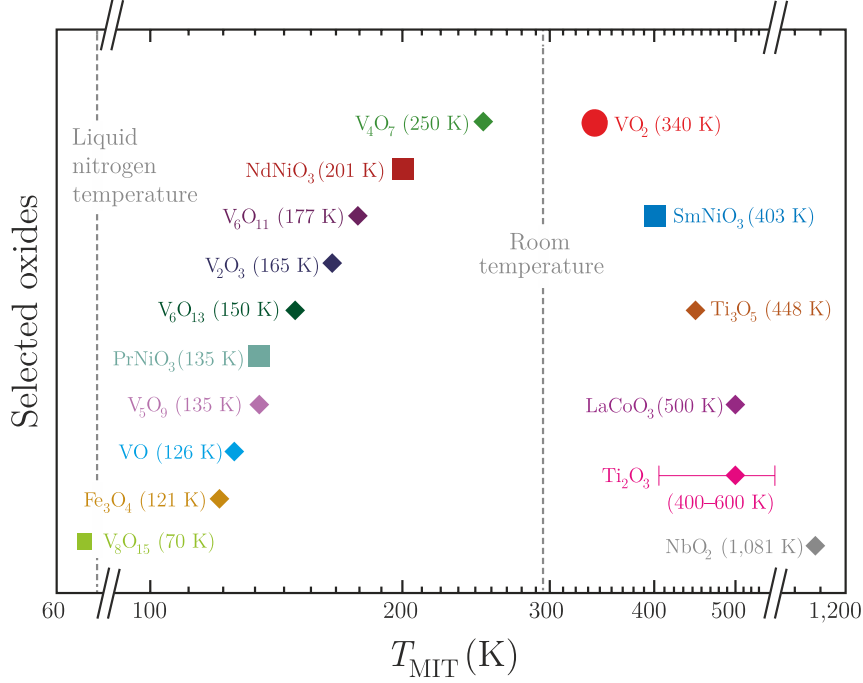


Fig. 33: Metal–insulator transition temperature T_{MIT} of some selected oxides (bulk crystals). External stress or substrate-driven constraints can significantly influence the transition temperature and the resistivity change. Adapted from [282].

a periodic potential into the Schrödinger equation for electrons and assuming a solution in the form of periodic Bloch’s wavefunctions [10]. What emerges from this improved model is the existence of band gaps, i.e., of regions in the electronic band structure where no electron states can exist. In insulators, the Fermi level E_F then lies within such a band gap, far away from any states that would be able to adopt electrons excited from the E_F and thus carry the current. In metals, on the contrary, E_F lies within a delocalized band with many states available. Although the aforementioned concept is the basis of our understanding of the fundamental distinction between metals, insulators, and semiconductors, a significant part of the physical reality is still completely ignored — particularly the electron–electron interactions and the crystalline disorder. When either or both these effects are strong enough, they can have striking influence on the electronic properties of metal oxides. For example, the strong Coulomb repulsion (electron–electron correlation) between conduction-band electrons can lead to their localization and subsequent insulating behaviour of the otherwise conductive oxides. The strongly correlated electrons are, in fact, the primary reason for appearance of variety of extraordinary phenomena like antiferromagnetism, high-temperature superconductivity, colossal magnetoresistance, and also the MITs discussed here [285].

In VO_2 , it is the subtle interplay between the atomic and electronic degrees of

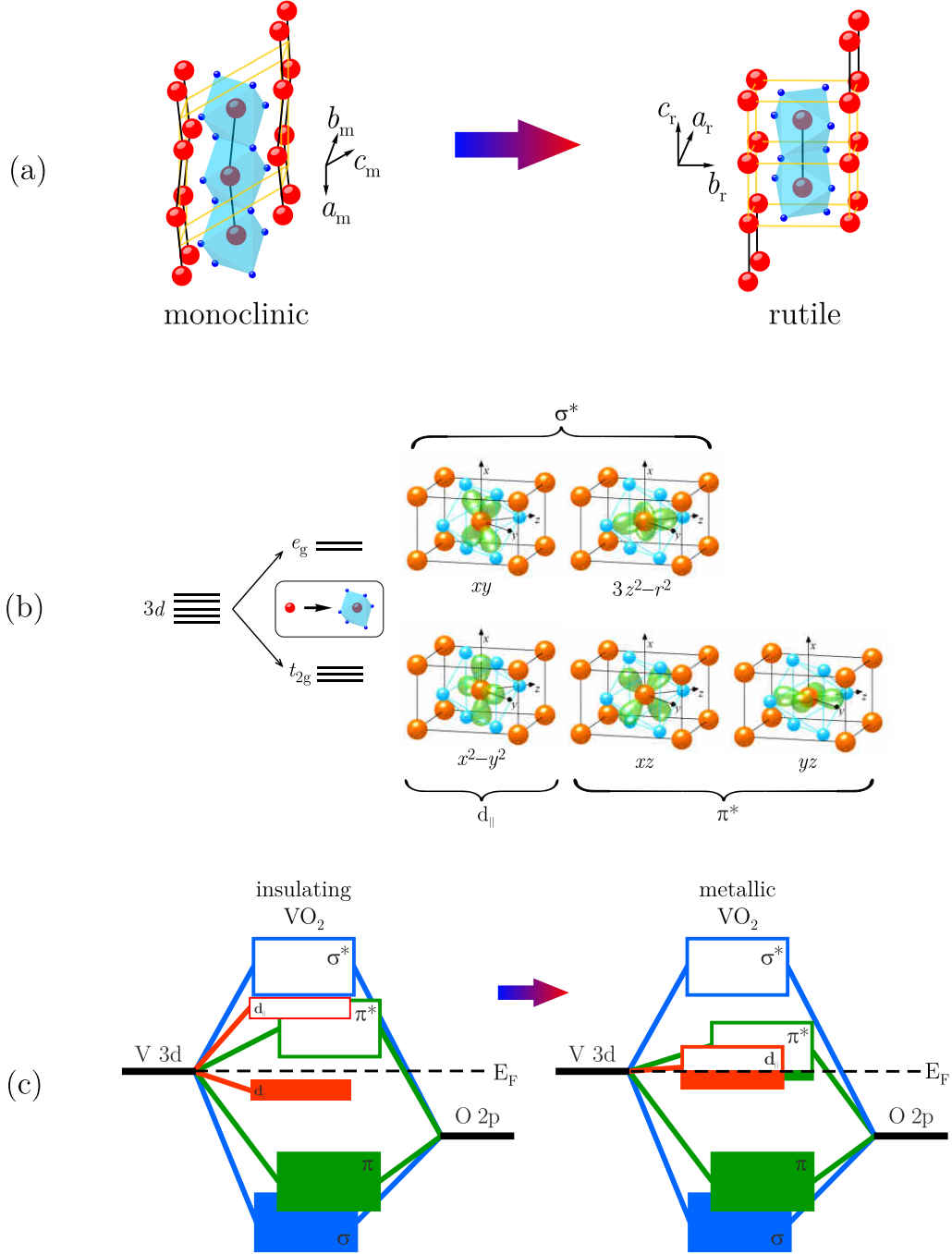


Fig. 34: (a) Crystal structures of the insulating (monoclinic) and metallic (rutile) phases of VO₂. Vanadium atoms are represented by the red spheres, oxygen atoms by the blue spheres, and the oxygen octahedra are highlighted by the light-blue shading. The unit cells are shown in yellow. (b) Crystal-field effects lead to splitting of the V 3d orbital into the low-energy t_{2g} part and the high-energy e_g part. The angular distributions of the corresponding V 3d orbitals are drawn relative to the local reference frame of the central vanadium atom. Adapted from [286]. (c) Schematic of the VO₂ band structure in the insulating (left) and metallic (right) states. The filled regions represent the filled electronic states below the Fermi level E_F (dashed line). Adapted from [287].

freedom which is responsible for its first-order transition from a low-temperature insulating phase to a high-temperature metallic phase. At RT, VO₂ has a monoclinic structure with a lowered crystal symmetry (P2₁/c space group). It has the characteristic tilted “zigzag” V-V pairs along the a_m axis due to Peierls instability and anti-ferroelectric effect (see Fig. 34a) [288]. Above the transition temperature, VO₂ transforms to a rutile structure (P4₂/mmn space group), the tilting disappears, vanadium atoms return to the centres of the octahedral cage formed by the oxygen atoms, and the unit cell is cut in half ($c_r \approx a_m/2$). The electronic structure of VO₂ is determined by the hybridization of O 2*p* and V 3*d* orbitals [286]. But because each vanadium atom is placed in the crystal field of its six nearest oxygen neighbours, the 10-fold degeneracy of the *d* level is partially lifted as triple-degenerate t_{2g} orbitals ($d_{x^2-y^2}$, d_{xz} , d_{yz}) and double-degenerate e_g orbitals (d_{xy} , $d_{3z^2-r^2}$) emerge [289] (Fig. 34b). Moreover, due to inequality between the oxygen ions on the equator and those on the tips of the octahedra, the t_{2g} orbitals further split into two double-degenerate π^* (e_g^π) orbitals and one $d_{||}$ (a_{1g}) orbital (Fig. 34c). The d-electrons of the vanadium ions experience two competing forces — Coulombic repulsions tend to localize the individual electrons at atomic lattice sites, while hybridization with the oxygen p-electron states tends to delocalize them. Even the subtle structural changes during MIT transition are then sufficient to push the overall electronic behaviour in either direction. In particular, the dimerization of the V ions along the a_m axis splits the highly directional $d_{||}$ orbitals into a bonding–antibonding pair, while the zigzag tilting, on the other hand, results in an energy upshift of the π^* orbitals [287]. Combined, these two effects lead to appearance of approximately 0.7 eV wide band gap and of the associated insulating behaviour of VO₂ below the MIT temperature. Note that the question of whether the sole structural changes are responsible for the MIT (Peierls theory) or whether the correlation effects play the major role and the structural change is only an accompanying phenomenon (Mott–Hubbard theory) has been a subject of much debate [290]. Regardless of the actual mechanism, the MIT can be nicely visualized by ellipsometric measurements of the dielectric function of VO₂, as shown in Fig. 35. At RT, the conventional polycrystalline VO₂ thin film behaves like a typical dielectric with moderate index of refraction and losses. Beyond T_{MIT} , however, the ε_1 becomes negative in the NIR range. Based on the knowledge of dielectric functions gained in the first chapter, this is a clear sign of metallic properties.

For the reasons stated above, the optical properties of VO₂ are extremely sensitive to even small changes of extrinsic parameters such as temperature, pressure, strain, or doping. Moreover, the phase transition can be triggered at subpicosecond timescales, which opens up a possibility of using VO₂ as an ultrafast switching material for photonics [282]. The most frequent approach to induce the MIT is na-

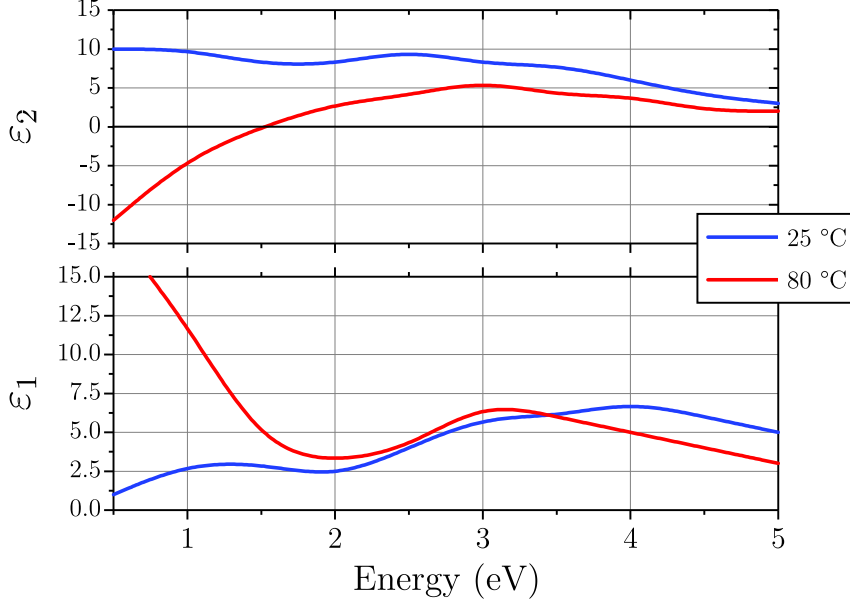


Fig. 35: Complex dielectric function $\varepsilon \equiv \varepsilon_1 + i\varepsilon_2$ of a conventional polycrystalline VO_2 thin film measured by spectroscopic ellipsometry at RT (25 °C, in blue) and above the MIT temperature (80 °C, in red).

turally the thermal triggering, i.e., changing the temperature via external heating or cooling. Other approaches to triggering the MIT in correlated oxides are summarized in Fig. 36. They include electrical, optical, magnetic, and strain stimuli. The versatility of the triggering approaches together with the extraordinary electronic properties of the VO_2 , lead both to a growing demand for the VO_2 growth on various substrates, in large quantities, and at the highest possible quality. So far, VO_2 has been synthesized in various forms including bulk, thin film, and even nanostructured morphologies [291]. The depositions have been done using numerous techniques such as pulsed laser deposition (PLD) [292], chemical vapor deposition (CVD) [293], sputtering [294], sol-gel synthesis [295], or electron beam evaporation [296].

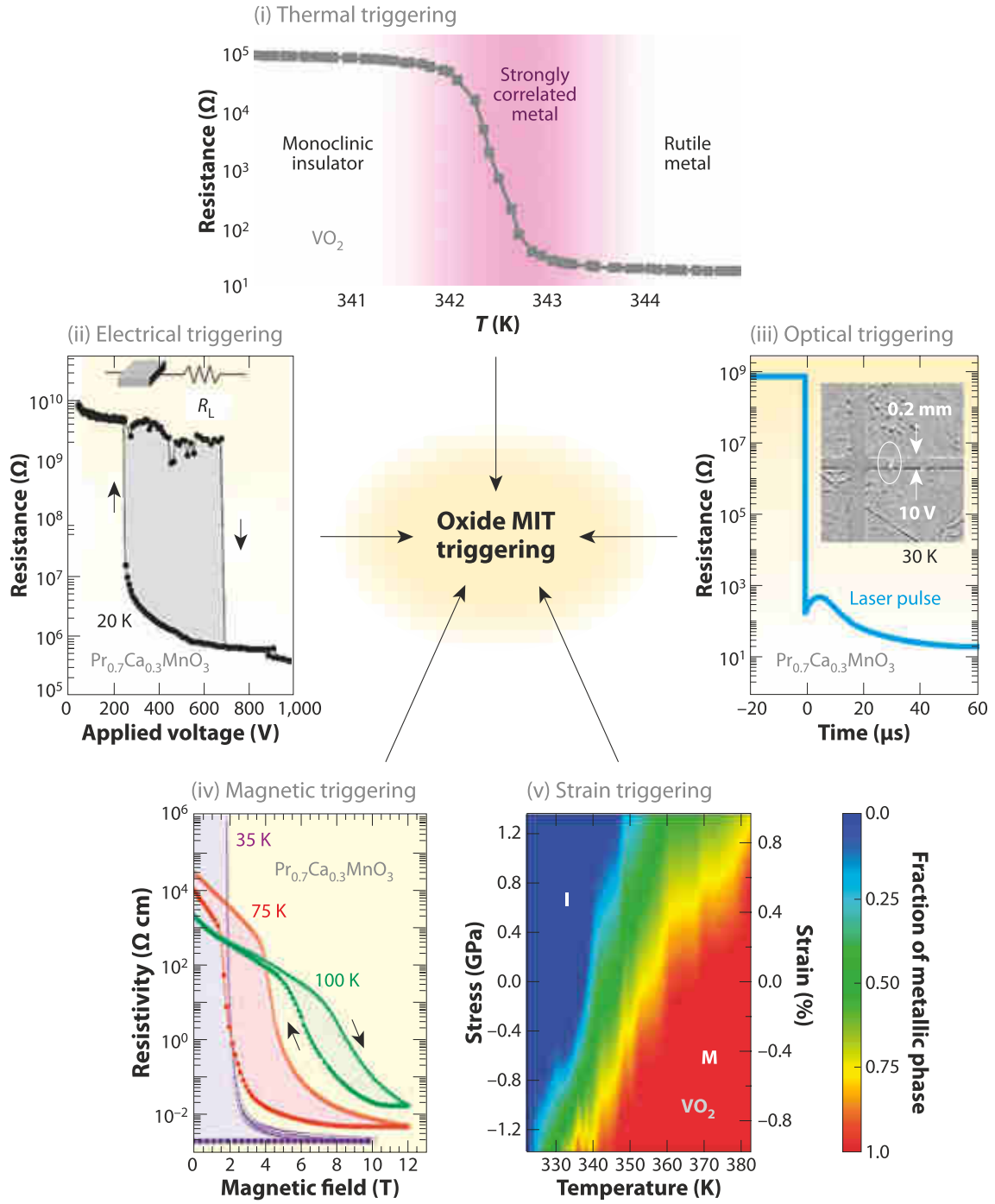


Fig. 36: MIT triggering approaches in correlated oxides. Adapted from [282].

4.3 VO₂ for optical modulation

In the beginning of this chapter we indicated that the optical response of plasmonic nanostructures can be controlled by interfacing them with some sort of active phase-change medium in their vicinity. No matter whether the MIT triggering signal is optical, electrical, thermal, or magnetic, the modulated LSPR response is necessarily transient — it reverts to its initial state together with the active substrate as soon as the external stimulus is removed. It is thus very challenging, unfortunately, to realize persistent and non-volatile LSPR tuning, which is a feature more than desirable for practical applications. We studied a possible solution to this problem using a model hybrid system of gold nanodiscs on top of a thin VO₂ film, which was controlled by ultraviolet (UV) light pulses and external heating (see the schematic in Fig. 37a). Thin VO₂ films with nominal thickness of 50 nm were prepared on glass substrates by PLD from a vanadium target with subsequent annealing in an oxygen atmosphere. Arrays of gold nanodiscs (diameter $D = 80\text{--}210$ nm, height $h = 25$ nm, pitch $p = 500$ nm) was fabricated by conventional EBL (see a representative SEM image in Fig. 37b).

The optical response of the arrays was measured in an IR microscope (Bruker Hyperion 2000) coupled with a Fourier-transform infrared (FTIR) spectrometer (Bruker Vertex 70), while the whole sample was attached to a temperature-controlled heating stage and was reversibly cycled across the MIT. Extinction spectra were then calculated from the transmission data as $1 - T/T_{\text{REF}}$, where T is transmission through the array and T_{REF} is transmission through a reference region without the nanodiscs. Representative extinction spectra for an array of nanodiscs ($D = 130$ nm) are shown in Fig. 37c, with a substantial blue shift of the strong dipolar plasmonic resonance apparent as the system is driven across the region of strong electron correlations (30 °C to 80 °C). By fitting the extinction spectra, we can find the resonance wavelength and thus visualize its hysteresis as a function of the substrate temperature (Fig. 37d). It is obvious that the evolution of the LSPR directly tracks the phase transition of the underlying film and that it can be used as an optical marker for changes of the local optical properties of the phase-change material.

Apart from the external temperature, UV light pulses can be used to trigger the insulator-to-metal transition from the prepared initial state because VO₂ has strong absorption in the UV range, as indicated by the large imaginary component of its dielectric function (see Fig. 35). The sequential UV pulses progressively increase the areal density of the metallic phase in the VO₂ film, the average dielectric response of the film is changed accordingly, and naturally also the LSPR is shifted. After sufficiently long illumination time, the metallic “nanopuddles” percolate and the VO₂ film is in the full metallic phase [298]. In the context of non-volatile memory

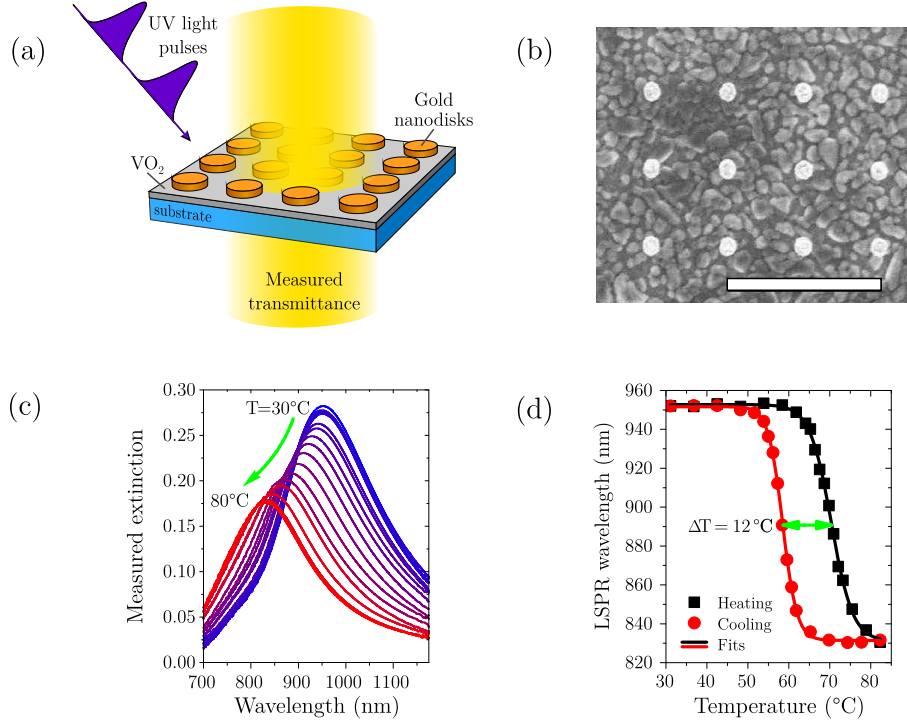


Fig. 37: (a) Model of a hybrid plasmonic phase-change device. An array of periodic Au nanodisks fabricated lithographically on a thin VO_2 film deposited on a SiO_2 substrate. Optical extinction measurements are conducted while successive UV-light pulses pump the VO_2 film into new states. The device is mounted on a temperature-controlled stage. (b) Plan-view SEM image of Au nanostructures patterned on a 50 nm thick VO_2 film. The scale bar is 1 μm . (c) Temperature-dependent extinction spectra for gold nanodisks ($D = 130$ nm) on VO_2 driven through a heating cycle with a temperature increment of 0.5°C around the phase-transition temperature. (d) Plasmon resonance hysteresis curve for the same structure extracted from (c). The black squares and red circles are the measured results for heating and cooling cycles, respectively, while the black and red solid lines are sigmoidal functions fits to the measured data. The green double-headed arrow defines the thermal hysteresis width. Adapted from [297].

applications, the key point is the presence of hysteresis during the phase transition, which enables persistent tuning of the LSPR. To demonstrate this feature, we pushed the VO_2 film into a strongly correlated metal state by maintaining the whole sample at temperatures around T_{MIT} . The system was then illuminated by successive UV light pulses and after each such pulse the extinction spectrum of the array was measured. Figure 38a shows how the LSPR is modulated by a set of UV pulses with constant power density while the whole hybrid system is kept within the MIT region (65°C and 68°C). The LSPR wavelength extracted from each extinction spectrum as a function of cumulated illumination time exhibits a substantial blueshift during the first few pulses, followed by gradual saturation even for very long additional

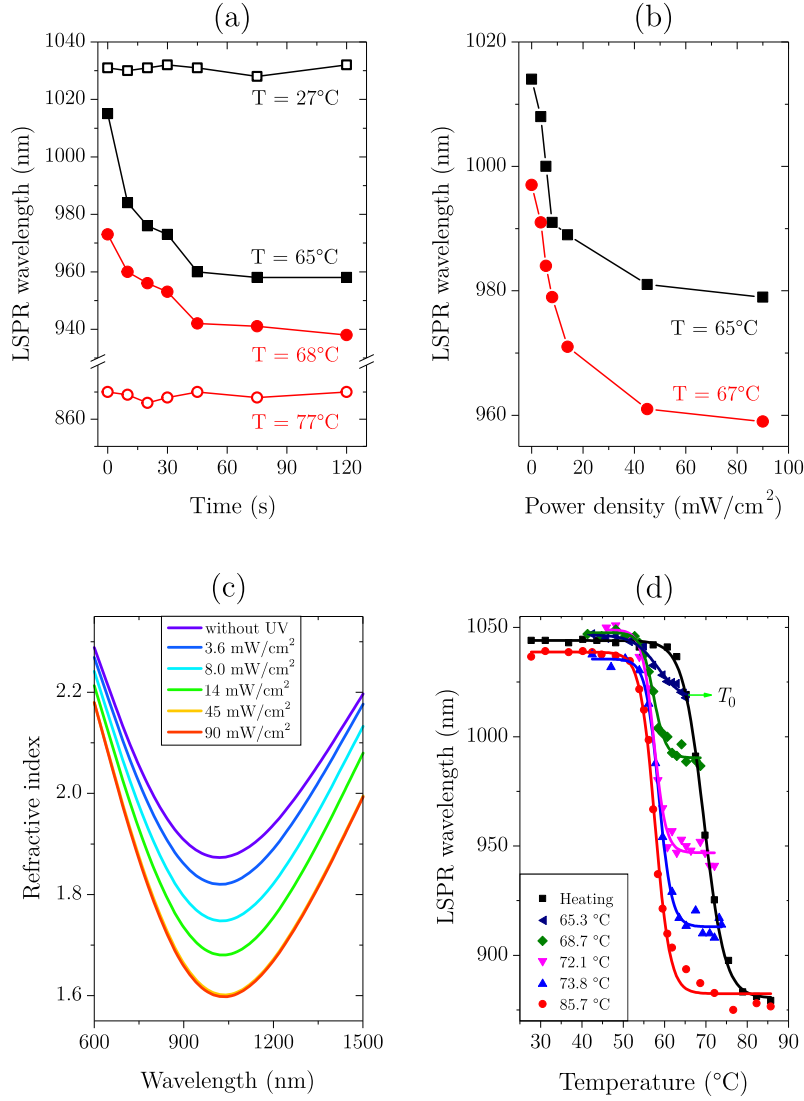


Fig. 38: Persistent optical tuning of LSPR by UV light pulses. (a) LSPR wavelength of Au nanodiscs (175 nm in diameter) on a VO_2 film (50 nm thick) as a function of the cumulated illumination time by a set of UV pulses with constant power density ($90 \text{ mW}/\text{cm}^2$). During the measurements, the whole sample was thermally latched at two different temperatures within the MIT region (65°C and 68°C) and also well below and above it (27°C and 77°C). Each of the first three pulses was 10 s long. They were followed by another two 15 s long and the last 45 s one. (b) LSPR wavelength shift for the same sample as a function of a pulse's power density (for a single 10 s long pulse). (c) Modulation of the refractive index of a bare VO_2 film. The data were extracted from fits of measured ellipsometric spectra for the sample held at 65°C which was illuminated the same way as in (b). (d) LSPR wavelength evolutions during cooling cycles that started from varying initial temperatures T_0 . The black squares are the resonance positions through the preceding heating cycle. The solid lines are sigmoidal fits to the measured data points. Adapted from [297].

UV illumination times. Such behaviour contrasts sharply with results of the control experiments performed well below (27°C) and above (77°C) the MIT, where the LSPR shows no sensitivity to the UV illumination. This observation provides some strong evidence that the correlated state is an indispensable prerequisite for the persistent optical LSPR tuning. Figure 38b shows results of a similar experiment where the LSPR modulation is achieved by UV light pulses now with constant duration (10 s) but with varying power density. A large blueshift and subsequent resonance saturation can be again observed the power density of the UV pulses increases. To verify that the observed shifts were related to the altered dielectric response of VO_2 , we used spectroscopic ellipsometry to characterize a bare VO_2 film under the same illumination protocol which was used for the hybrid plasmonic system. Refractive index of the VO_2 was then extracted from fits of the ellipsometric data by a sum of Gaussian and Lorentz oscillators. The results shown in Fig. 38c reveal a gradual decrease of the refractive index in the wavelength range of interest, which explains the observed blueshift of the measured LSPR wavelength.

The presented experiments reveal how the LSPR is “pinned” to the wavelength defined by the initial state of the VO_2 film. Subsequent UV light pulses persistently drive the LSPR towards blue-shifted resonance wavelengths as more and more VO_2 domains are switched from the insulating to the metallic state. The details of the system evolution after the triggering impulse fades away is an essential piece of information, especially with respect to practical long-lasting memory devices. This topic is studied in Fig. 38d, where the LSPR wavelength is plotted as a function of temperature during several cooling cycles starting from different initial temperatures T_0 . The key observation is that the LSPR wavelength does not depend on the instantaneous temperature, but it exhibits yet another hysteresis that depends on the entire history of the VO_2 substrate. This behaviour is an optical-frequency analogue of the voltage–current response of VO_2 in memristive memory devices [299]. Although UV pulses few tens of seconds long had to be used here, the phase transition dynamics of VO_2 is not intrinsically restricted to such slow time scales: The absorbed UV photons in the present experiment cause both transient local heating and electronic excitation, leading to formation of new metallic nano-puddles in the insulating VO_2 host and thus driving the film towards formation of the full metallic phase. If the UV energy density is high enough to cause the transition to occur by local heating, the reversion from the rutile metallic state to the insulating state could require nanoseconds to microseconds. If, on the other hand, the UV light pulse is ultrashort [300] and the transition proceeds primarily through electronic excitation to the recently observed metallic monoclinic state [301], the complete transition cycle could then occur on a picosecond time scale with no need for a structural phase transition. Such ultrafast optical triggering, along with the possibility to trigger

the phase transition by hot-electron injection — a process that can also occur on a sub-picosecond timescale when driven by femtosecond laser pulses [195] — make our hybrid design a viable one also for practical applications.

In this section, we showed that the extraordinary optical properties of the phase-change material like VO₂ can be imprinted into the LSPR of Au nanodiscs, which facilitates their utilization also at optical frequencies. We also demonstrated that these hybrid plasmonic systems behave like optical analogues of memristive systems, which can play a key role in developing ultra-dense information storage. In our design, the optical plasmonic functionality was achieved by fabrication of gold nanodiscs, i.e., by nanostructuring the gold thin film using EBL. But as we discussed in section 2.1, this process is often complicated and time-intensive. We will now show that the active plasmonic systems which can perform optical modulating functions can be fabricated without any nanostructuring process.

4.4 Epitaxial VO₂ metasurface

It has been already established in section 4.2 that VO₂ thin films can be prepared by various deposition processes. Their properties and surface morphology then of course strongly depend on the growth technique, pressure, temperature, and substrate [302]. Interestingly, in some cases it turned out that instead of the conventional polycrystalline thin films, the VO₂ grows in form of separated laterally confined nanobeams [291, 303, 304]. Such an extraordinary growth pattern was associated with minimization of surface energy during vapor–solid growth process, which leads to preferential formation of otherwise thermodynamically unfavourable facets that form the nanobeams [305]. In our work, we employed a similar strategy and we performed a single-step PLD onto an a-cut (11 $\bar{2}$ 0) face of a sapphire substrate. The unique combination of the in-plane lattice strains and relaxations then enforced an unusual growth pattern onto the VO₂.

The resulting morphology of the nanobeams was evaluated using SEM and AFM, which both revealed a strongly anisotropic polycrystalline structure with grains about 100–200 nm wide, 1–2 μ m long, and 40 nm high (see Fig. 39). The AFM measurements also provided evidence for a close-packed arrangement of the nanobeams, highlighting the self-limiting nature of the epitaxial growth along the [0001] direction of the sapphire substrate. The crystal orientation of the nanobeams with respect to the substrate was then identified by room-temperature X-ray diffraction (XRD). From a standard θ – 2θ XRD scan (Fig. 39d), it is evident that the nanobeams have a preferential orientation of (200) on the a-cut sapphire, which confirms their epitaxial nature [307].

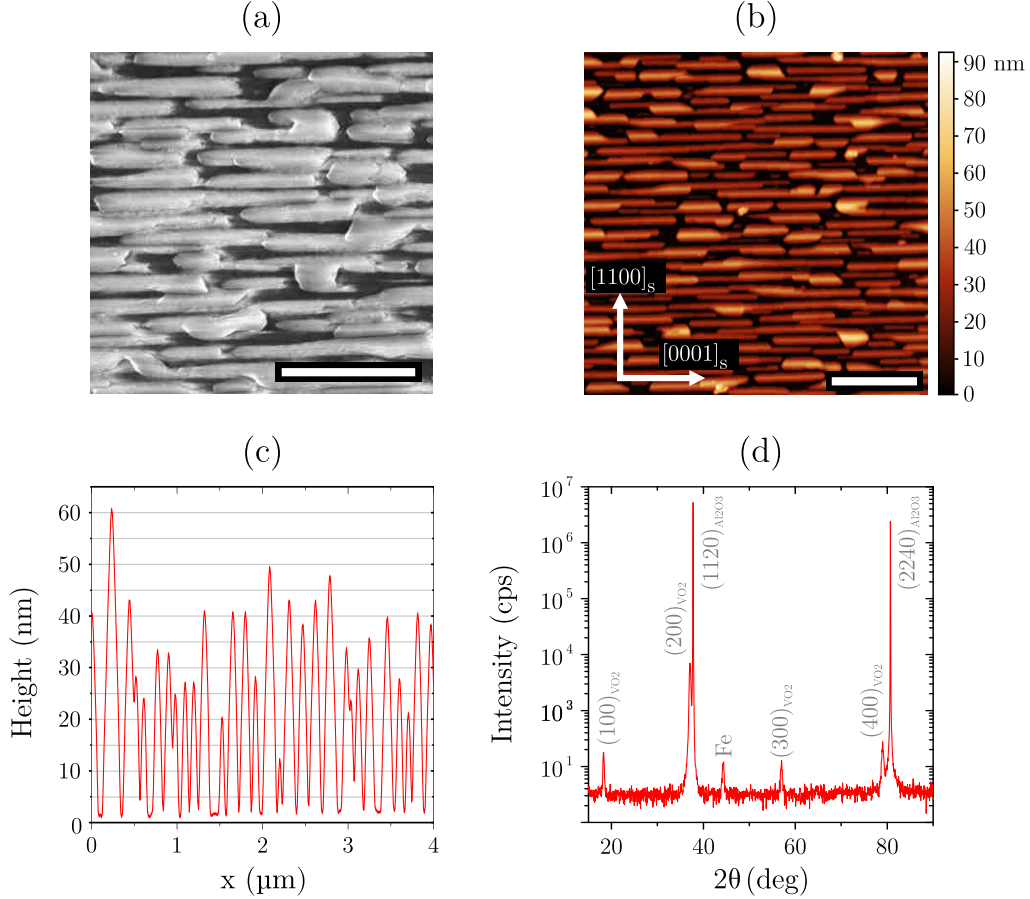


Fig. 39: (a) SEM and (b) AFM images of the epitaxial VO_2 nanobeams on a-cut sapphire substrate. Scale bars are 0.5 and 1 μm , respectively. The arrows denote the crystallographic directions of the substrate surface. (c) Typical AFM height profile measured across the VO_2 nanobeams in (b). (d) Room-temperature XRD spectrum of the same sample with diffraction maxima labelled in grey. Note the iron peak comes from a small part of the beam hitting the sample stage. Adapted from [306].

Optical properties of the VO_2 nanobeam layer were fully investigated using polarized FTIR spectroscopy. In Fig. 40a, the measured extinction spectra are presented for both insulating (RT) and metallic (80 $^\circ\text{C}$) state of the VO_2 . At RT, the dielectric nature of the nanobeams leads to high transmittance ($>80\%$) across the whole NIR spectral range (from 700 nm to 3 μm). Their elongated shape manifests itself as the small anisotropy at predominantly VIS wavelengths. Much more interesting variation of the optical properties can be observed when the nanobeams are metallic: For the incident light polarized parallel with their long axis, a monotonic increase of the IR extinction is obvious, similar to what can be seen in the conventional isotropic VO_2 thin films (cf. Fig. 35 or Ref. [308]). For the light polarized perpendicular to the nanobeams, however, we observe a broad extinction peak centred

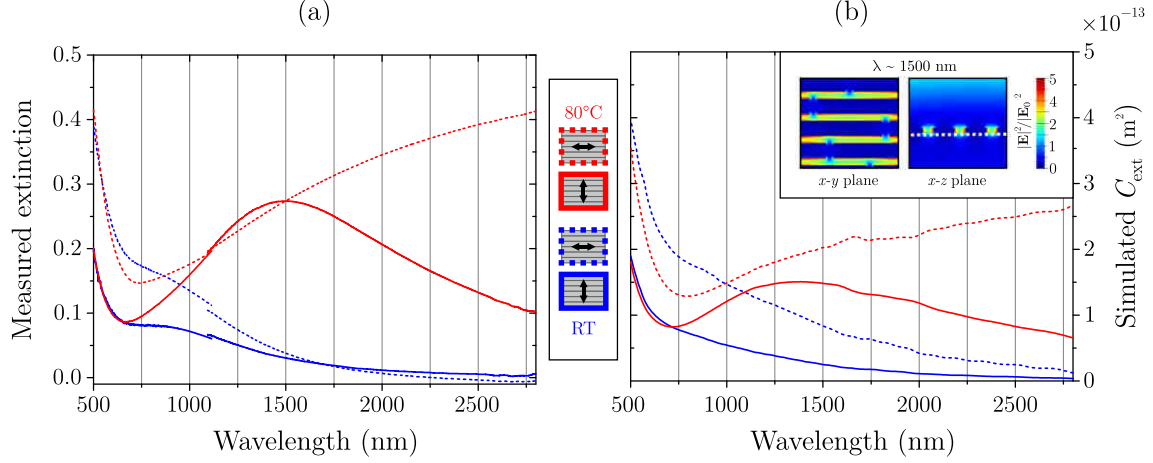


Fig. 40: (a) Measured and (b) simulated extinction spectra of the epitaxial VO₂ nanobeam layer for incident-light polarization along (dashed lines) or across (solid lines) the nanobeams for both insulating state of VO₂ (RT, blue lines) and the metallic state (80 °C, red lines). The inset in (b) shows in-plane (x - y) and out-of-plane (x - z) maps of electric field intensity enhancement in the metallic nanobeam layer at the LSPR wavelength. Adapted from [306].

around 1.5 μm that we ascribe to the excitation of LSPR. This plasmonic behaviour is a direct consequence of the lateral confinement of the conduction electrons in the metallic nanostructures that are otherwise achieved only by some sort of top-down nanofabrication. Due to the specific lateral size of our nanobeams, the spectral region of the largest extinction contrast between the insulating and metallic phase is located at the telecommunication wavelengths ($1260 \text{ nm} < \lambda < 1625 \text{ nm}$ [309]). Moreover, the reversible modulation depth [297] calculated from the experimental data is greater than 9 dB across all these important wavelengths. Although structurally anisotropic, our metasurface shows only weak polarization dependence in this spectral region, and what is more, around telecommunication C-band (1.5 μm) it is virtually isotropic. A device with such a high extinction contrast and broad bandwidth is highly desirable for many applications in the field of optical modulation, as these attributes are crucial for high signal-transmission capacity, better resistance to noise, and longer achievable distances [310]. Although in our experiments the modulation is performed using inherently slow external heating, it has been already demonstrated that the phase transition in VO₂ can be induced by optical pulses on ultrafast time scales [195], as discussed also in the previous section.

Apart from the MIT, there is an additional light-modulating capacity of our metasurface that stems from its optical anisotropy at IR wavelengths beyond 1.5 μm . While the insulating phase has almost perfectly isotropic response in this spectral region, the metallic VO₂ nanobeams provide very high extinction contrast between

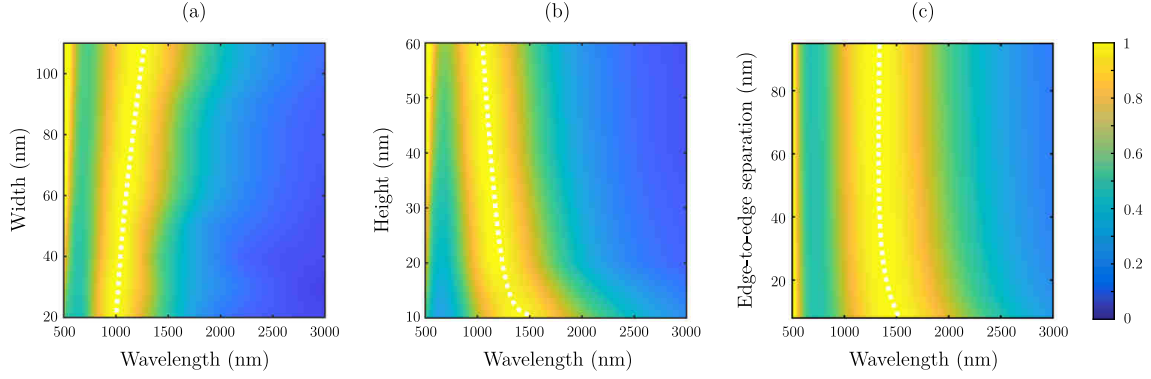


Fig. 41: Calculated extinction spectral maps for an individual infinitely long metallic VO_2 nanobeam on top of a sapphire substrate with (a) constant height of 30 nm and varying width, (b) constant width of 60 nm and varying height. (c) A similar simulation for two nanobeams with constant width of 100 nm and height of 30 nm, and varying separation between them. In all three cases, the incident light polarization was perpendicular to the nanobeams. The data were normalized to the NIR resonance peak (dashed white line). Adapted from [306].

light polarized across and along them (see Fig. 40a). This feature allows us to use an extra degree of freedom — polarization of the incident light — and superimpose it on top of the MIT-based switching. That way, two independent transmission modulation channels will become available. At wavelengths between 2 and $2.8\mu\text{m}$, in particular, these two channels for optical signals are well separated by at least 2.4 dB and they can be directly addressed by controlling the VO_2 MIT and the incident light polarization. Additionally, this approach can be used not only to modulate the intensity of light, but also to control the amplitudes of its orthogonal polarizations. Extra information could thus be encoded into the intensity difference between the two polarizations, which is not easily achievable in conventional bulk optics, and efficient polarization modulator between the circular and linear polarization would be created [311]. If an electric field instead of temperature would be used, this modulation could be much faster and therefore more useful for applications in communication technologies [312, 313].

To confirm the plasmonic nature of the demonstrated functionality and to provide deeper physical insight into the relationship between metasurface morphology and optical properties, we performed three-dimensional full-wave numerical simulations using a commercial FDTD solver (Lumerical). First, we aimed to reproduce the measured experimental spectra. To this end, we created a model corresponding to the sample morphology, which was obtained using SEM and AFM beforehand: VO_2 nanobeams of constant width (96 nm), height (28 nm), and length ($1.3\mu\text{m}$) were arranged into a lattice with a constant inter-rod spacing (48 nm) in both directions and

random offset along the anisotropy axis (see the inset of Fig. 40b). The dielectric function of VO_2 was obtained from Ref. [314], and the nanobeam length was extended further than the nominal simulation volume to avoid any residual scattering effect. In line with the experiment, the calculated extinction spectra for both phases of VO_2 and for two principal polarizations are plotted in Fig. 40b. Although small discrepancies appear, the agreement between the measured and calculated spectra is remarkable. Both the anisotropy of the dielectric metasurface in its insulating state and the resonant extinction observed in its metallic state are well reproduced. Moreover, we can infer from the electric field plots in the inset of Fig. 40b that the perpendicular polarization generates around fourfold increase in the electric field strength. Contrary to the typical situation, the plasmonic resonances in our experiments are of better quality (i.e., larger Q-factors) than those in simulations. We ascribe this to the high quality of the fabricated epitaxial nanobeams while using polycrystalline VO_2 dielectric function in the simulations.

To assess how the dimensions of VO_2 nanobeams influence the resulting optical properties of the metasurface, we performed another set of FDTD simulations, featuring only a single infinitely long metallic VO_2 nanobeam. First, the effect of nanobeam width was investigated while its height was fixed at 30 nm. The resulting extinction spectral map for incident light polarized across the nanobeam is shown in Fig. 41a. A characteristic redshift of the LSPR with increasing nanobeam width is clearly visible. The situation is quite opposite in the extinction map calculated for a nanobeam with fixed width (60 nm) and varying height (Fig. 41b). The blueshift of the resonance stems from the fact that the increase of height leads to less confinement of conduction electrons also in the lateral direction (effectively reducing the induced surface charge density). The last effect investigated was the edge-to-edge separation between nanobeams (Fig. 41c). A small redshift can be observed for the separation decreasing into the near-field regime (below 20 nm), suggesting the appearance of weak dipolar coupling [315]. Altogether, our simulations reveal the strong effect of structural parameters on the shape and position of the metasurface resonance. Translating this knowledge into technological applications, albeit still a significant challenge in terms of epitaxial fabrication, will require tuning the growth parameters of the VO_2 only.

The VO_2 metasurface studied here can play an important role not only by the control of light transmission via absorption (related to the imaginary part of the complex refractive index) but also via its phase-shifting properties (related to the real part). The enhanced light absorption contrast between the insulating and metallic phases of VO_2 is in fact accompanied by the similar contrast in terms of the transmitted light phase [308, 314, 316]. To visualize these phase-shifting properties, we set the incident polarization at 45° with respect to the nanobeams and we incor-

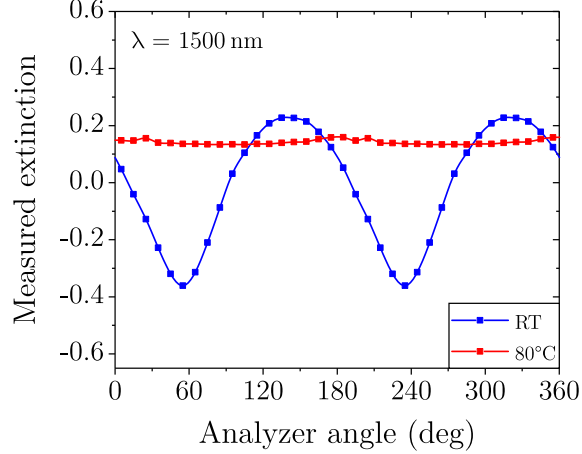


Fig. 42: Measured extinction of the epitaxial VO₂ metasurface (for incident-light polarization 45° with respect to the nanobeams) as a function of the analyzer angle (0° is parallel to the nanobeams). Results are shown for the insulating (RT, in blue) and metallic (80 °C, in red) state of the VO₂ at $\lambda = 1500$ nm where the sample is virtually isotropic. Note that the right half of the data is a copy of data from 0° to 180° and the extinction, defined in this chapter as $1 - T/T_{\text{REF}}$, can be negative or larger than one when measured with the polarizer–analyzer setup. Adapted from [306].

porated another polarizer (herein referred to as analyzer) into the detection branch of our IR microscope. Thus, an equal amount of light with the two principal polarizations (parallel and perpendicular to the VO₂ nanobeams) will interact with the sample. Due to anisotropic material dispersion, each of these two polarizations will acquire different phase during propagation through the metasurface, and the 45° linear polarization will be converted into an elliptical one. Given the transmissivity of the sample is equal for the two principal polarizations (at it is around 1500 nm for our sample, cf. Fig. 40a), a pure phase-shifting effect will be observed when the transmission will be measured as a function of the analyzer angle. We performed such an experiment and the results are presented in Fig. 42. The dielectric metasurface in the insulating phase behaves like a simple attenuator with the intensity oscillations according to Malus’s law for crossed polarizers [3]. But when the metasurface turns metallic at 80 °C, it starts to behave like a quarter-wave plate which turns the linearly polarized incident wave into a circularly polarized one, and the measured extinction becomes characteristically insensitive to the analyzer angle. This demonstrates the great versatility of our metasurface and proves it can function as a multifunctional device, controlling both the intensity and the phase of the transmitted light.

4.5 Conclusions

This chapter was devoted to strategies which can bring tunability into plasmonics. We began with an overview of the three main approaches to this problem: mechanical manipulations, control of charge-carrier density, and utilization of phase-change materials. Special emphasis was then placed upon on prototypical example of the phase-change materials, vanadium dioxide. Its main properties were described and the mechanism of its transition from the insulating to the metallic phase was elucidated. In line with the two distinctive ways how can be the phase-change materials incorporated into metasurfaces, two short studies were presented. In the first one, the VO_2 played a role of the substrate, thus influencing the plasmonic resonance of gold nanodiscs only indirectly. Nevertheless, the fingerprint of its metal-insulator transition was translated to the optical frequencies and the sample was thus suitable for storage of optical information via UV light pulse writing and VIS light read-out. In the second study, VO_2 itself formed the metasurface building blocks. This was, rather unconventionally, achieved not by top-down nanofabrication but by epitaxial self-limiting growth of VO_2 nanobeams on top of a sapphire substrate. A high-quality transverse plasmonic resonance of the nanobeams revealed itself in the experimental extinction spectra and it was possible to modulate its strength by means of external temperature or incident-light polarization. Moreover, we also demonstrated a pure phase-shifting ability of our nanobeam meta-atoms, a cornerstone feature for all types of metasurfaces.

5 PLASMONICS AND ELECTROCHEMISTRY

“I have been so electrically occupied of late that I feel as if hungry for a little chemistry; but then the conviction crosses my mind that these things hang together under one law, and that the more haste we make onwards, each in his own path, the sooner we shall arrive, and meet each other, at that state of knowledge of natural causes from which all varieties of effects may be understood and enjoyed.”

Letter to Eilhard Mitscherlich, 1838
MICHAEL FARADAY

All the previous pages revolved around two fundamental components of plasmonics — electrons and light. We discussed how they interact and which extraordinary outcomes can their interactions produce. But there is yet another relevant topic which has not been discussed here. It is the field of chemistry, where both electrons and photons play a very important role. From the most fundamental view, chemistry deals with interactions (bonds) amongst compounds of matter (atoms and molecules). These interactions are, almost universally, of electromagnetic origin, and thus electrons and photons naturally participate in them. Figure 43 shows a triangular diagram that describes the common aspects and relationships between plasmonics, photochemistry, and electrochemistry. It is symbolical that one of the founding fathers of the theory of electromagnetism, Michael Faraday, significantly contributed also to the field of electrochemistry [317]. In line with this fact is an

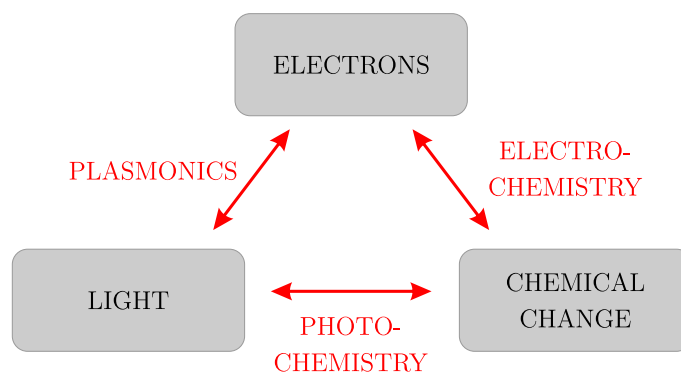


Fig. 43: Relationships and common aspects of plasmonics, photochemistry, and electrochemistry.

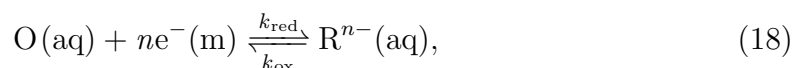
expectation that electrochemical studies could benefit from utilization of plasmonic materials and modern nanofabrication techniques. Successful examples include use of carbon nanotubes for signal amplification [318] or of metallic NPs for electrochemical detection of single base DNA mismatches [319]. Recently, electrochemical methods exploiting unique properties of nanostructured electrodes from TiO₂ also appeared [320, 321]. TiO₂ is not plasmonic in a traditional sense of the word, but as a renowned photocatalytic material it inherently unites electrons and photons as well.

In this chapter, we will expand on this interesting partnership. First, we will provide the fundamentals of electrochemistry, taken mainly from a physicist’s point of view. That is, with more focus on description of the energy landscape and driving forces during electrochemical experiments. Next, studies uniting plasmonics and electrochemistry will be briefly reviewed. Then we will take a closer look on utilization of plasmonic effects for photochemistry — we will present a collection of data from electrochemical experiments on electrodes covered by semiconductor nanotubes (NTs) decorated with gold nanoparticles.

5.1 Fundamentals of electrochemistry

Electrochemistry is a traditional branch of physical chemistry where charge carriers are employed in studying and controlling chemical reactions on surfaces of electrodes [322]. It is used in chemical and biological sensing (e.g., glucose sensors, gas detectors, pH meters), technological applications (e.g., electroplating), or energy storage (e.g., solar cells, batteries). The major benefit of electrochemistry is that it does not require complicated and expensive instrumentation, while it still provides accurate and detailed information about presence of various chemicals and/or about the ongoing chemical reactions. Besides, it is capable to do so *in situ*, requiring only very short measurement times [323].

Electrochemical processes always involve electron exchange reactions in which the oxidation states of atoms are modified. Any such reaction necessarily includes both a reduction process (gain of electrons, decrease in oxidation state) and a complementary oxidation process (loss of electrons, increase in oxidation state). These redox (reduction–oxidation) reactions often involve chemical species in the same phase of matter, but electrons can be also transferred through an interface between two phases (e.g., between a molecule in an aqueous solution and a metal electrode). A model redox reaction involving exchange of n electrons with the metal (m) electrode can be written in the form of equation



where O and R are the oxidized and reduced forms of the redox couple in the solution (aq), respectively. Rate constants k_{red} and k_{ox} then quantify the rate of the reaction in the respective directions. All chemical reactions are governed primarily by the laws of thermodynamics [324] — they can be described as proceeding within a landscape of the particular thermodynamic potential (e.g., internal energy, Gibbs free energy, etc.) while following the general energy minimization principle [325]. In this context, the chemical potential μ is a particularly important form of energy, which is related to the amount of chemical species in the system and thus to the chemical reactions as well. To describe the exchange of electrons in electrochemistry, however, one must unite this thermodynamical description of electrons located at the molecules in the solution with the description of electrons inside the solid-state electrode. From the perspective of a physicist, the conduction of electrons in the band structure of a material is transformed into a chemical electron transfer event at the solid–liquid interface. This issue is solved by introducing so-called electrochemical potential $\bar{\mu}$, which is a total potential that includes a contribution of the conventional chemical potential (internal, nonelectrical) but also of the pure electric potential (i.e., local electric potential energy per electron) [326]. In equilibrium, the chemical energies of the molecules in the solution and the electrical energies of electrons in the solid-state electrode must be balanced. Chemists often prefer to start from the kinetics present in the liquid and subsequently evaluate the charge transfer from/to an electrode [327]. Here, to keep this introduction concise, we will begin our description directly with the Nernst equation, the central equation of electrochemistry. It relates the interfacial potential difference $\Delta\phi = \phi_{\text{M}} - \phi_{\text{S}}$ between the electric potential of the metallic electrode ϕ_{M} and that of the solution ϕ_{S} , with the concentrations of the reduced c_{R} and oxidized c_{O} form of the redox molecules in the solution [328]:

$$\Delta\phi = A + \frac{RT}{nF} \ln \frac{c_{\text{O}}}{c_{\text{R}}}, \quad (19)$$

where R is the universal gas constant, F is the Faraday constants, and T is the absolute temperature. The constant A is the standard electrode potential of the redox process, which depends on the nature of the redox couple, ionic strength of the solution, temperature, etc. The Nernst equation reveals how the applied voltage supplies the necessary electrical energy and acts as an electrochemical “pressure” that drives the system out of equilibrium towards increased concentration of the desired form of the redox molecule. This is the fundamental physical principle behind almost all electrochemical methods. To better visualize the relevant physics of electron transfer processes, energy diagrams are often used (see Fig. 44a) [326]. The metal electrode is schematically described as a classic conduction band with the occupied states below the Fermi level E_{F} and the empty states above it. The

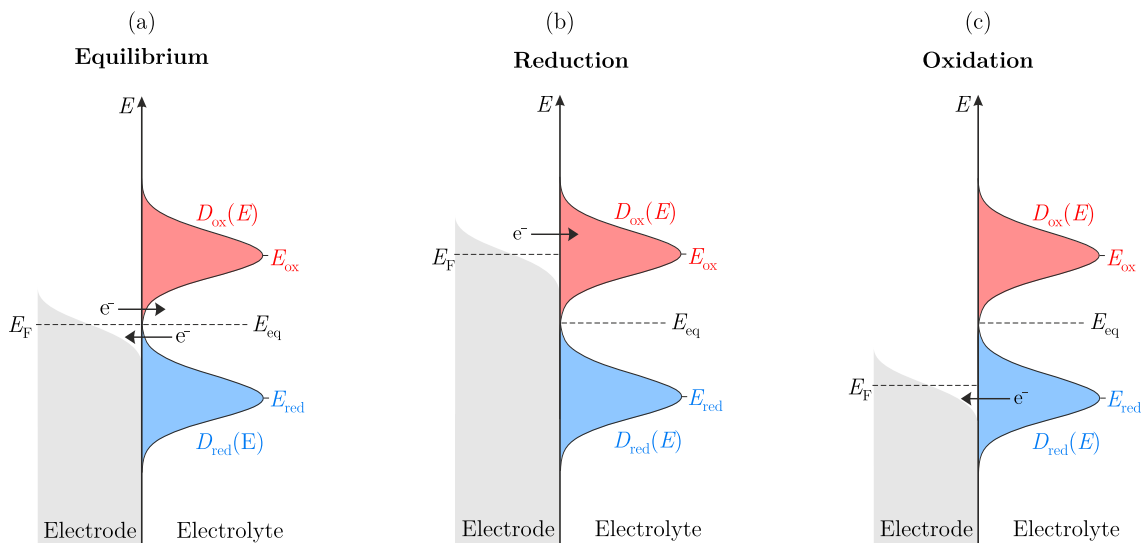


Fig. 44: Electronic states at the interface between a metal electrode and a redox couple in (a) equilibrium, (b) with a negative potential applied (cathodic conditions), (c) with a positive potential applied (anodic conditions).

molecular energy levels that can be involved in the electron transfer are located in the vicinity of the molecule's equilibrium Fermi level E_{eq} , which is broadened and split due to interactions with molecules of the solvent [329,330]. The density of the empty (oxidized) states $D_{\text{ox}}(E)$ is centred at energy E_{ox} , while that of the occupied (reduced) states $D_{\text{red}}(E)$ is located around E_{red} . The rate of the redox reactions can then be related to the overlap between the occupied levels of one of the phases (metal or solution) and the empty levels of the other phase at the same energy. When a negative potential with respect to the E_{eq} is applied (cathodic bias, Fig. 44b), the Fermi level of the electrode moves towards higher energies. This enhances the overlap between occupied electrode states and states on the oxidized molecules and thus promotes their reduction. The opposite situation arises when a potential more positive than the equilibrium one is applied, which results in the electron transfer from the reduced species to the electrode states (anodic bias, Fig. 44c).

In the previous paragraph, with the aid of the Nernst equation, it was established that the gradient of the electrochemical potentials is the driving force to which the system reacts and because of which it evolves and establishes a new equilibrium. This process is an intricate interplay of many variables describing the electrochemical system — electrical variables (potential, current), electrode variables (material, geometry), mass transfer (diffusion, adsorption) or solution variables (concentrations, pH). Electrochemical experiments are based on controlling some of these variables and observing how other variables respond [317]. This work will be focused almost exclusively on voltammetric techniques, which constitute an important part of the

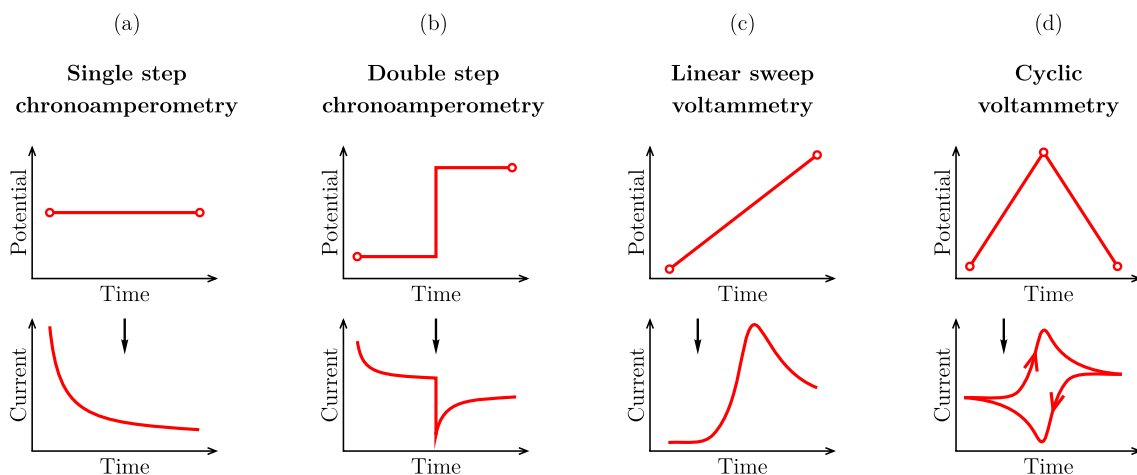


Fig. 45: Various types of time-varying potential programmes with corresponding current responses of selected voltammetric techniques.

broad field of electrochemistry, where the potential of the working electrode is varied and the current response of the system (voltammogram) is recorded. According to the particular temporal shapes of the applied voltage, different names are used for this class of techniques (see their summary in Fig. 45). In single- and double-step chronoamperometries, for example, one or two constant potential steps are applied, respectively. The current signal then corresponds both to the charging of the electrode's electric double layer and to the ongoing redox processes. In linear and cyclic voltammetries, linear time-varying potentials are applied. Based on the height, position, and shape of the recorded voltammogram, a quick identification and quantification of the species in the solution can be obtained, together with the information about reaction mechanisms and rate constants.

All voltammetric measurements require at least two electrodes — a working and a reference electrode — placed into an electrolyte solution. The working electrodes are made of various conductive materials like metals and their alloys (e.g., copper, gold, mercury, platinum), different forms of carbon materials (e.g., glassy carbon, pyrolytic graphite, graphene) or even transparent conductive oxides (e.g., indium tin oxide, fluorine-doped tin oxide). The required potential is applied on the working electrode, and it then facilitates the transfer of electrons (charge) to and from the reducible/oxidizable analyte, respectively. The reference electrode, which acts as the other half of the cell, must balance the charge added or removed by the working electrode. Besides, it should have a stable absolute potential so the potential of the working electrode can be gauged with respect to it. The whole circuit must be closed by a supporting electrolyte, ideally with low resistance R_s (e.g., highly concentrated solution of an electrochemically inactive salt), so the voltage drop occurs as close as possible to the electrodes. The problem of the two-electrode setup is that if

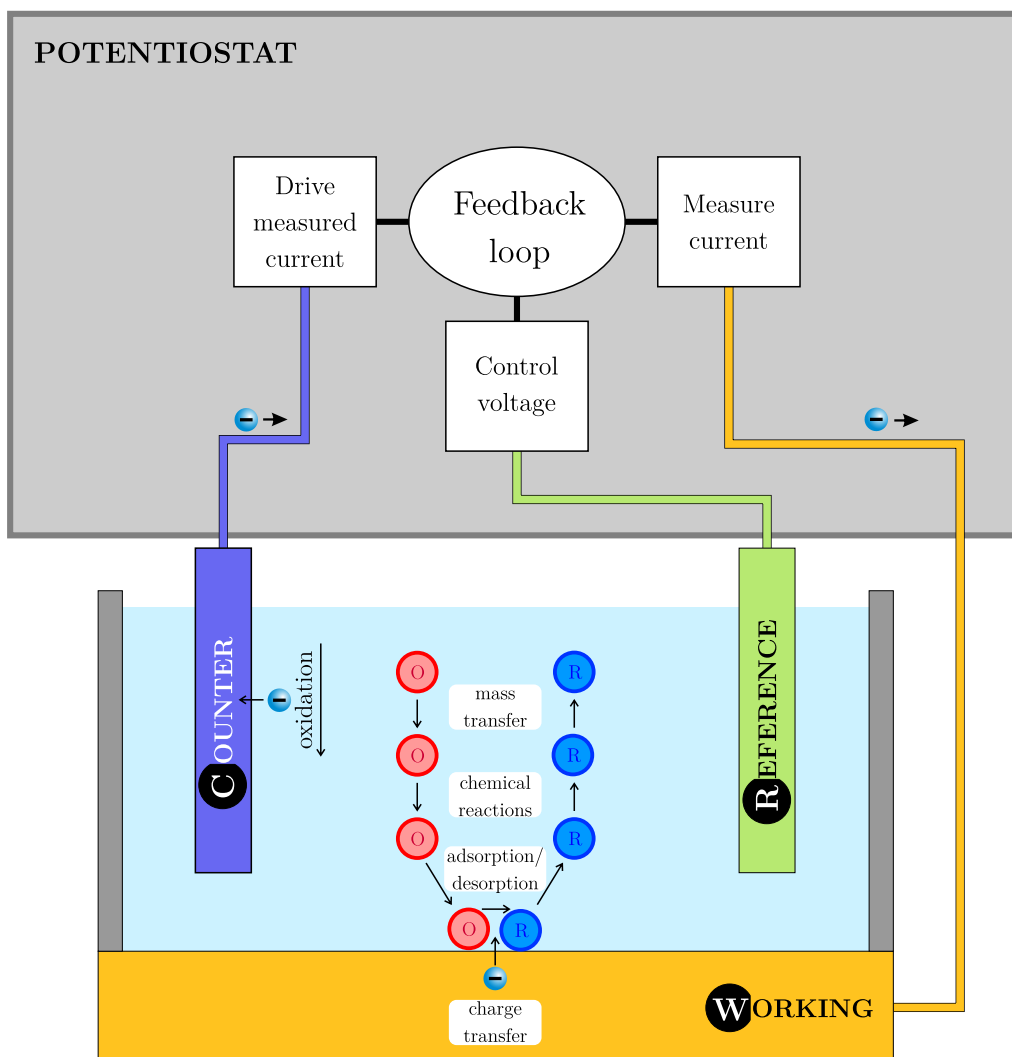


Fig. 46: Schematic of a three-electrode cell for voltammetric measurements, including the inner circuit of the potentiostat and an example of a typical reduction pathway on the working electrode.

the potential of the working electrode is measured during the passage of current i , some unwanted parasitic voltage drop equal to iR_s will be inevitably included in the measurements. The measured value of the potential will thus be partially also characteristic of the bulk solution and not of the electrode reactions themselves [331]. Moreover, the reference electrode will have to accommodate all the flowing current, which will push it away from its equilibrium potential. This will result in another error in the estimation of the working electrode's potential. To eliminate these two issues, the tasks of supplying the electrons and providing the reference potential are often divided between two separate electrodes — a dedicated reference electrode and a counter (auxiliary) electrode — which are connected with the working electrode in so-called three-electrode setup (see Fig. 46). In this setup, the reference electrode

does not have to carry any current, it provides a stable and reproducible potential (independent of the composition of the sample solution), and it thus acts as a good reference for measurements and control of the working electrode’s potential. The reference electrodes are generally made in the form of separate half-cells, where some selected stable complementary redox components, such as metallic salts Ag/AgCl or Hg/Hg₂Cl₂, are enclosed in a suitable inner electrolyte and separated from the studied solution by a salt bridge with porous frit. The standard potential of this system, given by the Nernst equation, is controlled only by the solubility equilibria of the metallic salt and concentration of the inner electrolyte [332]. The counter (auxiliary) electrode of the three-electrode setup enables transfer of all the electrons necessary to balance the current going through the working electrode. To supply such large currents, counter electrodes are of large surface area, which minimizes their necessary polarization, or swing to extreme potentials at the edges of the potential window, where they usually oxidize or reduce the components (water or protons, respectively) of the supporting electrolyte. To ensure their stability in a case of sudden swing to high potentials, counter electrodes are usually made of very stable and inert materials, like platinum or glassy carbon. The last remaining component of every electrochemical setup is a potentiostat, a feedback-controlled device which controls voltages on the working electrode while it ensures registration of the corresponding currents during the course of an experiment (Fig. 46).

In this section, the essential principles of electrochemistry were briefly introduced. Note that this field is very broad and only its most relevant parts were covered on a level of detail sufficient for understanding of the rest of this chapter. Now, several studies which combine plasmonics and electrochemistry will be overviewed.

5.2 Studies combining plasmonics and electrochemistry

When plasmonics comes together with electrochemistry, two combinations of the probing perturbation and the measured response can be investigated. In the first class of experiments, often called “spectro-electrochemistry”, the optical response is measured while the system is pushed out of equilibrium by changing its electrochemical potential. This can be done by adding chemically active species [333, 334] or, more often, by application of a voltage bias [335]. Electrochemistry can be combined with vibrational spectroscopies (IR [336] or Raman [337–339]) or with photoluminescence [340, 341]. (Electro)chemical properties can be also indirectly determined from plasmon-related features of the absorption or scattering spectra. Since the earliest reports of tuning LSPR wavelengths by applied voltage [342, 343],

spectro-electrochemistry has been used for analysis of nanoparticle charging [335] and ongoing chemical reactions [344,345]. It has also been considered for sensing applications [141, 346, 347]. Recently, spectro-electrochemical studies were performed also with single particle resolution [348–350]. That enabled observation of effects which were previously smeared out by ensemble averaging and it even raised some questions about interpretation of the previously published results [351–353].

The second class of investigations goes the other way around. The studied system is perturbed by a light pulse and its electrical response (photovoltage or photocurrent) is measured. Studies of this kind are often classified as “photo-electrochemical”. Historically, these experiments were used for elucidation of charge-separation effects in semiconductors for solar energy harvesting [354, 355]. Later, they were also utilized in investigations of plasmonic photocatalysis and photosensitization schemes [356]. In the context of this work it is very important that these methods are inherently suitable also for analysis of the hot-electron effects discussed on p. 43 [357–359], especially with respect to the direct activation of chemical transformations by them [186, 187, 190, 360–362] (see Fig. 47).

In all these studies and applications, the interface effects and electronic environment (band structure) critically influence the consequences of hot-electron excitations. Below, a study of hot-electron effects in a system composed of WS₂ NTs decorated with Au NPs will be presented. We chose WS₂ as a representative of a modern class of 2D materials, transition metal dichalcogenides (TMDs), which have many interesting optical and electronic properties, and which have been proposed as potentially useful for electrochemical sensing and photocatalysis. Our goal was to study how presence of photoexcited Au NPs influences photochemistry on electrodes covered by such plasmonically active NTs.

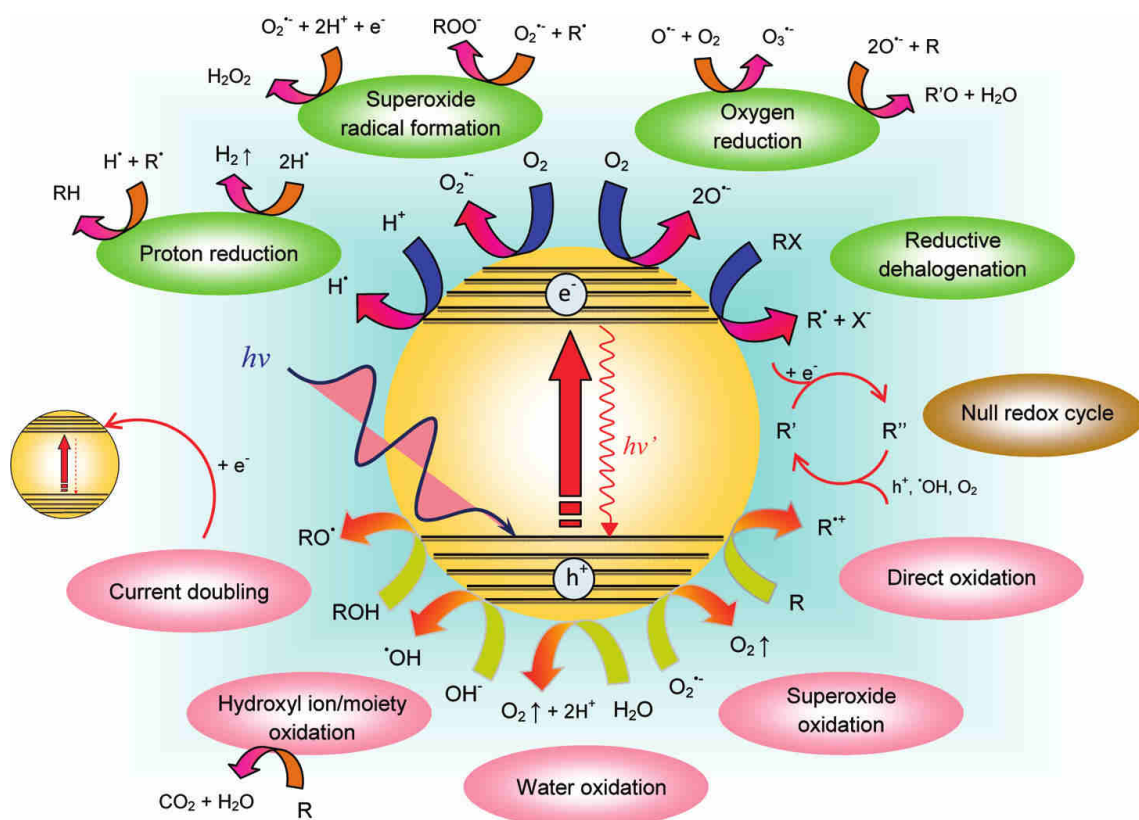


Fig. 47: Possible reaction pathways arising from the excitation of a plasmonic photocatalyst. Included are primary redox reactions and selected secondary radical reactions that can follow. R denotes the general organic electron donor molecule. Adapted from [363].

5.3 Hot-electron photochemistry on WS₂ nanotubes decorated with gold nanoparticles

Two types of solid-state contacts can arise at metal–semiconductor interfaces: ohmic and non-ohmic. Ohmic contacts have virtually zero potential barrier at the interface and they thus allow a flow of charge across the junction in both directions (they are non-rectifying). They have naturally very low resistance, which results in low power dissipation, and are therefore critical for performance and reliability of electronic devices. For many metal–semiconductor junctions, however, there exists a potential barrier significantly higher than the thermal energy of electrons, which leads to depletion of semiconductor’s charge carriers near the interface and to the rectifying (non-ohmic) effect on the flowing currents (see Fig. 48). The height of this so-called Schottky barrier Φ_B depends on the electron affinity of the semiconductor, on the work function of the metal, but also on the microscopic details of the junction morphology (presence of interface bonds, defects, etc.). Although unwanted and

detrimental for some applications, the rectifying function of the Schottky barrier is very useful in many devices that act like diodes. In the context of hot-electron photochemistry, the Schottky barrier is used to prevent recombination of the hot electrons with the hot holes [192, 193, 364]. That way, their lifetime is significantly increased and they can be utilized to drive chemical reactions or to sensitize the nearby materials [365–367]. Electrochemistry is an excellent tool to study such effects because it allows to tune the height of the Schottky barrier by application of voltage bias and to detect the photovoltage or photocurrent at the same time.

Here, we study the metal–semiconductor system of Au NPs on top of WS₂ nanotubes. WS₂ is a representative of a class of semiconductors named transition metal dichalcogenides (TMDs), which have become frequently studied especially due to existence of their 2D monolayer allotropes [368–371]. Unlike a prototypical 2D monolayer graphene, TMDs offer a direct band gap [372–374] and strong spin–orbit coupling [375], which render them potentially useful for applications in electronics [376] and valley physics [377]. TMDs have also their own inherent electrochemistry [378, 379] and have been proposed as a potentially useful material for electrochemical sensing [380, 381] or technical applications [382].

In our study, we use WS₂ in the form of multi-wall nanotubes, which offer very high surface-to-mass ratio and can be easily synthesized in large quantities [384]. The NTs have usually between 5–20 walls, they are 1–20 μm long and 30–200 nm in diameter (see Fig. 49). Unlike carbon NTs or NTs of various oxides, the WS₂ NTs consist of an outer layer of sulphur atoms, which are particularly suited for linking with noble metals due to formation of relatively strong sulphide bonds [385]. To decorate the NTs by Au NPs we followed the method described in Ref. [386]. Briefly, we took the WS₂ NTs provided by R. Tenne (Weizmann Institute of Science, Israel), resuspended them in isopropyl alcohol for target concentration of 0.65 mM and sonicated for 2 min. The prepared suspension was added into a boiling aqueous

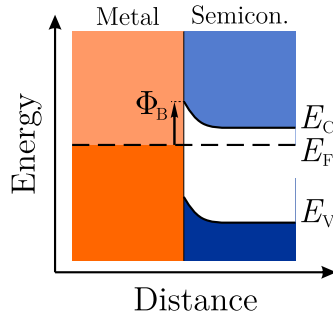


Fig. 48: Band diagram for a metal–semiconductor junction with the Schottky barrier. The Fermi levels E_F in both materials are equilibrated, E_V is the valence band edge, E_C is the conduction band edge, Φ_B is the Schottky barrier height.

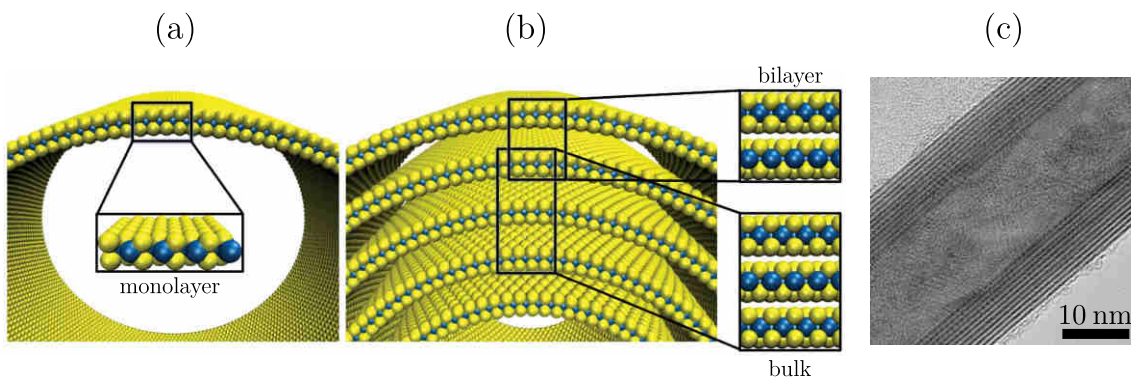


Fig. 49: (a,b) Structure models of WS₂ NTs. Sulphur – yellow, tungsten – blue. (a) Single-wall NT is composed of a WS₂ monolayer only. (b) Multi-wall NT is composed of bulk inner walls and a bilayer outer wall. Adapted from [383]. (c) TEM image of a typical multi-wall WS₂ NT. Image courtesy of Ing. Lukáš Kachtík.

solution of chloroauric acid and boiled for additional 3 min under vigorous stirring. The whole reaction mixture was then let to cool down to room temperature while still stirred. Note that the HAuCl₄/WS₂ molar ratio was adjusted to values between 1:20 and 1:5 in order to obtain the required mean Au NP size between 5 and 15 nm, respectively (see Fig. 50). For electrochemical investigations it was necessary to immobilize the decorated NTs onto a conductive substrate. We decided to use commercial glass slides covered by 120 nm of indium tin oxide (ITO, Delta Technologies). The thin film of ITO acts as a conductive layer (declared sheet resistance of 5–15 Ω □⁻¹) while it is still optically transparent and thus usable for spectroscopic studies. Note that prior to the drop-casting deposition of the control samples with bare WS₂ NTs, the glass slides were treated by Ar/O₂ plasma to lower their hydrophobicity. This was not necessary for NTs decorated by Au NPs.

Before any photo-electrochemical experiments could be performed, it was necessary to establish the main electrochemical parameters of the whole electrode and of its individual components. To this end, we employed so-called redox probes — molecules that can undergo redox reactions with very good reversibility and are thus often used to study electron transfer mechanism of nanostructured electrodes. By choosing an appropriate probe we can select how sensitive it will be towards various characteristics of the electrode. Some probes, for example, carry electrical charge and thus can be attracted or repelled by the surface charge present on the electrode. Some probes differ in their sensitivity towards surface chemistry. According to this property they are usually divided into two categories: “Outer-sphere” systems, which do not require absorption on the electrode surface for the redox reaction to occur, are insensitive to the surface defects and impurities but are strongly influenced by the electronic environment of the electrode (density of states) [387].

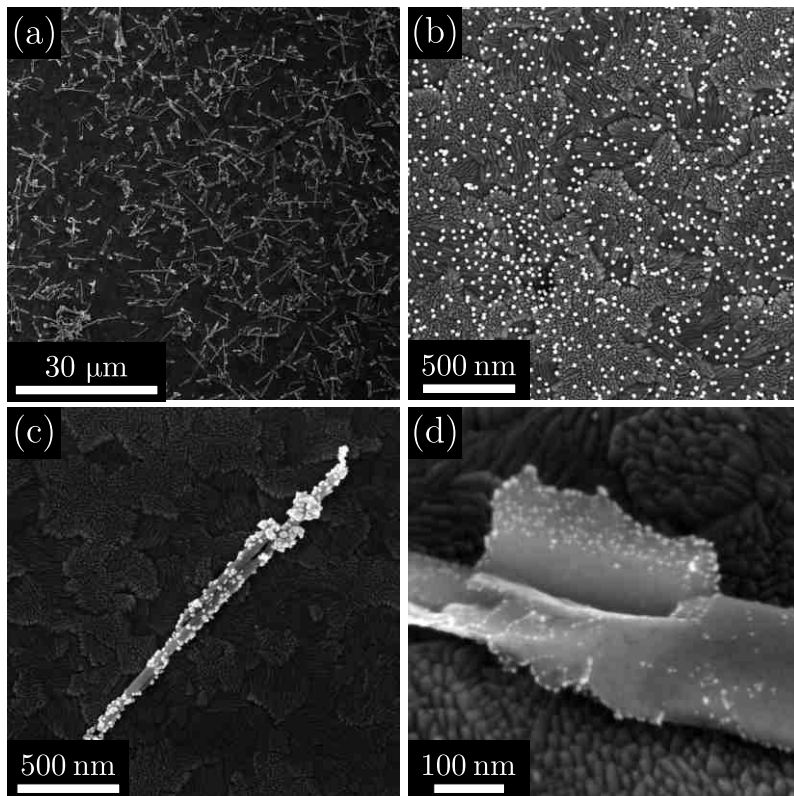
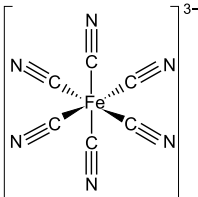
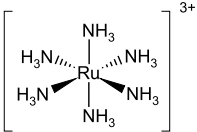
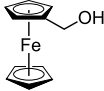


Fig. 50: SEM images of ITO electrodes covered by drop-casted nanotubes or nanoparticles. (a) Bare as-received NTs. (b) 20 nm gold colloidal NPs (c) NT decorated by approx. 15 nm Au NPs. (d) NT decorated by approx. 8 nm Au NPs.

“Inner-sphere” systems, on the other hand, require formation of covalent bridges with the electrode and are thus affected by the presence of an oxide passivating layer, adsorbates, or simply by different surface-terminating chemical groups [388]. For this study, we selected three redox probes — their most relevant properties are listed in Tab. 5.1.

First, we verified the potential window of a bare ITO electrode, which is a range of potentials where the electrode is stable and does not influence or even hamper the measurements. It is usually limited by chemical redox transformations of the electrode material itself or by decomposition of the solvent (water oxidation or hydrogen evolution). Our measurements showed, that ITO is stable between -0.5 and $+0.8$ V vs. Ag/AgCl reference electrode, in agreement with literature [389]. We can thus use the three redox probes with the equilibrium potentials E_{eq} within this range to perform cyclic voltammetry (CV) on our electrodes (see Fig. 51). The recorded voltammograms then provide information about charge transfer kinetics on the electrodes. The peak current i_p is proportional to the electroactive surface area and, in the case of reactions controlled by mass transport, it should be also proportional to the square root of the scan rate (see Randles-Ševčík equation [322]). From the

Tab. 5.1: Selected properties of the redox complexes used in this study. $E_{\text{eq,lit}}$ and $E_{\text{eq,exp}}$ are the equilibrium redox potentials obtained from the literature and from our experimental data, respectively.

	$\text{Fe}(\text{CN})_6^{3-}$	$\text{Ru}(\text{NH}_3)_6^{3+}$	FcMeOH
Name:	Ferricyanide	Hexaammine-ruthenium(III)	Ferrocene-methanol
Structure:			
Abbreviation:	Fe	Ru	Fc
Concentration:	0.5 mM	0.5 mM	0.1 mM
Charge:	Negative	Positive	Neutral
Surface sensitivity:	Inner-sphere	Outer-sphere	Outer sphere
$E_{\text{eq,lit}}$ (vs. Ag/AgCl)	180 mV	−150 mV	230 mV
$E_{\text{eq,exp}}$ (vs. Ag/AgCl)	180 mV	−170 mV	190 mV

peak separation ΔE_p we can infer the reversibility of the redox processes and thus the kinetics of the redox reaction. In the limit of fully reversible process with fast single electron transfer, $\Delta E_p \approx 57$ mV. An increase in peak separation beyond this value cannot be energetic in nature and must either correspond to slower electron transfer kinetics or increased uncompensated resistance [328].

We used these two characteristics to assess the ITO electrodes modified by AuNP@WS₂ NTs and we compare them with the reference measurements on (i) a bare ITO electrode, (ii) an ITO electrode covered by two densities of as-received WS₂ NTs without Au NPs, and (iii) an ITO electrode covered by colloidal gold NPs using a simple drop casting method (see Fig. 52). From the experimental results, several important details about our system can be deduced. First, it seems like the kinetics of the Ru complex is almost insensitive to the differences between our test electrodes. Both the peak current and separation are characteristic of the system with very good reversibility. This is most probably a consequence of Ru complex being considered as a prototypical outer-sphere system, mostly insensitive to the surface properties of our electrodes. The same should apply also for the Fc system, but its outer-sphere character has been recently questioned [390, 391]. This would lead to possible reversible adsorption, which can be one of the reasons for larger

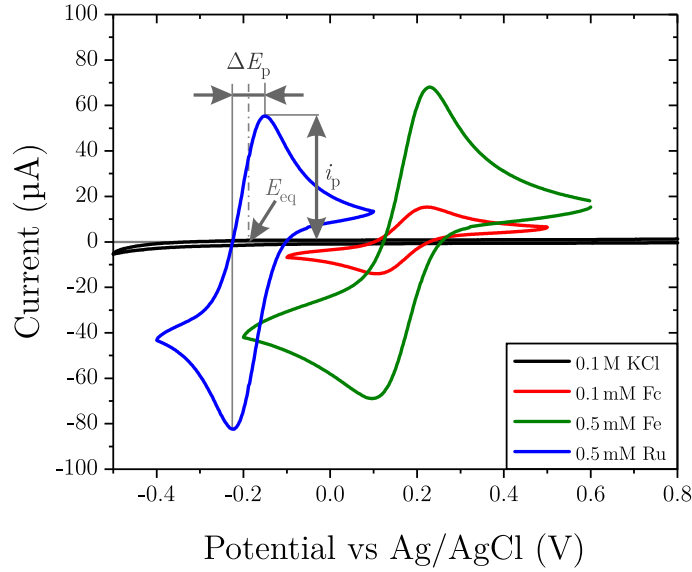


Fig. 51: Cyclic voltammetry on bare ITO electrodes. The potential window was verified in the electrolyte without redox probes (0.1 M solution of KCl). Then the three separate measurements were carried out with the three redox probes added to the base electrolyte (see details in Tab. 5.1). From such measurements we can extract not only the equilibrium potential E_{eq} of the redox system, but also the peak separation ΔE_p and peak current i_p , which characterize the electrode kinetics.

variability observed in experiments with the Fc and Fe redox systems. There, the main observation is that the presence of WS₂ NTs enhances the electron transfer and also seems to increase the electroactive surface area. Higher surface density of the NTs then only strengthens these two effects. When we modify the ITO substrate by commercially available colloidal gold NPs (BBI Solutions, diameter 20 nm, stabilized by citrate), we observe a similar behaviour. In some cases, the peak currents were even higher than in the case of the electrodes with WS₂ NTs, and the reversibility approached the aforementioned limit of 57 mV. Note, that the use of Au NPs, however, leads to a smaller available potential window because gold tends to oxidize at potentials beyond approx. 0.6 V vs. Ag/AgCl [392]. Surprisingly, the use of the ultimate electrode composed of the WS₂ NTs decorated by Au NPs caused in almost all cases a significant decrease of the peak currents and a very sluggish electron transfer. We ascribe this fact to a lower number of reactive sites on the surface of the decorated NTs, as the Au NPs are formed preferentially on the sulfide-terminated surface defects and thus block those very favourable reaction sites [386].

Having established the basic electrochemical properties of our hybrid electrodes and their individual constituents, we carried out also the photo-electrochemical experiments to further investigate the hot-electron effects. Cyclic voltammetry is not

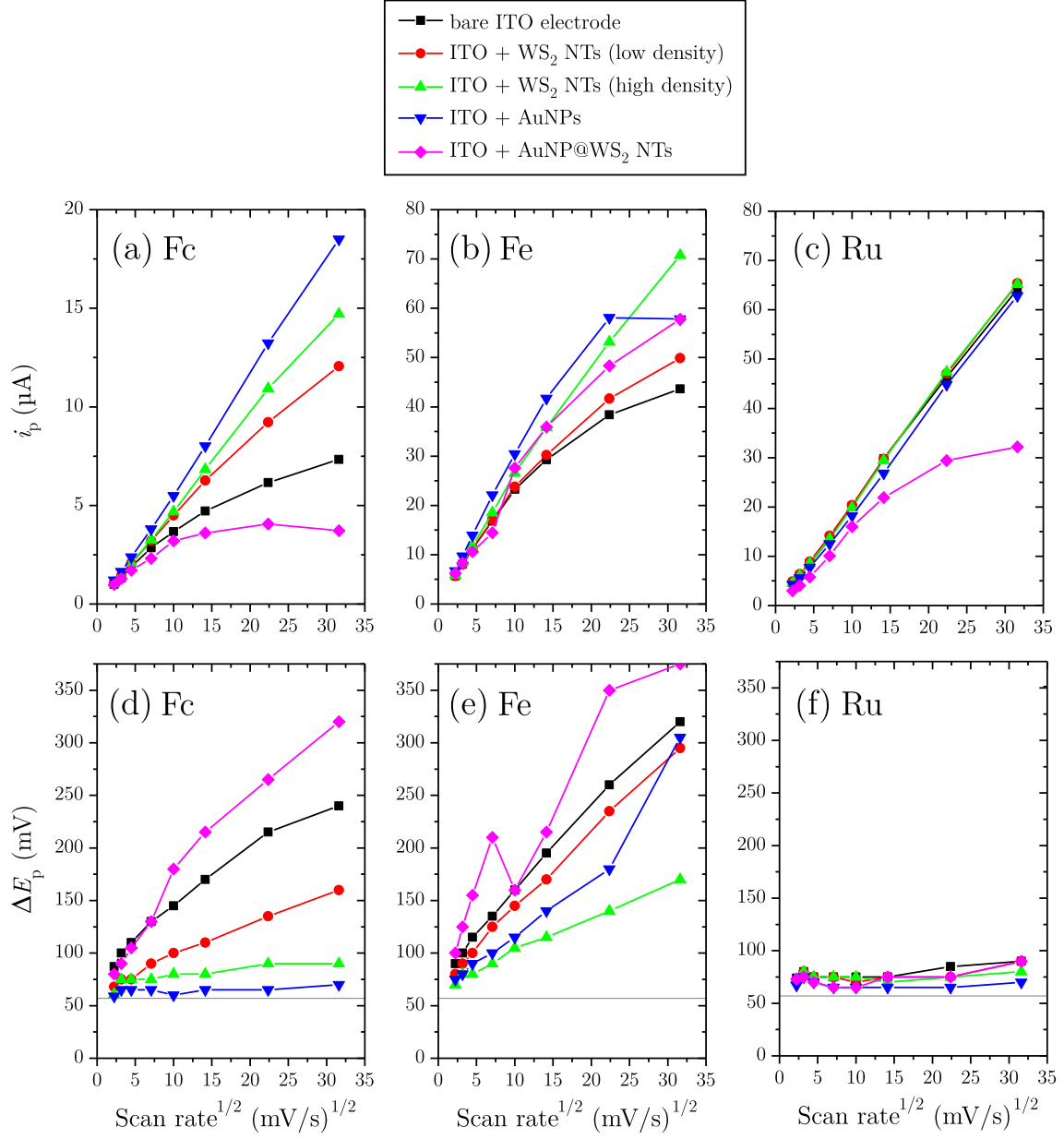


Fig. 52: (a,b,c) Peak currents i_p and (d,e,f) peak separations ΔE_p as functions of the square root of voltage scan rate. The data were extracted from CVs on several types of electrodes (see the legend) with the same three redox systems (labelled in the corners) as those in Fig. 51.

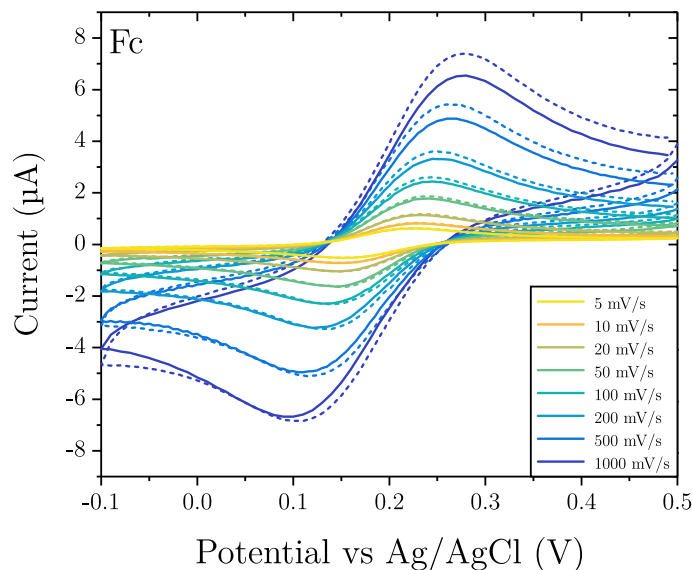


Fig. 53: Cyclic voltammetry on an ITO electrode covered by AuNP@WS₂ NTs. Solution of 0.1 mM Fc in 0.1 M KCl was used as the electrolyte. The voltammograms measured under illumination by 20 mW 532 nm green laser (dashed lines) exhibit slightly higher peak currents and negligibly smaller peak separation compared to the voltammograms without any illumination (solid lines).

an optimal method for this purpose because it is a dynamic technique, and as such it is influenced by both faradaic (i.e., connected with chemical conversion) and non-faradaic processes [393]. Indeed, the results of CV experiments with and without illumination (shown in Fig. 53) did not provide much information about intricacies of the photoexcitation process. The general trends in all samples at all scan rates were slightly increased peak currents and negligibly smaller peak separations. More details were obtained using static electrochemical methods, represented by chronoamperometry (CA) and open circuit potential (OCP) measurements. CA involves stepping the potential of the working electrode while monitoring the resulting current–time dependence (see Fig. 54a). This leads to changes in the concentration gradient in the vicinity of the surface and in particular, the gradual expansion of the diffusion layer associated with the depletion of the reactant (Fig. 54b). As a result, the current decays with time (Fig. 54c), following the Cottrell dependency $i \propto t^{-1/2}$ [322]. Here, we are not focused on this type of signal, however. We let the system to establish a quasi-equilibrium corresponding to a given electrode potential ($i \rightarrow 0$) and then we perturb it by a series of light pulses. The illumination leads to an instantaneous alteration of the electrochemical system as the photoelectrons are generated. Analysis of the evolution of the system after such perturbation permits deductions about electrode reactions and their rates to be made [394]. OCP measurements are complementary to the CA measurements like the voltage is com-

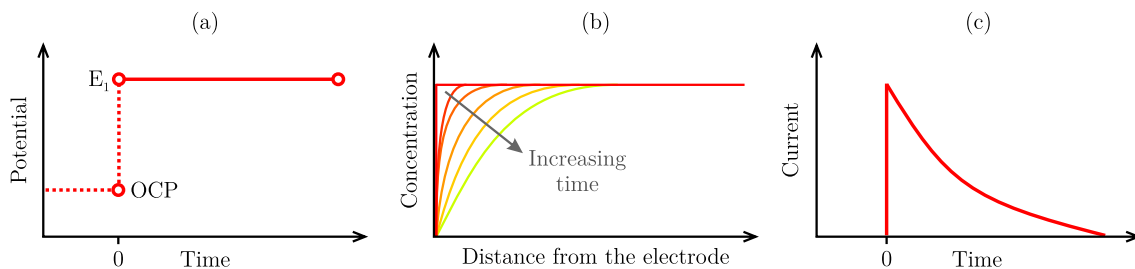


Fig. 54: Fundamentals of chronoamperometric experiments. (a) Potential–time waveform imposed on the system. Open circuit potential (OCP) is the value of potential before the circuit is closed at the measurement start. (b) Change in the spatial concentration profile of the reactant as the time progresses during the experiment. (c) The resulting current–time response.

plementary to the current. The difference lies in the fact that CA photocurrents can be measured on a system pushed out of its natural equilibrium by a voltage bias, whereas the open-circuit photovoltage is, by definition, measured in the open-circuit conditions — when the system is at its inherent value of electrochemical potential (given basically by the equilibrium potential of the solution).

The OCP measurements exhibited strong dependence on the illumination intensity, wavelength, and the electrode composition. To accentuate the observed photovoltage steps and to enable their rapid comparison, the dark background was subtracted from all measured OCP curves to get the ΔOCP which is plotted in Fig. 55. We also performed several control experiments on the individual electrode components — (i) bare ITO electrode, (ii) ITO covered by colloidal Au NPs, and (iii) ITO covered by WS₂ NTs with no Au NPs on top:

(i) Photovoltage steps on bare ITO electrodes were negative in all four solutions (KCl + three redox probes) and the ITO substrate thus behaved like an n-type semiconductor with a small Schottky barrier (Fig. 55a–b). These measured steps will constitute the background charge-separating capacity of our electrodes without any NTs or NPs. In blank KCl, the step magnitude was proportional to the photon energy (red 650 nm = 1.91 eV, green 532 nm = 2.33 eV, blue 450 nm = 2.75 eV). With the redox probes in the electrolyte, the magnitude of the steps generally decreased. The mechanism we put forward is a photo-excitation from mid-gap surface states of the ITO towards its conduction band. In that case, the holes left behind would participate in some sort of oxidation reaction (most probably the oxygen evolution reaction) and the photovoltage would gradually build up on the electrode. When the redox probes are present in the solution, they constitute a “sink” for the electrons because their equilibrium redox potentials are approximately on the same level or more negative than the Fermi level of ITO (Fig. 55c). This would naturally

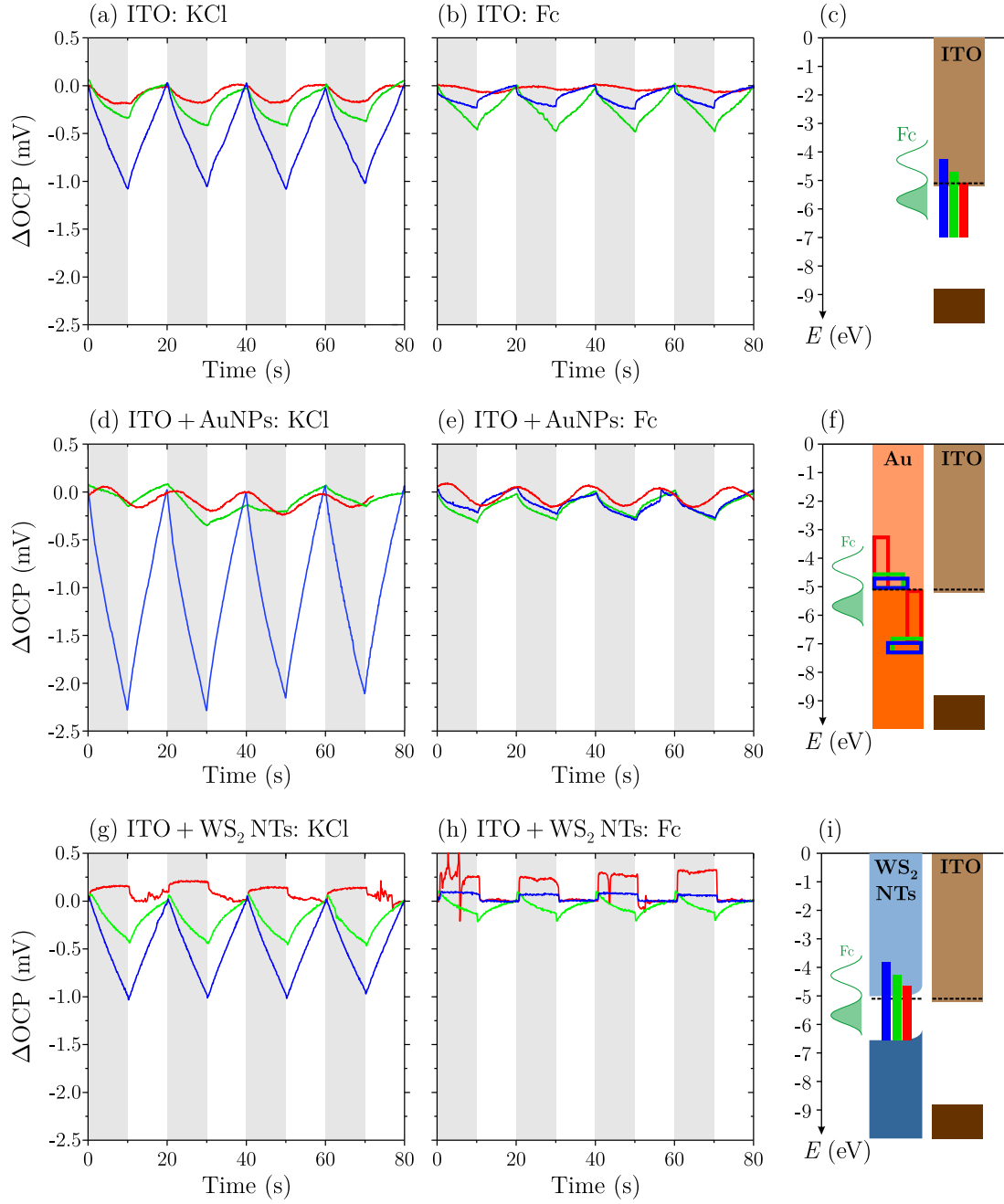


Fig. 55: Photovoltage steps measured on the three control samples in 0.1 M KCl (a,d,g) and in 0.1 mM Fc in 0.1 M KCl (b,e,h). The samples consisted of a bare ITO substrate (a–c), ITO covered by colloidal Au NPs (d–f), and ITO covered by WS₂ NTs with no Au NPs on top (g–i). Each colour line corresponds to a separate experiment, where the electrode was illuminated by a 60 mW laser of the respective wavelength, as described in the main text (10 s pulses are denoted by the grey shading). Note that the scales of all figures are the same. (c,f,i) Schematic band structures of the control samples with approximate Fermi levels (dashed lines), band gaps and work functions — all drawn in scale according to the literature data [395–397]. The laser photon energies (solid rectangles) or corresponding hot-electron distributions in gold (hollow rectangles) are also shown with appropriate colours and sizes.

lower the amount of separated charge carriers and thus also the photovoltage, as observed in the experiment.

(ii) On the control samples covered by colloidal Au NPs, we again observed exclusively negative photovoltages (Fig. 55d–e). The results for the green and red laser illumination were very similar to the bare ITO electrodes. This can be reasonably explained by the presence of ohmic contact between the gold and ITO. Without the Schottky barrier, nothing prevents the fast recombination of electrons and holes, and the photovoltage naturally cannot be established. An interesting situation appeared, however, with the blue laser illumination, where we observed almost twice as high ΔOCP compared to the bare ITO. We ascribe this effect to plasmon-mediated photo-oxidation of the citrate surfactant on the surface of NPs [188, 398]. It can be interpreted as follows. The illumination by blue light leads to the inter-band excitation of electrons in gold and to the rich population of hot holes (see Fig. 22 and related discussion on p. 43). The hot holes would then be consumed during the citrate oxidation, the recombination process would be hampered, and the large number of electrons left behind would contribute to the more negative photovoltage. If any of the three redox probes were present in the electrolyte, however, they would get quickly reduced by the hot electrons. This would counteract the voltage build-up and naturally cause the ΔOCP magnitude to fall down. The opposite process (oxidation of the redox complex by the hot holes) seems to be less likely, probably due to lower overlap between their distribution and distribution of the oxidized redox states. Also note that the influence of the citrate oxidation should not be permanent as it is an irreversible reaction with a limited number of reactants.

(iii) On the control samples covered only by WS_2 NTs, i.e. without any plasmonic elements, the results for the green and blue laser closely follow the aforementioned background contribution of the ITO substrate itself (Fig. 55g–i). This is understandable because the energy levels from which we assume the electrons get excited are approximately similar for both ITO and WS_2 . The situation is different, however, for the red laser illumination, which leads to clearly positive photovoltage steps. This can be explained, again, by taking a closer look at the band structure of the whole system. Because the work function of WS_2 NTs is slightly lower [395] than the work function of ITO [396, 397], a Schottky barrier of approximately 0.5 eV will arise between them. Photons of blue or green light have enough energy so the electrons excited by them from the conduction band of WS_2 can overcome the Schottky barrier, but the 1.9 eV of red laser photons is barely enough. This means that photoelectrons arising from red illumination must reside on the NTs and it will be the holes which will be drawn through the space-charge layer of the Schottky barrier into the ITO substrate. From the same reasons as in the previous cases, the presence of redox probes pushes the photovoltages to the positive direction. Note also the

transient photovoltages that appeared with the green illumination (Fig. 55h). As they become even more pronounced in the next experiments, they will be discussed later below.

After we have identified the effects corresponding to the individual components of our electrodes, we can proceed to study the outcomes of coupling them together within the system of AuNP@WS₂ NTs on the ITO substrate. For these hybrid samples, we observed exclusively positive photovoltages in all four electrolytes (see Fig. 56a–d). This fact can be explained by the presence of two Schottky barriers: one between gold and WS₂, and another between WS₂ and ITO (Fig. 56e). The appearance of positive photovoltage and related behaviour of photoelectrons in the NTs have been discussed above. Here, this effect is significantly enhanced by the hot electrons of Au NPs. The interband excitation (green and blue lasers) leads to “lukewarm” electrons close to the Fermi level and to hot holes well below it [180]. The former cannot cross the Schottky barrier (≈ 0.9 eV) and most probably reside on the NPs, while the latter can be efficiently captured by the NTs and transported to the ITO. This synergy then leads to the observed positive photovoltage, as opposed to the control samples. Illumination by the red laser, on the other hand, should lead to the intraband excitation of hot electrons in gold. These should have enough energy to pass over the Schottky barriers and thus neutralize the positive photovoltage. Surprisingly, we have observed not only the opposite effect, but even an enhanced one, compared to the other two laser colours. We put forward an explanation based on the finite life-time of the hottest charge carriers and the resulting limited transport distance, which have been already predicted by some theoretical works [205, 399]. If that scenario took place, the initial wide step-like distribution of hot electrons would quickly decay into the narrow one located close to the Fermi energy earlier than they could be harvested. No matter whether this would happen before or after they cross the first Schottky barrier to the WS₂, the large number of hot electrons would reside on the AuNP@WS₂ NTs and, therefore, could result in the enhanced photovoltages that were observed in the experiments.

Interesting results were also acquired in the experiments involving redox probes. The presence of Fc and Fe redox systems does not result in the shift of photovoltages towards more positive values, like it was the case with the control samples, but it has an opposite effect instead. Moreover, the Δ OCP steps tend to exhibit a strong transient behaviour with a sharp raise and a slow exponential decrease towards a steady-state value. Similar behaviour has been linked with the presence of recombination centres, mainly in the form of surface states [400, 401]. As was mentioned above, the Au NPs grow on the NTs preferentially on the sites with defects. It is thus more than probable that these defects play a role in the charge carrier recombination on the interface between gold and WS₂. Yet another intriguing situation

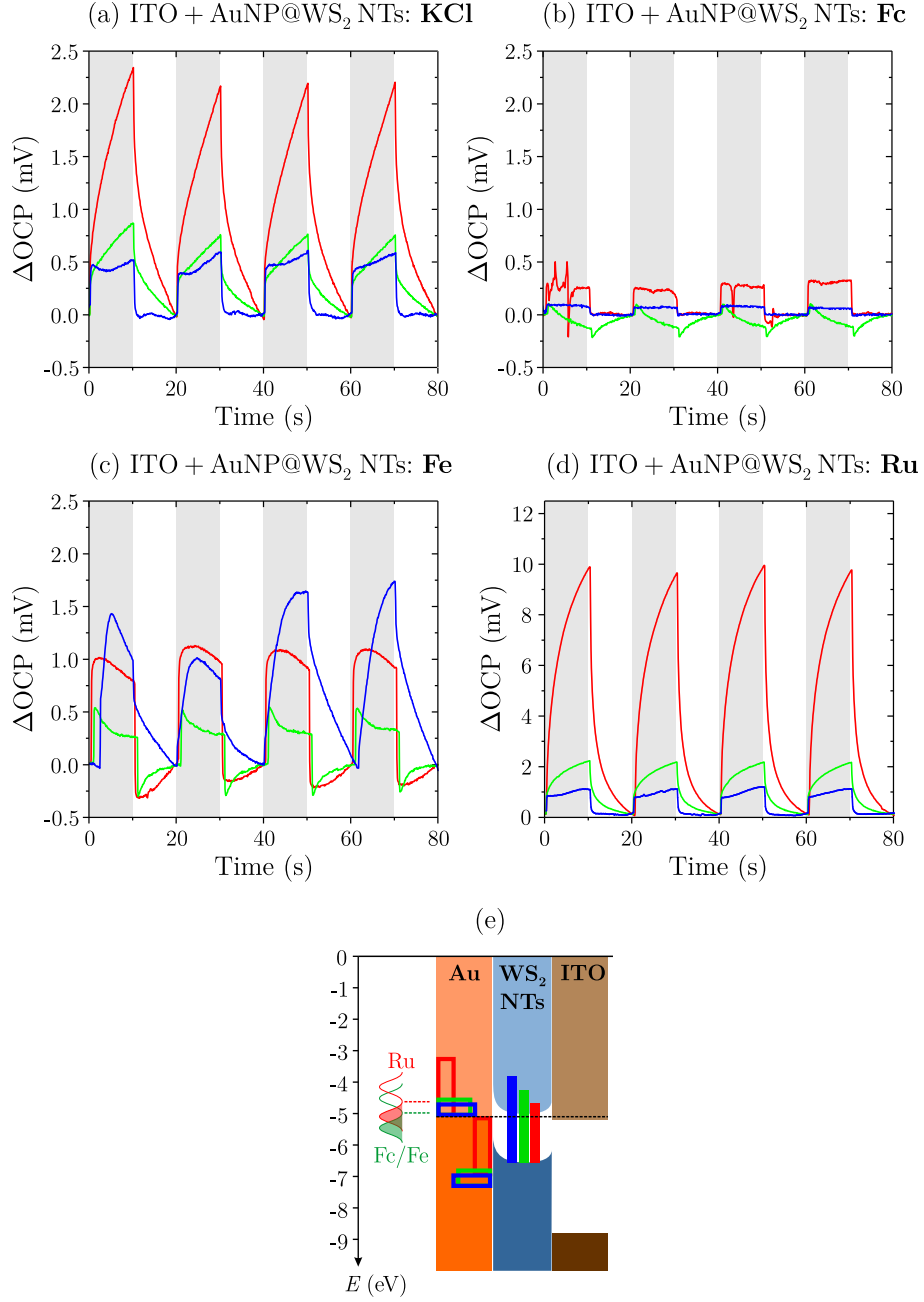


Fig. 56: Photovoltage steps measured on the hybrid samples with AuNP@WS₂ NTs on the ITO in (a) 0.1 M KCl, and (b,c,d) with the three redox probes added into the base electrolyte (see details in Tab. 5.1). Each colour line corresponds to a separate experiment, where the electrode was illuminated by a 60 mW laser of the respective wavelength, as described in the main text (10 s pulses are denoted by the grey shading). Note that the photovoltage scale of (d) is significantly larger than the rest of the plots. (e) Schematic band structure of the hybrid sample with equilibrated Fermi levels (dashed line). The Schottky barriers, band gaps, and work functions are all drawn in scale according to the literature data [395–397]. The laser photon energies exciting the WS₂ NTs (solid rectangles) and corresponding hot-electron distributions in gold (hollow rectangles) are also shown with appropriate colours and sizes.

arises when the Ru redox couple is used in the photovoltage experiments on these electrodes. The ΔOCP steps are then substantially higher when compared to the other three electrolytes, especially under the red illumination. Why these effects manifest themselves only for the certain combinations of sample, electrolyte, and laser colour, remains enigmatic at this stage. The most probable explanation is related to the parameters beyond our control, that is, to the interplay between amount of surface defects and exact values of Fermi levels on one side, and varying surface sensitivities and redox potentials of the redox probes on the other. Moreover, the detailed analysis of the photovoltage steps revealed that the aforementioned transients can go even below the value of dark OCP in some cases (see Fig. 56b). This suggests there are two competing processes at play, which are initiated by the light pulses — one prevailing at shorter time scales, the other one dominating after a couple of seconds.

In order to further investigate the underlying mechanisms, we also performed a set of chronoamperometric experiments, where the photocurrent steps are measured under intermittent illumination after the background “Cottrell” current decreased down to a negligible value (cf. Fig. 54). This technique gives complementary information to the OCP measurements, with an extra degree of freedom in the form of the possible voltage bias applied to the working electrode. The large amount of data acquired for both the control samples and the hybrid samples (Fig. 57), unfortunately did not provide any conclusive evidence for the mechanism behind the aforementioned anomalous effects. In particular, there were several abnormal peaks which could not be assigned to any distinctive property of the electrolyte or the sample. Together with the irregularities in the OCP measurements, these results lead to several concluding remarks about the hybrid electrode system studied here.

The nanostructured electrodes, represented here by the transparent conductive substrate covered by metal–semiconductor nanostructures, proved to be beneficial for both signal enhancement and improved reversibility. Via photocurrent and photovoltage measurements, we were able to identify several aspects of charge carrier transport across the Schottky barriers of such structures. Moreover, we showed that with the appropriate wavelength control, different behaviour of interband and intraband hot electrons can be investigated. Unfortunately, the limiting factor of our study is the insufficient reproducibility of the electrode morphology, as even with the highest care the drop-casting method inevitably leads to a certain degree of inhomogeneity in surface coverage. Moreover, the size and shape of the Au NPs on the surface of the NTs has also a non-zero distribution. With electrodes of better quality and/or reproducibility, the studies of this type may provide valuable information about the nature of photochemical processes facilitated by the hot electrons or about details of hot-electron photosensitization in energy-harvesting schemes.

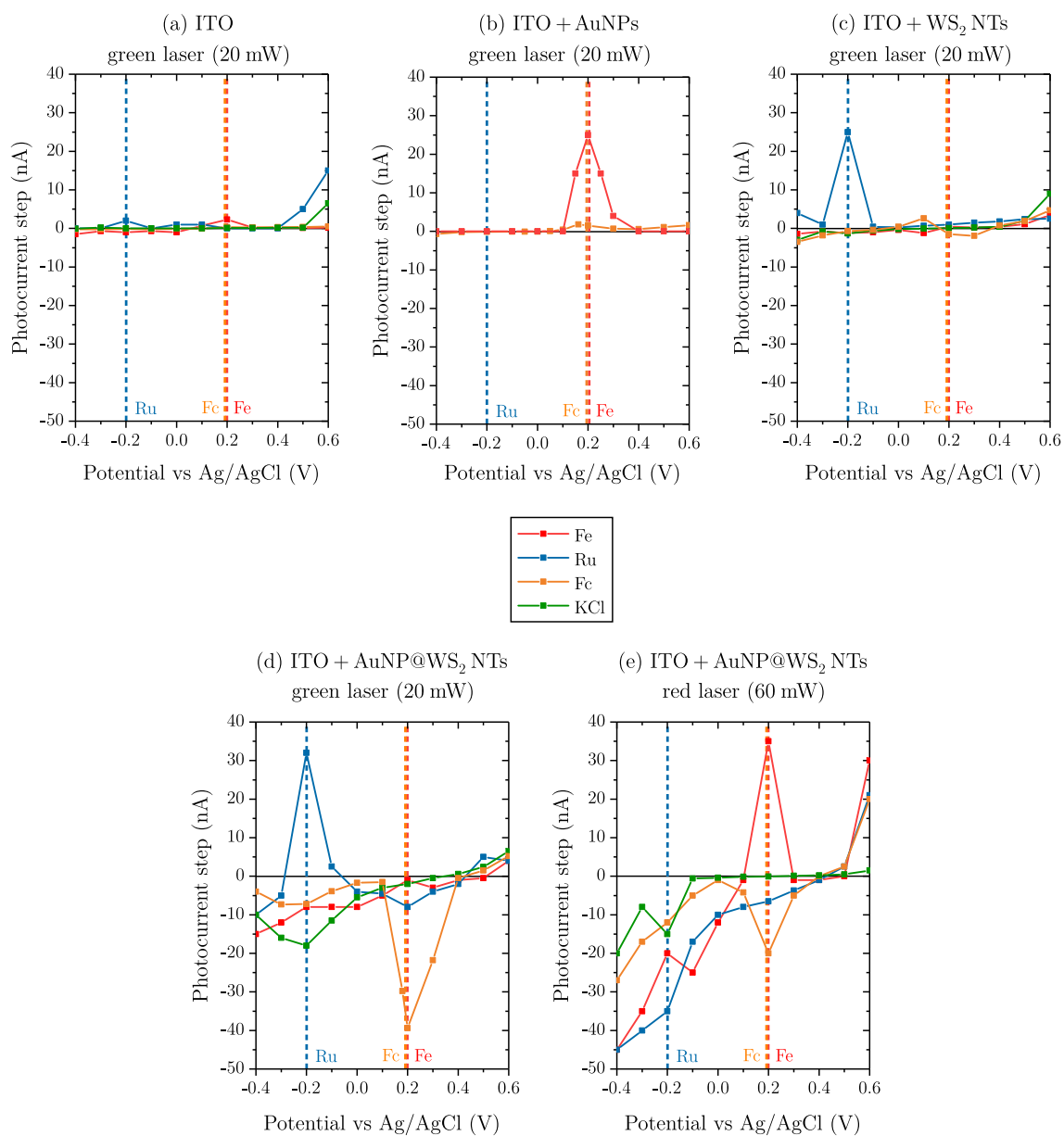


Fig. 57: Magnitude of photocurrent steps in all four electrolytes as a function of potential of the working electrode. The chopped illumination by green laser (a–d) or red laser (e) started after the background current significantly decreased. (a) Bare ITO electrode. (b) ITO covered by Au NPs. (c) ITO covered by bare WS₂ NTs. (d,e) Hybrid samples with AuNP@WS₂ NTs on the ITO. Approximate values of redox potentials of the redox probes are labelled by the vertical dashed lines.

5.4 Conclusions

This chapter started with an introduction to the common aspects and relationships amongst plasmonics, photochemistry, and electrochemistry. The fundamental principles of electrochemical processes were explained, with a special focus on charge-transfer processes between solid-state electrodes and chemical compounds in their vicinity. Although great variety of experimental techniques stems from these basic principles, here we described only the directly relevant ones. That is, the voltammetric and chronoamperometric techniques, together with the necessary experimental setup. A brief survey of the studies which brought together plasmonics and electrochemistry was then presented. Based on the nature of the external (probing) impulse and on the nature of the associated (detected) response, we divided them into two types: spectro-electrochemical ones, studying optical responses to chemical perturbations, and photo-electrochemical ones, proceeding the other way around. The rest of the chapter was devoted to a detailed report on the photo-electrochemical investigation of nanostructured plasmonically active electrodes made of WS₂ NTs decorated with Au NPs.

We introduced the individual building blocks of the electrodes step by step, and also elaborated on the experimental techniques and chemical redox probes used in this study. Based on our CV measurements we came to a conclusion that the modification of ITO electrodes by the WS₂ NTs translates into greater electroactive surface area and improved reversibility of the redox reactions on such electrodes. Using photovoltage and photocurrent experiments combining several sets of redox probes, three illumination wavelengths, and the necessary control samples, we aimed to elucidate the nature of hot-electron transport and photochemistry in the hybrid system of AuNP@WS₂ NTs. Although many clear signs of hot charge carriers manifested themselves in the measured data, the combination of a complicated electrode system with presumably inadequate level of control over its morphology lead to some anomalous or enigmatic results. We were thus unable to pinpoint the anticipated behaviour of the photoexcited hot electrons and holes. Nevertheless, such experimental techniques seem very promising for a similar type of studies, provided one has a better control over the surface chemistry, morphology, and inner structure of the electrodes. Better knowledge of the electronic environment of the whole system, backed by a solid experimental evidence, would also be beneficial. In this respect, Kelvin probe force microscopy, ultraviolet photoemission spectroscopy, or electrochemical impedance spectroscopy can all provide the necessary information about Fermi energies, work functions, and Schottky barriers. It would be also useful to aim for better integration with the inherently complementary class of spectroscopic methods. That way, the partnership between plasmonics and electrochemistry could

clarify some puzzling effects in the field of photochemistry, especially with respect to the surface sensitivity of photochemical reaction, Fermi level pinning at interfaces etc.

6 CONCLUSIONS AND FUTURE DIRECTIONS

“The outcome of any serious research can only be to make two questions grow where only one grew before.”

Evolution of the Scientific Point of View, 1919

THORSTEIN VEBLEN

This dissertation began with an introduction into the theory of surface plasmon polaritons. We described all their extraordinary properties like field confinement and enhancement, strong scattering and absorption, and the strong dependence of plasmonic resonances on the material properties and system geometry. These features are the cornerstones of many practical applications of plasmonics, which were reviewed in the second chapter. We also introduced the concept of metal nanostructures acting as optical nanoantennas and the main nanofabrication techniques which are used for their production. Then, three particular topics where plasmonic nanostructures are indispensable were discussed in more detail: plasmonic sensing, metamaterials and metasurfaces, and production of hot electrons.

Several potential research avenues emerged from the detailed description of these fields. First, it is the fact that plasmonic nanostructures can influence the polarization of light from a nearby nanoscale emitter. In the combined experimental and theoretical study, we showed at the single-particle level that plasmon-modulated up-conversion emission gets polarized according to the mutual relationship between the plasmonic modes of the nanostructure and the emission bands of the upconverting nanocrystals. Because our hybrid nanostructures were able to permeate through a cell membrane, they turn out to be a promising candidate for nonlinear fluorescent probes in high-contrast bioimaging applications. In even broader sense, the presented results raise a question whether this principle can be applied also to other combinations of quantum emitters and plasmonic nanostructures. Single-photon emitters like vacancy centres in diamond or hexagonal boron nitride are the principal component of quantum photonic computation technology. If the similar effects like those described here hold for them as well, plasmonic nanostructures could become a tool for manipulating the polarization — and therefore also spins — of the individual photons.

The second type of impact plasmonic nanostructures have on scattered light waves is the phase profile it imprints on them. This is the fundamental working

principle of all plasmonic metasurfaces. In our work, we showed that digital holographic microscopy is an excellent method suitable for quantitative visualization of this effect. It enables evaluation of the scattered phase in the whole field of view of an optical microscope at rates limited only by the camera specifications. When coupled with a spectrally tunable light source and a computer-driven stage, it also makes possible to create spectrally resolved 3D phase maps. In the future, it would be more than desirable to upgrade the measurement setup by a set of polarizing elements like polarizers, half-wave plates or quarter-wave plates. This would allow also for analysis of an increasingly popular class of metasurfaces based on the principle of geometric (Pancharatnam-Berry) phase. The extension out of the visible spectral range is also feasible, provided that the suitable optical components are used. Overall, the reported qualities of the digital off-axis holography establish it as a powerful imaging technique with a potential to become a versatile tool in the metamaterial research.

The next subject of discussion was the issue of active tunability of the metasurfaces. First, we listed several methods how tunability and switching can be incorporated into metasurfaces. One of these methods is utilization of phase-change materials than can undergo metal-insulator transition. We therefore elaborated on the archetypal phase-change material, vanadium dioxide. The mechanism of its phase-transition was explained together with possible switching strategies and also more details regarding its optical and electrical properties. Two studies involving this material were then presented. In the first one, the VO_2 served as an active substrate for plasmonic nanodiscs and the whole system acted like an optical-frequency analogue of memristive memory devices. In the second study, the VO_2 in the form of epitaxially grown nanobeams was itself the plasmonic building block of the metasurface. The demonstrated large modulation depth as well as the quarter-wave plate functionality render this self-assembled metasurface very interesting for practical applications in the near-infrared wavelength range. The natural extension of this work would be preparation of other types of VO_2 nanostructures without the time-intensive nanofabrication processes. Isolated hemispherical nanoparticles, which can act as nanoantennas, can be created by annealing of a continuous VO_2 film. A more sophisticated approach resides in utilization of epitaxial growth on a 3-fold symmetric surface of c-cut sapphire, which could lead to emergence of 3-fold symmetric nanostructures. These would then closely resemble the V-shaped nanoantennas, a classical metasurface building block. Another research project that can be envisioned based on the presented results is utilization of VO_2 for integrated plasmonic-dielectric metasurfaces. At temperatures below phase transition, the nanostructures would act as a dielectric resonators supporting the Mie resonances, while above the phase-transition temperature their resonances would be plasmonic.

By careful selection of dimensions and shape of the nanostructures, both these functionalities could be activated at the same frequency and easily switched from one to the other.

The last part of this thesis was devoted to the relationship between plasmonics and electrochemistry. The common ground of these two fields has been established and fundamentals of electrochemistry were introduced. This involved the solid-state-physics picture of electrochemical processes, description of driving forces in the electrochemical experiments, and a brief review of the studies uniting plasmonics and electrochemistry. The point was to provide the necessary foundation for a study devoted to hot-electron photochemistry on a plasmonically active metal–semiconductor electrodes. We showed that the presence of semiconducting transition-metal nanotubes can increase the electroactive surface area and improve the electron transfer rates. The presented results also establish electrochemical methods as a useful tool for analysis of hot-electron effects. Chronoamperometry and open circuit potential measurements, in particular, both provide information about the electronic structure of the hybrid electrodes and are sensitive to the photochemical and plasmonic effects too. Although the mechanism of hot-electron transfer in the system studied here was not fully clarified, the experiments helped to identify the possibilities that remain to be investigated: (i) One avenue for future investigation is use of larger variety of redox probes that would exhibit a larger range of redox potentials. This would enable broader tuning of the system’s Fermi energies and it could also clarify the sensitivity of the redox probes towards surface chemistry. Wider range of laser wavelengths would also improve our understanding of the system, especially in the case of sub-band-gap excitation. (ii) Second topic of future investigation is represented by temperature effects. Although the low laser powers used here were shown to raise the overall temperature of the system only insignificantly and despite the presence of media with large thermal conductivity, the possibility of creation of temperature hot spots have not been disproved in this work. The presence of nanoscale temperature hot spots could lead to increase reaction rates, faster diffusion and thus contribute to the photochemical effects. (iii) Third open question is related to the presence of citrate surfactant on the surface of gold nanoparticles in the case of control samples. The absolute energy levels of this molecule are not very well known and thus demand further verification. The preparation of control samples without surfactant on the surface of nanoparticles is challenging as one must abstain from using colloidal solution yet the conventional thin film deposition and temperature-assisted dewetting cannot be performed for the reasons of substrate stability. The control of size distribution in that case is also very limited. (iv) The last vital piece of information are the work functions of the individual components of our hybrid electrodes. The absolute positions of the Fermi levels of WS₂, gold,

or indium tin oxide are crucial for the Schottky barrier formation and thus also strongly influence the energetic landscape for the hot electrons generated by surface plasmon decay. Therefore, ultraviolet photoelectron spectroscopy or Kelvin probe force microscopy are highly desirable complementary techniques for analyses like this. Together with the issue of fabrication reproducibility, these aspects are often neglected in the contemporary studies regarding hot electron effects. To meet these challenging requirements is not an easy task. Hopefully, the results presented in this dissertation made it easier for those who will try to tackle them.

LIST OF ABBREVIATIONS

AFM	Atomic Force Microscopy
CA	Chronoamperometry
CCHM	Coherence-controlled Holographic Microscope
CL	Cathodoluminescence
CV	Cyclic Voltammetry
DDA	Discrete Dipole Approximation
DNA	Deoxyribonucleic Acid
DOP	Degree of Polarization
EBL	Electron Beam Lithography
EELS	Electron Energy Loss Spectroscopy
FDTD	Finite-difference Time-domain
FEM	Finite Element Method
FIB	Focused Ion Beam
FWHM	Full Width at Half Maximum
FT	Fourier-transform
FTIR	Fourier-transform infrared
GNR	Gold Nanorod
IR	Infrared
ITO	Indium Tin Oxide
LSP	Localized Surface Plasmon
LSPR	Localized Surface Plasmon Resonance
MEMS	Micro-electro-mechanical System
MIR	Mid-infrared
MIT	Metal-insulator Transition
NIR	Near-infrared
NP	Nanoparticle
NT	Nanotube
OCP	Open Circuit Potential

OPD	Optical Path Difference
PEEM	Photoelectron Emission Microscopy
PIRET	Plasmon-induced Resonance Energy Transfer
PLD	Pulsed Laser Deposition
RF	Radio-frequency
RT	Room Temperature
SEM	Scanning Electron Microscope
SERS	Surface-enhanced Raman Scattering
SEIRA	Surface-enhanced Infrared Absorption
SNOM	Scanning Near-field Optical Microscopy
SPP	Surface Plasmon Polariton
SPR	Surface Plasmon Resonance
TMD	Transition Metal Dichalcogenide
UC	Upconversion
UCNC	Upconversion Nanocrystals
UV	Ultraviolet
VIS	Visible
XRD	X-ray Diffraction

BIBLIOGRAPHY

- [1] Griffiths, D. J. *Introduction to Electrodynamics*. Cambridge University Press, 4th edn., 2013. ISBN 978-1108420419.
- [2] Maier, S. A. *Plasmonics: Fundamentals and Applications*. Springer, 2007. ISBN 978-0-387-33150-8. doi:[10.1007/0-387-37825-1](https://doi.org/10.1007/0-387-37825-1).
- [3] Fujiwara, H. *Spectroscopic Ellipsometry*. John Wiley & Sons, 2007. ISBN 978-0-470060193. doi:[10.1002/9780470060193](https://doi.org/10.1002/9780470060193).
- [4] Dressel, M. and Grüner, G. *Electrodynamics of Solids: Optical Properties of Electrons in Matter*. Cambridge University Press, 2002. ISBN 0-521-59253-4.
- [5] Zhang, S., Genov, D. A., Wang, Y., *et al.* Plasmon-Induced Transparency in Metamaterials. *Phys. Rev. Lett.*, 101 (4), **2008**, p. 047401. doi:[10.1103/PhysRevLett.101.047401](https://doi.org/10.1103/PhysRevLett.101.047401).
- [6] Liu, N., Langguth, L., Weiss, T., *et al.* Plasmonic analogue of electromagnetically induced transparency at the Drude damping limit. *Nat. Mater.*, 8 (9), **2009**, pp. 758–762. doi:[10.1038/nmat2495](https://doi.org/10.1038/nmat2495).
- [7] Zuloaga, J. and Nordlander, P. On the Energy Shift between Near-Field and Far-Field Peak Intensities in Localized Plasmon Systems. *Nano Lett.*, 11 (3), **2011**, pp. 1280–1283. doi:[10.1021/nl1043242](https://doi.org/10.1021/nl1043242).
- [8] Kats, M. a., Yu, N., Genevet, P., *et al.* Effect of radiation damping on the spectral response of plasmonic components. *Opt. Express*, 19 (22), **2011**, p. 21748. doi:[10.1364/OE.19.021748](https://doi.org/10.1364/OE.19.021748).
- [9] Yu, N. and Capasso, F. Flat optics: Controlling wavefronts with optical antenna metasurfaces. *IEEE J. Sel. Top. Quantum Electron.*, 19 (3), **2013**, pp. 2341–2342. doi:[10.1109/APS.2013.6711829](https://doi.org/10.1109/APS.2013.6711829).
- [10] Kittel, C. *Introduction to Solid State Physics*. John Wiley & Sons, 8th edn., 2005. ISBN 0-471-41526-X.
- [11] Palik, E. D. (ed.). *Hand book of Optical Constants of Solids*. Academic Press, 1985. ISBN 0-12-544420-6.
- [12] Scaffardi, L. B. and Tocho, J. O. Size dependence of refractive index of gold nanoparticles. *Nanotechnology*, 17 (5), **2006**, pp. 1309–1315. doi:[10.1088/0957-4484/17/5/024](https://doi.org/10.1088/0957-4484/17/5/024).
- [13] Ward, D. W. *Polaritonics: an intermediate regime between electronics and photonics*. Ph.D. thesis, MIT, 2005.
- [14] Low, T., Chaves, A., Caldwell, J. D., *et al.* Polaritons in layered two-dimensional materials. *Nat. Mater.*, 16 (2), **2017**, pp. 182–194. doi:[10.1038/nmat4792](https://doi.org/10.1038/nmat4792).
- [15] Basov, D. N., Fogler, M. M., and Garcia de Abajo, F. J. Polaritons in van der Waals materials. *Science*, 354 (6309), **2016**, pp. aag1992–aag1992. doi:[10.1126/science.aag1992](https://doi.org/10.1126/science.aag1992).
- [16] Cohen-Tannoudji, C., Diu, B., and Laloe, F. *Quantum Mechanics, Vol. 1*. Wiley, 1st edn., 1991, p. 409. ISBN 978-0471164333.
- [17] Novotny, L. Strong coupling, energy splitting, and level crossings: A classical perspective. *Am. J. Phys.*, 78 (11), **2010**, pp. 1199–1202. doi:[10.1119/1.3471177](https://doi.org/10.1119/1.3471177).

- [18] Chen, Y., Francescato, Y., Caldwell, J. D., *et al.* Spectral Tuning of Localized Surface Phonon Polariton Resonators for Low-Loss Mid-IR Applications. *ACS Photonics*, 1 (8), **2014**, pp. 718–724. doi:[10.1021/ph500143u](https://doi.org/10.1021/ph500143u).
- [19] Toudert, J. and Serna, R. Ultraviolet-visible interband plasmonics with p-block elements. *Opt. Mater. Express*, 6 (7), **2016**, p. 2434. doi:[10.1364/OME.6.002434](https://doi.org/10.1364/OME.6.002434).
- [20] Stephen Byrnes’s Personal Webpage. Available at <https://sjbyrnes.com/> (Accessed 2018-06-22).
- [21] Dastmalchi, B., Tassin, P., Koschny, T., and Soukoulis, C. M. A New Perspective on Plasmonics: Confinement and Propagation Length of Surface Plasmons for Different Materials and Geometries. *Adv. Opt. Mater.*, 4 (1), **2016**, pp. 177–184. doi:[10.1002/adom.201500446](https://doi.org/10.1002/adom.201500446).
- [22] Boltasseva, A. and Atwater, H. A. Low-Loss Plasmonic Metamaterials. *Science*, 331 (6015), **2011**, pp. 290–291. doi:[10.1126/science.1198258](https://doi.org/10.1126/science.1198258).
- [23] Zayats, A. V. and Smolyaninov, I. I. Near-field photonics: surface plasmon polaritons and localized surface plasmons. *J. Opt. A Pure Appl. Opt.*, 5 (4), **2003**, pp. S16–S50. doi:[10.1088/1464-4258/5/4/353](https://doi.org/10.1088/1464-4258/5/4/353).
- [24] Bohren, C. F. and Huffman, D. R. *Absorption and Scattering of Light by Small Particles*. Wiley, 2007, p. 530. ISBN 978-0-471293408. doi:[10.1002/9783527618156](https://doi.org/10.1002/9783527618156).
- [25] Johnson, P. B. and Christy, R. W. Optical constants of the noble metals. *Phys. Rev. B*, 6 (12), **1972**, pp. 4370–4379. doi:[10.1103/PhysRevB.6.4370](https://doi.org/10.1103/PhysRevB.6.4370).
- [26] Huang, X., Neretina, S., and El-Sayed, M. A. Gold Nanorods: From Synthesis and Properties to Biological and Biomedical Applications. *Adv. Mater.*, 21 (48), **2009**, pp. 4880–4910. doi:[10.1002/adma.200802789](https://doi.org/10.1002/adma.200802789).
- [27] Meier, M. and Wokaun, A. Enhanced fields on large metal particles: dynamic depolarization. *Opt. Lett.*, 8 (11), **1983**, p. 581. doi:[10.1364/OL.8.000581](https://doi.org/10.1364/OL.8.000581).
- [28] Losurdo, M., Giangregorio, M. M., Bianco, G. V., *et al.* Size dependence of the dielectric function of silicon-supported plasmonic gold nanoparticles. *Phys. Rev. B*, 82 (15), **2010**, p. 155451. doi:[10.1103/PhysRevB.82.155451](https://doi.org/10.1103/PhysRevB.82.155451).
- [29] Willets, K. A. and Van Duyne, R. P. Localized Surface Plasmon Resonance Spectroscopy and Sensing. *Annu. Rev. Phys. Chem.*, 58 (1), **2007**, pp. 267–297. doi:[10.1146/annurev.physchem.58.032806.104607](https://doi.org/10.1146/annurev.physchem.58.032806.104607).
- [30] Lee, K.-S. and El-Sayed, M. A. Dependence of the Enhanced Optical Scattering Efficiency Relative to That of Absorption for Gold Metal Nanorods on Aspect Ratio, Size, End-Cap Shape, and Medium Refractive Index. *J. Phys. Chem. B*, 109 (43), **2005**, pp. 20331–20338. doi:[10.1021/jp054385p](https://doi.org/10.1021/jp054385p).
- [31] Hao, F. and Nordlander, P. Efficient dielectric function for FDTD simulation of the optical properties of silver and gold nanoparticles. *Chem. Phys. Lett.*, 446 (1-3), **2007**, pp. 115–118. doi:[10.1016/j.cplett.2007.08.027](https://doi.org/10.1016/j.cplett.2007.08.027).
- [32] Adams, S. M., Campione, S., Capolino, F., and Ragan, R. Directing Cluster Formation of Au Nanoparticles from Colloidal Solution. *Langmuir*, 29 (13), **2013**, pp. 4242–4251. doi:[10.1021/la3051719](https://doi.org/10.1021/la3051719).

- [33] Eustis, S. and El-Sayed, M. A. Why gold nanoparticles are more precious than pretty gold: Noble metal surface plasmon resonance and its enhancement of the radiative and nonradiative properties of nanocrystals of different shapes. *Chem. Soc. Rev.*, 35 (3), **2006**, pp. 209–217. doi:[10.1039/B514191E](https://doi.org/10.1039/B514191E).
- [34] Biagioni, P., Huang, J.-S., and Hecht, B. Nanoantennas for visible and infrared radiation. *Reports Prog. Phys.*, 75 (2), **2012**, p. 024402. doi:[10.1088/0034-4885/75/2/024402](https://doi.org/10.1088/0034-4885/75/2/024402).
- [35] Yang, J. K. W., Cord, B., Duan, H., *et al.* Understanding of hydrogen silsesquioxane electron resist for sub-5-nm-half-pitch lithography. *J. Vac. Sci. Technol. B Microelectron. Nanom. Struct.*, 27 (6), **2009**, p. 2622. doi:[10.1116/1.3253652](https://doi.org/10.1116/1.3253652).
- [36] Wiley, B. J., Qin, D., and Xia, Y. Nanofabrication at High Throughput and Low Cost. *ACS Nano*, 4 (7), **2010**, pp. 3554–3559. doi:[10.1021/nm101472p](https://doi.org/10.1021/nm101472p).
- [37] Chen, Y., Chu, J., and Xu, X. Plasmonic Multibowtie Aperture Antenna with Fano Resonance for Nanoscale Spectral Sorting. *ACS Photonics*, 3 (9), **2016**, pp. 1689–1697. doi:[10.1021/acsphotonics.6b00345](https://doi.org/10.1021/acsphotonics.6b00345).
- [38] Huang, J.-S., Callegari, V., Geisler, P., *et al.* Atomically flat single-crystalline gold nanostructures for plasmonic nanocircuitry. *Nat. Commun.*, 1 (9), **2010**, p. 150. doi:[10.1038/ncomms1143](https://doi.org/10.1038/ncomms1143).
- [39] Rius, G., Llobet, J., Borriase, X., *et al.* Fabrication of complementary metal-oxide-semiconductor integrated nanomechanical devices by ion beam patterning. *J. Vac. Sci. Technol. B Microelectron. Nanom. Struct.*, 27 (6), **2009**, p. 2691. doi:[10.1116/1.3253550](https://doi.org/10.1116/1.3253550).
- [40] Xia, Y. and Whitesides, G. M. Soft lithography. *Annu. Rev. Mater. Sci.*, 28 (1), **1998**, pp. 153–184. doi:[10.1146/annurev.matsci.28.1.153](https://doi.org/10.1146/annurev.matsci.28.1.153).
- [41] Guo, L. J. Nanoimprint Lithography: Methods and Material Requirements. *Adv. Mater.*, 19 (4), **2007**, pp. 495–513. doi:[10.1002/adma.200600882](https://doi.org/10.1002/adma.200600882).
- [42] Im, H., Lee, S. H., Wittenberg, N. J., *et al.* Template-stripped smooth Ag nanohole arrays with silica shells for surface plasmon resonance biosensing. *ACS Nano*, 5 (8), **2011**, pp. 6244–6253. doi:[10.1021/nn202013v](https://doi.org/10.1021/nn202013v).
- [43] Tiefenauer, R. F., Tybrandt, K., Aramesh, M., and Vörös, J. Fast and Versatile Multiscale Patterning by Combining Template-Stripping with Nanotransfer Printing. *ACS Nano*, 12 (3), **2018**, pp. 2514–2520. doi:[10.1021/acsnano.7b08290](https://doi.org/10.1021/acsnano.7b08290).
- [44] Barth, J. V., Costantini, G., and Kern, K. Engineering atomic and molecular nanostructures at surfaces. *Nature*, 437 (7059), **2005**, pp. 671–679. doi:[10.1038/nature04166](https://doi.org/10.1038/nature04166).
- [45] Jin, Y. Engineering Plasmonic Gold Nanostructures and Metamaterials for Biosensing and Nanomedicine. *Adv. Mater.*, 24 (38), **2012**, pp. 5153–5165. doi:[10.1002/adma.201200622](https://doi.org/10.1002/adma.201200622).
- [46] Li, H. and Rothberg, L. Colorimetric detection of DNA sequences based on electrostatic interactions with unmodified gold nanoparticles. *Proc. Natl. Acad. Sci.*, 101 (39), **2004**, pp. 14036–14039. doi:[10.1073/pnas.0406115101](https://doi.org/10.1073/pnas.0406115101).
- [47] Howes, P. D., Chandrawati, R., and Stevens, M. M. Colloidal nanoparticles as advanced biological sensors. *Science*, 346 (6205), **2014**, pp. 1247390–1247390. doi:[10.1126/science.1247390](https://doi.org/10.1126/science.1247390).

- [48] Ojea-Jiménez, I., López, X., Arbiol, J., *et al.* Citrate-Coated Gold Nanoparticles As Smart Scavengers for Mercury (II) Removal from Polluted Waters. *ACS Nano*, 6 (3), **2012**, pp. 2253–2260. doi:[10.1021/nm204313a](https://doi.org/10.1021/nm204313a).
- [49] Paciotti, G. F., Myer, L., Weinreich, D., *et al.* Colloidal gold: a novel nanoparticle vector for tumor directed drug delivery. *Drug Deliv.*, 11 (3), **2004**, pp. 169–183. doi:[10.1080/10717540490433895](https://doi.org/10.1080/10717540490433895).
- [50] Lalander, C. H., Zheng, Y., Dhuey, S., *et al.* DNA-Directed Self-Assembly of Gold Nanoparticles onto Nanopatterned Surfaces: Controlled Placement of Individual Nanoparticles into Regular Arrays. *ACS Nano*, 4 (10), **2010**, pp. 6153–6161. doi:[10.1021/nm101431k](https://doi.org/10.1021/nm101431k).
- [51] Kolíbal, M., Konečný, M., Ligmajer, F., *et al.* Guided Assembly of Gold Colloidal Nanoparticles on Silicon Substrates Prepatterned by Charged Particle Beams. *ACS Nano*, 6 (11), **2012**, pp. 10098–10106. doi:[10.1021/nm3038226](https://doi.org/10.1021/nm3038226).
- [52] Tzeng, S.-D., Lin, K.-J., Hu, J.-C., *et al.* Templated Self-Assembly of Colloidal Nanoparticles Controlled by Electrostatic Nanopatterning on a Si₃N₄/SiO₂/Si Electret. *Adv. Mater.*, 18 (9), **2006**, pp. 1147–1151. doi:[10.1002/adma.200501542](https://doi.org/10.1002/adma.200501542).
- [53] Palleau, E., Sangeetha, N. M., Viau, G., *et al.* Coulomb force directed single and binary assembly of nanoparticles from aqueous dispersions by AFM nanoxerography. *ACS Nano*, 5 (5), **2011**, pp. 4228–35. doi:[10.1021/nm2011893](https://doi.org/10.1021/nm2011893).
- [54] Jiang, L., Sun, Y., Nowak, C., *et al.* Patterning of Plasmonic Nanoparticles into Multiplexed One-Dimensional Arrays Based on Spatially Modulated Electrostatic Potential. *ACS Nano*, 5 (10), **2011**, pp. 8288–8294. doi:[10.1021/nm202967f](https://doi.org/10.1021/nm202967f).
- [55] Cui, Y., Björk, M. T., Liddle, J. A., *et al.* Integration of colloidal nanocrystals into lithographically patterned devices. *Nano Lett.*, 4 (6), **2004**, pp. 1093–1098. doi:[10.1021/nl049488i](https://doi.org/10.1021/nl049488i).
- [56] Fan, J. a., Bao, K., Sun, L., *et al.* Plasmonic Mode Engineering with Templated Self-Assembled Nanoclusters. *Nano Lett.*, 12 (10), **2012**, pp. 5318–5324. doi:[10.1021/nl302650t](https://doi.org/10.1021/nl302650t).
- [57] Flauraud, V., Mastrangeli, M., Bernasconi, G. D., *et al.* Nanoscale topographical control of capillary assembly of nanoparticles. *Nat. Nanotechnol.*, 12 (1), **2016**, pp. 73–80. doi:[10.1038/nnano.2016.179](https://doi.org/10.1038/nnano.2016.179).
- [58] Tran, H., Ronaldson, K., Bailey, N. A., *et al.* Hierarchically ordered nanopatterns for spatial control of biomolecules. *ACS Nano*, 8 (11), **2014**, pp. 11846–53. doi:[10.1021/nm505548n](https://doi.org/10.1021/nm505548n).
- [59] Lloyd, J. A., Ng, S. H., Liu, A. C., *et al.* Plasmonic Nanolenses: Electrostatic Self-Assembly of Hierarchical Nanoparticle Trimers and Their Response to Optical and Electron Beam Stimuli. *ACS Nano*, 11 (2), **2017**, pp. 1604–1612. doi:[10.1021/acsnano.6b07336](https://doi.org/10.1021/acsnano.6b07336).
- [60] Liu, N. and Liedl, T. DNA-Assembled Advanced Plasmonic Architectures. *Chem. Rev.*, 118 (6), **2018**, pp. 3032–3053. doi:[10.1021/acs.chemrev.7b00225](https://doi.org/10.1021/acs.chemrev.7b00225).
- [61] Raziman, T. V., Wolke, R. J., and Martin, O. J. F. Optical forces in nanoplasmonic systems: how do they work, what can they be useful for? *Faraday Discuss.*, 178, **2015**, pp. 421–434. doi:[10.1039/C4FD00224E](https://doi.org/10.1039/C4FD00224E).
- [62] Lehmuskero, A., Johansson, P., Rubinsztein-Dunlop, H., *et al.* Laser Trapping of Colloidal Metal Nanoparticles. *ACS Nano*, 9 (4), **2015**, pp. 3453–3469. doi:[10.1021/acsnano.5b00286](https://doi.org/10.1021/acsnano.5b00286).

- [63] Gargiulo, J., Violi, I. L., Cerrota, S., *et al.* Accuracy and Mechanistic Details of Optical Printing of Single Au and Ag Nanoparticles. *ACS Nano*, 11 (10), **2017**, pp. 9678–9688. doi:[10.1021/acsnano.7b04136](https://doi.org/10.1021/acsnano.7b04136).
- [64] Grzelczak, M., Vermant, J., Furst, E. M., and Liz-Marzán, L. M. Directed self-assembly of nanoparticles. *ACS Nano*, 4 (7), **2010**, pp. 3591–3605. doi:[10.1021/nn100869j](https://doi.org/10.1021/nn100869j).
- [65] Kraus, T., Brodoceanu, D., Pazos-Perez, N., and Fery, A. Colloidal Surface Assemblies: Nanotechnology Meets Bioinspiration. *Adv. Funct. Mater.*, 23 (36), **2013**, pp. 4529–4541. doi:[10.1002/adfm.201203885](https://doi.org/10.1002/adfm.201203885).
- [66] Dykman, L. and Khlebtsov, N. Gold nanoparticles in biomedical applications: recent advances and perspectives. *Chem. Soc. Rev.*, 41 (6), **2012**, p. 2256. doi:[10.1039/c1cs15166e](https://doi.org/10.1039/c1cs15166e).
- [67] Learn.Genetics - Genetic Science Learning Center. Available at <http://learn.genetics.utah.edu/content/cells/scale/> (Accessed 2018-05-03).
- [68] Agio, M. and Alú, A. *Optical Antennas*. Cambridge University Press, 2013. ISBN 978-1-107-01414-5.
- [69] Ditlbacher, H., Hohenau, A., Wagner, D., *et al.* Silver nanowires as surface plasmon resonators. *Phys. Rev. Lett.*, 95 (25), **2005**, pp. 1–4. doi:[10.1103/PhysRevLett.95.257403](https://doi.org/10.1103/PhysRevLett.95.257403).
- [70] Cubukcu, E. and Capasso, F. Optical nanorod antennas as dispersive one-dimensional Fabry–Perot resonators for surface plasmons. *Appl. Phys. Lett.*, 95 (20), **2009**, p. 201101. doi:[10.1063/1.3262947](https://doi.org/10.1063/1.3262947).
- [71] Dorfmueller, J., Vogelgesang, R., Weitz, R. T., *et al.* Fabry-Perot Resonances in One-Dimensional Plasmonic Nanostructures. *Nano Lett.*, 9 (6), **2009**, pp. 2372–2377. doi:[10.1021/nl900900r](https://doi.org/10.1021/nl900900r).
- [72] Vahala, K. J. Optical microcavities. *Nature*, 424 (6950), **2003**, pp. 839–846. doi:[10.1038/nature01939](https://doi.org/10.1038/nature01939).
- [73] Novotny, L. Effective Wavelength Scaling for Optical Antennas. *Phys. Rev. Lett.*, 98 (26), **2007**, p. 266802. doi:[10.1103/PhysRevLett.98.266802](https://doi.org/10.1103/PhysRevLett.98.266802).
- [74] Kalousek, R., Dub, P., Brínek, L., and Šikola, T. Response of plasmonic resonant nanorods: an analytical approach to optical antennas. *Opt. Express*, 20 (16), **2012**, p. 17916. doi:[10.1364/OE.20.017916](https://doi.org/10.1364/OE.20.017916).
- [75] Giannini, V., Fernández-Domínguez, A. I., Sonnefraud, Y., *et al.* Controlling light localization and light-matter interactions with nanoplasmonics. *Small*, 6 (22), **2010**, pp. 2498–2507. doi:[10.1002/sml.201001044](https://doi.org/10.1002/sml.201001044).
- [76] Atwater, H. A. and Polman, A. Plasmonics for improved photovoltaic devices. *Nat. Mater.*, 9 (3), **2010**, pp. 205–213. doi:[10.1038/nmat2629](https://doi.org/10.1038/nmat2629).
- [77] Boriskina, S. V., Ghasemi, H., and Chen, G. Plasmonic materials for energy: From physics to applications. *Mater. Today*, 16 (10), **2013**, pp. 375–386. doi:[10.1016/j.mattod.2013.09.003](https://doi.org/10.1016/j.mattod.2013.09.003).
- [78] Brongersma, M. L., Cui, Y., and Fan, S. Light management for photovoltaics using high-index nanostructures. *Nat. Mater.*, 13 (5), **2014**, pp. 451–460. doi:[10.1038/nmat3921](https://doi.org/10.1038/nmat3921).
- [79] Mubeen, S., Lee, J., Lee, W.-R., *et al.* On the Plasmonic Photovoltaic. *ACS Nano*, 8 (6), **2014**, pp. 6066–6073. doi:[10.1021/nn501379r](https://doi.org/10.1021/nn501379r).

- [80] Knight, M. W., Sobhani, H., Nordlander, P., and Halas, N. J. Photodetection with active optical antennas. *Science*, 332 (6030), **2011**, pp. 702–704. doi:[10.1126/science.1203056](https://doi.org/10.1126/science.1203056).
- [81] Li, W. and Valentine, J. Metamaterial perfect absorber based hot electron photodetection. *Nano Lett.*, 14 (6), **2014**, pp. 3510–3514. doi:[10.1021/nl501090w](https://doi.org/10.1021/nl501090w).
- [82] Kim, U. J., Yoo, S., Park, Y., *et al.* Plasmon-Assisted Designable Multi-Resonance Photodetection by Graphene via Nanopatterning of Block Copolymer. *ACS Photonics*, 2 (4), **2015**, pp. 506–514. doi:[10.1021/ph500412p](https://doi.org/10.1021/ph500412p).
- [83] Thyagarajan, K., Rivier, S., Lovera, A., and Martin, O. J. Enhanced second-harmonic generation from double resonant plasmonic antennae. *Opt. Express*, 20 (12), **2012**, p. 12860. doi:[10.1364/OE.20.012860](https://doi.org/10.1364/OE.20.012860).
- [84] Aouani, H., Rahmani, M., Navarro-Cía, M., and Maier, S. A. Third-harmonic-upconversion enhancement from a single semiconductor nanoparticle coupled to a plasmonic antenna. *Nat. Nanotechnol.*, 9 (4), **2014**, pp. 290–294. doi:[10.1038/nnano.2014.27](https://doi.org/10.1038/nnano.2014.27).
- [85] Butet, J., Brevet, P.-F., and Martin, O. J. F. Optical Second Harmonic Generation in Plasmonic Nanostructures: From Fundamental Principles to Advanced Applications. *ACS Nano*, 9 (11), **2015**, pp. 10545–10562. doi:[10.1021/acs.nano.5b04373](https://doi.org/10.1021/acs.nano.5b04373).
- [86] Baffou, G. and Quidant, R. Thermo-plasmonics: using metallic nanostructures as nano-sources of heat. *Laser Photon. Rev.*, 7 (2), **2013**, pp. 171–187. doi:[10.1002/lpor.201200003](https://doi.org/10.1002/lpor.201200003).
- [87] Jack, C., Karimullah, A. S., Tullius, R., *et al.* Spatial control of chemical processes on nanostructures through nano-localized water heating. *Nat. Commun.*, 7, **2016**, p. 10946. doi:[10.1038/ncomms10946](https://doi.org/10.1038/ncomms10946).
- [88] Mutlu, M., Kang, J., Raza, S., *et al.* Thermoplasmonic Ignition of Metal Nanoparticles. *Nano Lett.*, 18 (3), **2018**, pp. 1699–1706. doi:[10.1021/acs.nanolett.7b04739](https://doi.org/10.1021/acs.nanolett.7b04739).
- [89] Challener, W. A., Peng, C., Itagi, A. V., *et al.* Heat-assisted magnetic recording by a near-field transducer with efficient optical energy transfer. *Nat. Photonics*, 3 (4), **2009**, pp. 220–224. doi:[10.1038/nphoton.2009.26](https://doi.org/10.1038/nphoton.2009.26).
- [90] Maier, S. A., Kik, P. G., Atwater, H. A., *et al.* Local detection of electromagnetic energy transport below the diffraction limit in metal nanoparticle plasmon waveguides. *Nat. Mater.*, 2 (4), **2003**, pp. 229–232. doi:[10.1038/nmat852](https://doi.org/10.1038/nmat852).
- [91] Willingham, B. and Link, S. Energy transport in metal nanoparticle chains via sub-radiant plasmon modes. *Opt. Express*, 19 (7), **2011**, pp. 6450–61. doi:[10.1364/OE.19.006450](https://doi.org/10.1364/OE.19.006450).
- [92] Vasilantonakis, N., Nasir, M. E., Dickson, W., *et al.* Bulk plasmon-polaritons in hyperbolic nanorod metamaterial waveguides. *Laser Photon. Rev.*, 9 (3), **2015**, pp. 345–353. doi:[10.1002/lpor.201400457](https://doi.org/10.1002/lpor.201400457).
- [93] Babicheva, V. E., Boltasseva, A., and Lavrinenko, A. V. Transparent conducting oxides for electro-optical plasmonic modulators. *Nanophotonics*, 4 (1), **2015**, pp. 165–185. doi:[10.1515/nanoph-2015-0004](https://doi.org/10.1515/nanoph-2015-0004).
- [94] Park, J., Kang, J.-h., Kim, S. J., *et al.* Dynamic Reflection Phase and Polarization Control in Metasurfaces. *Nano Lett.*, 17 (1), **2017**, pp. 407–413. doi:[10.1021/acs.nanolett.6b04378](https://doi.org/10.1021/acs.nanolett.6b04378).

- [95] Sherrott, M. C., Hon, P. W. C., Fountaine, K. T., *et al.* Experimental Demonstration of 230° Phase Modulation in Gate-Tunable Graphene–Gold Reconfigurable Mid-Infrared Metasurfaces. *Nano Lett.*, 17 (5), **2017**, pp. 3027–3034. doi:[10.1021/acs.nanolett.7b00359](https://doi.org/10.1021/acs.nanolett.7b00359).
- [96] Stockman, M. I. Spasers explained. *Nat. Photonics*, 2 (6), **2008**, pp. 327–329. doi:[10.1038/nphoton.2008.85](https://doi.org/10.1038/nphoton.2008.85).
- [97] Sorger, V. J. and Zhang, X. Spotlight on Plasmon Lasers. *Science*, 333 (August), **2011**, pp. 709–710. doi:[10.1126/science.1204862](https://doi.org/10.1126/science.1204862).
- [98] Wang, D., Wang, W., Knudson, M. P., *et al.* Structural Engineering in Plasmon Nanolasers. *Chem. Rev.*, 118 (6), **2017**, p. acs.chemrev.7b00424. doi:[10.1021/acs.chemrev.7b00424](https://doi.org/10.1021/acs.chemrev.7b00424).
- [99] Halas, N. J. and Moskovits, M. Surface-enhanced Raman spectroscopy: Substrates and materials for research and applications. *MRS Bull.*, 38 (08), **2013**, pp. 607–611. doi:[10.1557/mrs.2013.156](https://doi.org/10.1557/mrs.2013.156).
- [100] Adato, R., Aksu, S., and Altug, H. Engineering mid-infrared nanoantennas for surface enhanced infrared absorption spectroscopy. *Mater. Today*, 18 (8), **2015**, pp. 436–446. doi:[10.1016/j.mattod.2015.03.001](https://doi.org/10.1016/j.mattod.2015.03.001).
- [101] Neubrech, F., Huck, C., Weber, K., *et al.* Surface-enhanced infrared spectroscopy using resonant nanoantennas. *Chem. Rev.*, 117 (7), **2017**, pp. 5110–5145. doi:[10.1021/acs.chemrev.6b00743](https://doi.org/10.1021/acs.chemrev.6b00743).
- [102] Nylander, C., Liedberg, B., and Lind, T. Gas detection by means of surface plasmon resonance. *Sensors and Actuators*, 3, **1982**, pp. 79–88. doi:[10.1016/0250-6874\(82\)80008-5](https://doi.org/10.1016/0250-6874(82)80008-5).
- [103] Homola, J. Surface plasmon resonance sensors for detection of chemical and biological species. *Chem. Rev.*, 108, **2008**, pp. 462–493. doi:[10.1021/cr068107d](https://doi.org/10.1021/cr068107d).
- [104] Scarano, S., Mascini, M., Turner, A. P., and Minunni, M. Surface plasmon resonance imaging for affinity-based biosensors. *Biosens. Bioelectron.*, 25 (5), **2010**, pp. 957–966. doi:[10.1016/j.bios.2009.08.039](https://doi.org/10.1016/j.bios.2009.08.039).
- [105] Šířpová, H. and Homola, J. Surface plasmon resonance sensing of nucleic acids: A review. *Anal. Chim. Acta*, 773, **2013**, pp. 9–23. doi:[10.1016/j.aca.2012.12.040](https://doi.org/10.1016/j.aca.2012.12.040).
- [106] Kabashin, A. V., Patskovsky, S., and Grigorenko, A. N. Phase and amplitude sensitivities in surface plasmon resonance bio and chemical sensing. *Opt. Express*, 17 (23), **2009**, pp. 21191–21204. doi:[10.1364/OE.17.021191](https://doi.org/10.1364/OE.17.021191).
- [107] Kravets, V. G., Schedin, F., Jalil, R., *et al.* Singular phase nano-optics in plasmonic meta-materials for label-free single-molecule detection. *Nat. Mater.*, 12 (4), **2013**, pp. 304–309. doi:[10.1038/nmat3537](https://doi.org/10.1038/nmat3537).
- [108] Dostálek, J., Kasry, A., and Knoll, W. Long Range Surface Plasmons for Observation of Biomolecular Binding Events at Metallic Surfaces. *Plasmonics*, 2 (3), **2007**, pp. 97–106. doi:[10.1007/s11468-007-9037-8](https://doi.org/10.1007/s11468-007-9037-8).
- [109] Wen, Q., Han, X., Hu, C., and Zhang, J. Non-spectroscopic surface plasmon sensor with a tunable sensitivity. *Appl. Phys. Lett.*, 106 (03), **2015**, p. 031113. doi:[10.1063/1.4906453](https://doi.org/10.1063/1.4906453).
- [110] Nishi, H., Hiroya, S., and Tatsuma, T. Potential-Scanning Localized Surface Plasmon Resonance Sensor. *ACS Nano*, 9 (6), **2015**, pp. 6214–6221. doi:[10.1021/acs.nano.5b01577](https://doi.org/10.1021/acs.nano.5b01577).

- [111] Ligmajer, F. *Ordered and disordered arrays of colloidal nanoparticles for biomolecule detection*. Master's thesis, Brno University of Technology, Faculty of Mechanical Engineering, 2013.
- [112] Elghanian, R., Storhoff, J. J., Mucic, R. C., *et al.* Selective Colorimetric Detection of Polynucleotides Based on the Distance-Dependent Optical Properties of Gold Nanoparticles. *Science*, 277 (5329), **1997**, pp. 1078–1081. doi:[10.1126/science.277.5329.1078](https://doi.org/10.1126/science.277.5329.1078).
- [113] McFarland, A. D. and Van Duyne, R. P. Single Silver Nanoparticles as Real-Time Optical Sensors with Zeptomole Sensitivity. *Nano Lett.*, 3 (8), **2003**, pp. 1057–1062. doi:[10.1021/nl034372s](https://doi.org/10.1021/nl034372s).
- [114] Dahlin, A. B. Sensing applications based on plasmonic nanopores: The hole story. *Analyst*, 140 (14), **2015**, pp. 4748–4759. doi:[10.1039/C4AN02258K](https://doi.org/10.1039/C4AN02258K).
- [115] Yonzon, C. R., Jeoung, E., Zou, S., *et al.* A Comparative Analysis of Localized and Propagating Surface Plasmon Resonance Sensors: The Binding of Concanavalin A to a Monosaccharide Functionalized Self-Assembled Monolayer. *J. Am. Chem. Soc.*, 126 (39), **2004**, pp. 12669–12676. doi:[10.1021/ja047118q](https://doi.org/10.1021/ja047118q).
- [116] Dahlin, A. B., Wittenberg, N. J., Höök, F., and Oh, S.-H. Promises and challenges of nanoplasmonic devices for refractometric biosensing. *Nanophotonics*, 2 (2), **2013**, pp. 83–101. doi:[10.1515/nanoph-2012-0026](https://doi.org/10.1515/nanoph-2012-0026).
- [117] Svedendahl, M., Chen, S., Dmitriev, A., and Käll, M. Refractometric Sensing Using Propagating versus Localized Surface Plasmons: A Direct Comparison. *Nano Lett.*, 9 (12), **2009**, pp. 4428–4433. doi:[10.1021/nl902721z](https://doi.org/10.1021/nl902721z).
- [118] Schasfoort, R. B. M. and Tudos, A. J. (eds.). *Handbook of Surface Plasmon Resonance*. Royal Society of Chemistry, Cambridge, 2008. ISBN 978-0-85404-267-8. doi:[10.1039/9781847558220](https://doi.org/10.1039/9781847558220).
- [119] Dostálek, J. and Homola, J. Surface plasmon resonance sensor based on an array of diffraction gratings for highly parallelized observation of biomolecular interactions. *Sensors Actuators B Chem.*, 129 (1), **2008**, pp. 303–310. doi:[10.1016/j.snb.2007.08.012](https://doi.org/10.1016/j.snb.2007.08.012).
- [120] Tokel, O., Inci, F., and Demirci, U. Advances in Plasmonic Technologies for Point of Care Applications. *Chem. Rev.*, 114 (11), **2014**, pp. 5728–5752. doi:[10.1021/cr4000623](https://doi.org/10.1021/cr4000623).
- [121] Aćimović, S. S., Ortega, M. a., Sanz, V., *et al.* LSPR Chip for Parallel, Rapid, and Sensitive Detection of Cancer Markers in Serum. *Nano Lett.*, 14 (5), **2014**, pp. 2636–2641. doi:[10.1021/nl500574n](https://doi.org/10.1021/nl500574n).
- [122] Ament, I., Prasad, J., Henkel, A., *et al.* Single unlabeled protein detection on individual plasmonic nanoparticles. *Nano Lett.*, 12 (2), **2012**, pp. 1092–1095. doi:[10.1021/nl204496g](https://doi.org/10.1021/nl204496g).
- [123] Storhoff, J. J., Elghanian, R., Mucic, R. C., *et al.* One-Pot Colorimetric Differentiation of Polynucleotides with Single Base Imperfections Using Gold Nanoparticle Probes. *J. Am. Chem. Soc.*, 120 (9), **1998**, pp. 1959–1964. doi:[10.1021/ja972332i](https://doi.org/10.1021/ja972332i).
- [124] Chen, S., Svedendahl, M., Duyne, R. P. V., and Käll, M. Plasmon-enhanced colorimetric ELISA with single molecule sensitivity. *Nano Lett.*, 11 (4), **2011**, pp. 1826–1830. doi:[10.1021/nl2006092](https://doi.org/10.1021/nl2006092).
- [125] Quesada-González, D. and Merkoçi, A. Nanoparticle-based lateral flow biosensors. *Biosens. Bioelectron.*, 73, **2015**, pp. 47–63. doi:[10.1016/j.bios.2015.05.050](https://doi.org/10.1016/j.bios.2015.05.050).

- [126] Kedem, O., Vaskevich, A., and Rubinstein, I. Critical Issues in Localized Plasmon Sensing. *J. Phys. Chem. C*, 118 (16), **2014**, pp. 8227–8244. doi:[10.1021/jp409954s](https://doi.org/10.1021/jp409954s).
- [127] Špringer, T., Bocková, M., and Homola, J. Label-free biosensing in complex media: A referencing approach. *Anal. Chem.*, 85 (12), **2013**, pp. 5637–5640. doi:[10.1021/ac401062m](https://doi.org/10.1021/ac401062m).
- [128] Yuan, H., Khatua, S., Zijlstra, P., *et al.* Thousand-fold Enhancement of Single-Molecule Fluorescence Near a Single Gold Nanorod. *Angew. Chemie Int. Ed.*, 52 (4), **2013**, pp. 1217–1221. doi:[10.1002/anie.201208125](https://doi.org/10.1002/anie.201208125).
- [129] Bauch, M., Toma, K., Toma, M., *et al.* Plasmon-Enhanced Fluorescence Biosensors: a Review. *Plasmonics*, 9 (4), **2014**, pp. 781–799. doi:[10.1007/s11468-013-9660-5](https://doi.org/10.1007/s11468-013-9660-5).
- [130] Le Ru, E. and Etchegoin, P. G. *Principles of Surface Enhanced Raman Spectroscopy*. Elsevier, 2009, p. 688. ISBN 978-0-444-52779-0.
- [131] Osawa, M. Surface-Enhanced Infrared Absorption Spectroscopy. In J. M. Chalmers (ed.), *Handb. Vib. Spectrosc.* John Wiley & Sons, 2006. doi:[10.1002/0470027320.s0603](https://doi.org/10.1002/0470027320.s0603).
- [132] Moskovits, M. Surface-enhanced Raman spectroscopy: a brief retrospective. *J. Raman Spectrosc.*, 36 (6-7), **2005**, pp. 485–496. doi:[10.1002/jrs.1362](https://doi.org/10.1002/jrs.1362).
- [133] Nie, S. Probing Single Molecules and Single Nanoparticles by Surface-Enhanced Raman Scattering. *Science*, 275 (5303), **1997**, pp. 1102–1106. doi:[10.1126/science.275.5303.1102](https://doi.org/10.1126/science.275.5303.1102).
- [134] Chirumamilla, M., Toma, A., Gopalakrishnan, A., *et al.* 3D Nanostar Dimers with a Sub-10-nm Gap for Single-/Few-Molecule Surface-Enhanced Raman Scattering. *Adv. Mater.*, 26 (15), **2014**, pp. 2353–2358. doi:[10.1002/adma.201304553](https://doi.org/10.1002/adma.201304553).
- [135] Jeanmaire, D. L. and Van Duyne, R. P. Surface raman spectroelectrochemistry. *J. Electroanal. Chem. Interfacial Electrochem.*, 84 (1), **1977**, pp. 1–20. doi:[10.1016/S0022-0728\(77\)80224-6](https://doi.org/10.1016/S0022-0728(77)80224-6).
- [136] Albrecht, M. G. and Creighton, J. A. Anomalously intense Raman spectra of pyridine at a silver electrode. *J. Am. Chem. Soc.*, 99 (15), **1977**, pp. 5215–5217. doi:[10.1021/ja00457a071](https://doi.org/10.1021/ja00457a071).
- [137] Adato, R. and Altug, H. In-situ ultra-sensitive infrared absorption spectroscopy of biomolecule interactions in real time with plasmonic nanoantennas. *Nat. Commun.*, 4, **2013**, p. 2154. doi:[10.1038/ncomms3154](https://doi.org/10.1038/ncomms3154).
- [138] Huck, C., Neubrech, F., Vogt, J., *et al.* Surface-Enhanced Infrared Spectroscopy Using Nanometer-Sized Gaps. *ACS Nano*, 8 (5), **2014**, pp. 4908–4914. doi:[10.1021/nn500903v](https://doi.org/10.1021/nn500903v).
- [139] Bagheri, S., Weber, K., Gissibl, T., *et al.* Fabrication of Square-Centimeter Plasmonic Nanoantenna Arrays by Femtosecond Direct Laser Writing Lithography: Effects of Collective Excitations on SEIRA Enhancement. *ACS Photonics*, 2 (6), **2015**, pp. 779–786. doi:[10.1021/acsphotonics.5b00141](https://doi.org/10.1021/acsphotonics.5b00141).
- [140] Yavas, O., Svedendahl, M., Dobosz, P., *et al.* On-a-chip Biosensing Based on All-Dielectric Nanoresonators. *Nano Lett.*, 17 (7), **2017**, pp. 4421–4426. doi:[10.1021/acs.nanolett.7b01518](https://doi.org/10.1021/acs.nanolett.7b01518).
- [141] MacKenzie, R., Frascina, C., Sannomiya, T., *et al.* Optical Sensing with Simultaneous Electrochemical Control in Metal Nanowire Arrays. *Sensors*, 10 (11), **2010**, pp. 9808–9830. doi:[10.3390/s101109808](https://doi.org/10.3390/s101109808).
- [142] Marini, A., Silveiro, I., and García de Abajo, F. J. Molecular Sensing with Tunable Graphene Plasmons. *ACS Photonics*, 2 (7), **2015**, pp. 876–882. doi:[10.1021/acsphotonics.5b00067](https://doi.org/10.1021/acsphotonics.5b00067).

- [143] Cai, W. and Shalaev, V. *Optical Metamaterials*. Springer, 2010. ISBN 978-1-4419-1150-6. doi:[10.1007/978-1-4419-1151-3](#).
- [144] Landau, L. D. and Lifshitz, E. M. The dielectric permeability at very high frequencies. In *Electrodyn. Contin. media*. Pergamon Press, 1960.
- [145] Smith, D. R., Padilla, W. J., Vier, D. C., *et al.* Composite Medium with Simultaneously Negative Permeability and Permittivity. *Phys. Rev. Lett.*, 84 (18), **2000**, pp. 4184–4187. doi:[10.1103/PhysRevLett.84.4184](#).
- [146] Pendry, J. B. Negative Refraction Makes a Perfect Lens. *Phys. Rev. Lett.*, 85 (18), **2000**, pp. 3966–3969. doi:[10.1103/PhysRevLett.85.3966](#).
- [147] Liu, Y. and Zhang, X. Metamaterials: a new frontier of science and technology. *Chem. Soc. Rev.*, 40 (5), **2011**, p. 2494. doi:[10.1039/c0cs00184h](#).
- [148] Yu, N., Genevet, P., Kats, M. A., *et al.* Light Propagation with Phase Discontinuities: Generalized Laws of Reflection and Refraction. *Science*, 334 (6054), **2011**, pp. 333–337. doi:[10.1126/science.1210713](#).
- [149] Hsiao, H.-H., Chu, C. H., and Tsai, D. P. Fundamentals and Applications of Metasurfaces. *Small Methods*, 1 (4), **2017**, p. 1600064. doi:[10.1002/smt.201600064](#).
- [150] Kats, M. a., Genevet, P., Aoust, G., *et al.* Giant birefringence in optical antenna arrays with widely tailorable optical anisotropy. *Proc. Natl. Acad. Sci.*, 109 (31), **2012**, pp. 12364–12368. doi:[10.1073/pnas.1210686109](#).
- [151] Sun, S., Yang, K.-Y., Wang, C.-M., *et al.* High-Efficiency Broadband Anomalous Reflection by Gradient Meta-Surfaces. *Nano Lett.*, 12 (12), **2012**, pp. 6223–6229. doi:[10.1021/nl3032668](#).
- [152] Pors, A. and Bozhevolnyi, S. I. Plasmonic metasurfaces for efficient phase control in reflection. *Opt. Express*, 21 (22), **2013**, p. 27438. doi:[10.1364/OE.21.027438](#).
- [153] Batterman, R. W. Falling cats, parallel parking, and polarized light. *Stud. Hist. Philos. Sci. Part B - Stud. Hist. Philos. Mod. Phys.*, 34 (4), **2003**, pp. 527–557. doi:[10.1016/S1355-2198\(03\)00062-5](#).
- [154] Hasman, E., Kleiner, V., Biener, G., and Niv, A. Polarization dependent focusing lens by use of quantized Pancharatnam-Berry phase diffractive optics. *Appl. Phys. Lett.*, 82 (3), **2003**, pp. 328–330. doi:[10.1063/1.1539300](#).
- [155] Kuznetsov, A. I., Miroshnichenko, A. E., Brongersma, M. L., *et al.* Optically resonant dielectric nanostructures. *Science*, 354 (6314), **2016**, p. aag2472. doi:[10.1126/science.aag2472](#).
- [156] Genevet, P., Capasso, F., Aieta, F., *et al.* Recent advances in planar optics: From plasmonic to dielectric metasurfaces. *Optica*, 4 (1), **2017**, p. 139. doi:[10.1364/OPTICA.4.000139](#).
- [157] Khorasaninejad, M. and Capasso, F. Metalenses: Versatile multifunctional photonic components. *Science*, 358 (6367), **2017**, p. eaam8100. doi:[10.1126/science.aam8100](#).
- [158] Chen, W. T., Zhu, A. Y., Sanjeev, V., *et al.* A broadband achromatic metalens for focusing and imaging in the visible. *Nat. Nanotechnol.*, 13 (3), **2018**, pp. 220–226. doi:[10.1038/s41565-017-0034-6](#).
- [159] Genevet, P. and Capasso, F. Holographic optical metasurfaces: a review of current progress. *Reports Prog. Phys.*, 78 (2), **2015**, p. 024401. doi:[10.1088/0034-4885/78/2/024401](#).

- [160] Zheng, G., Mühlenbernd, H., Kenney, M., *et al.* Metasurface holograms reaching 80% efficiency. *Nat. Nanotechnol.*, 10 (4), **2015**, pp. 308–12. doi:[10.1038/nnano.2015.2](https://doi.org/10.1038/nnano.2015.2).
- [161] Wan, W., Gao, J., and Yang, X. Full-Color Plasmonic Metasurface Holograms. *ACS Nano*, 10 (12), **2016**, pp. 10671–10680. doi:[10.1021/acsnano.6b05453](https://doi.org/10.1021/acs.nano.6b05453).
- [162] Karimi, E., Schulz, S. a., De Leon, I., *et al.* Generating optical orbital angular momentum at visible wavelengths using a plasmonic metasurface. *Light Sci. Appl.*, 3 (5), **2014**, p. e167. doi:[10.1038/lsa.2014.48](https://doi.org/10.1038/lsa.2014.48).
- [163] Bouchard, F., De Leon, I., Schulz, S. A., *et al.* Optical spin-to-orbital angular momentum conversion in ultra-thin metasurfaces with arbitrary topological charges. *Appl. Phys. Lett.*, 105 (10), **2014**, p. 101905. doi:[10.1063/1.4895620](https://doi.org/10.1063/1.4895620).
- [164] Devlin, R. C., Ambrosio, A., Rubin, N. A., *et al.* Arbitrary spin-to-orbital angular momentum conversion of light. *Science*, 358 (6365), **2017**, pp. 896–901. doi:[10.1126/science.aao5392](https://doi.org/10.1126/science.aao5392).
- [165] Padgett, M., Courtial, J., and Allen, L. Light’s orbital angular momentum. *Phys. Today*, 57 (5), **2004**, pp. 35–40. doi:[10.1063/1.1768672](https://doi.org/10.1063/1.1768672).
- [166] Yu, N., Aieta, F., Genevet, P., *et al.* A broadband, background-free quarter-wave plate based on plasmonic metasurfaces. *Nano Lett.*, 12 (12), **2012**, pp. 6328–6333. doi:[10.1021/nl303445u](https://doi.org/10.1021/nl303445u).
- [167] Zhao, Y. and Alù, A. Tailoring the Dispersion of Plasmonic Nanorods To Realize Broadband Optical Meta-Waveplates. *Nano Lett.*, 13 (3), **2013**, pp. 1086–1091. doi:[10.1021/nl304392b](https://doi.org/10.1021/nl304392b).
- [168] Ding, F., Wang, Z., He, S., *et al.* Broadband High-Efficiency Half-Wave Plate: A Super-Cell Based Plasmonic Metasurface Approach. *ACS Nano*, 9 (4), **2015**, pp. 4111–4119. doi:[10.1021/acsnano.5b00218](https://doi.org/10.1021/acs.nano.5b00218).
- [169] Pors, A., Nielsen, M. G., and Bozhevolnyi, S. I. Plasmonic metagratings for simultaneous determination of Stokes parameters. *Optica*, 2 (8), **2015**, p. 716. doi:[10.1364/OPTICA.2.000716](https://doi.org/10.1364/OPTICA.2.000716).
- [170] Aieta, F., Kats, M. A., Genevet, P., and Capasso, F. Multiwavelength achromatic metasurfaces by dispersive phase compensation. *Science*, 347 (6228), **2015**, pp. 1342–1345. doi:[10.1126/science.aaa2494](https://doi.org/10.1126/science.aaa2494).
- [171] She, A., Zhang, S., Shian, S., *et al.* Adaptive metalenses with simultaneous electrical control of focal length, astigmatism, and shift. *Sci. Adv.*, 4 (2), **2018**, p. eaap9957. doi:[10.1126/sciadv.aap9957](https://doi.org/10.1126/sciadv.aap9957).
- [172] Shaltout, A. M., Kildishev, A. V., and Shalaev, V. M. Evolution of photonic metasurfaces: From static to dynamic. *J. Opt. Soc. Am. B*, 33 (3), **2016**, p. 501. doi:[10.1364/JOSAB.33.000501](https://doi.org/10.1364/JOSAB.33.000501).
- [173] West, P., Ishii, S., Naik, G., *et al.* Searching for better plasmonic materials. *Laser Photon. Rev.*, 4 (6), **2010**, pp. 795–808. doi:[10.1002/lpor.200900055](https://doi.org/10.1002/lpor.200900055).
- [174] Naik, G. V., Shalaev, V. M., and Boltasseva, A. Alternative plasmonic materials: Beyond gold and silver. *Adv. Mater.*, 25 (24), **2013**, pp. 3264–3294. doi:[10.1002/adma.201205076](https://doi.org/10.1002/adma.201205076).
- [175] Brongersma, M. L., Halas, N. J., and Nordlander, P. Plasmon-induced hot carrier science and technology. *Nat. Nanotechnol.*, 10 (1), **2015**, pp. 25–34. doi:[10.1038/nnano.2014.311](https://doi.org/10.1038/nnano.2014.311).

- [176] Giesecking, R. L., Ratner, M. A., and Schatz, G. C. Review of plasmon-induced hot-electron dynamics and related SERS chemical effects. In *Front. Plasmon Enhanc. Spectrosc. Vol. 1*, vol. 1245, pp. 1–22. American Chemical Society, 2016. doi:[10.1021/bk-2016-1245](https://doi.org/10.1021/bk-2016-1245).
- [177] Frese, K. W. Theoretical Models of Hot Carrier Effects at Metal-Semiconductor Electrodes. *J. Electrochem. Soc.*, 139 (11), **1992**, p. 3234. doi:[10.1149/1.2069059](https://doi.org/10.1149/1.2069059).
- [178] Hartland, G. V. Optical studies of dynamics in noble metal nanostructures. *Chem. Rev.*, 111 (6), **2011**, pp. 3858–3887. doi:[10.1021/cr1002547](https://doi.org/10.1021/cr1002547).
- [179] Yang, L.-M., Dornfeld, M., Frauenheim, T., and Ganz, E. Glitter in a 2D monolayer. *Phys. Chem. Chem. Phys.*, 17 (39), **2015**, pp. 26036–26042. doi:[10.1039/C5CP04222D](https://doi.org/10.1039/C5CP04222D).
- [180] Khurgin, J. B. How to deal with the loss in plasmonics and metamaterials. *Nat. Nanotechnol.*, 10 (1), **2015**, pp. 2–6. doi:[10.1038/nnano.2014.310](https://doi.org/10.1038/nnano.2014.310).
- [181] Khurgin, J., Tsai, W. Y., Tsai, D. P., and Sun, G. Landau Damping and Limit to Field Confinement and Enhancement in Plasmonic Dimers. *ACS Photonics*, 4 (11), **2017**, pp. 2871–2880. doi:[10.1021/acsp Photonics.7b00860](https://doi.org/10.1021/acsp Photonics.7b00860).
- [182] Hartland, G. V., Besteiro, L. V., Johns, P., and Govorov, A. O. What’s so Hot about Electrons in Metal Nanoparticles? *ACS Energy Lett.*, 2 (7), **2017**, pp. 1641–1653. doi:[10.1021/acsenerylett.7b00333](https://doi.org/10.1021/acsenerylett.7b00333).
- [183] Zhang, H. and Govorov, A. O. Optical generation of hot plasmonic carriers in metal nanocrystals: The effects of shape and field enhancement. *J. Phys. Chem. C*, 118 (14), **2014**, pp. 7606–7614. doi:[10.1021/jp500009k](https://doi.org/10.1021/jp500009k).
- [184] Li, J., Cushing, S. K., Meng, F., *et al.* Plasmon-induced resonance energy transfer for solar energy conversion. *Nat. Photonics*, 9 (9), **2015**, pp. 601–607. doi:[10.1038/nphoton.2015.142](https://doi.org/10.1038/nphoton.2015.142).
- [185] Moskovits, M. The case for plasmon-derived hot carrier devices. *Nat. Nanotechnol.*, 10 (1), **2015**, pp. 6–8. doi:[10.1038/nnano.2014.280](https://doi.org/10.1038/nnano.2014.280).
- [186] Christopher, P., Xin, H., Marimuthu, A., and Linic, S. Singular characteristics and unique chemical bond activation mechanisms of photocatalytic reactions on plasmonic nanostructures. *Nat. Mater.*, 11 (12), **2012**, pp. 1044–50. doi:[10.1038/nmat3454](https://doi.org/10.1038/nmat3454).
- [187] Mukherjee, S., Libisch, F., Large, N., *et al.* Hot Electrons Do the Impossible: Plasmon-Induced Dissociation of H₂ on Au. *Nano Lett.*, 13 (1), **2013**, pp. 240–247. doi:[10.1021/nl303940z](https://doi.org/10.1021/nl303940z).
- [188] Thrall, E. S., Steinberg, A. P., Wu, X., and Brus, L. E. The role of photon energy and semiconductor substrate in the plasmon-mediated photooxidation of citrate by silver nanoparticles. *J. Phys. Chem. C*, 117 (49), **2013**, pp. 26238–26247. doi:[10.1021/jp409586z](https://doi.org/10.1021/jp409586z).
- [189] Kale, M. J., Avanesian, T., Xin, H., *et al.* Controlling catalytic selectivity on metal nanoparticles by direct photoexcitation of adsorbate-metal bonds. *Nano Lett.*, 14 (9), **2014**, pp. 5405–5412. doi:[10.1021/nl502571b](https://doi.org/10.1021/nl502571b).
- [190] Linic, S., Aslam, U., Boerigter, C., and Morabito, M. Photochemical transformations on plasmonic metal nanoparticles. *Nat. Mater.*, 14 (6), **2015**, pp. 567–576. doi:[10.1038/nmat4281](https://doi.org/10.1038/nmat4281).
- [191] Hisatomi, T., Kubota, J., and Domen, K. Recent advances in semiconductors for photocatalytic and photoelectrochemical water splitting. *Chem. Soc. Rev.*, 43 (22), **2014**, pp. 7520–7535. doi:[10.1039/C3CS60378D](https://doi.org/10.1039/C3CS60378D).

- [192] Cushing, S. K. and Wu, N. Progress and Perspectives of Plasmon-Enhanced Solar Energy Conversion. *J. Phys. Chem. Lett.*, 7 (4), **2016**, pp. 666–675. doi:[10.1021/acs.jpcclett.5b02393](https://doi.org/10.1021/acs.jpcclett.5b02393).
- [193] Naldoni, A., Guler, U., Wang, Z., *et al.* Broadband Hot-Electron Collection for Solar Water Splitting with Plasmonic Titanium Nitride. *Adv. Opt. Mater.*, 5 (15), **2017**, p. 1601031. doi:[10.1002/adom.201601031](https://doi.org/10.1002/adom.201601031).
- [194] Fang, Z., Wang, Y., Liu, Z., *et al.* Plasmon-induced doping of graphene. *ACS Nano*, 6 (11), **2012**, pp. 10222–10228. doi:[10.1021/nm304028b](https://doi.org/10.1021/nm304028b).
- [195] Appavoo, K., Wang, B., Brady, N. F., *et al.* Ultrafast Phase Transition via Catastrophic Phonon Collapse Driven by Plasmonic Hot-Electron Injection. *Nano Lett.*, 14 (3), **2014**, pp. 1127–1133. doi:[10.1021/nl4044828](https://doi.org/10.1021/nl4044828).
- [196] Kang, Y., Najmaei, S., Liu, Z., *et al.* Plasmonic Hot Electron Induced Structural Phase Transition in a MoS₂ Monolayer. *Adv. Mater.*, 26 (37), **2014**, pp. 6467–6471. doi:[10.1002/adma.201401802](https://doi.org/10.1002/adma.201401802).
- [197] Clavero, C. Plasmon-induced hot-electron generation at nanoparticle/metal-oxide interfaces for photovoltaic and photocatalytic devices. *Nat. Photonics*, 8 (2), **2014**, pp. 95–103. doi:[10.1038/nphoton.2013.238](https://doi.org/10.1038/nphoton.2013.238).
- [198] White, T. P. and Catchpole, K. R. Plasmon-enhanced internal photoemission for photovoltaics: Theoretical efficiency limits. *Appl. Phys. Lett.*, 101 (7), **2012**, pp. 4–7. doi:[10.1063/1.4746425](https://doi.org/10.1063/1.4746425).
- [199] Fang, Y., Jiao, Y., Xiong, K., *et al.* Plasmon Enhanced Internal Photoemission in Antenna-Spacer-Mirror Based Au/TiO₂ Nanostructures. *Nano Lett.*, 15 (6), **2015**, pp. 4059–4065. doi:[10.1021/acs.nanolett.5b01070](https://doi.org/10.1021/acs.nanolett.5b01070).
- [200] Zhang, Y., Yam, C., and Schatz, G. C. Fundamental Limitations to Plasmonic Hot-Carrier Solar Cells. *J. Phys. Chem. Lett.*, 7 (10), **2016**, pp. 1852–1858. doi:[10.1021/acs.jpcclett.6b00879](https://doi.org/10.1021/acs.jpcclett.6b00879).
- [201] Reineck, P., Brick, D., Mulvaney, P., and Bach, U. Plasmonic Hot Electron Solar Cells: The Effect of Nanoparticle Size on Quantum Efficiency. *J. Phys. Chem. Lett.*, 7 (20), **2016**, pp. 4137–4141. doi:[10.1021/acs.jpcclett.6b01884](https://doi.org/10.1021/acs.jpcclett.6b01884).
- [202] Chalabi, H., Schoen, D., and Brongersma, M. L. Hot-electron photodetection with a plasmonic nanostripe antenna. *Nano Lett.*, 14 (3), **2014**, pp. 1374–1380. doi:[10.1021/nl4044373](https://doi.org/10.1021/nl4044373).
- [203] Wang, W., Klots, A., Prasai, D., *et al.* Hot Electron-Based Near-Infrared Photodetection Using Bilayer MoS₂. *Nano Lett.*, 15 (11), **2015**, pp. 7440–7444. doi:[10.1021/acs.nanolett.5b02866](https://doi.org/10.1021/acs.nanolett.5b02866).
- [204] Lin, L., Wang, M., Peng, X., *et al.* Opto-thermoelectric nanotweezers. *Nat. Photonics*, 12 (4), **2018**, pp. 195–201. doi:[10.1038/s41566-018-0134-3](https://doi.org/10.1038/s41566-018-0134-3).
- [205] Jermyn, A. S., Tagliabue, G., Atwater, H. A., *et al.* Far-from-equilibrium transport of excited carriers in nanostructures. *arXiv*, , **2017**. [arXiv:1707.07060](https://arxiv.org/abs/1707.07060).
- [206] Sykes, M. E., Stewart, J. W., Akselrod, G. M., *et al.* Enhanced generation and anisotropic Coulomb scattering of hot electrons in an ultra-broadband plasmonic nanopatch metasurface. *Nat. Commun.*, 8 (1), **2017**, p. 986. doi:[10.1038/s41467-017-01069-3](https://doi.org/10.1038/s41467-017-01069-3).

- [207] Van Dijk, M. A., Lippitz, M., and Orrit, M. Far-field optical microscopy of single metal nanoparticles. *Acc. Chem. Res.*, 38 (7), **2005**, pp. 594–601. doi:[10.1021/ar0401303](https://doi.org/10.1021/ar0401303).
- [208] Zijlstra, P. and Orrit, M. Single metal nanoparticles: optical detection, spectroscopy and applications. *Reports Prog. Phys.*, 74 (10), **2011**, p. 106401. doi:[10.1088/0034-4885/74/10/106401](https://doi.org/10.1088/0034-4885/74/10/106401).
- [209] Ringe, E., Sharma, B., Henry, A.-I., *et al.* Single nanoparticle plasmonics. *Phys. Chem. Chem. Phys. Phys. Chem. Chem. Phys. Phys. Chem. Chem. Phys.*, 1515121 (15), **2013**, pp. 4075–4460. doi:[10.1039/c3cp44574g](https://doi.org/10.1039/c3cp44574g).
- [210] Olson, J., Dominguez-Medina, S., Hoggard, A., *et al.* Optical characterization of single plasmonic nanoparticles. *Chem. Soc. Rev.*, 44 (1), **2015**, pp. 40–57. doi:[10.1039/C4CS00131A](https://doi.org/10.1039/C4CS00131A).
- [211] Gaiduk, A., Ruijgrok, P. V., Yorulmaz, M., and Orrit, M. Detection limits in photothermal microscopy. *Chem. Sci.*, 1 (3), **2010**, p. 343. doi:[10.1039/c0sc00210k](https://doi.org/10.1039/c0sc00210k).
- [212] Yorulmaz, M., Nizzero, S., Hoggard, A., *et al.* Single-Particle Absorption Spectroscopy by Photothermal Contrast. *Nano Lett.*, 15 (5), **2015**, pp. 3041–3047. doi:[10.1021/nl504992h](https://doi.org/10.1021/nl504992h).
- [213] Billaud, P., Marhaba, S., Grillet, N., *et al.* Absolute optical extinction measurements of single nano-objects by spatial modulation spectroscopy using a white lamp. *Rev. Sci. Instrum.*, 81 (4), **2010**, p. 043101. doi:[10.1063/1.3340875](https://doi.org/10.1063/1.3340875).
- [214] Lieb, M. A., Zavitsan, J. M., and Novotny, L. Single-molecule orientations determined by direct emission pattern imaging. *J. Opt. Soc. Am. B*, 21 (6), **2004**, p. 1210. doi:[10.1364/JOSAB.21.001210](https://doi.org/10.1364/JOSAB.21.001210).
- [215] Kurvits, J. A., Jiang, M., and Zia, R. Comparative analysis of imaging configurations and objectives for Fourier microscopy. *J. Opt. Soc. Am. A*, 32 (11), **2015**, p. 2082. doi:[10.1364/JOSAA.32.002082](https://doi.org/10.1364/JOSAA.32.002082).
- [216] Ramezani, M., Casadei, A., Grzela, G., *et al.* Hybrid Semiconductor Nanowire–Metallic Yagi–Uda Antennas. *Nano Lett.*, 15 (8), **2015**, pp. 4889–4895. doi:[10.1021/acs.nanolett.5b00565](https://doi.org/10.1021/acs.nanolett.5b00565).
- [217] Zayats, A. V., Smolyaninov, I. I., and Maradudin, A. A. Nano-optics of surface plasmon polaritons. *Phys. Rep.*, 408 (3-4), **2005**, pp. 131–314. doi:[10.1016/j.physrep.2004.11.001](https://doi.org/10.1016/j.physrep.2004.11.001).
- [218] Feber, B. L., Rotenberg, N., Beggs, D. M., *et al.* Simultaneous measurement of nanoscale electric and magnetic optical fields. *Nat. Photonics*, 8 (1), **2014**, pp. 43–46. doi:[10.1038/nphoton.2013.323](https://doi.org/10.1038/nphoton.2013.323).
- [219] Lemke, C., Schneider, C., Leißner, T., *et al.* Spatiotemporal Characterization of SPP Pulse Propagation in Two-Dimensional Plasmonic Focusing Devices. *Nano Lett.*, 13 (3), **2013**, pp. 1053–1058. doi:[10.1021/nl3042849](https://doi.org/10.1021/nl3042849).
- [220] Kahl, P., Wall, S., Witt, C., *et al.* Normal-Incidence Photoemission Electron Microscopy (NI-PEEM) for Imaging Surface Plasmon Polaritons. *Plasmonics*, 9 (6), **2014**, pp. 1401–1407. doi:[10.1007/s11468-014-9756-6](https://doi.org/10.1007/s11468-014-9756-6).
- [221] Spektor, G., Kilbane, D., Mahro, A. K., *et al.* Revealing the subfemtosecond dynamics of orbital angular momentum in nanoplasmonic vortices. *Science*, 355 (6330), **2017**, pp. 1187–1191. doi:[10.1126/science.aaj1699](https://doi.org/10.1126/science.aaj1699).

- [222] Coenen, T., Vesseur, E. J. R., Polman, A., and Koenderink, A. F. Directional Emission from Plasmonic Yagi–Uda Antennas Probed by Angle-Resolved Cathodoluminescence Spectroscopy. *Nano Lett.*, 11 (9), **2011**, pp. 3779–3784. doi:[10.1021/nl201839g](https://doi.org/10.1021/nl201839g).
- [223] Mignuzzi, S., Mota, M., Coenen, T., *et al.* Energy–Momentum Cathodoluminescence Spectroscopy of Dielectric Nanostructures. *ACS Photonics*, 5 (4), **2018**, pp. 1381–1387. doi:[10.1021/acsphotonics.7b01404](https://doi.org/10.1021/acsphotonics.7b01404).
- [224] Wu, Y., Li, G., and Camden, J. P. Probing Nanoparticle Plasmons with Electron Energy Loss Spectroscopy. *Chem. Rev.*, 118 (6), **2018**, pp. 2994–3031. doi:[10.1021/acs.chemrev.7b00354](https://doi.org/10.1021/acs.chemrev.7b00354).
- [225] Shekhar, P., Malac, M., Gaïnd, V., *et al.* Momentum-Resolved Electron Energy Loss Spectroscopy for Mapping the Photonic Density of States. *ACS Photonics*, 4 (4), **2017**, pp. 1009–1014. doi:[10.1021/acsphotonics.7b00103](https://doi.org/10.1021/acsphotonics.7b00103).
- [226] Schmidt, F.-P., Losquin, A., Hofer, F., *et al.* How Dark Are Radial Breathing Modes in Plasmonic Nanodisks? *ACS Photonics*, 5 (3), **2017**, pp. 861–866. doi:[10.1021/acsphotonics.7b01060](https://doi.org/10.1021/acsphotonics.7b01060).
- [227] Horák, M., Bukvišová, K., Švarc, V., *et al.* Comparative study of plasmonic antennas fabricated by electron beam and focused ion beam lithography. *Sci. Rep.*, 8 (1), **2018**, p. 9640. doi:[10.1038/s41598-018-28037-1](https://doi.org/10.1038/s41598-018-28037-1).
- [228] Simoncelli, S., Li, Y., Cortés, E., and Maier, S. A. Nanoscale Control of Molecular Self-Assembly Induced by Plasmonic Hot-Electron Dynamics. *ACS Nano*, 12 (3), **2018**, pp. 2184–2192. doi:[10.1021/acsnano.7b08563](https://doi.org/10.1021/acsnano.7b08563).
- [229] Zou, N., Chen, G., Mao, X., *et al.* Imaging Catalytic Hotspots on Single Plasmonic Nanostructures via Correlated Super-Resolution and Electron Microscopy. *ACS Nano*, 12 (6), **2018**, pp. 5570–5579. doi:[10.1021/acsnano.8b01338](https://doi.org/10.1021/acsnano.8b01338).
- [230] Li, Q., Pan, D., Wei, H., and Xu, H. Plasmon-Assisted Selective and Super-Resolving Excitation of Individual Quantum Emitters on a Metal Nanowire. *Nano Lett.*, 18 (3), **2018**, pp. 2009–2015. doi:[10.1021/acs.nanolett.7b05448](https://doi.org/10.1021/acs.nanolett.7b05448).
- [231] Liu, Y., Tu, D., Zhu, H., and Chen, X. Lanthanide-doped luminescent nanoprobe: controlled synthesis, optical spectroscopy, and bioapplications. *Chem. Soc. Rev.*, 42 (16), **2013**, p. 6924. doi:[10.1039/c3cs60060b](https://doi.org/10.1039/c3cs60060b).
- [232] Zheng, W., Tu, D., Huang, P., *et al.* Time-resolved luminescent biosensing based on inorganic lanthanide-doped nanoprobe. *Chem. Commun.*, 51 (20), **2015**, pp. 4129–4143. doi:[10.1039/C4CC10432C](https://doi.org/10.1039/C4CC10432C).
- [233] Liu, Q., Sun, Y., Yang, T., *et al.* Sub-10 nm Hexagonal Lanthanide-Doped NaLuF₄ Upconversion Nanocrystals for Sensitive Bioimaging in Vivo. *J. Am. Chem. Soc.*, 133 (43), **2011**, pp. 17122–17125. doi:[10.1021/ja207078s](https://doi.org/10.1021/ja207078s).
- [234] Wang, H.-Q., Batentschuk, M., Osvet, A., *et al.* Rare-Earth Ion Doped Up-Conversion Materials for Photovoltaic Applications. *Adv. Mater.*, 23 (22-23), **2011**, pp. 2675–2680. doi:[10.1002/adma.201100511](https://doi.org/10.1002/adma.201100511).
- [235] Taminiau, T. H., Stefani, F. D., Segerink, F. B., and van Hulst, N. F. Optical antennas direct single-molecule emission. *Nat. Photonics*, 2 (4), **2008**, pp. 234–237. doi:[10.1038/nphoton.2008.32](https://doi.org/10.1038/nphoton.2008.32).

- [236] He, J., Zheng, W., Ligmajer, F., *et al.* Plasmonic enhancement and polarization dependence of nonlinear upconversion emissions from single gold nanorod@SiO₂@CaF₂:Yb³⁺,Er³⁺ hybrid core-shell-satellite nanostructures. *Light Sci. Appl.*, 6 (5), **2017**, p. e16217. doi:[10.1038/lsa.2016.217](https://doi.org/10.1038/lsa.2016.217).
- [237] Zheng, W., Zhou, S., Chen, Z., *et al.* Sub-10 nm Lanthanide-Doped CaF₂ Nanoprobes for Time-Resolved Luminescent Biodetection. *Angew. Chemie Int. Ed.*, 52 (26), **2013**, pp. 6671–6676. doi:[10.1002/anie.201302481](https://doi.org/10.1002/anie.201302481).
- [238] Scarabelli, L., Sánchez-Iglesias, A., Pérez-Juste, J., and Liz-Marzán, L. M. A “Tips and Tricks” Practical Guide to the Synthesis of Gold Nanorods. *J. Phys. Chem. Lett.*, 6 (21), **2015**, pp. 4270–4279. doi:[10.1021/acs.jpcllett.5b02123](https://doi.org/10.1021/acs.jpcllett.5b02123).
- [239] Gorelikov, I. and Matsuura, N. Single-Step Coating of Mesoporous Silica on Cetyltrimethyl Ammonium Bromide-Capped Nanoparticles. *Nano Lett.*, 8 (1), **2008**, pp. 369–373. doi:[10.1021/nl0727415](https://doi.org/10.1021/nl0727415).
- [240] Tobing, L. Y. M., Zhang, D. H., Fong, K. E., *et al.* Polarization-Resolved Plasmon-Modulated Emissions of Quantum Dots Coupled to Aluminum Dimers with Sub-20 nm Gaps. *ACS Photonics*, 5 (4), **2018**, pp. 1566–1574. doi:[10.1021/acsphotonics.8b00009](https://doi.org/10.1021/acsphotonics.8b00009).
- [241] Chen, L., Rong, Y., Ren, M., *et al.* Selective Polarization Modification of Upconversion Luminescence of NaYF₄:Yb³⁺,Er³⁺ Nanoparticles by Plasmonic Nanoantenna Arrays. *J. Phys. Chem. C*, 122 (27), **2018**, pp. 15666–15672. doi:[10.1021/acs.jpcc.8b03975](https://doi.org/10.1021/acs.jpcc.8b03975).
- [242] Chen, W.-T. W.-Y., Lin, C.-H., and Chen, W.-T. W.-Y. Plasmonic phase transition and phase retardation: essential optical characteristics of localized surface plasmon resonance. *Nanoscale*, 5 (20), **2013**, pp. 9950–6. doi:[10.1039/c3nr02603e](https://doi.org/10.1039/c3nr02603e).
- [243] Neuman, T., Alonso-González, P., Garcia-Etxarri, A., *et al.* Mapping the near fields of plasmonic nanoantennas by scattering-type scanning near-field optical microscopy. *Laser Photon. Rev.*, 9 (6), **2015**, pp. 637–649. doi:[10.1002/lpor.201500031](https://doi.org/10.1002/lpor.201500031).
- [244] O’Brien, K., Lanzillotti-Kimura, N. D., Suchowski, H., *et al.* Reflective interferometry for optical metamaterial phase measurements. *Opt. Lett.*, 37 (19), **2012**, p. 4089. doi:[10.1364/OL.37.004089](https://doi.org/10.1364/OL.37.004089).
- [245] Gennaro, S. D., Sonnefraud, Y., Verellen, N., *et al.* Spectral interferometric microscopy reveals absorption by individual optical nanoantennas from extinction phase. *Nat. Commun.*, 5 (1), **2014**, p. 3748. doi:[10.1038/ncomms4748](https://doi.org/10.1038/ncomms4748).
- [246] Pshenay-Severin, E., Falkner, M., Helgert, C., and Pertsch, T. Ultra broadband phase measurements on nanostructured metasurfaces. *Appl. Phys. Lett.*, 104 (22), **2014**, p. 221906. doi:[10.1063/1.4881332](https://doi.org/10.1063/1.4881332).
- [247] Meshulach, D., Yelin, D., and Silberberg, Y. Real-time spatial-spectral interference measurements of ultrashort optical pulses. *J. Opt. Soc. Am. B*, 14 (8), **1997**, p. 2095. doi:[10.1364/JOSAB.14.002095](https://doi.org/10.1364/JOSAB.14.002095).
- [248] Dolling, G. Simultaneous Negative Phase and Group Velocity of Light in a Metamaterial. *Science*, 312 (5775), **2006**, pp. 892–894. doi:[10.1126/science.1126021](https://doi.org/10.1126/science.1126021).
- [249] Onishi, S., Matsuishi, K., Oi, J., *et al.* Spatiotemporal control of femtosecond plasmon using plasmon response functions measured by near-field scanning optical microscopy (NSOM). *Opt. Express*, 21 (22), **2013**, p. 26631. doi:[10.1364/OE.21.026631](https://doi.org/10.1364/OE.21.026631).

- [250] Kolman, P. and Chmelík, R. Coherence-controlled holographic microscope. *Opt. Express*, 18 (21), **2010**, p. 21990. doi:[10.1364/OE.18.021990](https://doi.org/10.1364/OE.18.021990).
- [251] Slabý, T., Kolman, P., Dostál, Z., *et al.* Off-axis setup taking full advantage of incoherent illumination in coherence-controlled holographic microscope. *Opt. Express*, 21 (12), **2013**, p. 14747. doi:[10.1364/OE.21.014747](https://doi.org/10.1364/OE.21.014747).
- [252] Lošťák, M., Chmelík, R., Slabá, M., and Slabý, T. Coherence-controlled holographic microscopy in diffuse media. *Opt. Express*, 22 (4), **2014**, p. 4180. doi:[10.1364/OE.22.004180](https://doi.org/10.1364/OE.22.004180).
- [253] Babocký, J., Křížová, A., Štrbková, L., *et al.* Quantitative 3D Phase Imaging of Plasmonic Metasurfaces. *ACS Photonics*, 4 (6), **2017**, pp. 1389–1397. doi:[10.1021/acsp Photonics.7b00022](https://doi.org/10.1021/acsp Photonics.7b00022).
- [254] Hecht, E. *Optics*. Addison-Wesley, 4th edn., 2002, p. 485. ISBN 0-321-18878-0.
- [255] Aieta, F., Genevet, P., Kats, M. a., *et al.* Aberration-free ultrathin flat lenses and axicons at telecom wavelengths based on plasmonic metasurfaces. *Nano Lett.*, 12 (9), **2012**, pp. 4932–4936. doi:[10.1021/nl302516v](https://doi.org/10.1021/nl302516v).
- [256] Zheludev, N. I. and Plum, E. Reconfigurable nanomechanical photonic metamaterials. *Nat. Nanotechnol.*, 11 (1), **2016**, pp. 16–22. doi:[10.1038/nnano.2015.302](https://doi.org/10.1038/nnano.2015.302).
- [257] Ee, H.-S. and Agarwal, R. Tunable Metasurface and Flat Optical Zoom Lens on a Stretchable Substrate. *Nano Lett.*, 16 (4), **2016**, pp. 2818–2823. doi:[10.1021/acs.nanolett.6b00618](https://doi.org/10.1021/acs.nanolett.6b00618).
- [258] Colburn, S., Zhan, A., and Majumdar, A. Varifocal zoom imaging with large area focal length adjustable metalenses. *Optica*, 5 (7), **2018**, p. 825. doi:[10.1364/OPTICA.5.000825](https://doi.org/10.1364/OPTICA.5.000825).
- [259] Zhu, W., Song, Q., Yan, L., *et al.* A Flat Lens with Tunable Phase Gradient by Using Random Access Reconfigurable Metamaterial. *Adv. Mater.*, 27 (32), **2015**, pp. 4739–4743. doi:[10.1002/adma.201501943](https://doi.org/10.1002/adma.201501943).
- [260] Zhao, X., Schalch, J., Zhang, J., *et al.* Electromechanically tunable metasurface transmission waveplate at terahertz frequencies. *Optica*, 5 (3), **2018**, p. 303. doi:[10.1364/OPTICA.5.000303](https://doi.org/10.1364/OPTICA.5.000303).
- [261] Ou, J.-Y., Plum, E., Zhang, J., and Zheludev, N. I. An electromechanically reconfigurable plasmonic metamaterial operating in the near-infrared. *Nat. Nanotechnol.*, 8 (4), **2013**, pp. 252–255. doi:[10.1038/nnano.2013.25](https://doi.org/10.1038/nnano.2013.25).
- [262] Tao, H., Strikwerda, A. C., Fan, K., *et al.* Reconfigurable Terahertz Metamaterials. *Phys. Rev. Lett.*, 103 (14), **2009**, p. 147401. doi:[10.1103/PhysRevLett.103.147401](https://doi.org/10.1103/PhysRevLett.103.147401).
- [263] van de Groep, J. and Brongersma, M. L. Metasurface Mirrors for External Control of Mie Resonances. *Nano Lett.*, 18 (6), **2018**, pp. 3857–3864. doi:[10.1021/acs.nanolett.8b01148](https://doi.org/10.1021/acs.nanolett.8b01148).
- [264] Zheludev, N. I. and Kivshar, Y. S. From metamaterials to metadevices. *Nat. Mater.*, 11 (11), **2012**, pp. 917–924. doi:[10.1038/nmat3431](https://doi.org/10.1038/nmat3431).
- [265] Chen, H.-T., Padilla, W. J., Zide, J. M. O., *et al.* Active terahertz metamaterial devices. *Nature*, 444 (7119), **2006**, pp. 597–600. doi:[10.1038/nature05343](https://doi.org/10.1038/nature05343).
- [266] Feigenbaum, E., Diest, K., and Atwater, H. A. Unity-Order Index Change in Transparent Conducting Oxides at Visible Frequencies. *Nano Lett.*, 10 (6), **2010**, pp. 2111–2116. doi:[10.1021/nl1006307](https://doi.org/10.1021/nl1006307).

- [267] Ma, Z., Li, Z., Liu, K., *et al.* Indium-Tin-Oxide for High-performance Electro-optic Modulation. *Nanophotonics*, 4 (1), **2015**, pp. 198–213. doi:[10.1515/nanoph-2015-0006](https://doi.org/10.1515/nanoph-2015-0006).
- [268] Papasimakis, N., Luo, Z., Shen, Z. X., *et al.* Graphene in a photonic metamaterial. *Opt. Express*, 18 (8), **2010**, pp. 8353–9. doi:[10.1364/OE.18.008353](https://doi.org/10.1364/OE.18.008353).
- [269] Emani, N. K., Chung, T.-F., Kildishev, A. V., *et al.* Electrical Modulation of Fano Resonance in Plasmonic Nanostructures Using Graphene. *Nano Lett.*, 14 (1), **2014**, pp. 78–82. doi:[10.1021/nl403253c](https://doi.org/10.1021/nl403253c).
- [270] Liang, G., Hu, X., Yu, X., *et al.* Integrated Terahertz Graphene Modulator with 100% Modulation Depth. *ACS Photonics*, 2 (11), **2015**, pp. 1559–1566. doi:[10.1021/acsphotonics.5b00317](https://doi.org/10.1021/acsphotonics.5b00317).
- [271] Wuttig, M. and Yamada, N. Phase-change materials for rewriteable data storage. *Nat. Mater.*, 6 (11), **2007**, pp. 824–832. doi:[10.1038/nmat2009](https://doi.org/10.1038/nmat2009).
- [272] Yao, Y., Shankar, R., Kats, M. A., *et al.* Electrically Tunable Metasurface Perfect Absorbers for Ultrathin Mid-Infrared Optical Modulators. *Nano Lett.*, 14 (11), **2014**, pp. 6526–6532. doi:[10.1021/nl503104n](https://doi.org/10.1021/nl503104n).
- [273] Tittl, A., Michel, A.-K. U., Schäferling, M., *et al.* A Switchable Mid-Infrared Plasmonic Perfect Absorber with Multispectral Thermal Imaging Capability. *Adv. Mater.*, 27 (31), **2015**, pp. 4597–4603. doi:[10.1002/adma.201502023](https://doi.org/10.1002/adma.201502023).
- [274] Earl, S. K., James, T. D., Gómez, D. E., *et al.* Switchable polarization rotation of visible light using a plasmonic metasurface. *APL Photonics*, 2 (1), **2017**, p. 016103. doi:[10.1063/1.4968840](https://doi.org/10.1063/1.4968840).
- [275] Dicken, M. J., Aydin, K., Pryce, I. M., *et al.* Frequency tunable near-infrared metamaterials based on VO₂ phase transition. *Opt. Express*, 17 (20), **2009**, pp. 18330–18339. doi:[10.1364/OE.17.018330](https://doi.org/10.1364/OE.17.018330).
- [276] Wang, Q., Rogers, E. T. F., Gholipour, B., *et al.* Optically reconfigurable metasurfaces and photonic devices based on phase change materials. *Nat. Photonics*, 10 (1), **2015**, pp. 60–65. doi:[10.1038/nphoton.2015.247](https://doi.org/10.1038/nphoton.2015.247).
- [277] Rensberg, J., Zhang, S., Zhou, Y., *et al.* Active Optical Metasurfaces Based on Defect-Engineered Phase-Transition Materials. *Nano Lett.*, 16 (2), **2016**, pp. 1050–1055. doi:[10.1021/acs.nanolett.5b04122](https://doi.org/10.1021/acs.nanolett.5b04122).
- [278] Karvounis, A., Gholipour, B., MacDonald, K. F., and Zheludev, N. I. All-dielectric phase-change reconfigurable metasurface. *Appl. Phys. Lett.*, 109 (5), **2016**, p. 051103. doi:[10.1063/1.4959272](https://doi.org/10.1063/1.4959272).
- [279] Chu, C. H., Tseng, M. L., Chen, J., *et al.* Active dielectric metasurface based on phase-change medium. *Laser Photonics Rev.*, 10 (6), **2016**, pp. 986–994. doi:[10.1002/lpor.201600106](https://doi.org/10.1002/lpor.201600106).
- [280] Ke, Y., Wen, X., Zhao, D., *et al.* Controllable Fabrication of Two-Dimensional Patterned VO₂ Nanoparticle, Nanodome, and Nanonet Arrays with Tunable Temperature-Dependent Localized Surface Plasmon Resonance. *ACS Nano*, 11 (7), **2017**, pp. 7542–7551. doi:[10.1021/acsnano.7b02232](https://doi.org/10.1021/acs.nano.7b02232).
- [281] Edwards, P., Kuznetsov, V., Slocombe, D., and Vijayaraghavan, R. The Electronic Structure and Properties of Solids. In *Compr. Inorg. Chem. II*, pp. 153–176. Elsevier, 2013. doi:[10.1016/B978-0-08-097774-4.00408-3](https://doi.org/10.1016/B978-0-08-097774-4.00408-3).

- [282] Yang, Z., Ko, C., and Ramanathan, S. Oxide Electronics Utilizing Ultrafast Metal-Insulator Transitions. *Annu. Rev. Mater. Res.*, 41 (1), **2011**, pp. 337–367. doi:[10.1146/annurev-matsci-062910-100347](https://doi.org/10.1146/annurev-matsci-062910-100347).
- [283] Morin, F. J. Oxides Which Show a Metal-to-Insulator Transition at the Neel Temperature. *Phys. Rev. Lett.*, 3 (1), **1959**, pp. 34–36. doi:[10.1103/PhysRevLett.3.34](https://doi.org/10.1103/PhysRevLett.3.34).
- [284] Rao, C. N. R. Virtues of marginally metallic oxides. *Chem. Commun.*, 19 (1), **1996**, p. 2217. doi:[10.1039/cc9960002217](https://doi.org/10.1039/cc9960002217).
- [285] Tokura, Y. Correlated-Electron Physics in Transition-Metal Oxides. *Phys. Today*, 56 (7), **2003**, pp. 50–55. doi:[10.1063/1.1603080](https://doi.org/10.1063/1.1603080).
- [286] Eyert, V. The metal-insulator transitions of VO₂: A band theoretical approach. *Ann. Phys.*, 11 (9), **2002**, pp. 650–704. doi:[10.1002/1521-3889\(200210\)11:9<650::AID-ANDP650>3.0.CO;2-K](https://doi.org/10.1002/1521-3889(200210)11:9<650::AID-ANDP650>3.0.CO;2-K).
- [287] Aetukuri, N. B., Gray, A. X., Drouard, M., *et al.* Control of the metal–insulator transition in vanadium dioxide by modifying orbital occupancy. *Nat. Phys.*, 9 (10), **2013**, pp. 661–666. doi:[10.1038/nphys2733](https://doi.org/10.1038/nphys2733).
- [288] Goodenough, J. B. The two components of the crystallographic transition in VO₂. *J. Solid State Chem.*, 3 (4), **1971**, pp. 490–500. doi:[10.1016/0022-4596\(71\)90091-0](https://doi.org/10.1016/0022-4596(71)90091-0).
- [289] Imada, M., Fujimori, A., and Tokura, Y. Metal-insulator transitions. *Rev. Mod. Phys.*, 70 (4), **1998**, pp. 1039–1263. doi:[10.1103/RevModPhys.70.1039](https://doi.org/10.1103/RevModPhys.70.1039).
- [290] Huffman, T. J., Hendriks, C., Walter, E. J., *et al.* Insulating phases of vanadium dioxide are Mott-Hubbard insulators. *Phys. Rev. B*, 95 (7), **2017**, p. 075125. doi:[10.1103/PhysRevB.95.075125](https://doi.org/10.1103/PhysRevB.95.075125).
- [291] Strelcov, E., Davydov, A. V., Lanke, U., *et al.* In situ monitoring of the growth, intermediate phase transformations and templating of single crystal VO₂ nanowires and nanoplatelets. *ACS Nano*, 5 (4), **2011**, pp. 3373–3384. doi:[10.1021/nn2007089](https://doi.org/10.1021/nn2007089).
- [292] Kim, D. H. and Kwok, H. S. Pulsed laser deposition of VO₂ thin films. *Appl. Phys. Lett.*, 65 (25), **1994**, pp. 3188–3190. doi:[10.1063/1.112476](https://doi.org/10.1063/1.112476).
- [293] Maruyama, T. and Ikuta, Y. Vanadium dioxide thin films prepared by chemical vapour deposition from vanadium(III) acetylacetonate. *J. Mater. Sci.*, 28 (18), **1993**, pp. 5073–5078. doi:[10.1007/BF00361182](https://doi.org/10.1007/BF00361182).
- [294] Nag, J. and Haglund Jr, R. F. Synthesis of vanadium dioxide thin films and nanoparticles. *J. Phys. Condens. Matter*, 20 (26), **2008**, p. 264016. doi:[10.1088/0953-8984/20/26/264016](https://doi.org/10.1088/0953-8984/20/26/264016).
- [295] Chae, B.-G., Kim, H.-T., Yun, S.-J., *et al.* Highly Oriented VO₂ Thin Films Prepared by Sol-Gel Deposition. *Electrochem. Solid-State Lett.*, 9 (1), **2006**, p. C12. doi:[10.1149/1.2135430](https://doi.org/10.1149/1.2135430).
- [296] Marvel, R. E., Appavoo, K., Choi, B. K., *et al.* Electron-beam deposition of vanadium dioxide thin films. *Appl. Phys. A*, 111 (3), **2013**, pp. 975–981. doi:[10.1007/s00339-012-7324-5](https://doi.org/10.1007/s00339-012-7324-5).
- [297] Lei, D. Y., Appavoo, K., Ligmajer, F., *et al.* Optically-Triggered Nanoscale Memory Effect in a Hybrid Plasmonic-Phase Changing Nanostructure. *ACS Photonics*, 2 (9), **2015**, pp. 1306–1313. doi:[10.1021/acsp Photonics.5b00249](https://doi.org/10.1021/acsp Photonics.5b00249).

- [298] Qazilbash, M. M., Brehm, M., Chae, B.-G., *et al.* Mott Transition in VO₂ Revealed by Infrared Spectroscopy and Nano-Imaging. *Science*, 318 (5857), **2007**, pp. 1750–1753. doi:[10.1126/science.1150124](https://doi.org/10.1126/science.1150124).
- [299] Driscoll, T., Kim, H.-T., Chae, B.-G., *et al.* Phase-transition driven memristive system. *Appl. Phys. Lett.*, 95 (4), **2009**, p. 043503. doi:[10.1063/1.3187531](https://doi.org/10.1063/1.3187531).
- [300] Cavalleri, A., Dekorsy, T., Chong, H. H. W., *et al.* Evidence for a structurally-driven insulator-to-metal transition in VO₂: A view from the ultrafast timescale. *Phys. Rev. B*, 70 (16), **2004**, p. 161102. doi:[10.1103/PhysRevB.70.161102](https://doi.org/10.1103/PhysRevB.70.161102).
- [301] Dönges, S. A., Khatib, O., O’Callahan, B. T., *et al.* Ultrafast Nanoimaging of the Photoinduced Phase Transition Dynamics in VO₂. *Nano Lett.*, 16 (5), **2016**, pp. 3029–3035. doi:[10.1021/acs.nanolett.5b05313](https://doi.org/10.1021/acs.nanolett.5b05313).
- [302] Marvel, R. E., Harl, R. R., Craciun, V., *et al.* Influence of deposition process and substrate on the phase transition of vanadium dioxide thin films. *Acta Mater.*, 91, **2015**, pp. 217–226. doi:[10.1016/j.actamat.2015.03.009](https://doi.org/10.1016/j.actamat.2015.03.009).
- [303] Guiton, B. S., Gu, Q., Prieto, A. L., *et al.* Single-crystalline vanadium dioxide nanowires with rectangular cross sections. *J. Am. Chem. Soc.*, 127 (2), **2005**, pp. 498–499. doi:[10.1021/ja045976g](https://doi.org/10.1021/ja045976g).
- [304] Zhang, J., Jin, H., Chen, Z., *et al.* Self-Assembling VO₂ Nanonet with High Switching Performance at Wafer-Scale. *Chem. Mater.*, 27 (21), **2015**, pp. 7419–7424. doi:[10.1021/acs.chemmater.5b03314](https://doi.org/10.1021/acs.chemmater.5b03314).
- [305] Cheng, Y., Wong, T., Ho, K., and Wang, N. The structure and growth mechanism of VO₂ nanowires. *J. Cryst. Growth*, 311 (6), **2009**, pp. 1571–1575. doi:[10.1016/j.jcrysgro.2009.01.002](https://doi.org/10.1016/j.jcrysgro.2009.01.002).
- [306] Ligmajer, F., Kejík, L., Tiwari, U., *et al.* Epitaxial VO₂ Nanostructures: A Route to Large-Scale, Switchable Dielectric Metasurfaces. *ACS Photonics*, 5 (7), **2018**, pp. 2561–2567. doi:[10.1021/acsphotonics.7b01384](https://doi.org/10.1021/acsphotonics.7b01384).
- [307] Zhang, H., Chang, H., Guo, J., and Zhang, T. Microstructure of epitaxial VO₂ thin films deposited on (1120) sapphire by MOCVD. *J. Mater. Res.*, 9 (09), **1994**, pp. 2264–2271. doi:[10.1557/JMR.1994.2264](https://doi.org/10.1557/JMR.1994.2264).
- [308] Kana Kana, J., Ndjaka, J., Vignaud, G., *et al.* Thermally tunable optical constants of vanadium dioxide thin films measured by spectroscopic ellipsometry. *Opt. Commun.*, 284 (3), **2011**, pp. 807–812. doi:[10.1016/j.optcom.2010.10.009](https://doi.org/10.1016/j.optcom.2010.10.009).
- [309] Whitaker, J. C. (ed.). *The Electronics Handbook*. CRC Press, 2nd edn., 2005, p. 881. ISBN 9780849318894.
- [310] Reed, G. T., Mashanovich, G., Gardes, F. Y., and Thomson, D. J. Silicon optical modulators. *Nat. Photonics*, 4 (8), **2010**, pp. 518–526. doi:[10.1038/nphoton.2010.179](https://doi.org/10.1038/nphoton.2010.179).
- [311] Liu, Q. and Liu, M. Circular-polarization modulator. *Nat. Photonics*, 11 (10), **2017**, pp. 614–616. doi:[10.1038/s41566-017-0015-1](https://doi.org/10.1038/s41566-017-0015-1).
- [312] Gopalakrishnan, G., Ruzmetov, D., and Ramanathan, S. On the triggering mechanism for the metal–insulator transition in thin film VO₂ devices: electric field versus thermal effects. *J. Mater. Sci.*, 44 (19), **2009**, pp. 5345–5353. doi:[10.1007/s10853-009-3442-7](https://doi.org/10.1007/s10853-009-3442-7).

- [313] Jeong, J., Aetukuri, N., Graf, T., *et al.* Suppression of Metal-Insulator Transition in VO₂ by Electric Field-Induced Oxygen Vacancy Formation. *Science*, 339 (6126), **2013**, pp. 1402–1405. doi:[10.1126/science.1230512](https://doi.org/10.1126/science.1230512).
- [314] Verleur, H. W., Barker, A. S., and Berglund, C. N. Optical Properties of VO₂ between 0.25 and 5 eV. *Rev. Mod. Phys.*, 172 (3), **1968**, pp. 788–798. doi:[10.1103/RevModPhys.40.737](https://doi.org/10.1103/RevModPhys.40.737).
- [315] Rechberger, W., Hohenau, a., Leitner, a., *et al.* Optical properties of two interacting gold nanoparticles. *Opt. Commun.*, 220 (1-3), **2003**, pp. 137–141. doi:[10.1016/S0030-4018\(03\)01357-9](https://doi.org/10.1016/S0030-4018(03)01357-9).
- [316] Kakiuchida, H., Jin, P., Nakao, S., and Tazawa, M. Optical Properties of Vanadium Dioxide Film during Semiconductive–Metallic Phase Transition. *Jpn. J. Appl. Phys.*, 46 (No. 5), **2007**, pp. L113–L116. doi:[10.1143/JJAP.46.L113](https://doi.org/10.1143/JJAP.46.L113).
- [317] Bagotsky, V. S. *Fundamentals of Electrochemistry*. Wiley, 2006, p. 191. ISBN 13 978-0-471-70058-6.
- [318] Wu, L., Xiong, E., Zhang, X., *et al.* Nanomaterials as signal amplification elements in DNA-based electrochemical sensing. *Nano Today*, 9 (2), **2014**, pp. 197–211. doi:[10.1016/j.nantod.2014.04.002](https://doi.org/10.1016/j.nantod.2014.04.002).
- [319] Mehrgardi, M. a. and Ahangar, L. E. Silver nanoparticles as redox reporters for the amplified electrochemical detection of the single base mismatches. *Biosens. Bioelectron.*, 26 (11), **2011**, pp. 4308–4313. doi:[10.1016/j.bios.2011.04.020](https://doi.org/10.1016/j.bios.2011.04.020).
- [320] She, G., Huang, X., Jin, L., *et al.* SnO₂ Nanoparticle-Coated ZnO Nanotube Arrays for High-Performance Electrochemical Sensors. *Small*, 10 (22), **2014**, pp. 4685–4692. doi:[10.1002/sml.201401471](https://doi.org/10.1002/sml.201401471).
- [321] Takahiro, K., Naya, S.-i., and Tada, H. Highly Active Supported Plasmonic Photocatalyst Consisting of Gold Nanoparticle-Loaded Mesoporous Titanium(IV) Oxide Overlay and Conducting Substrate. *J. Phys. Chem. C*, 118 (46), **2014**, pp. 26887–26893. doi:[10.1021/jp5094542](https://doi.org/10.1021/jp5094542).
- [322] Wang, J. *Analytical Electrochemistry*. Wiley, 2006, pp. 1–250. ISBN 9780471790303. doi:[10.1002/0471790303](https://doi.org/10.1002/0471790303).
- [323] Batchelor-Mcauley, C., Dickinson, E. J. F., Rees, N. V., *et al.* New electrochemical methods. *Anal. Chem.*, 84 (2), **2012**, pp. 669–684. doi:[10.1021/ac2026767](https://doi.org/10.1021/ac2026767).
- [324] Atkins, P. *Four Laws That Drive the Universe*. Oxford University Press, 2007. ISBN 978-0199232369.
- [325] Atkins, P. and de Paula, J. *Atkins' Physical Chemistry*. OUP Oxford, 8th edn., 2010. ISBN 9780199543373.
- [326] Compton, R. G., Laborda, E., and Ward, K. R. *Understanding Voltammetry: Simulation of Electrode Processes*. Imperial College Press, 2014. ISBN 978-1-78326-323-3.
- [327] Bevan, K. H., Hossain, M. S., Iqbal, A., and Wang, Z. Exploring Bridges between Quantum Transport and Electrochemistry. I. *J. Phys. Chem. C*, 120 (1), **2016**, pp. 179–187. doi:[10.1021/acs.jpcc.5b09653](https://doi.org/10.1021/acs.jpcc.5b09653).
- [328] Compton, R. G. and Banks, C. *Understanding Voltammetry*. Imperial College Press, 2010, pp. 1–34. ISBN 978-1-84816-585-4.

- [329] Conway, B. E., Bockris, J. O., Yeager, E., *et al.* (eds.). *Comprehensive Treatise of Electrochemistry: Volume 7 - Kinetics and Mechanisms of Electrode Processes*. Springer, 1983, p. 539. ISBN 978-1-4613-3586-3.
- [330] Morisaki, H. Electronic State Densities of Aquo-Complex Ions in Water Determined by Electrochemical Tunneling Spectroscopy. *J. Electrochem. Soc.*, 136 (6), **1989**, p. 1710. doi:[10.1149/1.2096997](https://doi.org/10.1149/1.2096997).
- [331] Bard, A. J. and Faulkner, L. R. *Electrochemical Methods: Fundamentals and Applications*. Wiley, 2nd edn., 2001, p. 25. ISBN 0-471-04372-9.
- [332] Faulkner, L. R. Electrochemical Characterization of Chemical Systems. In *Phys. Methods Mod. Chem. Anal.*, p. 235. Elsevier, 1983. doi:[10.1016/B978-0-12-430803-9.50018-5](https://doi.org/10.1016/B978-0-12-430803-9.50018-5).
- [333] Henglein, A. Physicochemical properties of small metal particles in solution: "microelectrode" reactions, chemisorption, composite metal particles, and the atom-to-metal transition. *J. Phys. Chem.*, 97 (21), **1993**, pp. 5457–5471. doi:[10.1021/j100123a004](https://doi.org/10.1021/j100123a004).
- [334] Mulvaney, P. Surface Plasmon Spectroscopy of Nanosized Metal Particles. *Langmuir*, 12 (3), **1996**, pp. 788–800. doi:[10.1021/la9502711](https://doi.org/10.1021/la9502711).
- [335] Mulvaney, P., Pérez-Juste, J., Giersig, M., *et al.* Drastic surface plasmon mode shifts in gold nanorods due to electron charging. *Plasmonics*, 1 (1), **2006**, pp. 61–66. doi:[10.1007/s11468-005-9005-0](https://doi.org/10.1007/s11468-005-9005-0).
- [336] Christensen, P. and Hamnett, A. In-situ techniques in electrochemistry — ellipsometry and FTIR. *Electrochim. Acta*, 45 (15-16), **2000**, pp. 2443–2459. doi:[10.1016/S0013-4686\(00\)00332-7](https://doi.org/10.1016/S0013-4686(00)00332-7).
- [337] Cortés, E., Etchegoin, P. G., Le Ru, E. C., *et al.* Monitoring the electrochemistry of single molecules by surface-enhanced Raman spectroscopy. *J. Am. Chem. Soc.*, 132 (51), **2010**, pp. 18034–18037. doi:[10.1021/ja108989b](https://doi.org/10.1021/ja108989b).
- [338] Yuan, T., Le Thi Ngoc, L., Van Nieuwkastele, J., *et al.* In situ surface-enhanced Raman spectroelectrochemical analysis system with a hemin modified nanostructured gold surface. *Anal. Chem.*, 87 (5), **2015**, pp. 2588–2592. doi:[10.1021/ac504136j](https://doi.org/10.1021/ac504136j).
- [339] Zaleski, S., Cardinal, M. F., Klingsporn, J. M., and Van Duyne, R. P. Observing Single, Heterogeneous, One-Electron Transfer Reactions. *J. Phys. Chem. C*, 119 (50), **2015**, pp. 28226–28234. doi:[10.1021/acs.jpcc.5b10652](https://doi.org/10.1021/acs.jpcc.5b10652).
- [340] Wilson, A. J. and Willets, K. A. Visualizing Site-Specific Redox Potentials on the Surface of Plasmonic Nanoparticle Aggregates with Superlocalization SERS Microscopy. *Nano Lett.*, 14 (2), **2014**, pp. 939–945. doi:[10.1021/nl404347a](https://doi.org/10.1021/nl404347a).
- [341] Liu, J., Hill, C. M., Pan, S., and Liu, H. Interfacial charge transfer events of BODIPY molecules: single molecule spectroelectrochemistry and substrate effects. *Phys. Chem. Chem. Phys.*, 16 (42), **2014**, pp. 23150–23156. doi:[10.1039/C4CP02950J](https://doi.org/10.1039/C4CP02950J).
- [342] Ung, T., Giersig, M., Dunstan, D., and Mulvaney, P. Spectroelectrochemistry of colloidal silver. *Langmuir*, 13 (6), **1997**, pp. 1773–1782. doi:[10.1021/la960863z](https://doi.org/10.1021/la960863z).
- [343] Chapman, R. and Mulvaney, P. Electro-optical shifts in silver nanoparticle films. *Chem. Phys. Lett.*, 349 (5-6), **2001**, pp. 358–362. doi:[10.1016/S0009-2614\(01\)01145-9](https://doi.org/10.1016/S0009-2614(01)01145-9).

- [344] Novo, C., Funston, A. M., and Mulvaney, P. Direct observation of chemical reactions on single gold nanocrystals using surface plasmon spectroscopy. *Nat. Nanotechnol.*, 3 (10), **2008**, pp. 598–602. doi:[10.1038/nnano.2008.246](https://doi.org/10.1038/nnano.2008.246).
- [345] Jain, P. K., Manthiram, K., Engel, J. H., *et al.* Doped nanocrystals as plasmonic probes of redox chemistry. *Angew. Chemie Int. Ed.*, 52 (51), **2013**, pp. 13671–13675. doi:[10.1002/anie.201303707](https://doi.org/10.1002/anie.201303707).
- [346] Sannomiya, T., Dermutz, H., Hafner, C., *et al.* Electrochemistry on a Localized Surface Plasmon Resonance Sensor. *Langmuir*, 26 (10), **2010**, pp. 7619–7626. doi:[10.1021/la9042342](https://doi.org/10.1021/la9042342).
- [347] Dahlin, A. B., Dielacher, B., Rajendran, P., *et al.* Electrochemical plasmonic sensors. *Anal. Bioanal. Chem.*, 402 (5), **2012**, pp. 1773–1784. doi:[10.1007/s00216-011-5404-6](https://doi.org/10.1007/s00216-011-5404-6).
- [348] Novo, C., Funston, A. M., Gooding, A. K., and Mulvaney, P. Electrochemical Charging of Single Gold Nanorods. *J. Am. Chem. Soc.*, 131 (41), **2009**, pp. 14664–14666. doi:[10.1021/ja905216h](https://doi.org/10.1021/ja905216h).
- [349] Chirea, M., Collins, S. S. E., Wei, X., and Mulvaney, P. Supporting Information for : Spectroelectrochemistry of Silver Deposition on Single Gold Nanocrystals. *J. Phys. Chem. Lett.*, 5 (24), **2014**, pp. 4331–4335. doi:[10.1021/jz502349x](https://doi.org/10.1021/jz502349x).
- [350] Hill, C. M., Bennett, R., Zhou, C., *et al.* Single Ag Nanoparticle Spectroelectrochemistry via Dark Field Scattering and Fluorescence Microscopies. *J. Phys. Chem. C*, 119 (12), **2015**, p. 150302101608005. doi:[10.1021/jp511637a](https://doi.org/10.1021/jp511637a).
- [351] Byers, C. P., Hoener, B. S., Chang, W.-S. S., *et al.* Single-Particle Plasmon Voltammetry (spPV) for Detecting Anion Adsorption. *Nano Lett.*, 16 (4), **2016**, pp. 2314–2321. doi:[10.1021/acs.nanolett.5b04990](https://doi.org/10.1021/acs.nanolett.5b04990).
- [352] Hoener, B. S., Zhang, H., Heiderscheit, T. S., *et al.* Spectral Response of Plasmonic Gold Nanoparticles to Capacitive Charging: Morphology Effects. *J. Phys. Chem. Lett.*, 8 (12), **2017**, pp. 2681–2688. doi:[10.1021/acs.jpcclett.7b00945](https://doi.org/10.1021/acs.jpcclett.7b00945).
- [353] Sundaresan, V., Monaghan, J. W., and Willets, K. A. Visualizing the Effect of Partial Oxide Formation on Single Silver Nanoparticle Electrodissolution. *J. Phys. Chem. C*, 122 (5), **2018**, pp. 3138–3145. doi:[10.1021/acs.jpcc.7b11824](https://doi.org/10.1021/acs.jpcc.7b11824).
- [354] Nozik, A. J. Photoelectrochemistry: Applications to Solar Energy Conversion. *Annu. Rev. Phys. Chem.*, 29 (1), **1978**, pp. 189–222. doi:[10.1146/annurev.pc.29.100178.001201](https://doi.org/10.1146/annurev.pc.29.100178.001201).
- [355] Memming, R. Photoelectrochemical solar energy conversion. In *Electrochem. II*, pp. 79–112. Springer-Verlag, Berlin/Heidelberg, 2005. doi:[10.1007/BFb0018072](https://doi.org/10.1007/BFb0018072).
- [356] Hou, W. and Cronin, S. B. A review of surface plasmon resonance-enhanced photocatalysis. *Adv. Funct. Mater.*, 23 (13), **2013**, pp. 1612–1619. doi:[10.1002/adfm.201202148](https://doi.org/10.1002/adfm.201202148).
- [357] Brus, L. Noble Metal Nanocrystals: Plasmon Electron Transfer Photochemistry and Single-Molecule Raman Spectroscopy. *Acc. Chem. Res.*, 41 (12), **2008**, pp. 1742–1749. doi:[10.1021/ar800121r](https://doi.org/10.1021/ar800121r).
- [358] Nishijima, Y., Ueno, K., Kotake, Y., *et al.* Near-Infrared Plasmon-Assisted Water Oxidation. *J. Phys. Chem. Lett.*, 3 (10), **2012**, pp. 1248–1252. doi:[10.1021/jz3003316](https://doi.org/10.1021/jz3003316).
- [359] Xiao, M., Jiang, R., Wang, F., *et al.* Plasmon-enhanced chemical reactions. *J. Mater. Chem. A*, 1 (19), **2013**, p. 5790. doi:[10.1039/c3ta01450a](https://doi.org/10.1039/c3ta01450a).

- [360] Mubeen, S., Lee, J., Singh, N., *et al.* An autonomous photosynthetic device in which all charge carriers derive from surface plasmons. *Nat. Nanotechnol.*, 8 (4), **2013**, pp. 247–251. doi:[10.1038/nnano.2013.18](https://doi.org/10.1038/nnano.2013.18).
- [361] Zhang, H. and Govorov, a. O. Giant circular dichroism of a molecule in a region of strong plasmon resonances between two neighboring gold nanocrystals. *Phys. Rev. B*, 87 (7), **2013**, p. 075410. doi:[10.1103/PhysRevB.87.075410](https://doi.org/10.1103/PhysRevB.87.075410).
- [362] Cortés, E., Xie, W., Cambiasso, J., *et al.* Plasmonic hot electron transport drives nano-localized chemistry. *Nat. Commun.*, 8, **2017**, p. 14880. doi:[10.1038/ncomms14880](https://doi.org/10.1038/ncomms14880).
- [363] Teoh, W. Y., Scott, J. A., and Amal, R. Progress in heterogeneous photocatalysis: From classical radical chemistry to engineering nanomaterials and solar reactors. *J. Phys. Chem. Lett.*, 3 (5), **2012**, pp. 629–639. doi:[10.1021/jz3000646](https://doi.org/10.1021/jz3000646).
- [364] Zheng, B. Y., Zhao, H., Manjavacas, A., *et al.* Distinguishing between plasmon-induced and photoexcited carriers in a device geometry. *Nat. Commun.*, 6 (1), **2015**, p. 7797. doi:[10.1038/ncomms8797](https://doi.org/10.1038/ncomms8797).
- [365] Tian, Y. and Tatsuma, T. Mechanisms and Applications of Plasmon-Induced Charge Separation at TiO₂ Films Loaded with Gold Nanoparticles. *J. Am. Chem. Soc.*, 127 (20), **2005**, pp. 7632–7637. doi:[10.1021/ja042192u](https://doi.org/10.1021/ja042192u).
- [366] Nishijima, Y., Ueno, K., Yokota, Y., *et al.* Plasmon-Assisted Photocurrent Generation from Visible to Near-Infrared Wavelength Using a Au-Nanorods/TiO₂ Electrode. *J. Phys. Chem. Lett.*, 1 (13), **2010**, pp. 2031–2036. doi:[10.1021/jz1006675](https://doi.org/10.1021/jz1006675).
- [367] Ng, C., Cadusch, J. J., Dligatch, S., *et al.* Hot Carrier Extraction with Plasmonic Broadband Absorbers. *ACS Nano*, 10 (4), **2016**, pp. 4704–4711. doi:[10.1021/acsnano.6b01108](https://doi.org/10.1021/acs.nano.6b01108).
- [368] Wang, Q. H., Kalantar-Zadeh, K., Kis, A., *et al.* Electronics and optoelectronics of two-dimensional transition metal dichalcogenides. *Nat. Nanotechnol.*, 7 (11), **2012**, pp. 699–712. doi:[10.1038/nnano.2012.193](https://doi.org/10.1038/nnano.2012.193).
- [369] Chhowalla, M., Shin, H. S., Eda, G., *et al.* The chemistry of two-dimensional layered transition metal dichalcogenide nanosheets. *Nat. Chem.*, 5 (4), **2013**, pp. 263–275. doi:[10.1038/nchem.1589](https://doi.org/10.1038/nchem.1589).
- [370] Castellanos-Gomez, A. Why all the fuss about 2D semiconductors? *Nat. Photonics*, 10 (4), **2016**, pp. 202–204. doi:[10.1038/nphoton.2016.53](https://doi.org/10.1038/nphoton.2016.53).
- [371] Manzeli, S., Ovchinnikov, D., Pasquier, D., *et al.* 2D transition metal dichalcogenides. *Nat. Rev. Mater.*, 2 (8), **2017**, p. 17033. doi:[10.1038/natrevmats.2017.33](https://doi.org/10.1038/natrevmats.2017.33).
- [372] Kuc, A., Zibouche, N., and Heine, T. Influence of quantum confinement on the electronic structure of the transition metal sulfide TS₂. *Phys. Rev. B*, 83 (24), **2011**, p. 245213. doi:[10.1103/PhysRevB.83.245213](https://doi.org/10.1103/PhysRevB.83.245213).
- [373] Mak, K. F., Lee, C., Hone, J., *et al.* Atomically Thin MoS₂: A New Direct-Gap Semiconductor. *Phys. Rev. Lett.*, 105 (13), **2010**, p. 136805. doi:[10.1103/PhysRevLett.105.136805](https://doi.org/10.1103/PhysRevLett.105.136805).
- [374] Mak, K. F. and Shan, J. Photonics and optoelectronics of 2D semiconductor transition metal dichalcogenides. *Nat. Photonics*, 10 (4), **2016**, pp. 216–226. doi:[10.1038/nphoton.2015.282](https://doi.org/10.1038/nphoton.2015.282).
- [375] Xu, X., Yao, W., Xiao, D., and Heinz, T. F. Spin and pseudospins in layered transition metal dichalcogenides. *Nat. Phys.*, 10 (5), **2014**, pp. 343–350. doi:[10.1038/nphys2942](https://doi.org/10.1038/nphys2942).

- [376] Radisavljevic, B., Radenovic, A., Brivio, J., *et al.* Single-layer MoS₂ transistors. *Nat. Nanotechnol.*, 6 (3), **2011**, pp. 147–150. doi:[10.1038/nnano.2010.279](https://doi.org/10.1038/nnano.2010.279).
- [377] Schaibley, J. R., Yu, H., Clark, G., *et al.* Valleytronics in 2D materials. *Nat. Rev. Mater.*, 1 (11), **2016**, p. 16055. doi:[10.1038/natrevmats.2016.55](https://doi.org/10.1038/natrevmats.2016.55).
- [378] Chia, X., Eng, A. Y. S., Ambrosi, A., *et al.* Electrochemistry of Nanostructured Layered Transition-Metal Dichalcogenides. *Chem. Rev.*, 115 (21), **2015**, pp. 11941–11966. doi:[10.1021/acs.chemrev.5b00287](https://doi.org/10.1021/acs.chemrev.5b00287).
- [379] Velický, M., Bissett, M. A., Woods, C. R., *et al.* Photoelectrochemistry of Pristine Mono- and Few-Layer MoS₂. *Nano Lett.*, 16 (3), **2016**, pp. 2023–2032. doi:[10.1021/acs.nanolett.5b05317](https://doi.org/10.1021/acs.nanolett.5b05317).
- [380] Pumera, M. and Loo, A. H. Layered transition-metal dichalcogenides (MoS₂ and WS₂) for sensing and biosensing. *TrAC Trends Anal. Chem.*, 61, **2014**, pp. 49–53. doi:[10.1016/j.trac.2014.05.009](https://doi.org/10.1016/j.trac.2014.05.009).
- [381] Sarkar, D., Xie, X., Kang, J., *et al.* Functionalization of Transition Metal Dichalcogenides with Metallic Nanoparticles: Implications for Doping and Gas-Sensing. *Nano Lett.*, 15 (5), **2015**, pp. 2852–2862. doi:[10.1021/nl504454u](https://doi.org/10.1021/nl504454u).
- [382] Zhang, J., Liu, S., Liang, H., *et al.* Hierarchical Transition-Metal Dichalcogenide Nanosheets for Enhanced Electrocatalytic Hydrogen Evolution. *Adv. Mater.*, 27 (45), **2015**, pp. 7426–7431. doi:[10.1002/adma.201502765](https://doi.org/10.1002/adma.201502765).
- [383] Ghorbani-Asl, M., Zibouche, N., Wahiduzzaman, M., *et al.* Electromechanics in MoS₂ and WS₂: nanotubes vs. monolayers. *Sci. Rep.*, 3 (1), **2013**, p. 2961. doi:[10.1038/srep02961](https://doi.org/10.1038/srep02961).
- [384] Zak, A., Ecker, L. S., Efrati, R., *et al.* Large-scale Synthesis of WS₂ Multiwall Nanotubes and their Dispersion, an Update. *Sensors Transducers J.*, 12 (October), **2011**, pp. 1–10.
- [385] Shahar, C., Levi, R., Cohen, S. R., and Tenne, R. Gold Nanoparticles as Surface Defect Probes for WS₂ Nanostructures. *J. Phys. Chem. Lett.*, 1 (2), **2010**, pp. 540–543. doi:[10.1021/jz900332h](https://doi.org/10.1021/jz900332h).
- [386] Polyakov, A. Y., Yadgarov, L., Popovitz-Biro, R., *et al.* Decoration of WS₂ Nanotubes and Fullerene-Like MoS₂ with Gold Nanoparticles. *J. Phys. Chem. C*, 118 (4), **2014**, pp. 2161–2169. doi:[10.1021/jp407388h](https://doi.org/10.1021/jp407388h).
- [387] Chen, P. and McCreery, R. L. Control of Electron Transfer Kinetics at Glassy Carbon Electrodes by Specific Surface Modification. *Anal. Chem.*, 68 (22), **1996**, pp. 3958–3965. doi:[10.1021/ac960492r](https://doi.org/10.1021/ac960492r).
- [388] McCreery, R. L. Advanced Carbon Electrode Materials for Molecular Electrochemistry. *Chem. Rev.*, 108 (7), **2008**, pp. 2646–2687. doi:[10.1021/cr068076m](https://doi.org/10.1021/cr068076m).
- [389] Benck, J. D., Pinaud, B. A., Gorlin, Y., and Jaramillo, T. F. Substrate selection for fundamental studies of electrocatalysts and photoelectrodes: Inert potential windows in acidic, neutral, and basic electrolyte. *PLoS One*, 9 (10), **2014**. doi:[10.1371/journal.pone.0107942](https://doi.org/10.1371/journal.pone.0107942).
- [390] Mampallil, D., Mathwig, K., Kang, S., and Lemay, S. G. Reversible adsorption of outer-sphere redox molecules at Pt electrodes. *J. Phys. Chem. Lett.*, 5 (3), **2014**, pp. 636–640. doi:[10.1021/jz402592n](https://doi.org/10.1021/jz402592n).

- [391] Kostiuchenko, Z. A., Glazer, P. J., Mendes, E., and Lemay, S. G. Chemical physics of electroactive materials – the oft-overlooked faces of electrochemistry. *Faraday Discuss.*, 199, **2017**, pp. 9–28. doi:[10.1039/C7FD00117G](https://doi.org/10.1039/C7FD00117G).
- [392] Jing, C., Rawson, F. J., Zhou, H., *et al.* New insights into electrocatalysis based on plasmon resonance for the real-time monitoring of catalytic events on single gold nanorods. *Anal. Chem.*, 86 (11), **2014**, pp. 5513–5518. doi:[10.1021/ac500785u](https://doi.org/10.1021/ac500785u).
- [393] Koryta, J., Dvořák, J., and Kavan, L. *Principles of Electrochemistry*. Wiley, 2nd edn., 1993, p. 249. ISBN 0-471-93838-6.
- [394] Brett, C. M. A. and Brett, A. M. O. *Electrochemistry: Principles, Methods, and Applications*. Oxford University Press, 1993. ISBN 978-0198553885.
- [395] Voldman, A., Zbaida, D., Cohen, H., *et al.* A Nanocomposite of Polyaniline/Inorganic Nanotubes. *Macromol. Chem. Phys.*, 214 (18), **2013**, pp. 2007–2015. doi:[10.1002/macp.201300283](https://doi.org/10.1002/macp.201300283).
- [396] Kim, J., Lägél, B., Moons, E., *et al.* Kelvin probe and ultraviolet photoemission measurements of indium tin oxide work function: a comparison. *Synth. Met.*, 111-112, **2000**, pp. 311–314. doi:[10.1016/S0379-6779\(99\)00354-9](https://doi.org/10.1016/S0379-6779(99)00354-9).
- [397] Ishii, M., Mori, T., Fujikawa, H., *et al.* Improvement of organic electroluminescent device performance by in situ plasma treatment of indium–tin-oxide surface. *J. Lumin.*, 87-89, **2000**, pp. 1165–1167. doi:[10.1016/S0022-2313\(99\)00581-5](https://doi.org/10.1016/S0022-2313(99)00581-5).
- [398] Wu, X., Thrall, E. S., Liu, H., *et al.* Plasmon induced photovoltage and charge separation in citrate-stabilized gold nanoparticles. *J. Phys. Chem. C*, 114 (30), **2010**, pp. 12896–12899. doi:[10.1021/jp102720r](https://doi.org/10.1021/jp102720r).
- [399] Narang, P., Sundararaman, R., and Atwater, H. A. Plasmonic hot carrier dynamics in solid-state and chemical systems for energy conversion. *Nanophotonics*, 5 (1), **2016**, pp. 96–111. doi:[10.1515/nanoph-2016-0007](https://doi.org/10.1515/nanoph-2016-0007).
- [400] Perone, S. P., Richardson, J. H., Deutscher, S. B., *et al.* Laser-Induced Photoelectrochemistry: Time-Resolved Coulostatic-Flash Studies of Photooxidation at n-TiO₂ Electrodes. *J. Electrochem. Soc.*, 127 (12), **1980**, p. 2580. doi:[10.1149/1.2129524](https://doi.org/10.1149/1.2129524).
- [401] Le Formal, F., Sivula, K., and Grätzel, M. The Transient Photocurrent and Photovoltage Behavior of a Hematite Photoanode under Working Conditions and the Influence of Surface Treatments. *J. Phys. Chem. C*, 116 (51), **2012**, pp. 26707–26720. doi:[10.1021/jp308591k](https://doi.org/10.1021/jp308591k).

LIST OF PUBLICATIONS

This thesis is based on the following publications (newest to oldest):

- [A1] **Ligmajer, F.**, Kejřík, L., Tiwari, U., Qiu, M., Nag, J., Konečný, M., říkola, T., Jin, W., Haglund, R. F., Appavoo, K., and Lei, D. Y. Epitaxial VO₂ Nanostructures: A Route to Large-Scale, Switchable Dielectric Metasurfaces. *ACS Photonics*, 5 (7), **2018**, pp. 2561–2567. doi:[10.1021/acsphotonics.7b01384](https://doi.org/10.1021/acsphotonics.7b01384)

Author's contribution: defining methodology, performing experiments, analysing data, writing the manuscript.

- [A2] He, J., Zheng, W., **Ligmajer, F.**, Chan, C.-F., Bao, Z., Wong, K.-L., Chen, X., Hao, J., Dai, J., Yu, S.-F., and Lei, D. Y. Plasmonic enhancement and polarization dependence of nonlinear upconversion emissions from single gold nanorod@SiO₂@CaF₂:Yb³⁺,Er³⁺ hybrid core-shell-satellite nanostructures. *Light Sci. Appl.*, 6 (5), **2017**, p. e16217. doi:[10.1038/lsa.2016.217](https://doi.org/10.1038/lsa.2016.217)

Author's contribution: analysing experimental data and results of numerical simulations, developing the model, co-writing the manuscript.

- [A3] Babocký, J., Křížová, A., řtrbková, L., Kejřík, L., **Ligmajer, F.**, Hrtoň, M., Dvořák, P., Týč, M., řolláková, J., Křápek, V., Kalousek, R., Chmelík, R., and říkola, T. Quantitative 3D Phase Imaging of Plasmonic Metasurfaces. *ACS Photonics*, 4 (6), **2017**, pp. 1389–1397. doi:[10.1021/acsphotonics.7b00022](https://doi.org/10.1021/acsphotonics.7b00022)

Author's contribution: developing software for spectra analysis, analysing experimental data and results of numerical simulations, co-writing the manuscript.

- [A4] Lei, D. Y., Appavoo, K., **Ligmajer, F.**, Sonnefraud, Y., Haglund, R. F., and Maier, S. A. Optically-Trigged Nanoscale Memory Effect in a Hybrid Plasmonic-Phase Changing Nanostructure. *ACS Photonics*, 2 (9), **2015**, pp. 1306–1313. doi:[10.1021/acsphotonics.5b00249](https://doi.org/10.1021/acsphotonics.5b00249)

Author's contribution: performing experiments, analysing data, co-writing the manuscript.

Other related publications (newest to oldest):

- [B1] Daňhel, A., **Ligmajer, F.**, říkola, T., Walcarius, A., and Fojta, M. Electrodeposition of silver amalgam particles on ITO – Towards novel electrode material. *J. Electroanal. Chem.*, 821, **2018**, pp. 53–59. doi:[10.1016/j.jelechem.2017.12.008](https://doi.org/10.1016/j.jelechem.2017.12.008)
- [B2] Dvořák, P., Édes, Z., Kvapil, M., řamořil, T., **Ligmajer, F.**, Hrtoň, M., Kalousek, R., Křápek, V., Dub, P., Spousta, J., Varga, P., and říkola, T. Imaging of near-field interference patterns by aperture-type SNOM – influence of illumination wavelength and polarization state. *Opt. Express*, 25 (14), **2017**, p. 16560. doi:[10.1364/OE.25.016560](https://doi.org/10.1364/OE.25.016560)

- [B3] Babocký, J., Dvořák, P., **Ligmajer, F.**, Hrtoň, M., Šikola, T., Bok, J., and Fiala, J. Patterning large area plasmonic nanostructures on nonconductive substrates using variable pressure electron beam lithography. *J. Vac. Sci. Technol. B*, 34 (6), **2016**, p. 06K801. doi:[10.1116/1.4966959](https://doi.org/10.1116/1.4966959)
- [B4] **Ligmajer, F.**, Druckmüllerová, Z., Měch, R., Kolíbal, M., and Šikola, T. Fabrication of Ordered Arrays of Metallic Nanoparticles on Semiconductor Substrates and Their Characterization by Spectroscopic Ellipsometry (in Czech). *Jemná Mech. a Opt.*, 59 (6), **2014**
- [B5] Dvořák, P., **Ligmajer, F.**, Šamořil, T., Hrtoň, M., Klement, R., Babocký, J., Tuček, M., Spousta, J., and Šikola, T. Application of Reflective Optical Spectroscopy for Experimental Studies of Plasmonic Nanostructures (in Czech). *Jemná Mech. a Opt.*, 59 (6), **2014**
- [B6] Kolíbal, M., Konečný, M., **Ligmajer, F.**, Škoda, D., Vystavěl, T., Zlámal, J., Varga, P., and Šikola, T. Guided Assembly of Gold Colloidal Nanoparticles on Silicon Substrates Prepatterned by Charged Particle Beams. *ACS Nano*, 6 (11), **2012**, pp. 10098–10106. doi:[10.1021/nm3038226](https://doi.org/10.1021/nm3038226)

Optically-Triggered Nanoscale Memory Effect in a Hybrid Plasmonic-Phase Changing Nanostructure

Dang Yuan Lei,^{*,†} Kannatassen Appavoo,^{‡,§} Filip Ligmajer,^{†,||} Yannick Sonnefraud,[⊥] Richard F. Haglund, Jr.,^{‡,⊙} and Stefan A. Maier[#]

[†]Department of Applied Physics, The Hong Kong Polytechnic University, Hong Kong, China

[‡]Interdisciplinary Materials Science Program, Vanderbilt University, Nashville, Tennessee 37235-0106, United States

[§]Centre for Functional Nanomaterials, Brookhaven National Laboratory, Upton, New York 11973, United States

^{||}Central European Institute of Technology, Brno University of Technology, Technická 10, 61669 Brno, Czech Republic

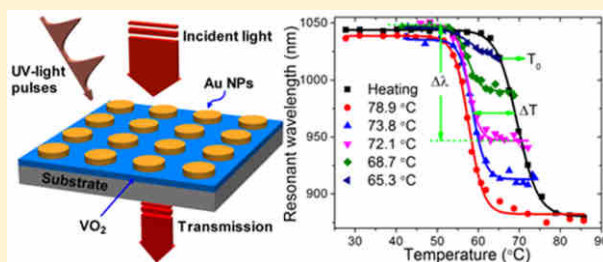
[⊥]Institut Néel, CNRS UPR2940, 25 rue des Martyrs BP166, 38042 Grenoble Cedex 9, France

[⊙]Department of Physics and Astronomy, Vanderbilt University, Nashville, Tennessee 37235-1807, United States

[#]Department of Physics, Imperial College London, London SW7 2AZ, United Kingdom

ABSTRACT: Nanoscale devices, such as all-optical modulators and electro-optical transducers, can be implemented in heterostructures that integrate plasmonic nanostructures with functional active materials. Here we demonstrate all-optical control of a nanoscale memory effect in such a heterostructure by coupling the localized surface plasmon resonance (LSPR) of gold nanodisk arrays to a phase-changing material (PCM), vanadium dioxide (VO₂). By latching the VO₂ in a distinct correlated metallic state during the insulator-to-metal transition (IMT), while concurrently exciting the hybrid nanostructure with one or more ultraviolet optical pulses, the entire phase space of this correlated state can be accessed optically to modulate the plasmon response. We find that the LSPR modulation depends strongly but linearly on the initial latched state, suggesting that the memory effect encoded in the plasmon resonance wavelength is linked to the strongly correlated electron states of the VO₂. The continuous, linear variation of the electronic and optical properties of these model heterostructures opens the way to multiple design strategies for hybrid devices with novel optoelectronic functionalities, which can be controlled by an applied electric or optical field, strain, injected charge, or temperature.

KEYWORDS: surface plasmons, metal nanoparticles, vanadium dioxides, plasmonic memory effect, phase transformation



Metallic nanostructures support localized surface plasmons (LSPs) and surface-plasmon polaritons (SPPs), coherent oscillations of conduction electrons at metal–dielectric interfaces.¹ Surface plasmon excitations occur in ultrasmall mode volumes, generating high local electric fields in passive nanophotonic devices ranging from plasmon waveguides to plasmon lenses.^{2,3} The optical response of plasmonic structures can be controlled by electro-optical,^{4–6} thermal-optical,^{7–9} or magneto-optical properties^{10–13} of functional materials in close proximity. All-optical modulation of SPP propagation in metal films^{14,15} and of LSPs in metal nanostructures^{16–19} is also well-known. In all these schemes, however, the modulated plasmon response is necessarily transient; the metal nanostructures revert to their initial plasmonic states as soon as the external stimulus is removed. On the other hand, in many applications it would be desirable to retain functionality in a plasmonic device even after the triggering signal disappeared, allowing tunable, persistent modulation of plasmonic properties. Accessing multiple plasmonic states linearly and repeatedly by active control of plasmon modes could enhance functionality in

optoelectronic devices²⁰ and enable on-chip integration of optical and electronic functionalities.

Phase-change materials (PCMs), already widely used in rewritable optical data storage and nonvolatile electronic memory,²¹ offer unique possibilities for persistent, reversible tuning of surface plasmons by combining PCMs with metal nanostructures to create new or multiple plasmonic functionalities. A promising PCM for this purpose is vanadium dioxide (VO₂) with its strong correlations among orbital, spin, and lattice degrees of freedom. A modest external stimulus can switch VO₂ through noncongruent electronic (from insulating to metallic) and structural (from M1 monoclinic to R rutile) phase transformations. When VO₂ is heated, this insulator-to-metal transition (IMT) occurs near a critical temperature (*T*_c) of 68 °C in bulk crystals²² and thin films.²³ The IMT can also be induced mechanically,²⁴ electrically,²⁵ optically,²⁶ and by

Received: May 9, 2015

Published: August 13, 2015

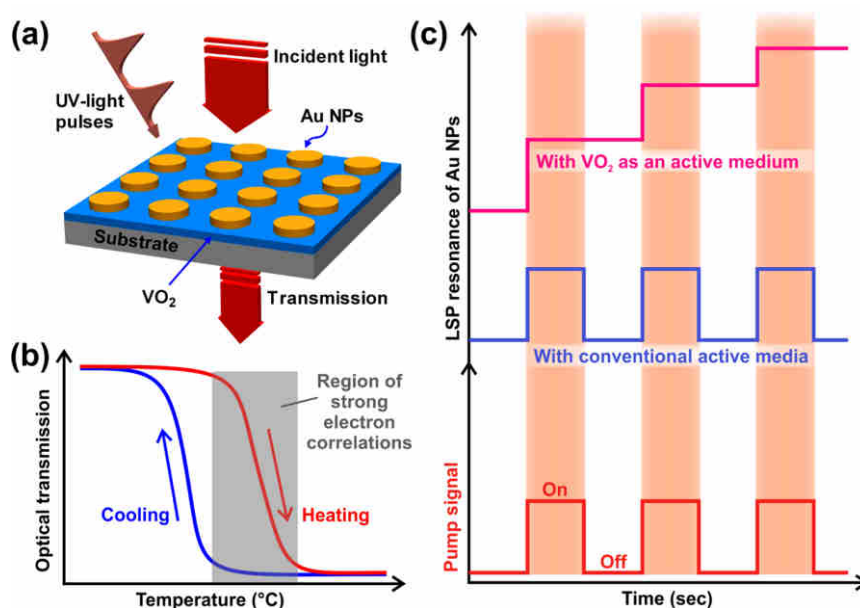


Figure 1. Model for persistent tuning of a “memplasmon” resonance. (a) Experimental schematic for the heating cycle of the phase transition: (a) Array of periodic Au nanodisks fabricated lithographically on a thin VO₂ film deposited on a SiO₂ substrate. Optical extinction measurements are conducted while successive UV-light pulses pump the VO₂ film into new states. The device is mounted on a temperature-controlled stage. (b) Hysteretic response in the optical transmission of VO₂, showing the region of strong electron–electron correlations during the heating cycle of the phase transition (shaded gray area). (c) Schematic comparison of plasmon resonance modulation schemes with conventional active media (blue) and the phase-transforming VO₂ (pink) when pumped by successive optical pump pulses (red). The strongly correlated electron state in the VO₂ is initialized and maintained by setting substrate temperature.

charge injection,²⁷ enabling active modulation of LSPs and SPPs in metallic nanostructures integrated with VO₂.^{28–31}

Although it is generally understood how plasmons are modulated in hybrid nanostructures switched between the fully insulating and fully metallic states,³² the potential for exploiting the entire strongly correlated phase space of a PCM has never been demonstrated at the nanoscale. In this paper, we show how the plasmonic state of a model hybrid nanostructure can be controlled by sampling different initial states within the region of strong electron correlations. We demonstrate persistent optical modulation of localized surface plasmon resonance (LSPR) in a model heterostructure comprising Au nanodisks lithographically patterned on a thin VO₂ film. Throughout the temperature window of the IMT, the VO₂ can be latched thermally in the selected strongly correlated metallic state.³³ Because of the hysteretic response of the first-order VO₂ phase transition, the LSPR can be persistently tuned by successive ultraviolet (UV) light pulses as long as the system remains in the latched, initial state. This dynamic is highly repeatable, lasts for several hours, and persists as long as the external stimulus is not varied.^{34,35} Hence, the entire phase-space of this PCM can be optically addressed when the hybrid nanomaterial is latched at different starting temperatures during the IMT.

More interestingly, the subsequent temporal evolution of the LSPR depends strongly on the initial temperature from which the system is cooled, implying that the LSPR “memorizes” the initial state prepared in the hybridized plasmonic nanostructure and the strongly correlated electron state in the VO₂. It is crucial to note that here the temperature is simply a proxy for the parameter that describes the initial, latched state of the VO₂ PCM. Known properties of VO₂ suggest, therefore, that the novel resonant memory effect described here should be

observable, regardless of whether the initial state is prepared by optically, electrically, or mechanically initializing the hybrid plasmonic-phase-changing heterostructure.

MECHANISM OF PERSISTENT TUNING OF A “MEMPLASMON” RESONANCE

Figure 1 shows the hybrid plasmonic-phase-change optical material, comprising periodic arrays of Au nanostructures on a thin VO₂ film (see Figure 1a), along with a schematic of the mechanism for persistently tuning the LSPR in Au nanostructures interacting with the strongly correlated metallic state of the VO₂. When the VO₂ layer is initialized in the strong-correlation regime (shaded area, Figure 1b) by setting the temperature, each successive UV-light pulse transforms more crystalline nanodomains of the VO₂ into the metallic state without recovering the initial state, manifested by a continuous change in optical transmission. This yields persistent tuning of the resonant plasmon response of Au nanostructures on top of the VO₂ film, unlike nonphase-changing, active plasmonic systems with transient resonance modulation (Figure 1c).

SAMPLE FABRICATION AND LARGE MODULATION OF LSPR VIA PHASE TRANSFORMATION

Thin VO₂ films with nominal thickness of 50 nm were fabricated on glass substrates by pulsed laser ablation of a vanadium target in 250 mTorr oxygen. Subsequent annealing of the samples at 450 °C for 40 min in 10 mTorr oxygen rendered the film stoichiometric, crystalline, and switching. A complete description of the protocol for characterizing optical response and crystal structure can be found elsewhere.²³ Four different arrays of Au nanodisks were fabricated by electron-beam

lithography on the VO₂ film; the nominal diameter D of the Au nanostructures was varied from 80 to 210 nm while keeping the thickness constant at 25 nm. The Au nanodisks were arranged on a square lattice with a pitch of 500 nm, shorter than the wavelength of interest (above 600 nm) in order to avoid diffraction effects in the transmission measurements. Figure 2a shows typical SEM images of the Au nanostructures, exhibiting reproducibility over a large area.

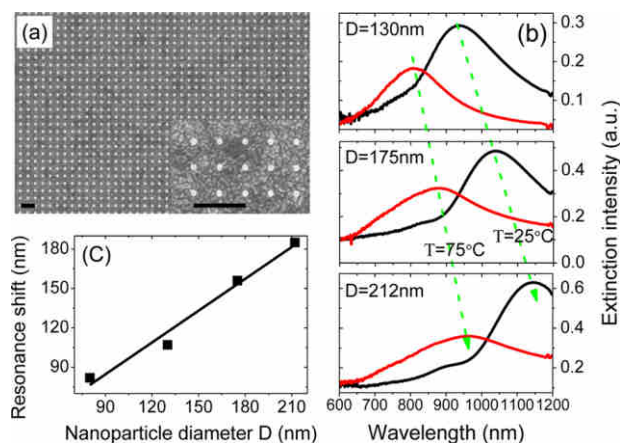


Figure 2. Modulation of localized surface plasmon resonances. (a) Plan-view SEM image of Au nanostructures patterned on a 50 nm thick VO₂ film. Inset: Nanostructure array at higher magnification. Scale bars are 1 μ m in each case. (b) Measured extinction spectra of Au nanostructures for three diameters D at room- (black) and high-temperature (red). (c) Plasmon resonance peak shift due to the phase transformation of VO₂ film as a function of nanostructure diameter (black squares) with linear fit (black line).

Extinction spectra of the arrays, defined as $(1 - \text{Transmission})$, were acquired in an inverted optical microscope (Bruker Hyperion 2000) integrated with a Fourier-transform infrared spectrometer.³⁰ Extinction spectra were measured, while a Peltier thermoelectric element mounted on the sample stage cycled the VO₂ film through its phase transition by heating and cooling through a set temperature program. The external temperature was maintained within ± 0.1 °C over the entire measurement cycle in all experiments. Figure 2b shows the extinction spectra of three Au nanostructure arrays acquired below ($T = 25$ °C, black curves) and above ($T = 75$ °C, red curves) the insulator-to-metal transition of VO₂ and reveals that the LSPR of Au nanodisks experiences a substantial blue-shift due to the IMT.

The shift in LSPR for each array is plotted as a function of nanostructure diameter in Figure 2c and shows that the larger Au nanostructures also exhibit larger resonance shifts because the dielectric contrast in VO₂ during its phase transformation increases with wavelength,³⁶ further shifting the LSPR. In addition, the evanescent near-fields associated with the larger Au nanodisks sample a larger interaction volume in the phase-transforming VO₂ film. The ensemble of Au nanodisks is distributed over a VO₂ film having a broad range of grain sizes, each of which switches at a statistically determined temperature.³⁷ Hence, the average LSPR tuning should be the same for each nanostructure array and is expected to be a function of the effective or mean-field fraction of metallic phase in the underlying polycrystalline VO₂ layer.

■ HYSTERETIC VARIATION OF LOCALIZED SURFACE PLASMON RESONANCE

We next investigate the changes in the LSPR in Au nanostructures during the phase transformation of VO₂ by measuring extinction spectra for the array of 130 nm diameter Au nanodisks while reversibly cycling the VO₂ film across the strong-correlation regime (30–80 °C), with a resolution as small as 0.5 °C. The measured extinction spectra in Figure 3a for the hybrid system show smooth transitions in both resonance wavelength and LSPR intensity. By fitting the extinction spectra, we can map the hysteresis in resonance wavelength of the Au LSPR as a function of substrate temperature (Figure 3b). The hystereses of the Au LSPR and the far-field transmission of a bare VO₂ film (50 nm thick, Figure 3d) exhibit similar widths. The close similarity between the two hysteresis curves indicates that the evolution of the Au LSPR tracks the phase-transition properties of the underlying VO₂ film and can properly be used as an optical marker for the change in local optical properties in the phase-changing material. The slight reduction in thermal hysteresis width ΔT for the LSPR compared to that for the bare VO₂ film can be attributed to the presence of additional nucleation sites at the Au/VO₂ interface, which facilitate the phase-transformation of VO₂ by reducing the phase-transition barrier energy.³⁸

To further correlate the LSPR modulation with the phase changing dynamics of VO₂, Figure 3c and e show, respectively, the plasmon resonance wavelength of the Au nanodisks and the transmission intensity of the bare VO₂ film as a function of the VO₂ metallic fraction that is determined from the hysteretic parameters shown in Figure 3b,d by using the method described in ref 48. The results demonstrate a linear relationship between both plasmon resonance wavelength and transmission intensity, and the metallic fraction of VO₂, thereby indicating a continuous, linear variation of the electronic and optical properties of both systems.

■ PERSISTENT OPTICAL TUNING OF LSPR USING SUCCESSIVE UV-LIGHT PULSES

Apart from the external temperature, UV-light pulses can be used to trigger the insulator-to-metal transition from the prepared initial state because VO₂ has strong absorption in the UV range, as indicated by the large imaginary component of its dielectric function.³⁶ Successive UV-illumination pulses also increase the areal density of the metallic phase in VO₂, gradually changing the average dielectric response of the film and consequently altering the persistent tuning characteristic of the LSPR. After a sufficiently long illumination time, the metallic nanopuddles connect percolatively and leave the VO₂ film in a pure metallic phase.

The hysteresis during the VO₂ phase transition allows for persistent tuning of the Au nanostructure LSPR when the external temperature is biased within the temperature range where strong electron–electron correlation exists. To demonstrate this effect, we prepared the VO₂ film in a strongly correlated metal state by maintaining the array and its substrate at a sequence of constant temperatures. The system was then illuminated by successive UV-light pulses either with a constant power density and varying pulse durations or with different power densities at constant pulse duration (varying fluence). After each such pulse sequence, we measured the extinction spectrum of the Au nanodisk array. Control experiments were also performed at two temperatures well below and above the

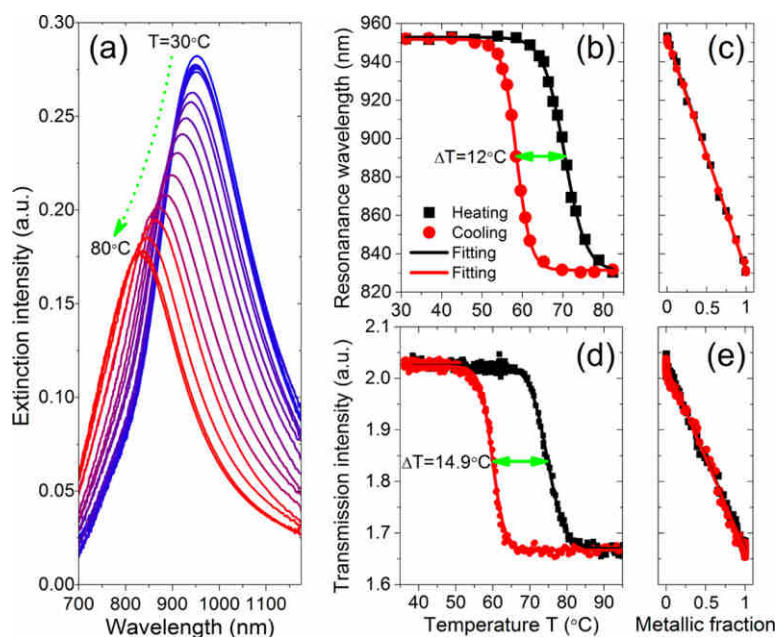


Figure 3. Hysteretic response of localized surface plasmon resonance. (a) Temperature-dependent extinction spectra for Au nanostructures of 130 nm diameter on VO₂ through the heating cycle with a temperature increment of 0.5 °C around the phase-transition temperature. (b) Plasmon resonance hysteresis curve for the same structure extracted from (a). (d) Ensemble transmission hysteresis curve of a 50 nm VO₂ film. Here the sample was illuminated by a tungsten lamp and the integrated, unpolarized transmission intensity was recorded as a function of temperature using an InGaAs photodetector. In both (b) and (d), the black squares and red circles are the measured results for heating and cooling cycles, respectively, while the black and red solid lines are sigmoidal functions fits to the measured data. The green double-headed arrows define the thermal hysteresis width for each system. (c, e) Plasmon resonance wavelength from (b) and transmission intensity from (d) as a function of the VO₂ effective metallic fraction, respectively.

critical temperature of VO₂, and the corresponding extinction spectra were recorded for comparison with those collected at temperatures within the strongly correlated range. To verify that the plasmon resonance shift observed in Au nanodisks was due to the altered dielectric response of VO₂, spectroscopic ellipsometry³⁹ was used to characterize a bare VO₂ film of the same thickness (50 nm) and the change in dielectric response was measured using the same UV-illumination protocol used for the hybrid plasmonic system. The dielectric function of VO₂ was extracted by fitting the ellipsometric data with a sum of one Gaussian and one Lorentz oscillator under a global-minimization algorithm.

Figure 4a shows how the plasmon resonance is modulated by UV illumination for different pulse durations at constant power density (90 mW/cm²) while keeping the hybrid system at 64 and 68 °C, respectively. The LSPR wavelength extracted from each extinction spectrum as a function of total illumination time exhibits a substantial blue-shift after the initial few pulses, followed by a gradual saturation in the resonance wavelength for much longer pulse durations. Such behavior contrasts sharply with results from the control experiments performed at 27 °C (not shown) and 77 °C, in which the LSPR wavelength shows no sensitivity whatsoever to the UV illumination. Figure 4b shows similar results when the LSPR wavelength is modulated by UV-light pulses of constant duration (10 s) but with various power densities: A large blue-shift and subsequent resonance saturation also occurs when gradually increasing the power density of single UV-light pulses. The inset in Figure 4b plots the dispersive refractive index of the bare VO₂ film extracted from spectroscopic ellipsometry as a function of the UV-illumination power density at a constant temperature of 65

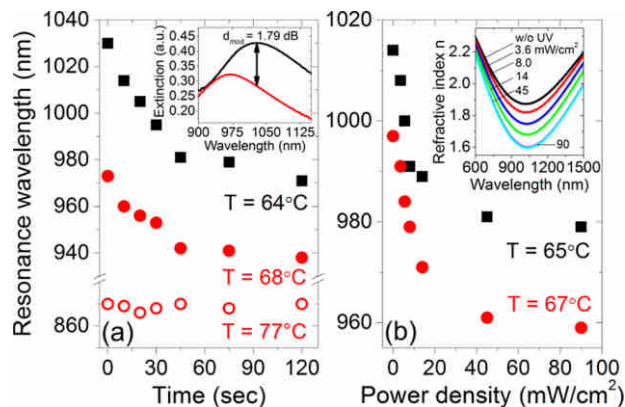


Figure 4. Persistent optical tuning of LSPR by UV-light pulses. (a) Plasmon resonance wavelength of the Au nanodisks of 175 nm diameter on the VO₂ film as a function of the total UV illumination time with a constant power density of 90 mW/cm², while the whole sample was thermally latched at two different temperatures within the phase transition region, 64 °C (black squares) and 68 °C (red circles), and also above (77 °C, red empty circles). Each of the first three pulses has a duration of 10 s, followed by another two pulses of 15 s, respectively, and the last one of 45 s. Inset shows the measured extinction spectra for the sample latched at 64 °C before (black) and after (red) 120 s UV illumination, and the modulation depth (i.e., extinction ratio) at a wavelength of 1029 nm is calculated to be 1.79 dB. (b) Resonance shift for the same structure as a function of the power density of each UV-light pulse of 10 s duration. Inset shows the dispersive refractive index for a 50 nm bare VO₂ film illuminated at the same conditions as above.

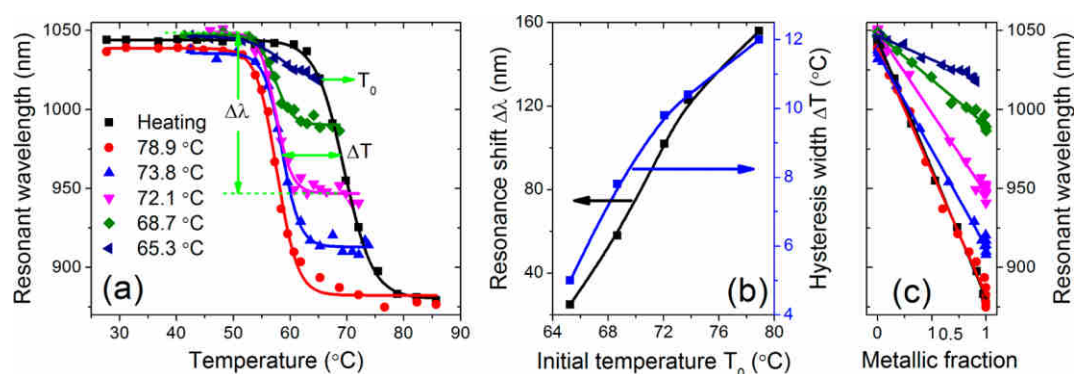


Figure 5. Temperature evolution of LSPR retraining the initial temperature states. (a) LSPR wavelength evolutions for 175 nm-diameter Au nanodisks on VO_2 through cooling cycles starting from different initial temperatures T_0 (red circles to dark-blue left-triangles). The black squares are the resonance positions through the heating cycle. The quantities ΔT and $\Delta\lambda$ represent the thermal hysteresis width and the resonance shift amplitude for each initial state of the film, with results shown in (b) as a function of initial bias temperature T_0 . Solid lines in (a) are sigmoidal fits to the measured data points, while black and blue solid lines in (b) are guides to the eye. The plasmon resonance wavelength extracted from (a) for different initial temperatures and heating cycles are replotted in (c) as a function of the effective metallic fraction of the VO_2 .

°C, which reveals a gradual decrease in the refractive index of VO_2 in the wavelength range of interest and accounts for the observed blue-shift in the LSPR of Au nanostructures.

In analogy to the general definition of modulation depth for silicon photonic modulators,⁴⁰ here we define the extinction ratio $10 \log(I_0/I_{\text{UV}})$ as the modulation depth for the Au/ VO_2 hybrid heterostructure, where I_0 and I_{UV} are the extinction intensities at a specific plasmonic wavelength for the system thermally latched within the phase transition region of VO_2 before and after a certain period of UV illumination, respectively. The inset of Figure 4a shows the measured extinction spectra for the Au nanodisks of 175 nm diameter on the VO_2 film before and after 120 s, 90 mW/cm² UV illumination under the bias temperature of 64 °C, from which the modulation depth at the plasmonic wavelength 1029 nm is calculated to be 1.79 dB. Note that this value might be underestimated because in the extinction calculation the transmission of each Au nanodisk array was normalized with respect to the transmitted light through a bare VO_2 area in close proximity to the array. This implies that the extinction contribution from the VO_2 itself has not been taken into account in the calculation of modulation depth.

EVOLUTION TRACES OF LSPR REGISTERING THE INITIAL TEMPERATURE STATES

In a temperature-controlled memristive device driven by the VO_2 phase transition, the resistance takes different paths for cooling and heating cycles; in particular, the time evolution of the resistance depends strongly on the bias temperature from which the cooling cycle starts.⁴¹ This means that the initial temperature states or the associated information stored in the system can be retrieved by monitoring the evolving path of the system resistance. More generally, in a memristive metal/oxide/metal nanodevice, this corresponds to the hysteretic response of I – V curves in which the applied voltage and resultant current follow a highly nonlinear relationship and the evolutionary history of the current–voltage relationship depends on the initial bias voltage.^{42,43}

The optical-frequency, plasmon memory resonance described in this experiment exhibits features analogous to such memristive behavior. Figure 5a plots LSPR wavelength as a function of temperature during the cooling cycle starting from

different bias temperatures. Each such evolutionary path is unique, yielding a characteristic parameter pair, thermal hysteresis width and resonance shift, for each bias temperature (Figure 5b). The unique evolution of the LSPR can also be observed by plotting the plasmon resonance wavelengths (extracted from Figure 5a for each different initial temperature and heating cycle) as a function of the effective metallic fraction of VO_2 (Figure 5c). The strong similarity between a memristive response^{41–43} and the behavior of the hybrid plasmonic system further supports the idea that an optical-frequency plasmon resonance of the metallic nanostructure can store and read out the “memory” of the initial hybridized state in a broad range of phase-transforming materials like VO_2 .

DISCUSSION

The hysteretic nature of the first-order phase transition in VO_2 is the key to realizing the persistent plasmon resonance tuning in practice. In this experimental configuration a bias temperature somewhere in the transition region from insulator to metal, that is, between 60 and 80 °C (Figure 4), initializes the VO_2 in a strongly correlated state. The UV-modulation experiments reveal that the LSPR of Au nanostructures is “pinned” at a wavelength defined by the initial state of the VO_2 film and the duration of illumination. Successive UV-light pulses drive the LSPR to a new wavelength as more VO_2 domains are switched from insulating to metallic. The hysteretic response of this hybridized heterostructure after the triggering impulse fades away (as demonstrated in Figure 5) is then essential for the long-lasting memory of the UV-light induced change which is “imprinted” into the LSPR frequency.

As noted in the discussion of Figure 5, this LSPR memory effect in metal nanostructures resembles in some ways the memory capacitance and memristive responses of VO_2 in memory metamaterials⁴⁴ and phase-transition-based memory devices.⁴¹ However, the plasmon memory resonance observed here at optical to near-infrared frequencies is based on the hybrid response of the Au nanodisks and the hysteretic response of VO_2 . This is distinctly different from the metamaterial memristive system⁴⁴ that exploits the hysteresis in VO_2 dielectric constants at terahertz or microwave frequencies. Finally, it should be noted that, although UV pulses of a few tens of seconds were used in this study, the

phase transition dynamics of VO_2 is not intrinsically restricted to slow time scales. The absorbed UV light in the present experiment causes both transient local heating and electronic excitation, leading to the formation of new metallic nanopuddles in the insulating VO_2 host and driving the film toward completed formation of the metallic, rutile phase. If the UV energy density is high enough to cause the transition to occur by local heating, the reversion from the rutile metallic state to the insulating state could require nanoseconds to microseconds. If, on the other hand, the UV light pulse is ultrashort²⁶ and the transition proceeds primarily through electronic excitation to the recently observed metallic monoclinic state,^{45–47} the complete transition cycle could then occur on a picosecond time scale without a structural phase transition, making it possible to consider practical applications. Another potential route to an ultrafast device using the hybrid material system demonstrated here would be by electron injection initiated by resonant excitation of a noble-metal nanoparticle.²⁷

The plasmon memory resonance effect can be generalized in a number of ways. Because the critical temperature and the slope of the hysteresis curve for a VO_2 film can be substantially altered by impurity doping,⁴⁸ electrical bias,⁴⁹ charge injection,²⁷ or substrate-induced strain,⁵⁰ even for the ultrafast laser-driven phase transition,⁵¹ a plasmon memory device can, in principle, be operated at lower temperatures, and over a broader temperature range, than what is demonstrated here. Conversely, since the initial strongly correlated metal state can be prepared by applied bias voltage, charge injection, strain, or laser illumination, a plasmon memory device can be designed to operate at a constant temperature. The thermal hysteresis width of the IMT in VO_2 can be altered by changing fabrication parameters to yield differing grain sizes in a film,²³ ordered arrays of nanostructures,³⁰ or strained one-dimensional nanostructures.²⁴ Flexible control over both the transition temperature and hysteresis width of the VO_2 also allows for stable modulation of the plasmon resonance wavelength.

Other nanostructure configurations can easily be imagined: For example, one could imagine a double-layer lithography³² procedure in which one would remove all the VO_2 outside the range of the plasmon near-field, leaving a double-layer Au/VO_2 heterostructure array with a defined pitch. Finally, since the phase transformation in VO_2 is associated with strong electron–electron correlations, the plasmon memory resonance offers a unique opportunity to monitor the interaction between the collective oscillation of free electrons in the surface plasmons and strongly correlated electrons during the interband transitions in VO_2 .⁵²

Although these experiments employed Au nanostructure arrays, the behavior observed here should also occur in individual metal nanostructures and be observable using single-particle spectroscopy to monitor the plasmon resonance shift. In fact, single-particle studies could explore the metal-to-insulator phase-transition on the nanoscale by monitoring electromagnetic near fields associated with localized surface plasmons. For example, an individual metal nanostructure used as a nanoprobe could detect coexisting insulating and metallic phases in VO_2 and the divergence of the real dielectric function near the onset of the insulator-to-metal transition.

CONCLUSION

We have demonstrated a novel plasmon memory resonance by hybridizing the surface plasmon resonance in metallic nanostructures with the strong electron–electron correlation

effects in a phase-changing VO_2 thin film. Analogous to the memristive response of VO_2 , this plasmon memory resonance exhibits persistent tuning of the resonance frequency when illuminated by ultraviolet light, in contrast to plasmon modulation schemes using conventional active media. The temperature and temporal evolution of the observed memplasmon resonance depends critically on the correlated initial state of the VO_2 and, thus, enables reversible operation of the device to reinitialize the hybrid plasmonic memory material.

This memory effect on the resonance frequency of a plasmonic nanostructure due to the strong electron–electron correlations in VO_2 exhibits an optical analog of memory circuit devices, the plasmon memory resonance, but now in the optical to near-infrared range rather than the microwave and THz range.^{41–43} Nanoscale integration of plasmonic structures with phase-changing materials, such as VO_2 , could enable further miniaturization of an entire class of memory devices for next-generation nanophotonic circuitry, simply because such devices would work at shorter wavelengths than THz or microwave-based devices. The dual-excitation scheme presented in this work could potentially be extended to other hybrid plasmonic/PCM systems, incorporating the controlled metal-to-insulator phase transition in NdNiO_3 ,⁵³ colossal magnetoresistance in perovskite materials like LaMnO_3 ,⁵⁴ and $\text{Pr}_{0.7}\text{Ca}_{0.3}\text{MnO}_3$.⁵⁵

Combined with novel nanostructure architectures³² and excitation schemes,⁵⁶ this proof-of-concept demonstration has a significant impact on the possibilities for transferring the basic concepts in conventional circuits, such as memristive behavior and memory capacitance, to nanoscale optical devices operating in the visible and near-infrared regimes.

AUTHOR INFORMATION

Corresponding Author

*E-mail: dylei@polyu.edu.hk.

Notes

The authors declare no competing financial interest.

ACKNOWLEDGMENTS

D.Y.L. acknowledges support from the Hong Kong Polytechnic University (1-ZVCG). Y.S. and S.A.M. acknowledge support from the United Kingdom Engineering and Physical Sciences Research Council and the Leverhulme Trust Foundation. K.A. and R.F.H. acknowledge support from the National Science Foundation (ECE-0801980); sample nanofabrication and characterization at Vanderbilt University used facilities renovated and upgraded with support from the National Science Foundation (ARI-R2 DMR-0963361). F.L. acknowledges support from the European Regional Development Fund (CEITEC, CZ.1.05/1.1.00/02.0068).

REFERENCES

- (1) Maier, S. A. *Plasmonics: Fundamentals and Applications*; Springer: New York, 2007.
- (2) Bozhevolnyi, S. I.; Volkov, V. S.; Devaux, S.; Laluet, J.-Y.; Ebbesen, T. W. Channel plasmon subwavelength waveguide components including interferometers and ring resonators. *Nature* **2006**, *440*, 508.
- (3) Liu, Z.; Steele, J. M.; Sritravanich, W.; Pikus, Y.; Sun, C.; Zhang, X. Focusing surface plasmons with a plasmonic lens. *Nano Lett.* **2005**, *5*, 1726–1729.
- (4) Müller, J.; Sönnichsen, C.; von Poschinger, H.; von Plessen, G.; Klar, T. A.; Feldmann, J. Electrically controlled light scattering with single metal nanoparticles. *Appl. Phys. Lett.* **2002**, *81*, 171.

- (5) Dicken, M. J.; Sweatlock, L. A.; Pacifici, D.; Lezec, H. J.; Bhattacharya, K.; Atwater, H. A. Electrooptic modulation in thin film barium titanate plasmonic interferometers. *Nano Lett.* **2008**, *8*, 4048–4052.
- (6) Neutens, P.; Van Dorpe, P.; De Vlaminck, I.; Lagae, L.; Borghs, G. Electrical detection of confined gap plasmons in metal–insulator–metal waveguides. *Nat. Photonics* **2009**, *3*, 283.
- (7) Suh, J. Y.; Donev, E. U.; Lopez, R.; Feldman, L. C.; Haglund, R. F. Modulated optical transmission of subwavelength hole arrays in metal-VO₂ films. *Appl. Phys. Lett.* **2006**, *88*, 133115.
- (8) Lei, D. Y.; Appavoo, K.; Sonnefraud, Y.; Haglund, R. F., Jr.; Maier, S. A. Single-particle plasmon resonance spectroscopy of phase transition in vanadium dioxide. *Opt. Lett.* **2010**, *35*, 3988.
- (9) Ren, F.; Wang, X.; Wang, A. X. Thermo-optic modulation of plasmonic bandgap on metallic photonic crystal slab. *Appl. Phys. Lett.* **2013**, *102*, 181101.
- (10) Temnov, V. V.; Armelles, G.; Woggon, U.; Guzatov, D.; Cebollada, A.; Garcia-Martin, A.; Garcia-Martin, J.-M.; Thomay, T.; Leitenstorfer, A.; Bratschkitsch, R. Active magneto-plasmonics in hybrid metal–ferromagnet structures. *Nat. Photonics* **2010**, *4*, 107.
- (11) Belotelov, V. I.; Akimov, I. A.; Pohl, M.; Kotov, V. A.; Kasture, S.; Vengurlekar, A. S.; Gopal, A. V.; Yakovlev, D. R.; Zvezdin, A. K.; Bayer, M. Enhanced magneto-optical effects in magnetoplasmonic crystals. *Nat. Nanotechnol.* **2011**, *6*, 370.
- (12) Bonanni, V.; Bonetti, S.; Pakizeh, T.; Pirzadeh, Z.; Chen, J.; Nogués, J.; Vavassori, P.; Hillenbrand, R.; Åkerman, J.; Dmitriev, A. Designer magnetoplasmonics with nickel nanoferromagnets. *Nano Lett.* **2011**, *11*, 5333–5338.
- (13) Chin, J. Y.; Steinle, T.; Wehler, T.; Dregely, D.; Weiss, T.; Belotelov, V. I.; Stritzker, B.; Giessen, H. Nonreciprocal plasmonics enables giant enhancement of thin-film Faraday rotation. *Nat. Commun.* **2013**, *4*, 1599.
- (14) MacDonald, K. F.; Sámson, Z. L.; Stockman, M. I.; Zheludev, N. I. Ultrafast active plasmonics. *Nat. Photonics* **2009**, *3*, 55.
- (15) Pacifici, D.; Lezec, H. J.; Atwater, H. A. All-optical modulation by plasmonic excitation of CdSe quantum dots. *Nat. Photonics* **2007**, *1*, 402.
- (16) Utikal, T.; Stockman, M. I.; Heberle, A. P.; Lippitz, M.; Giessen, H. All-optical control of the ultrafast dynamics of a hybrid plasmonic system. *Phys. Rev. Lett.* **2010**, *104*, 113903.
- (17) Wurtz, G. A.; Pollard, R.; Hendren, W.; Wiederrecht, G. P.; Podolskiy, V. A.; Zayats, A. V. Designed ultrafast optical nonlinearity in a plasmonic nanorod metamaterial enhanced by nonlocality. *Nat. Nanotechnol.* **2011**, *6*, 107.
- (18) Abb, M.; Albella, P.; Aizpurua, J.; Muskens, O. L. All-optical control of a single plasmonic nanoantenna-ITO hybrid. *Nano Lett.* **2011**, *11*, 2457–2463.
- (19) Zhu, Y.; Hu, X.; Fu, Y.; Yang, H.; Gong, Q. Ultralow-power and ultrafast all-optical tunable plasmon-induced transparency in metamaterials at optical communication range. *Sci. Rep.* **2013**, *3*, 2338.
- (20) Hoessbacher, C.; Fedoryshyn, Y.; Emboras, A.; Melikyan, A.; Kohl, M.; Hillerkuss, D.; Hafner, C.; Leuthold, J. The plasmonic memristor: a latching optical switch. *Optica* **2014**, *1*, 198–202.
- (21) Wuttig, M.; Yamada, N. Phase-change materials for rewritable data storage. *Nat. Mater.* **2007**, *6*, 824.
- (22) Morin, F. J. Oxides which show a metal-to-insulator transition at the Neel temperature. *Phys. Rev. Lett.* **1959**, *3*, 34–36.
- (23) Suh, J. Y.; Lopez, R.; Feldman, L. C.; Haglund, R. F. Semiconductor to metal phase transition in the nucleation and growth of VO₂ nanoparticles and thin films. *J. Appl. Phys.* **2004**, *96*, 1209.
- (24) Wei, J.; Wang, Z.; Chen, W.; Cobden, D. H. New aspects of the metal–insulator transition in single-domain vanadium dioxide nano-beams. *Nat. Nanotechnol.* **2009**, *4*, 420.
- (25) Qazilbash, M. M.; Li, Z. Q.; Podzorov, V.; Brehm, M.; Keilmann, F.; Chae, B. G.; Kim, H. T.; Basov, D. N. Electrostatic modification of infrared response in gated structures based on VO₂. *Appl. Phys. Lett.* **2008**, *92*, 241906.
- (26) Cavalleri, A.; Dekorsy, Th.; Chong, H. H. W.; Kieffer, J. C.; Schoenlein, R. W. Evidence for a structurally-driven insulator-to-metal transition in VO₂: A view from the ultrafast timescale. *Phys. Rev. B: Condens. Matter Mater. Phys.* **2004**, *70*, 161102(R).
- (27) Appavoo, K.; Wang, B.; Brady, N. F.; Seo, M.; Nag, J.; Prasankumar, R. P.; Hilton, D. J.; Pantelides, S. T.; Haglund, R. F., Jr. Ultrafast phase transition via catastrophic phonon collapse driven by plasmonic hot-electron injection. *Nano Lett.* **2014**, *14*, 1127–1133.
- (28) Dicken, M. J.; Aydin, K.; Pryce, I. M.; Sweatlock, L. A.; Boyd, E. M.; Walavalkar, S.; Ma, J.; Atwater, H. A. Frequency tunable near-infrared metamaterials based on VO₂ phase transition. *Opt. Express* **2009**, *17*, 18330.
- (29) Seo, M.; Kyoung, J.; Park, H.; Koo, S.; Kim, H.-S.; Bernien, H.; Kim, B. J.; Choe, J. H.; Ahn, Y. H.; Kim, H.-T.; Park, N.; Park, Q.-H.; Ahn, K.; Kim, D.-S. Active terahertz nanoantennas based on VO₂ phase transition. *Nano Lett.* **2010**, *10*, 2064–2068.
- (30) Appavoo, K.; Lei, D. Y.; Sonnefraud, Y.; Wang, B.; Pantelides, S. T.; Maier, S. A.; Haglund, R. F., Jr. Role of defects in the phase transition of VO₂ nanoparticles probed by plasmon resonance spectroscopy. *Nano Lett.* **2012**, *12*, 780–786.
- (31) Ye, J.; Van Dorpe, P. Plasmonic behaviors of gold dimers perturbed by a single nanoparticle in the gap. *Nanoscale* **2012**, *4*, 7205.
- (32) Appavoo, K.; Haglund, R. F., Jr. Polarization selective phase-change nanomodulator. *Sci. Rep.* **2014**, *4*, 6771.
- (33) Qazilbash, M. M.; Brehm, M.; Chae, B. G.; Ho, P.-C.; Andreev, G. O.; Kim, B.-J.; Yun, S. J.; Balatsky, A. V.; Maple, M. B.; Keilmann, F.; Kim, H.-T.; Basov, D. N. Mott transition in VO₂ revealed by infrared spectroscopy and nano-imaging. *Science* **2007**, *318*, 1750.
- (34) Coy, H.; Cabrera, R.; Sepúlveda, N.; Fernández, F. E. Optoelectronic and all-optical multiple memory states in vanadium dioxide. *J. Appl. Phys.* **2010**, *108*, 113115.
- (35) Gurvitch, M.; Luryi, S.; Polyakov, A.; Shalalov, A. Nonhysteretic behavior inside the hysteresis loop of VO₂ and its possible application in infrared imaging. *J. Appl. Phys.* **2009**, *106*, 104504.
- (36) Verleur, H. W.; Barker, A. S.; Berglund, C. N. Optical properties of VO₂ between 0.25 and 5 eV. *Phys. Rev.* **1968**, *172*, 788.
- (37) Lopez, L.; Feldman, L. C.; Haglund, R. F. Size-dependent optical properties of VO₂ nanoparticle arrays. *Phys. Rev. Lett.* **2004**, *93*, 177403.
- (38) Appavoo, K.; Haglund, R. F., Jr. Detecting nanoscale size dependence in VO₂ phase transition using a split-ring resonator metamaterial. *Nano Lett.* **2011**, *11*, 1025–1031.
- (39) Lei, D. Y.; Kéna-Cohen, S.; Zou, B.; Petrov, P. K.; Sonnefraud, Y.; Breeze, J.; Maier, S. A.; Alford, N. M. Spectroscopic ellipsometry as an optical probe of strain evolution in ferroelectric thin films. *Opt. Express* **2012**, *20*, 4419.
- (40) Reed, G. T.; Mashanovich, G.; Gardes, F. Y.; Thomson, D. J. Silicon optical modulators. *Nat. Photonics* **2010**, *4*, 518.
- (41) Driscoll, T.; Kim, H.-T.; Chae, B.-G.; Di Ventra, M.; Basov, D. N. Phase-transition driven memristive system. *Appl. Phys. Lett.* **2009**, *95*, 043503.
- (42) Strukov, D. B.; Snider, G. S.; Stewart, D. R.; Williams, R. S. The missing memristor found. *Nature* **2008**, *453*, 80.
- (43) Yang, J. J.; Pickett, M. D.; Li, X.; Ohlberg, D. A. A.; Stewart, D. R.; Williams, R. S. Memristive switching mechanism for metal/oxide/metal nanodevices. *Nat. Nanotechnol.* **2008**, *3*, 429.
- (44) Driscoll, T.; Kim, H.-T.; Chae, B.-G.; Kim, B.-J.; Lee, Y.-W.; Jokerst, N. M.; Palit, S.; Smith, D. R.; Di Ventra, M.; Basov, D. N. Memory metamaterials. *Science* **2009**, *325*, 1518.
- (45) Laverock, J.; Kittiwatanakul, S.; Zakharov, A. A.; Niu, Y. R.; Chen, B.; Wolf, S. A.; Lu, J. W.; Smith, K. E. Direct observation of decoupled structural and electronic transitions and an ambient pressure monoclinic-like metallic phase of VO₂. *Phys. Rev. Lett.* **2014**, *113*, 216402.
- (46) Morrison, V. R.; Chatelain, R. P.; Tiwari, K. L.; Hendaoui, A.; Bruhacs, A.; Chaker, M.; Siwick, B. J. A photoinduced metal-like phase of monoclinic VO₂ revealed by ultrafast electron diffraction. *Science* **2014**, *346*, 445–448.
- (47) Wegkamp, D.; Herzog, M.; Xian, L.; Gatti, M.; Cudazzo, P.; McGahan, C. L.; Marvel, R. E.; Haglund, R. F.; Rubio, A.; Wolf, M.;

Stähler, J. Instantaneous band-gap collapse in photoexcited monoclinic VO₂ due to photocarrier doping. *Phys. Rev. Lett.* **2014**, *113*, 216401.

(48) Shibuya, K.; Kawasaki, M.; Tokura, Y. Metal-insulator transition in epitaxial V_{1-x}W_xO₂ ($0 \leq x \leq 0.33$) thin films. *Appl. Phys. Lett.* **2010**, *96*, 022102.

(49) Yang, Z.; Hart, S.; Ko, C.; Yacoby, A.; Ramanathan, S. Studies on electric triggering of the metal-insulator transition in VO₂ thin films between 77 and 300 K. *J. Appl. Phys.* **2011**, *110*, 033725.

(50) Wu, J.; Gu, Q.; Guiton, B. S.; de Leon, N. P.; Ouyang, L.; Park, H. Strain-induced self organization of metal-insulator domains in single-crystalline VO₂ nanobeams. *Nano Lett.* **2006**, *6*, 2313–2317.

(51) Pashkin, A.; Kübler, C.; Ehrke, H.; Lopez, R.; Halabica, A.; Haglund, R. F., Jr.; Huber, R.; Leitenstorfer, A. Ultrafast insulator-metal phase transition in VO₂ studied by multiterahertz spectroscopy. *Phys. Rev. B: Condens. Matter Mater. Phys.* **2011**, *83*, 195120.

(52) Ferrara, D. W.; Nag, J.; MacQuarrie, E. R.; Kaye, A. B.; Haglund, R. F., Jr. Plasmonic probe of the semiconductor to metal phase transition in vanadium dioxide. *Nano Lett.* **2013**, *13*, 4169–4175.

(53) Asanuma, S.; Xiang, P.-H.; Yamada, H.; Sato, H.; Inoue, I. H.; Akoh, H.; Sawa, A.; Ueno, K.; Shimotani, H.; Yuan, H.; Kawasaki, M.; Iwasa, Y. Tuning of the metal-insulator transition in electrolyte-gated NdNiO₃ thin films. *Appl. Phys. Lett.* **2010**, *97*, 142110.

(54) Ramirez, A. P. Colossal magnetoresistance. *J. Phys.: Condens. Matter* **1997**, *9*, 8171–8199.

(55) Fiebig, M.; Miyano, K.; Tomioka, Y.; Tokura, Y. Visualization of the local insulator-metal transition in Pr_{0.7}Ca_{0.3}MnO₃. *Science* **1998**, *280*, 1925–1928.

(56) Aouani, H.; Rahmani, M.; Navarro-Cia, M.; Maier, S. A. Third-harmonic-upconversion enhancement from a single semiconductor nanoparticle coupled to a plasmonic antenna. *Nat. Nanotechnol.* **2014**, *9*, 290–294.

Quantitative 3D Phase Imaging of Plasmonic Metasurfaces

Jiří Babocký,^{†,‡} Aneta Křížová,^{†,‡} Lenka Štrbková,[†] Lukáš Kejík,[†] Filip Ligmajer,^{†,§} Martin Hrtoň,^{†,§} Petr Dvořák,^{†,§} Matěj Týč,[†] Jana Čolláková,^{†,§} Vlastimil Křápek,^{†,§} Radek Kalousek,^{†,§} Radim Chmelík,^{†,§} and Tomáš Šíkola^{*,†,§}

[†]Central European Institute of Technology, Purkyňova 123, Brno, 612 00, Czech Republic

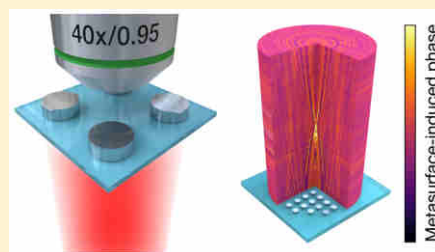
[‡]TESCAN Brno, s.r.o., Libušina tř. 1, 623 00 Brno, Czech Republic

[§]Institute of Physical Engineering, Brno University of Technology, Technická 2896/2, Brno, 616 69, Czech Republic

Supporting Information

ABSTRACT: Coherence-controlled holographic microscopy (CCHM) is a real-time, wide-field, and quantitative light-microscopy technique enabling 3D imaging of electromagnetic fields, providing complete information about both their intensity and phase. These attributes make CCHM a promising candidate for performance assessment of phase-altering metasurfaces, a new class of artificial materials that allow to manipulate the wavefront of passing light and thus provide unprecedented functionalities in optics and nanophotonics. In this paper, we report on our investigation of phase imaging of plasmonic metasurfaces using holographic microscopy. We demonstrate its ability to obtain phase information from the whole field of view in a single measurement on a prototypical sample consisting of silver nanodisc arrays. The experimental data were validated using FDTD simulations and a theoretical model that relates the obtained phase image to the optical response of metasurface building blocks. Finally, in order to reveal the full potential of CCHM, we employed it in the analysis of a simple metasurface represented by a plasmonic zone plate. By scanning the sample along the optical axis we were able to create a quantitative 3D phase map of fields transmitted through the zone plate. The presented results prove that CCHM is inherently suited to the task of metasurface characterization. Moreover, as the temporal resolution is limited only by the camera framerate, it can be even applied in analysis of actively tunable metasurfaces.

KEYWORDS: metasurface, plasmonic, phase, nanoantenna, holographic microscopy, 3D imaging



One of the fastest-growing areas of research in photonics is the field of metasurfaces,^{1–3} where nanoantennas and their ability to control light–matter interaction are utilized in light focusing,^{4–12} polarizing,^{13–16} and holography.^{17–20} In many of these metasurfaces, tailoring the near-field phase response among the individual building blocks is used to modify (e.g., to focus or to bend) the wavefront of light beam and thus modulate its far-field projection. In order to assess the performance of metasurfaces and verify their characteristics predicted by numerical simulations, it is of great importance to be able to quantitatively assess the phase distribution of the electric field in the sample plane, a process which is usually referred to as quantitative phase imaging. However, there are only few methods adequate to this task: (1) Traditionally, ellipsometry has been a method of choice for characterizing optical properties of materials,²¹ giving access also to their phase-altering properties.²² Its use in analysis of metasurfaces is, however, restricted to the special cases where the working principle of respective metasurface is manipulation of phase difference between s- and p-polarized light. Moreover, it often involves an inverse analysis, which becomes troublesome when dealing with samples of unknown structure and composition. (2) Scattering-type scanning near-field optical microscopy (s-SNOM), on the other hand, provides remarkable subdiffraction

lateral resolution and allows investigation of complex near-field patterns generated by nanoantennas, including the phase response.²³ Yet as it is a scanning probe technique, it is inherently slow. Further, its spectral window is usually limited to the infrared region, as the possibility of its extension to the visible has been only rarely reported.^{24,25} (3) The most straightforward acquisition of metasurfaces' phase spectra has been achieved with methods based on interferometry. These involve spectroscopic interferometries either with broadband continuous light sources^{26–31} or ultrashort laser pulses,^{32–36} where the phase shift between the reference and sample beam is determined with the aid of Fourier transformations between relevant domains (temporal/spatial and their corresponding reciprocals). The drawbacks associated with these methods involve problematic dispersion compensation, necessity of introducing a precise delay, and necessity of spectrum sampling with high resolution. Moreover, all aforementioned interferometric approaches provide phase information only from a single spot of a sample (whether optically focused or not). This seriously limits their use for characterization of metamaterials,

Received: January 11, 2017

Published: May 9, 2017

as the measured phase is either an average from a large sample area or a single value from a diffraction-limited spot.

Here we present a powerful quantitative phase-imaging technique that keeps all the benefits of the aforementioned interferometric approaches, provides unambiguous phase information from the whole field of view and thus overcomes the necessity for lateral sample scanning. Our method, which is based on principles of holographic microscopy, is fast and real-time, limited only by the speed of a CCD detector, and allows wide-field analysis of phase properties in situ, even in the diffuse environment.³⁷ To validate our approach, we first applied it to well-known plasmonic disc-shaped nanoantennas, where the phase of transmitted light can be easily predicted and controlled. Then we present an analytical model that relates the obtained phase image to the resonant properties of nanoantennas and thus provides a general framework for the use of holographic microscopy in metamaterial phase analysis. Finally, we demonstrate the unique features and large potential of this method by performing a 3D phase mapping of wavefronts behind a plasmonic zone plate.

RESULTS AND DISCUSSION

The principal element of our work is the coherence-controlled holographic microscopy (CCHM) and its ability to image both the amplitude and the phase of optical fields. Until now, it has found its use exclusively in fast characterization of live biological samples, where the phase contrast arises from the optical path difference.³⁸ Here, we employ it for the first time for spectrally resolved imaging of plasmonic metasurfaces, where the phase change is governed by the scattering properties of individual plasmonic building blocks. This included an upgrade of the conventional CCHM optical setup with a tunable laser and generalization of its theoretical framework toward arbitrary-distributed scatterers (see [Methods](#) for detailed description of CCHM and our experimental setup). The imaging of plasmonic nanoantennas by digital holographic microscopy was previously reported by Suck et al.,³⁹ who demonstrated the use of digital heterodyne holography for imaging of far-field maps produced by plasmonic nanoantennas. In their work, however, they focused only on measuring the intensity of the scattered field using the Kretschmann configuration⁴⁰ and monochromatic illumination. We take full advantage of the ability of CCHM to reconstruct the optical fields including their phase, which gives us more complete information about the fundamental properties of plasmonic antennas and which could be extremely valuable for design and optical characterization of metasurfaces and metamaterials.

Benchmark Sample. To demonstrate the capabilities of our method, we evaluated the phase response of a benchmark sample consisting of multiple arrays of plasmonic nanostructures ([Figure 1](#)). In order to have a simple, polarization independent response, we used silver disc-shaped nanoantennas with diameters ranging from 50 to 200 nm. In each array ($10 \times 10 \mu\text{m}$), the pitch was set to double of the disc diameter, so that the nanoantennas covered the same percentage of the surface ($\approx 20\%$). SEM analysis (see [Supporting Information, Figures S1 and S2](#)) revealed that due to limited resolution of PMMA, the fabrication of the arrays with 50 and 60 nm nanodiscs was not successful, and we left them out from subsequent optical measurements.

First, we measured extinction spectra of the aforementioned nanodisc arrays using conventional confocal optical spectroscopy (spot size $2 \mu\text{m}$) to verify their quality and spectral

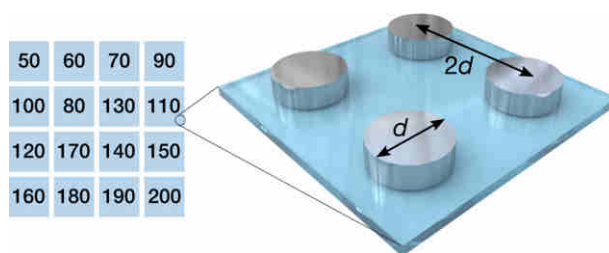


Figure 1. Benchmark sample consisted of silver nanodisc arrays (blue squares). Diameter d of nanodiscs (in nm) is denoted in each blue square; pitch of all arrays was fixed as $2d$.

position of their plasmonic resonances ([Figure 2a](#)). Strong dipolar plasmonic modes of the nanodiscs are apparent in the visible and near-infrared part of the spectrum, and in line with our expectations, they shift toward longer wavelengths with increasing nanodisc diameter.

The measurements were complemented by FDTD simulations of nanodisc arrays with geometrical parameters identical to those from the experiment. As simulations of the entire nanodisc arrays would require unreasonable computational power, we decided to simplify the task by employing periodic boundary conditions. In this way we were able to account for the mutual interaction while keeping the computational time short. The resulting extinction spectra are displayed in [Figure 2b](#), with the resonance peaks blue-shifted with respect to the experimental ones roughly by 20 nm for larger discs and by almost 90 nm for the smallest one. Additional simulations revealed that this spectral shift can be attributed to fabrication imperfections and a thin oxide layer that rapidly forms on the surface of silver nanodiscs (see [Figures S3 and S4 in Supporting Information](#)). Also note that the use of periodic boundary conditions leads to the appearance of a pronounced dip in the extinction spectrum, which moves toward longer wavelengths with increasing disc size and which is the result of a strong diffractive coupling between nanodiscs.^{41,42} However, in view of the fact that the calculated spectra adequately capture the resonant nature of the optical response of the fabricated nanodisc arrays and the absolute spectral position of the resonance is not central for our analysis of the image formation in CCHM (we are more interested in its relative position with respect to the phase profile obtained by CCHM), we consider the agreement between the simulations and the experiment to be sufficient for our purposes.

Next, we used our CCHM setup to obtain a series of images of the amplitude and phase distribution in the plane of nanodisc arrays (sample plane) while we swept the illumination wavelength in the 10 nm steps across the whole accessible spectral range of our microscope. In the subset of measured series of phase images, presented in [Figure 2c](#) (top), we can observe a rapid phase flip that moves toward arrays filled with larger discs (and with resonances at higher wavelengths) as the illumination wavelength is increased. The speckles observed in [Figure 2c](#) do not correspond to individual antennas as the size of these speckles (about $1.4 \mu\text{m}$) is pronouncedly larger than the antenna pitch (up to 400 nm for the largest antennas), as apparent from the zoom-in view (see [Supporting Information, Figure S5](#)). The random noise is caused by fabrication imperfections in terms of a variation of nanodisc dimensions (see further discussion in [Supporting Information](#)). To better visualize the information contained in the phase images, we

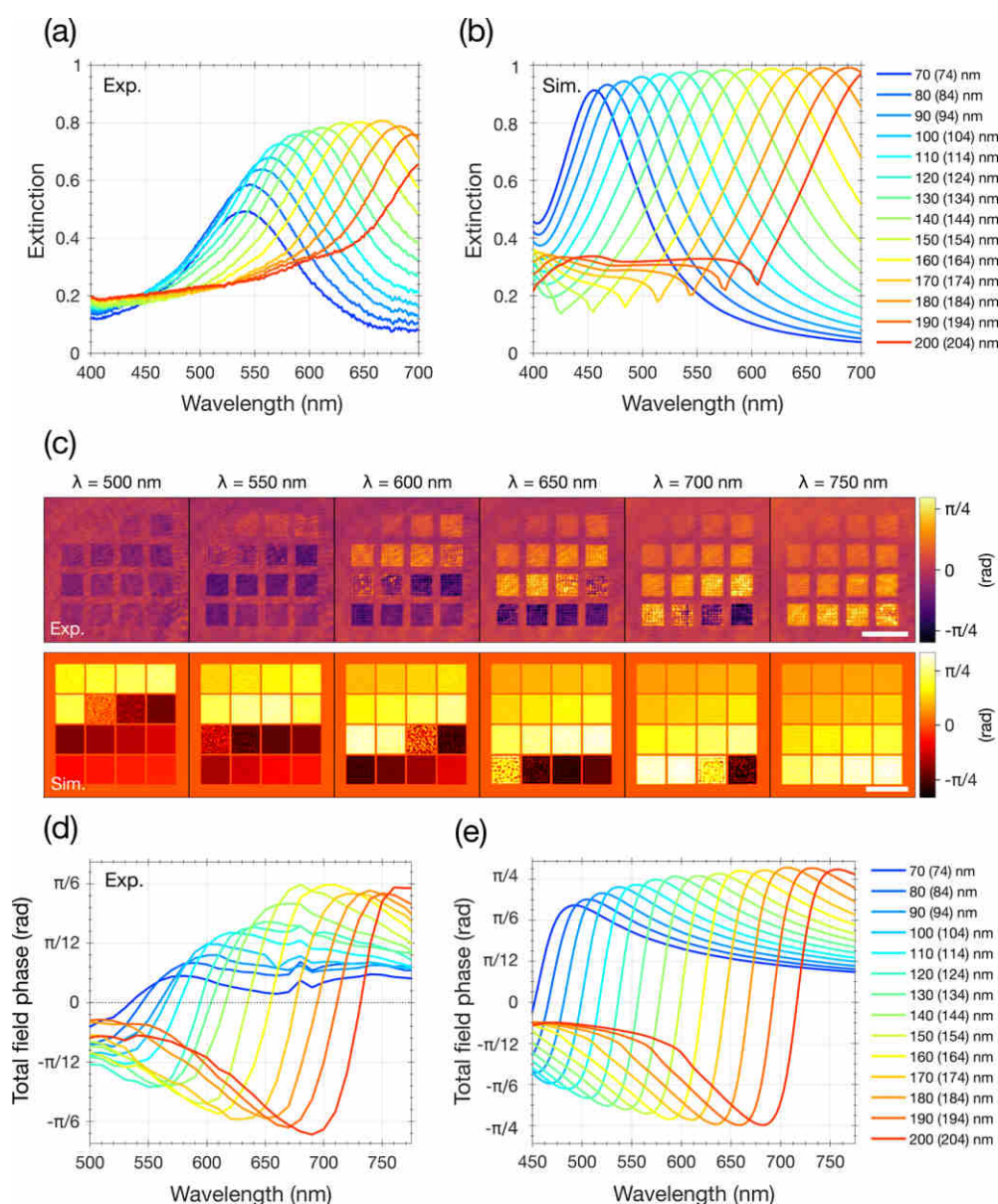


Figure 2. (a) Experimental and (b) FDTD-calculated extinction spectra of silver nanodisc arrays on glass. Both show characteristic plasmon resonances that red-shift with increasing disc diameter (indicated by line colors). The experimental extinction in (a) has been calculated by eq 1, T/T_{REF} , where T is the transmission through the nanodisc array and (T_{REF}) the transmission through the bare substrate. (c) Quantitative phase images of silver nanodisc arrays at a selected subset of illumination wavelengths, measured in CCHM (top) and theoretically calculated (bottom). Scale bars are 20 μm . (d, e) Spectra of the total field phase at nanodisc arrays of various dimensions extracted from the full set of measured CCHM images (d) and from numerical simulations (e). The small mismatch between measured extinction maxima and zero-crossings in the measured phase spectra is caused by a slight oxidation of our silver nanodiscs during the time between the two measurements.

have extracted the average phase value for each array at all measured wavelengths and plotted the resulting spectra in Figure 2d (while compensating for a small background signal by subtracting the phase outside the arrays). Note that there is no need for phase unwrapping and corrections for 2π phase ambiguity when dealing with plasmonic metasurfaces since their phase shifts are typically smaller than 2π .

Apparently, the phase measured by CCHM exhibits an S-shaped flip from positive (above resonance) to negative values (below resonance) and goes to zero in both regions far from the resonance. That is in contrast with considerations based on a classical model of simple resonant systems, where the phase

changes monotonically from 0 to π (with $\pi/2$ at the resonance).⁴³ Although a single silver disc can be definitely considered such a simple resonant system, propagation of the scattered field through the microscope can lead to its significant phase shift. Furthermore, as the CCHM microscope detects the superposition of this scattered field with the original incident wave, the final phase image strongly depends on their relative amplitudes and phases. In the following, we will present a theoretical description of CCHM image formation that incorporates both of these aspects and is capable to fully reproduce the experimental data. With the optical response of individual building blocks as the only input of our model, we

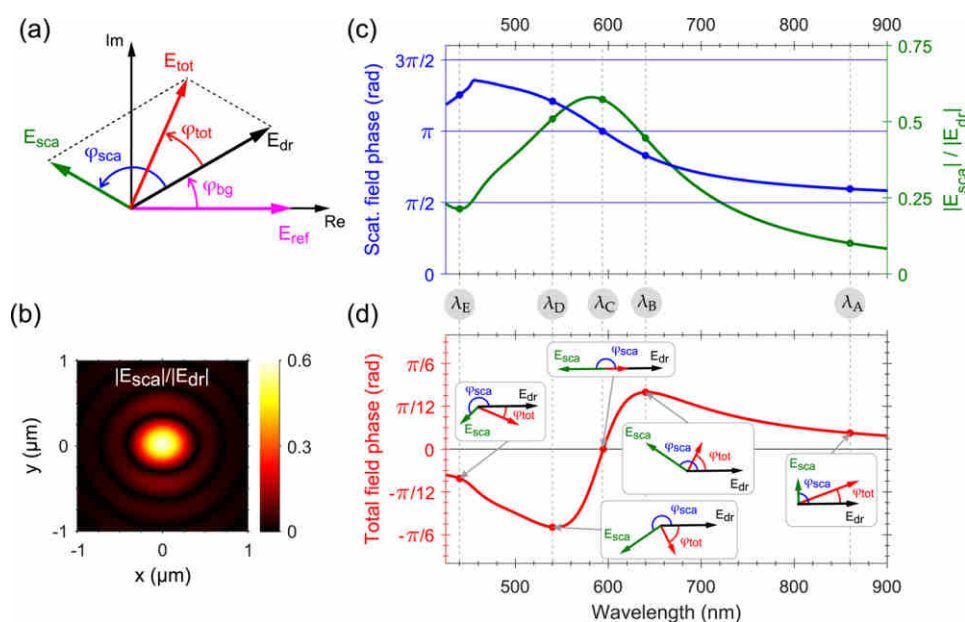


Figure 3. (a) Phasor diagram of the fields forming the signal measured in CCHM. Note that we follow a convention where a phase shift in the counterclockwise direction represents a phase delay. The field that drives the plasmonic structures is denoted as E_{dr} and it is phase-shifted with respect to the reference field E_{ref} by φ_{bg} due to an inevitable path difference between sample and reference arms. The field scattered by nanodiscs (E_{sca}) lags behind the driving one by an angle φ_{sca} . The total measured field E_{tot} is a sum of E_{dr} and E_{sca} , and its phase shift φ_{tot} with respect to the driving field is the ultimate quantity measured in CCHM. (b) Calculated distribution of the electric field amplitude produced in the image plane of the microscope (NA = 0.95, $\lambda = 580$ nm) by a single silver nanodisc with diameter 154 nm. (c) Calculated scattered field phase (blue) and amplitude (green) spectra for the 154 nm nanodisc; the values at each wavelength are extracted from the central part of field distributions that were obtained the same way as in (b); the values of the amplitude and phase at selected wavelengths $\lambda_A - \lambda_E$ (labeled by dots) are used in (d) to elucidate the total field phase formation using phasor diagrams. (d) Calculated phase spectrum of the total field resulting from the superposition of scattered and driving fields (with the superposition of phasors sketched in the boxes).

can thus calculate the phase distribution produced by an arbitrary metasurface that is directly comparable with the experiment.

Theoretical Description. To describe how the fields in the object plane translate into the image plane and how the spatial filtering (diffraction) affects the detected phase distribution, we shall invoke the theory of CCHM imaging, which is fundamentally similar to the classical Abbe theory.^{44,45} Disregarding the geometrical effects like inversion and magnification, the image formed in the image plane corresponds to the convolution of the distribution of sources in the object plane with the amplitude point spread function (PSF) of the microscope. In the reciprocal space this amounts to multiplying the Fourier transform of the sources' distribution by the coherent transfer function (CTF) of the microscope (i.e., the Fourier transform of the PSF). The above can be mathematically put as

$$E_{sca}(x_{img}, y_{img}) \sim \iint dx_{obj} dy_{obj} \text{PSF}(x_{img} - x_{obj}, y_{img} - y_{obj}) P(x_{obj}, y_{obj}) \\ = \iint_{-\infty}^{\infty} dk_x dk_y e^{ik_x x_{img}} e^{ik_y y_{img}} P(k_x, k_y) \text{CTF}(k_x, k_y) \quad (1)$$

where x_{img} , y_{img} denote the spatial coordinates in the image plane, x_{obj} , y_{obj} are the spatial coordinates in the object plane, k_x , k_y stand for the coordinates in the reciprocal space, and $P(x_{obj}, y_{obj})$ defines the distribution of the sources within the object plane. Note that throughout this work we shall use PSF and CTF to describe the impulse response of our system to a radiating point dipole. In this way the sources $P(x_{obj}, y_{obj})$ can be readily identified as the polarization vector induced within

our plasmonic structures. Furthermore, instead of using the continuous polarization vector we shall work with its integral over the volume of the individual discs, thus approximating them with a set of discrete point dipoles $p(x_{obj}, y_{obj})$ of matching strength and orientation. Since the size of the discs is relatively small and we are interested only in the dipolar mode, such simplification should not significantly affect our results.

The electric field in the object plane produced by a single point dipole located at (x_{obj}, y_{obj}) can be written in a compact form using the formalism of the dyadic Green's functions

$$E_{sca}^{dip}(x, y) = \omega^2 \mu_0 \hat{G}(x - x_{obj}, y - y_{obj}) p \\ = \omega^2 \mu_0 \iint_{-\infty}^{\infty} dk_x dk_y e^{ik_x x} e^{ik_y y} \hat{M}(k_x, k_y) p e^{-ik_x x_{obj}} e^{-ik_y y_{obj}} \quad (2)$$

where ω is the angular frequency, μ_0 the free space permeability, and p denotes the complex amplitude of the dipole. Note that the dyadic Green's function \hat{G} and its Fourier transform \hat{M} generally depend on the surroundings of the dipole. In the context of our experiment, we consider the dipole to be situated right on top of a planar glass substrate with an index of refraction $n = 1.47$. The relevant expressions for \hat{G} and \hat{M} can be found in ref 46.

Due to a cutoff in the spatial frequencies that can be transferred by an optical microscope (a fact that also manifests as the inherent inability to resolve two objects less than roughly half a wavelength apart), we need to restrict the integration in eq 2 to a region $\sqrt{k_x^2 + k_y^2} \leq \text{NA} \frac{2\pi}{\lambda}$, where λ denotes the free

space wavelength and NA is the numerical aperture of the used microscope objective (NA = 0.95 in our experiment).⁴⁴ Although a more elaborate procedure incorporating parameters such as the numerical apertures of all microscope components or the type of illumination is available,⁴⁷ the simple cutoff is sufficient for our purposes since it adequately captures the major principle of image formation in CCHM. Finally, the expressions for CTF and PSF, which allow us to mathematically propagate the fields produced by an arbitrary planar distribution of dipoles, are obtained by comparing eq 2 to eq 1

$$\text{CTF}(k_x, k_y) = \omega^2 \mu_0 \hat{M}(k_x, k_y) \Theta \left(\text{NA} \frac{2\pi}{\lambda} - \sqrt{k_x^2 + k_y^2} \right) \quad (3)$$

$$\begin{aligned} \text{PSF}(x, y) &= \text{IFFT}\{\text{CTF}(k_x, k_y)\} \\ &= \omega^2 \mu_0 \iint_{\sqrt{k_x^2 + k_y^2} \leq \text{NA} 2\pi/\lambda} dk_x dk_y e^{ik_x x} e^{ik_y y} \hat{M}(k_x, k_y) \end{aligned} \quad (4)$$

where $\Theta(z)$ is the Heaviside step function and $\text{IFFT}\{\}$ stands for the inverse Fourier transform.

Relying on the assumption that our nanodiscs are small enough to be approximated by point dipoles of matching optical properties, we used eq 4 to calculate the field distribution (essentially the PSF) produced in the image plane of the microscope by a single $D = 150$ nm silver disc at $\lambda = 580$ nm (see Figure 3b). Note that although we consider here a solitary disc, its optical response already incorporates the interaction with neighboring nanodiscs since it was obtained from the FDTD simulations of infinite nanodisc arrays (that were presented in Figure 2b). As expected for a point-like source, the calculated field distribution is very similar to an Airy disc. We repeated the calculations for all other experimentally relevant wavelengths, extracted the amplitudes and also the values of phase at centers of the Airy discs, and plotted the resulting spectra in Figure 3c. The phase spectrum strongly resembles the aforementioned ideal resonant system with two exceptions: The minor ones are the sharp feature around 460 nm and the incomplete π -shift when crossing the resonance. The former is due to the diffractive coupling between nanodiscs, while the latter has its origin in the optical properties of silver, namely in the interband transitions that affect the real part of its dielectric function even far away from their spectral positions.⁴⁷ The third, more important difference, is that the scattered field gains an additional $\pi/2$ phase delay after it propagates through the microscope. This can be readily explained on mathematical grounds: The field of a point dipole at its origin can be broken down into two parts, a purely real diverging term that is in phase with the driving field and a purely imaginary term, which is finite but shifted in phase by $\pi/2$. Importantly, only the latter is transferred through the microscope and participates in the image formation.⁴⁶ Thus, in the end, the diffraction not only limits the spatial resolution we can achieve, but it can also distort the information about the phase distribution in the object plane. As we shall see below, the additional $\pi/2$ phase delay is the main reason why our experimental data assume both positive and negative values. Note that one encounters the same phase shift when looking at the field scattered by an infinite plane of dipoles.⁴⁸ In that case, however, the reason for the $\pi/2$ lag is not the integration limits (i.e., spatial-frequency cutoff) but the singularity in the integrand itself (i.e., the $P(k_x, k_y)$ being the Dirac function).

Diffraction effects obviously play a critical role in the quantitative phase imaging. However, there is one more aspect of CCHM that must be taken into account in order to explain the characteristic S-shape of the measured phase spectra: In holographic microscopy, the electromagnetic field in the object arm is generally a superposition of scattered (or otherwise perturbed) and incident waves. It is this “total field” that eventually interferes with the field transferred by the reference arm. We present a simple phasor representation of the aforementioned process in Figure 3a. The phasor of the reference field E_{ref} (violet arrow) is fixed to the x -axis, the phasor of the driving field E_{dr} (black arrow) is shifted with respect to the reference field by an angle φ_{bg} that corresponds to the path difference between the object and reference arms caused by instrument imperfections. This background signal is eventually compensated by simple subtraction from the resulting image. The phasor of the field scattered by the plasmonic structures E_{sca} (green arrow) lags behind the driving field by an angle φ_{sca} as discussed above (see Figure 3c). The quantity we ultimately measure with CCHM is the phase delay φ_{tot} of the total field $E_{\text{tot}} = E_{\text{dr}} + E_{\text{sca}}$ (red arrow) with respect to the driving field.³⁸ The presented phasor representation helps us to recognize the fact that the driving field is superposed to the scattered field and significantly alters the wavefront unless we filter it out, for example, via polarization resolved measurements. Therefore, a valid comparison between experiment and theory requires not only consideration of the field scattered by individual nanodiscs as in Figure 3c, but rather the full analysis of the total field E_{tot} , as we will demonstrate now using the schematics in Figure 3d: For wavelengths well above the resonance (λ_A), the phasor of the scattered field is almost perpendicular to the driving field ($\approx \pi/2$ delay), which is a crucial prerequisite for a high phase contrast. However, the amplitude of the scattered field is rather small and the total phase delay is therefore only minute. As we move closer toward the resonance (λ_B), the orientation of the scattered field becomes largely antiparallel to the driving field ($\approx 4\pi/5$ delay). This is, however, redeemed by a substantial increase in its amplitude, resulting in a high total phase contrast. Once the scattered and driving fields become purely antiparallel (λ_C), the total phase rapidly falls to zero and turns increasingly negative as the phase delay of the scattered field exceeds π (λ_D). Eventually, by moving away from the resonance (λ_E) the amplitude of the scattered field starts to drop again and the phase contrast vanishes.

In order to theoretically validate the measured CCHM images that are shown in Figure 2d, we employed the same procedure as in the calculation of the field intensity and total phase maps of a single disc: First of all, we approximate each disc by a point dipole positioned at its center. The strength and the phase of the dipole was estimated from FDTD simulations, which were performed separately for each disc size. The resulting scattered field in the image plane is obtained, after transition from the continuous (eq 1) to the discrete representation, either by taking the convolution of PSF (defined in eq 4) with the discrete distribution of dipoles or alternatively by multiplying its Fourier transform by CTF (defined in eq 3) and taking the inverse Fourier transform

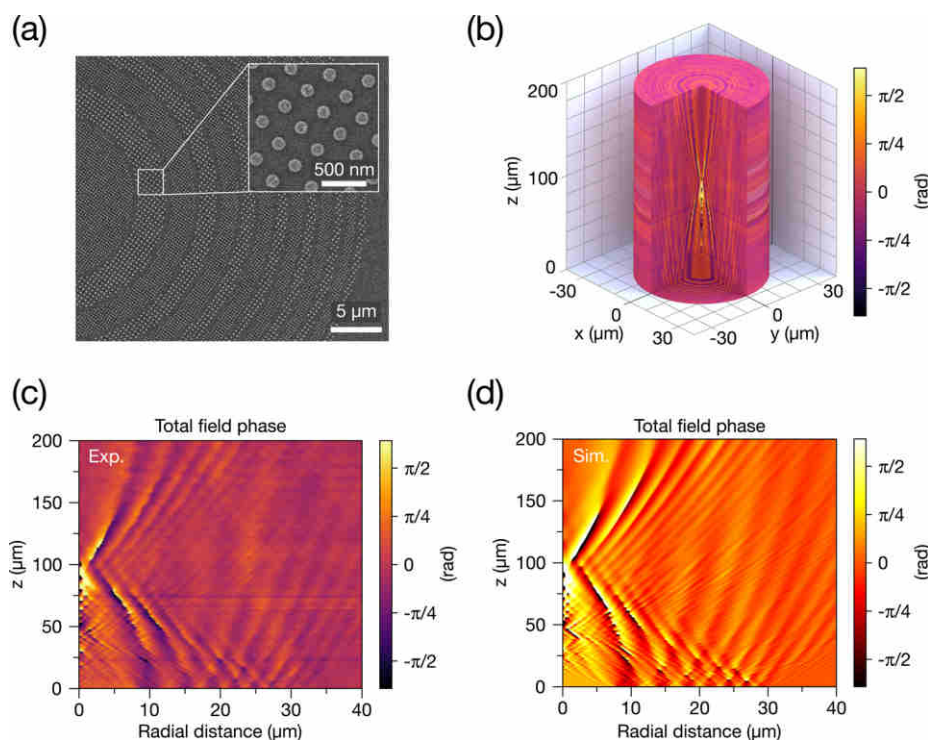


Figure 4. (a) SEM micrograph of the fabricated zone plate where individual zones are formed by silver nanodiscs (130 and 190 nm). (b) 3D visualization of the measured total phase distribution in the half-space above the plasmonic zone-plate. Measured (c) and simulated (d) phase map in the xz -plane above the zone plate where the main ($z \approx 100 \mu\text{m}$) and subsidiary ($z \approx 50 \mu\text{m}$, $z \approx 25 \mu\text{m}$) focal points are clearly distinguishable close to the zero radial distance.

$$E_{\text{sca}}^{\text{array}}(x_{\text{img}}, y_{\text{img}}) = \sum_{j=1}^N \text{PSF}(x_{\text{img}} - x_j, y_{\text{img}} - y_j) p_j$$

$$= \iint_{\sqrt{k_x^2 + k_y^2} \leq NA/2\pi/\lambda} dk_x dk_y e^{ik_x x_{\text{img}}} e^{ik_y y_{\text{img}}} \text{CTF}(k_x, k_y) p(k_x, k_y) \quad (5)$$

where p_j are the complex amplitudes of the individual dipoles and $p(k_x, k_y) = \sum_{j=1}^N p_j e^{-ik_x x_j} e^{-ik_y y_j}$ is the Fourier transform of their distribution. Even though CTF offers a closed form expression and the equidistant distribution of dipoles in arrays of a particular size makes the calculation of its Fourier transform rather straightforward, the calculations in the reciprocal space are prone to numerical errors. For that reason, we decided to follow the PSF convolution approach and utilize the whole framework established so far to calculate a series of total phase images. We present the results directly below the corresponding experimentally obtained images in Figure 2c. From their comparison, it is clear that our model reproduces well all the important features observed in the measured CCHM images. In order to make a quantitative comparison, we have extracted the average phase from each array in our calculated images and plotted the resulting spectra in Figure 2e. While there are slight differences in the phase flip amplitudes and spectral positions, our model reproduces nicely the experimental data shown in Figure 2d, with their characteristic S-shaped phase flips situated close to the disc resonances. The ability of our theoretical model to reliably predict and interpret the outcomes of measurements facilitates the use of CCHM for design of plasmonic devices with complex functionality, namely for direct

inspection and verification of inner workings of metasurfaces based on new and unexplored concepts.

3D Phase Imaging. So far we have used CCHM only for evaluation of phase distribution in a single plane. Its major benefit, however, is the ability to produce 3D phase maps by z -stacking images taken at different defocus levels. To demonstrate the usefulness of this feature for characterization of plasmonic metamaterials, we have decided to perform a 3D phase imaging of the electric field produced behind a focusing plasmonic metasurface based on the principle of a zone plate (see Figure 4a). The zone plate was designed and fabricated according to a well-known analytical model which, for a desired focal length ($100 \mu\text{m}$), defines the overall geometry.⁴⁹ We have chosen the operational wavelength in the middle of our experimental range (630 nm) and filled the individual zones with previously studied nanodiscs (130 and 190 nm) that maximized the phase difference at this wavelength (approximately $\pi/5$, see Figure 2d). Although the analytical model prescribes a π -phase difference between the neighboring zones, even such a considerably smaller phase step is sufficient for acceptable focusing performance.

Using the precise sample positioning, we were then able to create a 3D experimental quantitative phase map of wavefronts propagating from the zone plate by z -stacking a series of CCHM phase images acquired above the sample plane in $1 \mu\text{m}$ steps (Figure 4b). The detail of the cross-section in the xz -plane, displayed in Figure 4c, clearly reveals stripes of constant phase originating at the sample surface and converging toward the main focal point at $z \approx 100 \mu\text{m}$, which is in good agreement with its planned position. We can also observe subsidiary focal points. Their positions, however, do not coincide with those of

an ideal zone plate (e.g., the secondary focal point should be situated at one-third and not at one-half of the zone plate focal length). We ascribe this discrepancy to the fact that the field distribution produced by our nanodiscs does not fully match the one from the design. More specifically, the transition between neighboring zones is not abrupt but gradual which makes them effectively narrower (see Figure S6 and related discussion in Supporting Information). Nevertheless, by feeding the real nanodisc distribution into the theoretical apparatus described above, we obtained a phase distribution (see Figure 4d) that perfectly matches experimental results, including the positions of the subsidiary focal points. The large phase values near the focal point nicely illustrate the fact that the total phase is a product of both phase and also amplitude of the scattered wave.

CONCLUSIONS

We have demonstrated the suitability of CCHM for optical characterization of plasmonic metasurfaces, especially those where the desired optical properties are achieved by an appropriate modulation of the phase of the passing electromagnetic wave. As a benchmark test we performed spectroscopic measurements of phase shifts produced by silver nanodisc arrays. The major advantage of CCHM over other phase-measuring techniques is its ability to provide spatially resolved phase information in the whole field of view in a single measurement at time scales limited only by the camera framerate. For a first time, we have utilized this unique property to create a 3D phase map of fields transmitted through a plasmonic zone plate. In addition, by recalling the basic principles governing the image formation in conventional microscopy, we have developed a model that enables theoretical prediction of the CCHM measurement results. This includes even measurements of phase changes caused by arbitrarily distributed scatterers, which constitutes a major and novel extension of the CCHM to the domain of nanophotonics. Although all our measurements are performed with plasmonic metasurfaces in the visible range, the whole concept can be extended not only to shorter or longer wavelengths (provided that the setup is composed of suitable optical elements and detector) but also to other types of metasurfaces (e.g., dielectric ones). We believe that the qualities described in this contribution justify our view of CCHM as a unique imaging technique with the potential to become a versatile tool in metamaterial and metasurface research.

METHODS

Coherence Controlled Holographic Microscopy. In our experiments, we used a coherence-controlled holographic microscope (CCHM) that was developed at our institute and is now commercially available (Tescan Q-Phase).⁵⁰ Although it is conventionally used for fast imaging of live biological samples using incoherent light sources,³⁸ we equipped it with a supercontinuum laser (Fianium SC480–10) with an acousto-optic tunable filter (AOTF) to perform spectrally resolved imaging of plasmonic nanostructures. The principle of CCHM is based on off-axis incoherent holography.^{38,47} Briefly, the light coming from a source is split into object and reference arms first (see Figure 5). The light in the object arm interacts with a studied sample, whereas the light in the identical reference arm passes only through a reference sample without nanoantennas. Both beams then interfere in a CCD detector plane, forming a

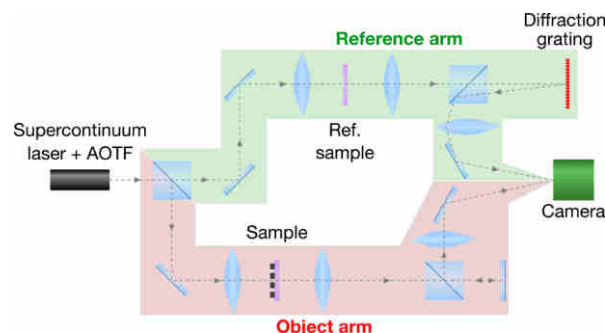


Figure 5. Optical setup of a coherence-controlled holographic microscope equipped with a supercontinuum laser and an acousto-optic tunable filter (AOTF). Detailed description can be found, for example, in ref 38.

pattern of interference fringes. As the beams interfere at an angle (off-axis setup), the phase-containing terms in the Fourier transform of the resulting interference pattern are (spatially) separated from amplitude-only ones. This allows us to independently extract these terms and then numerically reconstruct the complex amplitude of the wave at each point of the studied sample.⁵¹ Note that the lateral resolution of CCHM is comparable to conventional wide field optical microscopes, as discussed and demonstrated in ref 38. The temporal resolution depends on the camera sensitivity and light source intensity. Typical acquisition time for one phase image was approximately 300 ms with the current experimental setup. Covering the whole spectral region with 31 phase images usually took us several minutes, mainly due to lags caused by slow manual control of the laser wavelength.

Sample Fabrication. All nanostructures were fabricated by electron beam lithography (Tescan Mira 3 SEM with Raith Elphy EBL system) in 140 nm thick PMMA layer on a glass substrate. A thin layer of conductive polymer (Allresist Electra 92) was spin-coated on top of the resist to reduce charging effects during the exposure. Samples were developed in MIBK:IPA (1:3) solution (immersed for 60 s) and rinsed in IPA for 30 s. The development was followed by evaporation of 3 nm of Ti and 40 nm of Ag. The fabrication was finished by the lift-off process in acetone.

ASSOCIATED CONTENT

Supporting Information

The Supporting Information is available free of charge on the ACS Publications website at DOI: 10.1021/acsp Photonics.7b00022.

FDTD simulations of solitary nanodiscs and calculated field distributions behind ideal and realistic zone plates (PDF).

AUTHOR INFORMATION

Corresponding Author

*E-mail: sikola@fme.vutbr.cz.

ORCID

Filip Ligmajer: 0000-0003-0346-4110

Petr Dvořák: 0000-0003-3659-9249

Notes

The authors declare the following competing financial interest(s): J.B. and A.K. are employees of Tescan, a company

producing coherence-controlled holographic microscopes such as the one used in this study. All other authors declare no competing interests.

ACKNOWLEDGMENTS

This work was supported by the Grant Agency of the Czech Republic (Grant Nos. 15-21581S and 15-14612S), MEYS CR (Project No. LQ1601 – CEITEC 2020), Technology Agency of the Czech Republic (Grant No. TE01020233), and BUT (Project No. FSI/STI-J-15-2897). We acknowledge CEITEC Nano Research Infrastructure and Core Facility Experimental Biophotonics (both supported by MEYS CR within projects LM2015041 and LM2015062) for providing us with access to their facilities.

REFERENCES

- (1) Yu, N.; Capasso, F. Flat Optics with Designer Metasurfaces. *Nat. Mater.* **2014**, *13*, 139–150.
- (2) Kildishev, A. V.; Boltasseva, A.; Shalae, V. M. Planar Photonics with Metasurfaces. *Science* **2013**, *339*, 1232009–1232009.
- (3) Zouhdi, S.; Sihvola, A.; Vinogradov, A. P. *Metamaterials and Plasmonics: Fundamentals, Modelling, Applications*; Springer Netherlands: Dordrecht, 2009.
- (4) Yu, N.; Genevet, P.; Kats, M. A.; Aieta, F.; Tetienne, J.-P.; Capasso, F.; Gaburro, Z. Light Propagation with Phase Discontinuities: Generalized Laws of Reflection and Refraction. *Science* **2011**, *334*, 333–337.
- (5) Li, Z.; Palacios, E.; Butun, S.; Aydin, K. Visible-Frequency Metasurfaces for Broadband Anomalous Reflection and High-Efficiency Spectrum Splitting. *Nano Lett.* **2015**, *15*, 1615–1621.
- (6) Khorasaninejad, M.; Chen, W. T.; Oh, J.; Capasso, F. Super-Dispersive Off-Axis Meta-Lenses for Compact High Resolution Spectroscopy. *Nano Lett.* **2016**, *16*, 3732–3737.
- (7) Khorasaninejad, M.; Zhu, A. Y.; Roques-Carnes, C.; Chen, W. T.; Oh, J.; Mishra, I.; Devlin, R. C.; Capasso, F. Polarization-Insensitive Metalenses at Visible Wavelengths. *Nano Lett.* **2016**, *16*, 7229–7234.
- (8) Garoli, D.; Zilio, P.; Gorodetski, Y.; Tantussi, F.; De Angelis, F. Beaming of Helical Light from Plasmonic Vortices via Adiabatically Tapered Nanotip. *Nano Lett.* **2016**, *16*, 6636–6643.
- (9) Ee, H.-S.; Agarwal, R. Tunable Metasurface and Flat Optical Zoom Lens on a Stretchable Substrate. *Nano Lett.* **2016**, *16*, 2818–2823.
- (10) Zhan, A.; Colburn, S.; Trivedi, R.; Fryett, T. K.; Dodson, C. M.; Majumdar, A. Low-Contrast Dielectric Metasurface Optics. *ACS Photonics* **2016**, *3*, 209–214.
- (11) Lin, D.; Holsteen, A. L.; Maguid, E.; Wetzstein, G.; Kik, P. G.; Hasman, E.; Brongersma, M. L. Photonic Multitasking Interleaved Si Nanoantenna Phased Array. *Nano Lett.* **2016**, *16*, 7671–7676.
- (12) Huntington, M. D.; Lauhon, L. J.; Odom, T. W. Subwavelength Lattice Optics by Evolutionary Design. *Nano Lett.* **2014**, *14*, 7195–7200.
- (13) Zhao, Y.; Alù, A. Tailoring the Dispersion of Plasmonic Nanorods To Realize Broadband Optical Meta-Waveplates. *Nano Lett.* **2013**, *13*, 1086–1091.
- (14) Abasahl, B.; Dutta-Gupta, S.; Santschi, C.; Martin, O. J. F. Coupling Strength Can Control the Polarization Twist of a Plasmonic Antenna. *Nano Lett.* **2013**, *13*, 4575–4579.
- (15) Duempelmann, L.; Luu-Dinh, A.; Gallinet, B.; Novotny, L. Four-Fold Color Filter Based on Plasmonic Phase Retarder. *ACS Photonics* **2016**, *3*, 190–196.
- (16) Zeng, J.; Gao, J.; Luk, T. S.; Litchinitser, N. M.; Yang, X. Structuring Light by Concentric-Ring Patterned Magnetic Metamaterial Cavities. *Nano Lett.* **2015**, *15*, 5363–5368.
- (17) Huang, L.; Chen, X.; Mühlenbernd, H.; Zhang, H.; Chen, S.; Bai, B.; Tan, Q.; Jin, G.; Cheah, K.-W.; Qiu, C.-W.; Li, J.; Zentgraf, T.; Zhang, S. Three-Dimensional Optical Holography Using a Plasmonic Metasurface. *Nat. Commun.* **2013**, *4*, n/a.
- (18) Chen, W. T.; Yang, K.-Y.; Wang, C.-M.; Huang, Y.-W.; Sun, G.; Chiang, I.-D.; Liao, C. Y.; Hsu, W.-L.; Lin, H. T.; Sun, S.; Zhou, L.; Liu, A. Q.; Tsai, D. P. High-Efficiency Broadband Meta-Hologram with Polarization-Controlled Dual Images. *Nano Lett.* **2014**, *14*, 225–230.
- (19) Zheng, G.; Mühlenbernd, H.; Kenney, M.; Li, G.; Zentgraf, T.; Zhang, S. Metasurface Holograms Reaching 80% Efficiency. *Nat. Nanotechnol.* **2015**, *10*, 308–312.
- (20) Huang, Y.-W.; Chen, W. T.; Tsai, W.-Y.; Wu, P. C.; Wang, C.-M.; Sun, G.; Tsai, D. P. Aluminum Plasmonic Multi-Color Meta-Hologram. *Nano Lett.* **2015**, *15*, 3122–3127.
- (21) Oates, T. W. H.; Wormeester, H.; Arwin, H. Characterization of Plasmonic Effects in Thin Films and Metamaterials Using Spectroscopic Ellipsometry. *Prog. Surf. Sci.* **2011**, *86*, 328–376.
- (22) Chen, W.-Y.; Lin, C.-H.; Chen, W.-T. Plasmonic Phase Transition and Phase Retardation: Essential Optical Characteristics of Localized Surface Plasmon Resonance. *Nanoscale* **2013**, *5*, 9950–9956.
- (23) Neuman, T.; Alonso-González, P.; Garcia-Etxarri, A.; Schnell, M.; Hillenbrand, R.; Aizpurua, J. Mapping the near Fields of Plasmonic Nanoantennas by Scattering-Type Scanning near-Field Optical Microscopy. *Laser Photon. Rev.* **2015**, *9*, 637–649.
- (24) Taubner, T.; Hillenbrand, R.; Keilmann, F. Performance of Visible and Mid-Infrared Scattering-Type near-Field Optical Microscopes. *J. Microsc.* **2003**, *210*, 311–314.
- (25) Li, Y.; Zhou, N.; Raman, A.; Xu, X. Three-Dimensional Mapping of Optical near Field with Scattering SNOM. *Opt. Express* **2015**, *23*, 18730–18735.
- (26) Drachev, V. P.; Cai, W.; Chettiar, U.; Yuan, H.-K.; Sarychev, A. K.; Kildishev, A. V.; Klimeck, G.; Shalae, V. M. Experimental Verification of an Optical Negative-Index Material. *Laser Phys. Lett.* **2006**, *3*, 49–55.
- (27) Stoller, P.; Jacobsen, V.; Sandoghdar, V. Measurement of the Complex Dielectric Constant of a Single Gold Nanoparticle. *Opt. Lett.* **2006**, *31*, 2474–2476.
- (28) Börzsönyi, A.; Kovács, A. P.; Görbe, M.; Osvay, K. Advances and Limitations of Phase Dispersion Measurement by Spectrally and Spatially Resolved Interferometry. *Opt. Commun.* **2008**, *281*, 3051–3061.
- (29) O'Brien, K.; Lanzillotti-Kimura, N. D.; Suchowski, H.; Kante, B.; Park, Y.; Yin, X.; Zhang, X. Reflective Interferometry for Optical Metamaterial Phase Measurements. *Opt. Lett.* **2012**, *37*, 4089.
- (30) Gennaro, S. D.; Sonnefraud, Y.; Verellen, N.; Van Dorpe, P.; Moshchalkov, V. V.; Maier, S. a.; Oulton, R. F. Spectral Interferometric Microscopy Reveals Absorption by Individual Optical Nanoantennas from Extinction Phase. *Nat. Commun.* **2014**, *5*, 3748.
- (31) Pshenay-Severin, E.; Falkner, M.; Helgert, C.; Pertsch, T. Ultra Broadband Phase Measurements on Nanostructured Metasurfaces. *Appl. Phys. Lett.* **2014**, *104*, 221906.
- (32) Lepetit, L.; Chériaux, G.; Joffe, M. Linear Techniques of Phase Measurement by Femtosecond Spectral Interferometry for Applications in Spectroscopy. *J. Opt. Soc. Am. B* **1995**, *12*, 2467.
- (33) Meshulach, D.; Yelin, D.; Silberberg, Y. Real-Time Spatial-spectral Interference Measurements of Ultrashort Optical Pulses. *J. Opt. Soc. Am. B* **1997**, *14*, 2095.
- (34) Dorrer, C.; Belabas, N.; Likforman, J.-P.; Joffe, M. Spectral Resolution and Sampling Issues in Fourier-Transform Spectral Interferometry. *J. Opt. Soc. Am. B* **2000**, *17*, 1795.
- (35) Dolling, G. Simultaneous Negative Phase and Group Velocity of Light in a Metamaterial. *Science* **2006**, *312*, 892–894.
- (36) Onishi, S.; Matsushita, K.; Oi, J.; Harada, T.; Kusaba, M.; Hirokawa, K.; Kannari, F. Spatiotemporal Control of Femtosecond Plasmon Using Plasmon Response Functions Measured by near-Field Scanning Optical Microscopy (NSOM). *Opt. Express* **2013**, *21*, 26631.
- (37) Lošťák, M.; Chmélík, R.; Slabá, M.; Slabý, T. Coherence-Controlled Holographic Microscopy in Diffuse Media. *Opt. Express* **2014**, *22*, 4180.

- (38) Slabý, T.; Kolman, P.; Dostál, Z.; Antoš, M.; Lošták, M.; Chmelík, R. Off-Axis Setup Taking Full Advantage of Incoherent Illumination in Coherence-Controlled Holographic Microscope. *Opt. Express* **2013**, *21*, 14747.
- (39) Suck, S. Y.; Bidault, S.; Bonod, N.; Collin, S.; Bardou, N.; De Wilde, Y.; Tessier, G. Digital Heterodyne Holography Reveals the Non-Quasi-Static Scattering Behaviour of Transversally Coupled Nanodisk Pairs. *Int. J. Opt.* **2012**, *2012*, 1–8.
- (40) Kretschmann, E.; Raether, H. Radiative Decay of Non-Radiative Surface Plasmons Excited by Light. *Z. Naturforsch., A: Phys. Sci.* **1968**, *23*, 2135–2136.
- (41) Auguié, B.; Barnes, W. L. Collective Resonances in Gold Nanoparticle Arrays. *Phys. Rev. Lett.* **2008**, *101*, 1–4.
- (42) Kravets, V. G.; Schedin, F.; Grigorenko, a. N. Extremely Narrow Plasmon Resonances Based on Diffraction Coupling of Localized Plasmons in Arrays of Metallic Nanoparticles. *Phys. Rev. Lett.* **2008**, *101*, 1–4.
- (43) Yu, N.; Capasso, F. Flat Optics: Controlling Wavefronts with Optical Antenna Metasurfaces. *IEEE Antennas Propag. Soc. AP-S Int. Symp.* **2013**, *19*, 2341–2342.
- (44) Born, M.; Wolf, E. *Principles of Optics*; Cambridge University Press, 1999.
- (45) Chmelík, R.; Slabá, M.; Kollárová, V.; Slabý, T.; Lošták, M.; Čolláková, J.; Dostál, Z. The Role of Coherence in Image Formation in Holographic Microscopy. *Prog. Opt.* **2014**, *59*, 267–336.
- (46) Novotny, L.; Hecht, B. *Principles of Nano-Optics*, 2nd ed.; Cambridge University Press, 2012.
- (47) Cai, W.; Shalaev, V. *Optical Metamaterials*; Springer: New York, NY, 2010.
- (48) Fujiwara, H. *Spectroscopic Ellipsometry*; Wiley Blackwell (John Wiley & Sons), 2007.
- (49) Attwood, D. *Soft X-Rays and Extreme Ultraviolet Radiation: Principles and Applications*; Cambridge University Press, 2007.
- (50) Kolman, P.; Chmelík, R. Coherence-Controlled Holographic Microscope. *Opt. Express* **2010**, *18*, 21990.
- (51) Kreis, T. Digital Holographic Interference-Phase Measurement Using the Fourier-Transform Method. *J. Opt. Soc. Am. A* **1986**, *3*, 847.

ORIGINAL ARTICLE

Plasmonic enhancement and polarization dependence of nonlinear upconversion emissions from single gold nanorod@SiO₂@CaF₂:Yb³⁺,Er³⁺ hybrid core–shell–satellite nanostructures

Jijun He¹, Wei Zheng², Filip Ligmajer³, Chi-Fai Chan⁴, Zhiyong Bao¹, Ka-Leung Wong⁴, Xueyuan Chen², Jianhua Hao¹, Jiyun Dai¹, Siu-Fung Yu¹ and Dang Yuan Lei¹

Lanthanide-doped upconversion nanocrystals (UCNCs) have recently become an attractive nonlinear fluorescence material for use in bioimaging because of their tunable spectral characteristics and exceptional photostability. Plasmonic materials are often introduced into the vicinity of UCNCs to increase their emission intensity by means of enlarging the absorption cross-section and accelerating the radiative decay rate. Moreover, plasmonic nanostructures (e.g., gold nanorods, GNRs) can also influence the polarization state of the UC fluorescence—an effect that is of fundamental importance for fluorescence polarization-based imaging methods yet has not been discussed previously. To study this effect, we synthesized GNR@SiO₂@CaF₂:Yb³⁺,Er³⁺ hybrid core–shell–satellite nanostructures with precise control over the thickness of the SiO₂ shell. We evaluated the shell thickness-dependent plasmonic enhancement of the emission intensity in ensemble and studied the plasmonic modulation of the emission polarization at the single-particle level. The hybrid plasmonic UC nanostructures with an optimal shell thickness exhibit an improved bioimaging performance compared with bare UCNCs, and we observed a polarized nature of the light at both UC emission bands, which stems from the relationship between the excitation polarization and GNR orientation. We used electrodynamic simulations combined with Förster resonance energy transfer theory to fully explain the observed effect. Our results provide extensive insights into how the coherent interaction between the emission dipoles of UCNCs and the plasmonic dipoles of the GNR determines the emission polarization state in various situations and thus open the way to the accurate control of the UC emission anisotropy for a wide range of bioimaging and biosensing applications.

Light: Science & Applications (2017) 6, e16217; doi:10.1038/lsa.2016.217; published online 19 May 2017

Keywords: Förster resonance energy transfer; gold nanorods; lanthanide-doped upconversion nanocrystals; plasmon-enhanced nonlinear fluorescence; polarization modulation

INTRODUCTION

Lanthanide-doped upconversion nanocrystals (UCNCs), which can absorb low-energy photons and emit high-energy photons by an anti-Stokes process^{1–3}, show great promise for numerous applications ranging from bioimaging^{4,5} and photothermal therapy^{6,7} to solar cells^{8,9}. Compared with conventional fluorescent materials such as organic dyes or quantum dots, lanthanide-doped UCNCs exhibit some unique properties, including excellent photostability, narrow and tunable emission bands, long luminescence lifetimes and relatively low cytotoxicity. Furthermore, their near-infrared excitation band is located in the so-called ‘biological transparency window’, thus promising high-penetration depth and low-photothermal damage in biological tissues². However, UCNCs often suffer from low-emission

efficiency due to several factors such as structural defects, the small absorption cross-sections of the activator ions and the intrinsic nature of the anti-Stokes emission^{10,11}.

Many chemical and physical methods have been developed to enhance the emission efficiency of UCNCs, including host lattice manipulation^{12,13}, surface passivation^{14–17}, energy transfer modulation^{18–20} and the plasmonic enhancement effect^{21–34}. Using the last approach, the UC luminescence efficiency is highly increased by coupling UCNCs with localized surface plasmon resonances (LSPRs)—collective oscillations of free electrons in metal nanoparticles such as gold nanospheres or gold nanorods (GNRs). The two possible mechanisms of plasmon-enhanced UC luminescence can be simply summarized as follows. First, the plasmon-enhanced local

¹Department of Applied Physics, The Hong Kong Polytechnic University, Hong Kong, China; ²Key Laboratory of Optoelectronic Materials Chemistry and Physics, Fujian Institute of Research on the Structure of Matter, Chinese Academy of Sciences, Fuzhou, Fujian 350002, China; ³Central European Institute of Technology, Brno University of Technology, Brno 61669, Czech Republic and ⁴Department of Chemistry, Hong Kong Baptist University, Hong Kong, China
Correspondence: DY Lei, Email: dylei@polyu.edu.hk

Received 23 February 2016; revised 31 August 2016; accepted 4 September 2016; accepted article preview online 6 September 2016

electric field in the vicinity of the metal nanoparticles can increase the excitation rate of the lanthanide sensitizer ions (e.g., Yb^{3+}), which then absorb more near-infrared photons. Second, in the UC emission process, the radiative decay rate of the lanthanide activator ions (e.g., Er^{3+} , Tm^{3+} or Ho^{3+}) can also be increased by a plasmon-induced localized density of photonic states³⁵. Most of the previous studies on the coupling of UC luminescence and LSPR have focused on obtaining the highest possible intensity enhancement by means of harnessing both of these approaches^{23,24,26,29,36,37}. However, in the study by van Hulst and co-workers³⁸ on the closely related subject of plasmon-modulated fluorescence, it was established that it is not just the intensity of the emitted light that is modified by the LSPR but also its polarization state. So far, this aspect has been largely overlooked in studies on the plasmonic modulation of UC luminescence.

In the present work, we report the simultaneous luminescence intensity enhancement and polarization state modulation in $\text{GNR@SiO}_2\text{:CaF}_2\text{:Yb}^{3+},\text{Er}^{3+}$ (core-shell-satellite) hybrid nanostructures. First, the distance dependence of the plasmon-enhanced UC luminescence was investigated by gradually increasing the thickness of the silica spacer, and the advantage of the hybrid nanostructures was demonstrated in bioimaging experiments. Next, we examined the polarization state of the UC emissions from individual hybrid nanostructures. We found that the interaction between the two emission bands of the UCNCs and the two orthogonal plasmonic modes of the GNRs results in an extraordinary polarization state of the UC luminescence, which is controlled by the excitation polarization. We also performed comprehensive electrodynamic simulations to obtain a better understanding of the underlying physical mechanisms responsible for our experimental observations. By linking the results of experiments and simulations in the realm of Förster resonance energy transfer theory, we were able to fully explain how the spatial relationships between regions of enhanced electric field intensity and dipole orientations lead to the enhancement or suppression of UC emissions with a particular polarization state. To the best of our knowledge, this is the first work analyzing the plasmon-induced polarization state of the UC luminescence—a feature that is particularly important for the polarization-sensitive applications of fluorescence in diagnostics and imaging^{39–43}.

MATERIALS AND METHODS

Materials

Tetrachloroauric acid ($\text{HAuCl}_4\cdot 3\text{H}_2\text{O}$), sodium borohydride (NaBH_4), cetyltrimethyl ammonium bromide (CTAB), ascorbic acid (AA), silver nitrate (AgNO_3) and tetraethyl orthosilicate (TEOS) were purchased from Sigma-Aldrich (St. Louis, MO, United States). All chemicals were used without further treatment, and deionized water was used for all experiments.

Synthesis of the GNRs

The GNRs were synthesized according to the seed-mediated growth method⁴⁴. The seed solution was prepared by mixing 0.25 ml of 0.01 M HAuCl_4 with 9.75 ml of 0.1 M CTAB solution, and then 0.6 ml freshly prepared ice-cold aqueous solution of 0.01 M NaBH_4 was injected into it. After a 1 min rapid inversion, the seed solution was kept at room temperature for 2–5 h before use. Next, 2 ml of 0.01 M HAuCl_4 , 0.4 ml of 0.01 M AgNO_3 , 0.32 ml of 0.1 M AA, 0.8 ml of 1 M HCl and 40 ml 0.1 M CTAB were mixed to form the growth solution for GNRs. Finally, the growth was initiated by injecting 10 μl of the seed solution into the growth solution, and the solution was left undisturbed at room temperature for at least 6 h. The as-prepared GNRs have an ensemble longitudinal LSPR wavelength at 724 nm. By

adding 1.5 ml more 0.01 M HAuCl_4 , the longitudinal LSPR wavelength will be reduced to 655 nm through the anisotropic oxidation of the GNRs.

Synthesis of mesoporous silica coating on the GNRs

The GNR@SiO_2 nanostructures were obtained via a modified Stöber method⁴⁵. A total of 10 ml of as-synthesized GNRs were centrifuged once at 6500 r.p.m. for 20 min to remove the excess CTAB. The precipitate was re-dispersed into 10 ml of deionized water, and 100 μl of 0.1 M NaOH aqueous solution was added to adjust the pH of the solution to 10–11. Then, 25, 30, 40, 50 and 65 μl of 10 vol% TEOS methanol solution were, respectively, added under gentle stirring. The mixture solution was kept stirring for 12 h until the reactions were complete. The resultant hybrid nanostructures were washed twice at 5500 r.p.m. for 10 min to remove the CTAB and re-dispersed in water of the same volume.

Synthesis of $\text{CaF}_2\text{:Yb}^{3+},\text{Er}^{3+}$ NCs and attachment to GNRs

The synthesis procedures of the hybrid nanostructures were briefly described earlier⁴⁶. Monodisperse, sub-10 nm $\text{CaF}_2\text{:18% Yb}^{3+}, 2\% \text{Er}^{3+}$ NCs were synthesized through a sodium co-doping co-precipitation route with a subsequent acid-washing treatment. The detailed fabrication procedures can be found in our previous works^{47,48}. The GNR@SiO_2 showed a negative zeta potential of -24.8 mV, derived from the dissociation of silanols. The $\text{CaF}_2\text{:Yb}^{3+},\text{Er}^{3+}$ NCs were positively charged, with a zeta potential of $+49.7$ mV. Therefore, by mixing 0.2 ml of ligand-free UCNC solution with 3 ml of silica-coated GNR solution, the UCNCs were attached on the surface of the GNR@SiO_2 through electrostatic attraction after 10 h.

Cell incubation

Human cervical carcinoma HeLa cells were purchased from American Type Culture Collection (ATCC) (#CCL-185, ATCC, Manassas, VA, USA). The HeLa cells were cultured in Dulbecco's Modified Eagle Medium (DMEM) supplemented with 10% fetal bovine serum (FBS) 1% penicillin and streptomycin at 37 °C in the presence of 5% CO_2 . To apply the $\text{GNR@SiO}_2\text{:CaF}_2\text{:Yb}^{3+},\text{Er}^{3+}$ hybrid nanostructures for UC bioimaging, the HeLa cells were incubated in DMEM containing 1 $\mu\text{g ml}^{-1}$ of the hybrid nanostructures at 37 °C for 24 h under 5% CO_2 and then washed with PBS sufficiently to remove the excess hybrid nanostructures. A control sample was also prepared by applying bare $\text{CaF}_2\text{:Yb}^{3+},\text{Er}^{3+}$ NCs for the bioimaging.

In-vitro UC luminescence bioimaging

The bioimaging of the HeLa cells incubated with pristine $\text{CaF}_2\text{:Yb}^{3+},\text{Er}^{3+}$ NCs and hybrid $\text{GNR@SiO}_2\text{:CaF}_2\text{:Yb}^{3+},\text{Er}^{3+}$ nanostructures was performed on a commercial confocal laser scanning microscope. The samples were excited by a 980 nm wavelength laser, and two visible UC emission channels were detected in the green (500–600 nm) and red (600–700 nm) spectral regions.

Characterization

The morphological features of the pristine GNR@SiO_2 and $\text{GNR@SiO}_2\text{:CaF}_2\text{:Yb}^{3+},\text{Er}^{3+}$ hybrid nanostructures were characterized with a JEM-2100F field-emission transmission electron microscope (TEM) (JEOL USA, Peabody, MA, USA) operating at 300 kV and an upgraded JEOL JSM-633F field-emission scanning electron microscope (SEM) (JEOL USA, Peabody, MA, USA). The absorption spectra of the GNRs in water were measured with a Shimadzu UV2550 Spectrophotometer (Shimadzu Corporation, Kyoto, Japan). Zeta-potential measurements were carried out using a Malvern Zetasizer

3000 HAS (Malvern Instruments Ltd, Malvern, UK). The UC luminescence spectra of the pristine and hybrid UCNCs in the solution phase were collected on a UK Edinburgh Instruments FLS900 Fluorescence Spectrometer (Edinburgh Instruments Ltd, Livingston, UK) equipped with a CNI MDL-III-980 diode laser (Changchun New Industries Optoelectronics Tech. Co., Ltd, Changchun, China). Lifetime measurements were performed on a UK Edinburgh Instruments FLS900 Fluorescence Spectrometer with a time-correlated single-photon counting module, whereas a 980 nm pulse laser generated by a Continuum Panther EX optical parametric oscillator (Continuum located, San Jose, CA, USA) was used as the excitation source. The single-particle scattering and UC luminescence spectra of the individual nanostructures were recorded with a home-built, polarization-resolved dark-field microscope equipped with a CNI MDL-III-980 diode laser. All the measured spectra were corrected for the spectral sensitivity and polarization response of the system.

RESULTS AND DISCUSSION

The synthesis procedure of the $\text{GNR@SiO}_2\text{:CaF}_2\text{:Yb}^{3+},\text{Er}^{3+}$ core-shell-satellite nanostructures is illustrated in Figure 1a. First, CTAB-coated GNRs were grown in an aqueous solution using a seed-mediated method^{49,50}. It is well-known that GNRs exhibit two LSPR modes: a transverse one and a longitudinal one. The plasmon wavelength of the latter can be flexibly tuned across the whole visible and near-infrared region by precisely tailoring the aspect ratio of the GNRs⁵¹. To study the influence of the LSPR on the UC emission properties, here we tuned the transverse and longitudinal LSPR wavelengths of the GNRs to match the two emission bands of the $\text{CaF}_2\text{:Yb}^{3+},\text{Er}^{3+}$ NCs. The average length and diameter of the synthesized CTAB-coated GNRs that met these requirements were determined to be 82 ± 7 nm and 32 ± 3 nm, respectively (see TEM images in Figure 1c–1e and Supplementary Fig. S1). If the UCNCs were attached in direct contact with the GNRs, the excited activators could undergo nonradiative decay due to energy and possible charge transfer to the metal nanoparticles. This would result in a lower luminescence enhancement or even quenching. To avoid this undesired process and examine the distance-dependent plasmon-enhanced

UC luminescence, we synthesized several batches of GNRs covered with mesoporous silica spacers with several thicknesses (9, 15, 19, 23 and 35 nm) via a modified Stöber method (see TEM images in Figure 1c and 1d; Supplementary Fig. S1a–S1e)⁴⁵. After the silica coating, the longitudinal plasmon peak red-shifts by 10–30 nm due to the increased refractive index of the surrounding medium, as shown in Supplementary Fig. S2 (Ref. 44). The $\text{CaF}_2\text{:Yb}^{3+},\text{Er}^{3+}$ NCs were synthesized through a sodium co-doping co-precipitation route followed by an acid-washing treatment^{47,48}, which provides a solution of monodisperse, positively charged NCs with good water solubility^{47,52}. Their average diameter was determined to be 7.5 nm from a TEM analysis (see Figure 1b for a representative TEM micrograph). As silica in aqueous solution is typically negatively charged, the UCNCs can be easily attached onto the surface of the GNR@SiO_2 nanostructures through electrostatic attraction⁵³. The TEM images in Figure 1e and Supplementary Fig. S1f–S1h show that the $\text{GNR@SiO}_2\text{:CaF}_2\text{:Yb}^{3+},\text{Er}^{3+}$ hybrid nanostructures were successfully formed after the simple mixing of the two constituent solutions. A detailed TEM analysis showed that nearly all the GNR@SiO_2 nanoparticles were attached to a certain number of UCNCs, and approximately 50% of the UCNCs were left unbound.

The UC luminescence was measured using illumination by a 980-nm continuous wave diode laser with a power density of ~ 10 W cm^{-2} . Figure 2a shows that the emission spectrum of the bare $\text{CaF}_2\text{:Yb}^{3+},\text{Er}^{3+}$ NCs exhibits two emission bands centered at 540 nm (green) and 660 nm (red), which correspond to the $^2\text{H}_{11/2}, ^4\text{S}_{3/2} \rightarrow ^4\text{I}_{15/2}$ and $^4\text{F}_{9/2} \rightarrow ^4\text{I}_{15/2}$ transitions of Er^{3+} ions, respectively (see the energy-level diagram in Supplementary Fig. S3)^{3,10}. Although the UC emission spectra of the $\text{GNR@SiO}_2\text{:CaF}_2\text{:Yb}^{3+},\text{Er}^{3+}$ hybrid nanostructures show the same spectral shape as the bare UCNCs, the emission intensity is strongly influenced by the distance between the GNRs and UCNCs (the silica shell thickness), as shown in Figure 2b. Figure 2c shows the extracted emission enhancement factor as a function of the silica shell thickness by calculating the ratio of the integrated emission intensities (510–570 nm for green emission and 630–680 nm for red emission) of each hybrid nanostructure and the

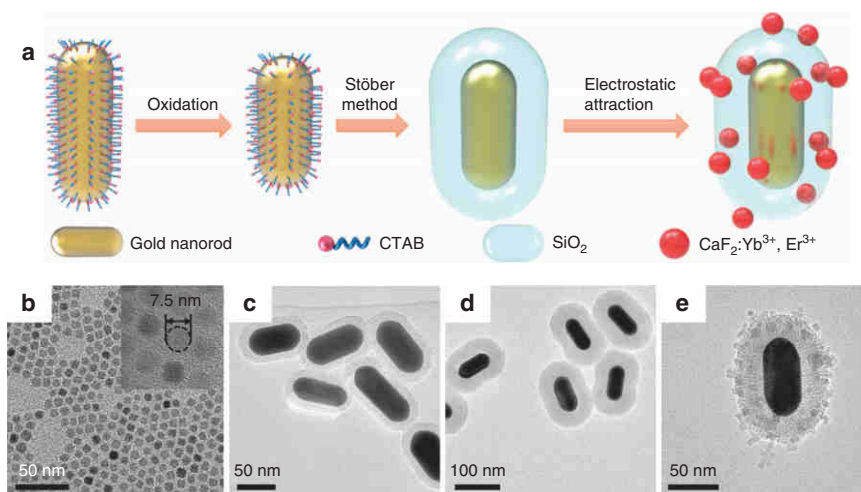


Figure 1 (a) Synthesis procedure of the $\text{GNR@SiO}_2\text{:CaF}_2\text{:Yb}^{3+},\text{Er}^{3+}$ hybrid nanostructures. CTAB-capped GNRs were oxidized to decrease their aspect ratio and obtain a suitable LSPR wavelength. In the next step, the GNRs were covered with a silica spacer, and the UCNCs were then attached to their surface by electrostatic attraction. (b–e) TEM images of (b) bare $\text{CaF}_2\text{:Yb}^{3+},\text{Er}^{3+}$ NCs, (c) GNR@SiO_2 (9 nm) nanostructures, (d) GNR@SiO_2 (35 nm) nanostructures and (e) GNR@SiO_2 (23 nm) $\text{@CaF}_2\text{:Yb}^{3+},\text{Er}^{3+}$ hybrid nanostructures.

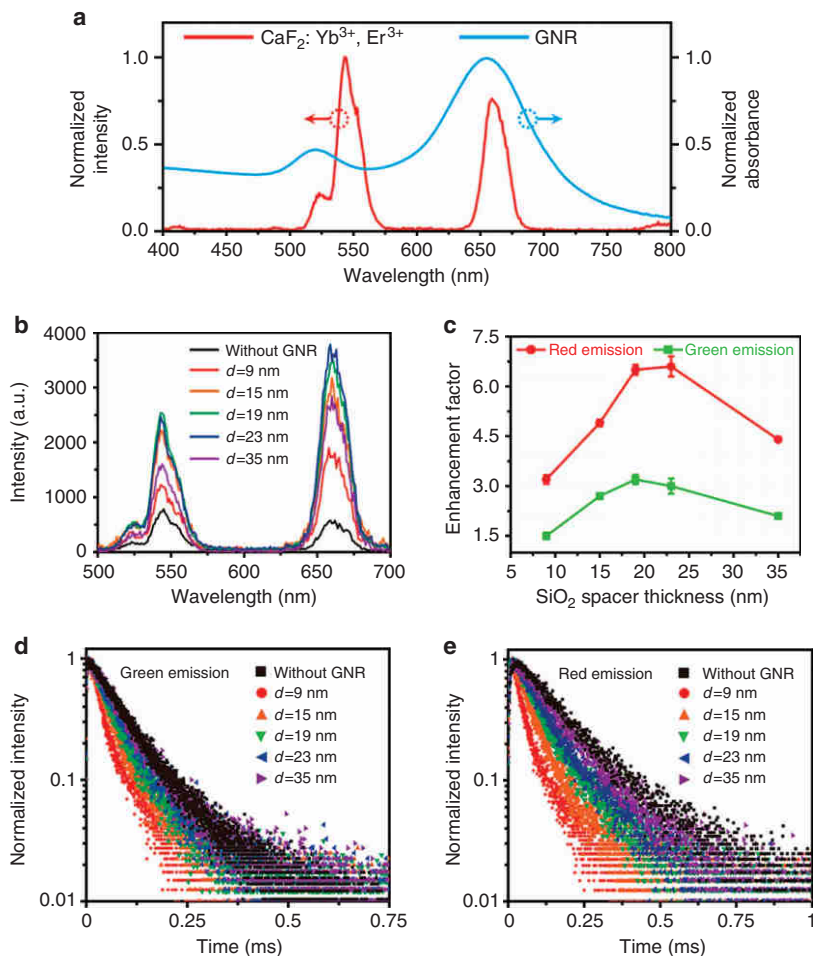


Figure 2 (a) Emission spectrum of bare $\text{CaF}_2:\text{Yb}^{3+}, \text{Er}^{3+}$ NCs (red) and absorbance spectrum of GNRs in water (blue). (b) Emission spectra of bare $\text{CaF}_2:\text{Yb}^{3+}, \text{Er}^{3+}$ NCs and GNR@ $\text{SiO}_2/\text{CaF}_2:\text{Yb}^{3+}, \text{Er}^{3+}$ nanostructures with different silica spacer thicknesses (the concentration of UCNCs in all samples was fixed at 0.32 mg ml^{-1}). (c) Luminescence enhancement factors for both green and red emission bands as a function of the silica spacer thickness. The enhancement factors were extracted from the emission spectra shown in b. Error bars in the figure represent the standard deviation of three enhancement factors calculated for three measurements. (d, e) UC luminescence decay curves for the d green and e red emissions of GNR@ $\text{SiO}_2/\text{CaF}_2:\text{Yb}^{3+}, \text{Er}^{3+}$ with different silica spacer thicknesses.

bare UCNCs. First, the intensity enhancement of both the green and red emission bands increases as the thickness of the silica spacer increases from 9 nm. When the spacer thickness reaches 19 nm, the enhancement factor of the green emission reaches its maximum value (3). However, the highest value of the red emission enhancement factor (6.7) is substantially larger than that of its green counterpart and occurs with a slightly thicker silica spacer (23 nm). Although the difference between the enhancement factors of the different UC emission bands has been reported by other groups, the enhancement factor of the green emission was usually the larger of the two^{22–24,29,54}. We ascribe this contradiction to the fact that in those works, the plasmonic materials of choice were metal nanospheres, which have only one plasmonic peak located near the green emission band of Er^{3+} ions, unlike the GNRs used in our experiment^{23,24,32,54}. It is natural that in those cases, the LSPR will have significant influence only on the green emission band. In our case, the stronger longitudinal plasmon resonance of the GNRs generates a larger enhancement factor for the

red emission than for the green emission. Note that the enhancement factor reported here could be significantly underestimated due to the presence of unbound UCNCs in the mixed solution and that the enhancement factor for the red emission band can be well above an order of magnitude on attaching all the UCNCs onto the GNR@ SiO_2 .

To test the utility of the GNR@ $\text{SiO}_2/\text{CaF}_2:\text{Yb}^{3+}, \text{Er}^{3+}$ hybrid nanostructures in biological imaging, we carried out a cellular imaging experiment with HeLa cells. The hybrid nanostructures with 19-nm thick silica shells were selected to be incubated with HeLa cells at 37°C for 24 h under 5% CO_2 . Figure 3a–3d and Supplementary Fig. S4 show images of the live HeLa cells after incubation with the hybrid nanostructures captured at randomly selected sample areas with a laser scanning confocal multiphoton microscope. We recorded the UC luminescence of the hybrid nanostructures in both the green (500–600 nm, Figure 3b) and red emission (600–700 nm, Figure 3c) channels. An overlay of the green-channel, red-channel and bright-field images demonstrates that the hybrid nanostructures had crossed

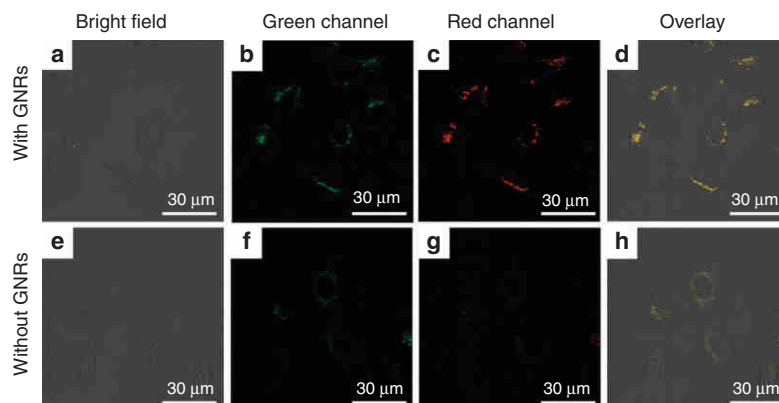


Figure 3 Confocal laser scanning microscopy images of HeLa cells incubated with GNR@SiO₂(19 nm)@CaF₂:Yb³⁺,Er³⁺ hybrid nanostructures (top row: **a**, bright field image; **b**, green channel image; **c**, red channel image and **d**, overlay imaging.) and CaF₂:Yb³⁺,Er³⁺ NCs (bottom row: **e**, bright field image; **f**, green channel image; **g**, red channel image and **h**, overlay imaging).

the cell membrane and accumulated in the cytoplasmic region. For comparison, a control cellular imaging experiment was carried out on HeLa cells incubated with bare CaF₂:Yb³⁺,Er³⁺ NCs. Under the same laser power, the UC luminescence intensity in the HeLa cells incubated with the bare UCNCs was lower than that in the cells incubated with the hybrid nanostructures. Our results demonstrate that the GNR@SiO₂@CaF₂:Yb³⁺,Er³⁺ hybrid nanostructures can be used as a promising nonlinear fluorescent probe for high-contrast bioimaging applications.

To further understand the interaction between the LSPR and UC luminescence, we measured the UC luminescence lifetimes of both GNR@SiO₂@CaF₂:Yb³⁺,Er³⁺ hybrid nanostructures and the bare CaF₂:Yb³⁺,Er³⁺ NCs. As shown in Figure 2d and 2e, the UC luminescence lifetimes of the hybrid nanostructures are significantly shorter than those of the bare UCNCs. For the thickest spacer in our experiments (35 nm), the lifetimes of both the green and red emissions are almost equal to those of the bare UCNCs (88.5 and 166.4 μs, respectively). As the thickness of the silica spacer decreases to 9 nm, the lifetimes of the two emissions reach minimum values of 39.4 and 51.3 μs, respectively. The calculation details of the UC luminescence lifetimes can be found in the Supplementary Information and Supplementary Fig. S5. This verifies the fact that—similar to the emission from plasmon-coupled fluorescence dyes—the GNRs introduce new (radiative and nonradiative) decay pathways into the emission process of the nearby UCNCs and thus reduce the luminescence lifetimes of the UCNCs⁵⁵.

Once we have understood the plasmonic enhancement properties of our hybrid nanostructures, we turn to inquire into the influences of the LSPR of the GNRs on the polarization states of the UC emissions and the relevant physical mechanisms. To that end, we studied both the scattering and fluorescence properties of the hybrid nanostructures at the single-particle level. The measurements were carried out using a home-built optical system that is adapted on the base of an Olympus BX51 optical microscope (Olympus Corporation, Tokyo, Japan) (for a scheme of our optical system, see Supplementary Fig. S6). A 100-W tungsten white-light lamp was employed as an excitation source for the dark-field scattering measurements, and a light beam of a CNI MDL-III-980 diode laser (980 nm, 1 W) was introduced into the light path by a dichroic mirror to excite the UC luminescence. The laser light was linearly polarized, and its polarization direction was precisely controlled using a 980 nm half-wave plate. Both the scattering and fluorescence signals of the individual nanostructures were collected by a

combination of an Acton SpectraPro 2300i spectrograph (Princeton Instruments, Trenton, NJ, USA) and a Princeton Instruments PIXIS 400 CCD (Princeton Instruments). During the measurement, a broadband polarizer (hereafter called an analyzer) in front of the spectrograph was rotated at 30° per step to determine the polarization state of both the scattered light and the UC emissions. The samples were prepared by depositing GNR@SiO₂(19 nm)@CaF₂:Yb³⁺,Er³⁺ nanostructures on a glass slide at a surface number density of $\sim 3 \times 10^4 \text{ mm}^{-2}$. To verify the orientation of the observed hybrid nanostructures, the samples were subsequently imaged by SEM.

The correlated SEM and scattering images of the GNR@SiO₂@CaF₂:Yb³⁺,Er³⁺ hybrid nanostructures are shown in Figure 4a. The SEM analysis confirmed that every bright spot in the scattering image corresponds to a well-separated individual hybrid nanostructure. Figure 4b shows a representative dark-field scattering spectrum of a single hybrid nanostructure selected from the ensemble shown in Figure 4a (marked with a star), with a characteristic peak at 662 nm resulting from a longitudinal LSPR. A peak corresponding to the transverse LSPR does not manifest itself in the scattering spectrum, as it is much weaker than the longitudinal one⁵⁶. Figure 4c shows a polar plot of the scattering intensity of the same single nanostructure as a function of the analyzer angle. We can observe a typical dipole-like pattern, which is well-fitted by a cosine-squared function. For convenience, the zero analyzer angle is defined as parallel to the long axis of the GNR core (as shown in the inset of Figure 4a). To analyze the polarization state of the light quantitatively, a parameter called the degree of polarization (DOP) is defined as

$$\text{DOP} = \frac{I_{\max} - I_{\min}}{I_{\max} + I_{\min}} \quad (1)$$

where I_{\max} and I_{\min} are the maximum and minimum intensities in the polar plot, respectively (a totally polarized light has a DOP of 1, whereas an un-polarized light has a DOP of 0). In our case, the large DOP of the scattered light (0.92) arises from the inherently polarized longitudinal LSPR mode of the GNR core, which can be regarded as an electric dipole oscillating along the long axis of the GNR. The orientation of a particular hybrid nanostructure can thus be easily determined from its scattering polar plot without a need for verification by SEM imaging⁵⁷.

After the scattering measurement, we switched the optical system to fluorescence mode and measured the UC emission from the very same hybrid nanostructure (Figure 5). The UC emission spectra were

recorded as the angle of analyzer varied from 0 to 2π , whereas the polarization of the excitation laser was either parallel (Figure 5a) or perpendicular (Figure 5d) to the long axis of the hybrid nanostructure,

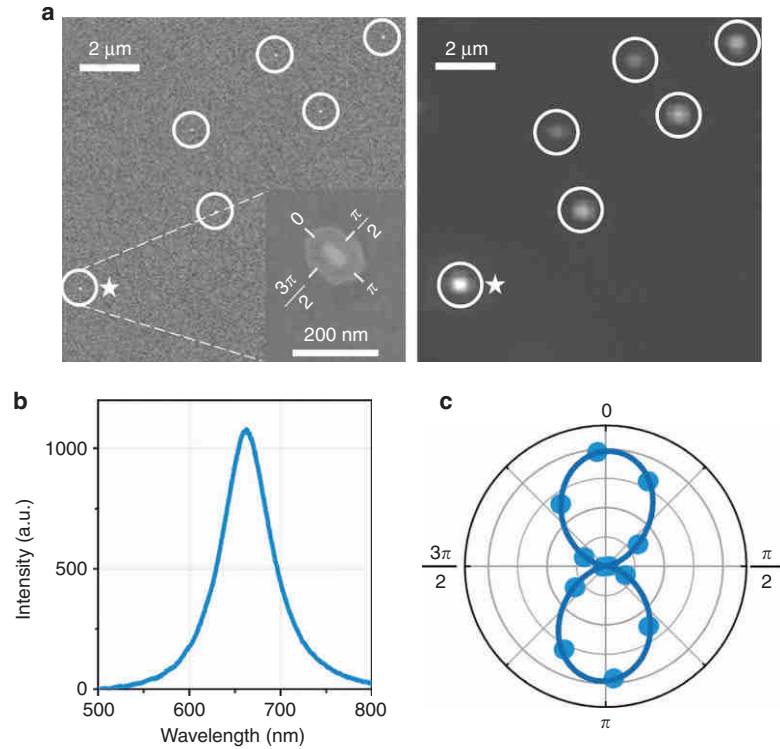


Figure 4 (a) Correlated SEM (left) and scattering (right) images of the GNR@SiO₂@CaF₂:Yb³⁺,Er³⁺ hybrid nanostructures. Each nanostructure is indicated by a circle. The inset of the SEM picture shows a selected single hybrid nanostructure that was used in the following experiments. (b) Scattering spectrum of the selected hybrid nanostructure. (c) Polar plots of the scattering intensity as a function of the analyzer angle (the solid line corresponds to a cosine-squared fit of the experimental data). For convenience, we define the analyzer angle as shown in the inset of the SEM picture in a.

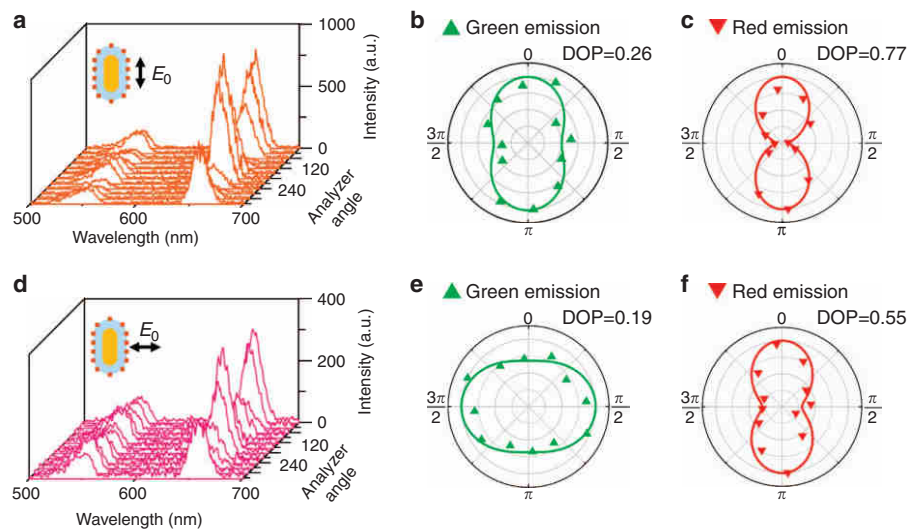


Figure 5 (a) UC emission spectra obtained as the analyzer angle varied from 0– 2π under excitation polarization parallel to the long axis of the hybrid nanostructure. From these spectra, the polar plots were extracted for the green (b) and red (c) emissions. (d) UC emission spectra under perpendicular excitation and corresponding polar plots for green (e) and red (f) emissions. The lines in the polar plots are cosine-squared fits of the experimental data. The calculated DOPs are shown in the top right corner of each polar plot.

and we observed in both cases that the emission intensities fluctuated periodically as the analyzer was rotated. These results clearly indicate that the UC luminescence became polarized when the UCNCs were in the vicinity of a GNR. To better visualize this polarization dependence in the spectra, we have extracted polar plots of the UC emission at green and red emission wavelengths (Figure 5b, 5e and 5c, 5f, respectively) and calculated the corresponding DOPs. For the case of the parallel excitation, both the green and red emissions follow the scattering polarization pattern of the GNR itself (Figure 4c), although the DOP of the green emission is slightly reduced. In the case of the perpendicular excitation, the red emission is still polarized along the long axis of the GNR like in the previous case, but surprisingly, the green emission pattern (again with somewhat lowered DOP) is now oriented in the direction perpendicular to the GNR long axis. The origins of the polarized UC emissions and their distinctly different polarization states will be described below in detail.

The emission polarization in an individual hybrid nanostructure can arise from two possible sources: one is the electromagnetic coupling between the GNR LSPR and the UC luminescence, and the other is the linearly polarized excitation⁵⁸. Let us first consider the emission polarization caused by the excitation laser. During an excitation process, when the incident electric field is parallel to the absorption dipole of a sensitizer ion (Yb^{3+}), the ion has the greatest chance to undergo an absorption process. Similarly, when the activator ion (Er^{3+}) has the same dipole orientation as the excited sensitizer, its prospect of obtaining the energy from the sensitizer is the highest. To identify the contribution of the excitation laser to the DOP of the UC luminescence, we prepared a sample with bare $\text{CaF}_2:\text{Yb}^{3+},\text{Er}^{3+}$ NCs drop-casted onto a glass slide. The UC luminescence from a $5 \times 5 \mu\text{m}$ area of the glass slide was recorded (Supplementary Fig. S7), and the corresponding DOPs were calculated in the same manner as above. The DOPs for the green and red emissions of the UCNCs without GNRs are rather low, 0.11 and 0.10, respectively, and follow the polarization of the excitation laser. This indicates that although a linearly polarized excitation laser will impose its polarization on the UC emission, its contribution is not large enough to explain the total DOP that we have observed in the case of UCNCs in the vicinity of GNRs. The rest of the DOP must therefore be a result of the coupling between the LSPR and UC luminescence. To better understand the underlying physical mechanisms of this coupling, we performed a set of finite-difference time-domain calculations, which showed us how UCNCs located at different positions contribute to the overall emission in two different experimental situations.

A GNR (diameter 32 nm, length 82 nm) was modeled as a cylindrical body capped with two hemispheres, and the dielectric function of gold was modeled using the Drude–Lorentz dispersion model⁴⁴. The GNR was covered in a uniform silica layer with a thickness of 19 nm and a refractive index of 1.43. To verify that our model was correct, we calculated the extinction cross-section spectrum of the GNR@SiO₂ nanostructure in air (Supplementary Fig. S8). The pronounced longitudinal LSPR peak at 668 nm matches well with the one in our experiment (Figure 4b). It is also worthwhile to evaluate the electric field intensity distribution around the GNR@SiO₂ nanostructure, as the UC emission intensity is proportional to the square of the excitation power density²¹. Two maps of the excitation field enhancement were thus calculated—following the experimental conditions—under a linearly polarized 980-nm excitation source either parallel (Figure 6a) or perpendicular (Figure 6b) to the long axis of the GNR@SiO₂. In the case of parallel excitation, as high as an 8-fold intensity enhancement occurs on the silica surface due to the non-resonant excitation of the longitudinal localized surface plasmon of GNR, and the enhanced

electric field is mainly concentrated in regions around the tips of the GNR@SiO₂ (we refer to them as L-positions). When the excitation polarization is perpendicular to the long axis of the GNR@SiO₂, the regions with high intensity enhancement are now located along the sides of the GNR@SiO₂ (we refer to them as T-positions), and the maximum intensity enhancement is approximately threefold.

Because the emissions from the UCNCs located in the above-mentioned regions of high-electric field intensity will dominate the overall UC emission of the whole hybrid nanostructure, we will now investigate how this fact influences the polarization state of the emitted light. To this end, we calculated the emission properties of an activator ion, represented as a Hertzian dipole, that was placed at either the T- or L-position with its emission wavelength set at either 540 nm (green emission) or 660 nm (red emission), according to the corresponding experimental values. The GNR@SiO₂ nanostructure was located at the origin, and its orientation was along the Z axis (Figure 6c). Because we expect the activator ions in our hybrid nanostructures to be randomly oriented, we consider their emissions to be a linear combination of three dipoles oriented along the X, Y and Z axes. Following the experimental conditions, we evaluated the angular dependencies of the calculated emission intensities with respect to the polarization state in the far-field Y–Z plane (corresponding to the light collection by a microscope objective), and we present them in Figure 6d as normalized polar plots. When the dipole is located in position L, both the green and red emissions are highly polarized along the long axis of the GNR@SiO₂, closely resembling the behavior observed in the experiment (Figure 5b and 5c). For the dipole in position T, the simulated polar plot confirms that the radiation patterns of the green and red emissions are perpendicular to each other and have a decreased DOP. However, despite this remarkable agreement, these results still do not clarify the underlying physical mechanism of the polarized UC emissions.

To explain the results of our experiments and simulations, we need to find an effective theoretical model that can directly analyze the polarization properties of UC emissions. Selvin and co-workers⁵⁹ reported that the emission anisotropy from lanthanide ions could be evaluated by regarding them as electric dipoles and calculating the dipole–dipole interaction. However, their method cannot account for the plasmon-induced effect on the polarized emission from Er^{3+} because it is applicable only to studying the intrinsic emission anisotropy of lanthanide ions. Here, we analyzed the coupling between GNRs and UCNCs based on the mechanism proposed by Wang's group: an emitter can transfer its energy to a nearby GNR by exciting its LSPR⁵⁸. This energy transfer is attributed to a near-field interaction between the emission dipole of the UCNC and the plasmonic dipole of the GNR. Such a process can be characterized as a type of Förster resonance energy transfer (FRET), and its efficiency can be given by

$$\eta_{\text{ET}} = \frac{1}{1 + (r/R_0)^6} \quad (2)$$

where R_0 is the so-called Förster radius, and r is the distance between the activator and the GNR core. The Förster radius is the main characteristic of the interaction strength, and it is defined as the distance at which $\eta_{\text{ET}} = 50\%$ (so that a larger R_0 means that interaction will also happen at longer distances). The Förster radius can be further determined as

$$R_0^6 \propto \kappa^2 \int_0^\infty f_A(\lambda) \epsilon_G(\lambda) \lambda^4 d\lambda \quad (3)$$

where κ is an orientation factor that is determined by the orientations of the activator and the plasmonic dipole and the relative position between them, $f_A(\lambda)$ is the normalized activator emission spectrum,

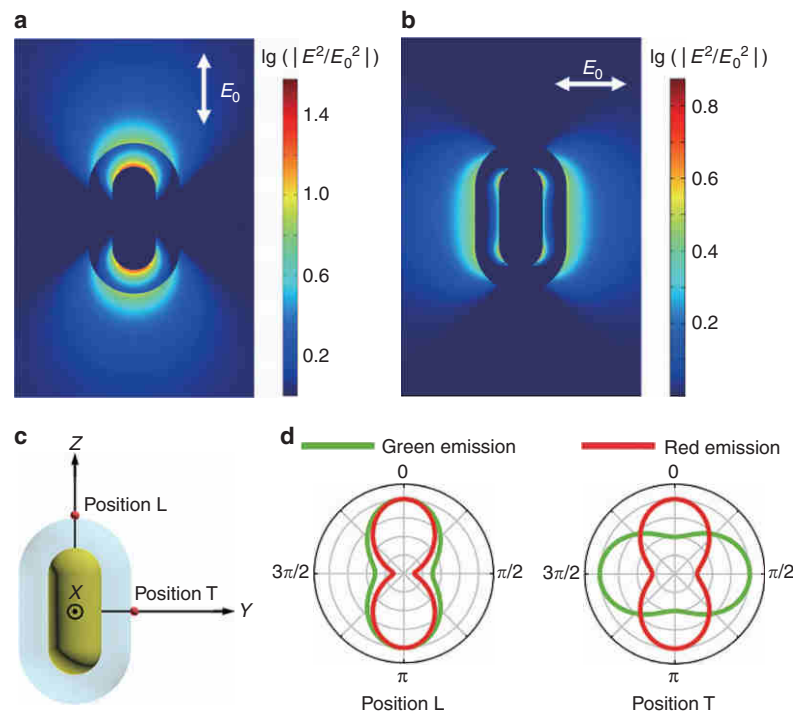


Figure 6 Calculated electric field intensity enhancement under a 980-nm excitation polarized parallel to (a) the long axis and (b) short axis of a single GNR@SiO₂ nanostructure. The enhancement factors are logarithmically scaled. (c) 3D diagram of GNR@SiO₂ with a dipole source placed at the two intersections of the silica surface with the coordinate axes Y and Z, indicated as positions T and L, respectively. (d) Polar plots of normalized calculated emission intensities of dipole sources with green (540 nm) and red (660 nm) emissions located at positions L and T.

and $\epsilon_G(\lambda)$ is the extinction spectrum of the GNR. From this equation, it follows that the FRET will occur only when there is an overlap between the $f_A(\lambda)$ and $\epsilon_G(\lambda)$. Keeping in mind the shapes of these spectra in our case (Figure 2a), this means that the green and red emissions will be modulated by the transverse and longitudinal plasmonic dipoles, respectively. To help us estimate the magnitudes of these interactions, we first calculated the FRET efficiency for the coupling between the red-emitter and the longitudinal plasmonic dipole using Equation (3) (details of the calculation in the Supplementary Information). As a consequence of the good spectral overlap, the efficiency is very high in this case, regardless of whether the emitter is located in position L (82%) or position T (94%). Combined with the large scattering cross-section of the longitudinal resonance, this leads to the red emission coming almost exclusively from the longitudinal plasmonic dipole. Accordingly, the observed red emission will follow the polarization pattern of the longitudinal dipole, as confirmed by both experiment and simulation here and also in works by others^{58,60,61}.

In the case of coupling between the green-emitter and the transverse plasmonic dipole, we have to analyze the results in more detail because the polarization of the green-emission pattern is position-dependent. First, let us explore the efficiency of the FRET. As a result of the moderate overlap and smaller extinction cross-section, the calculated efficiency (the calculation is reproduced in full detail in the Supplementary Information) is now 31% for the green emitter in position L and 84% in position T. This tells us that the green emission will be composed of contributions from both the excited transverse plasmonic dipole and the bare emitters themselves. To clarify how

these two contributions affect the shape of the polarization patterns, Figure 7 shows the calculated charge distribution on the surface of a GNR@SiO₂ excited by a green-emission dipole in various positions. For the green-emission dipole in position L, when it is oriented parallel to the transverse axis of the GNR (Figure 7a), the induced charge distribution corresponds to a resonant transverse plasmonic dipole antiparallel to the green-emission dipole⁶². The radiative but antiparallel coherent charge oscillation will tend to be canceled out by the remaining part of the green-dipole emission that did not undergo FRET. In contrast, when the dipole is oriented parallel to the longitudinal axis of the GNR (Figure 7b), a non-resonant quadrupole charge distribution is induced in the GNR. The zero spectral overlap and dark nature of this mode jointly result in the negligible influence of the GNR on the UC emission in this configuration (this is consistent with the FRET theory, as the κ factor for this case is zero—see the discussion in Supplementary Information). Therefore, although the GNR itself does not act as a nanoantenna in this case, the destructive interference in the case of the other possible orientation leads to the plasmon-modulated green emission being polarized along the long axis of the GNR, as seen in the experiment and simulation. For the green-emission dipoles located in position T, the results are in many aspects analogous. When the green-emission dipole is oriented perpendicular to the transverse axis of the GNR (Figure 7c), a non-resonant quadrupole charge distribution is induced in the GNR again, leading to the UC emission being radiated to the far-field almost unperturbed. For a parallel-oriented green-emission dipole (Figure 7d), the induced charge distribution corresponds to a resonant plasmonic dipole, but—unlike in the previous case—with a

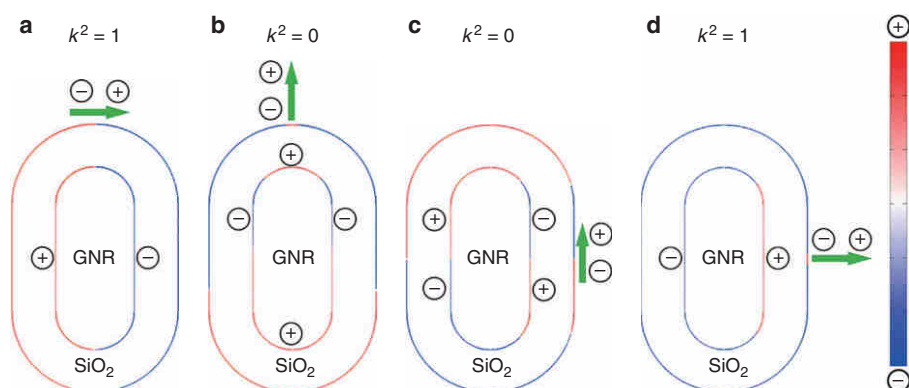


Figure 7 Calculated charge distribution on the surface of a GNR@SiO₂ excited by a green-emission dipole in position L (**a**, **b**) and position T (**c**, **d**). The dipoles are oriented either parallel **a**, **d** or perpendicular **b**, **c** to the orientation of the transverse plasmonic dipole of the GNR. Note that the green-emission dipole orientation is represented by enlarged black arrows and the nature of the induced charge configurations is labeled by +/− signs.

parallel rather than an antiparallel orientation⁶². This will lead to constructive interference with the remaining uncoupled part, and these dipoles will thus dominate the green-emission from position T, which will become polarized as the transverse dipole of the GNR.

To provide an even better visualization of the difference between the polarization patterns of green and red emissions from dipolar emitters at position T of a bare GNR (without a SiO₂ shell), we performed another set of finite-difference time-domain calculations to simulate the 3D emission patterns of a single dipolar source located in the vicinity of a bare GNR. The dipoles are set at a 45° angle to the long axis of the GNR to keep our discussion simple and at the same time to represent the real situation of the random-oriented dipoles of the UCNCs. The results of our simulations are summarized in Figure 8 for a set of distances between the dipole and the core of the GNR—covering a region between 20 and 100 nm. From the 3D emission patterns, one can clearly see that the emission pattern of a dipole in the close vicinity of a GNR becomes significantly warped as the GNR ‘imprints’ a polarized plasmon-scattered light into it, in sharp contrast to the well-known doughnut-shaped radiation pattern of a bare dipole source. In the case of the green-emission dipole, the emission pattern bends towards the Y axis as the FRET takes place, and the emission becomes modified by the transverse plasmonic dipole of the GNR (Figure 8a). When the distance between the dipole source and the GNR increases, the emission pattern returns back to the doughnut shape for a bare dipole as the modulation effect of the plasmonic dipole rapidly fades away. For the red emission dipole in the closest vicinity of the GNR, the FRET efficiency approaches 100%, and the emission pattern is dominated by the longitudinal dipole of the GNR (Figure 8b). This influence decreases much slowly owing to the larger Förster radius for the red emission (see the comparison of the calculated Förster radii for the GNR@SiO₂ nanostructure shown in Supplementary Table S2).

Because the plasmon-induced polarized UC emission can be observed only at the single-particle level, the emission intensity from one GNR@SiO₂@CaF₂:Yb³⁺,Er³⁺ hybrid nanostructure is very low, which limits its potential applications in real life. In the last section of this paper, we propose a template-assisted self-assembly method to obtain an intense polarized UC emission from an array of hybrid nanostructures. In this approach, a transparent glass substrate would be first patterned with a series of slots using electron-beam lithography to act as a template. The GNR@SiO₂@CaF₂:Yb³⁺,Er³⁺ hybrid

nanostructures could be assembled into the slots by a template-assisted self-assembly method reported by Kagan’s group^{25,31}. The shape of the slots should be precisely designed so that each slot could be occupied by only one hybrid nanostructure. Figure 9 shows the schematic of an array of GNR@SiO₂@CaF₂:Yb³⁺,Er³⁺ hybrid nanostructures assembled on a transparent glass template. When the polarization of the excitation laser is parallel to either the long or short axis of the hybrid nanostructure, this array structure could generate polarized UC emissions with strong intensity, and the polarization direction could be easily switched by excitation polarization. The proposed system can find wide applications ranging from illuminators in spectrometers to polarization-sensitive nanoscale photodetectors^{40,63}.

CONCLUSIONS

In summary, we developed a facile and effective method for the large-scale synthesis of hybrid GNR@SiO₂@CaF₂:Yb³⁺,Er³⁺ core-shell-satellite nanostructures. By the precise control of the thickness of the silica shell, the distance-dependent plasmon-enhanced UC luminescence was investigated. The highest UC emission enhancement was obtained for the shell thickness ~20 nm, and the enhancement factors reached 3 and 6.7 for the green and red emissions, respectively. Furthermore, we fully analyzed the polarization state of the UC emissions from a single hybrid nanostructure illuminated by an excitation laser with polarization parallel or perpendicular to the long axis of the GNR. Our results demonstrate the unusual polarized nature of the light at the two UC emission bands, which was dictated by the relationship between the excitation polarization and the GNR orientation, namely, that the polarization of the red emission is insensitive to the polarization state of the excitation laser, whereas the green emission follows the excitation polarization. Utilizing electrodynamic calculations and FRET theory, we analyzed the complicated relationship between the emission dipoles and plasmonic dipoles and elucidated how their orientations and mutual positions determine the polarization state of the UC emission in various situations. Our findings open a new method to control the UC emission polarization by introducing a plasmonic nanomaterial with a specific structure. Finally, our bioimaging experiments and proposed ordered plasmonic UC nanostructure arrays demonstrate that this technique can bring novel functions to UCNCs and is therefore relevant and advantageous for all applications based on their extraordinary properties.

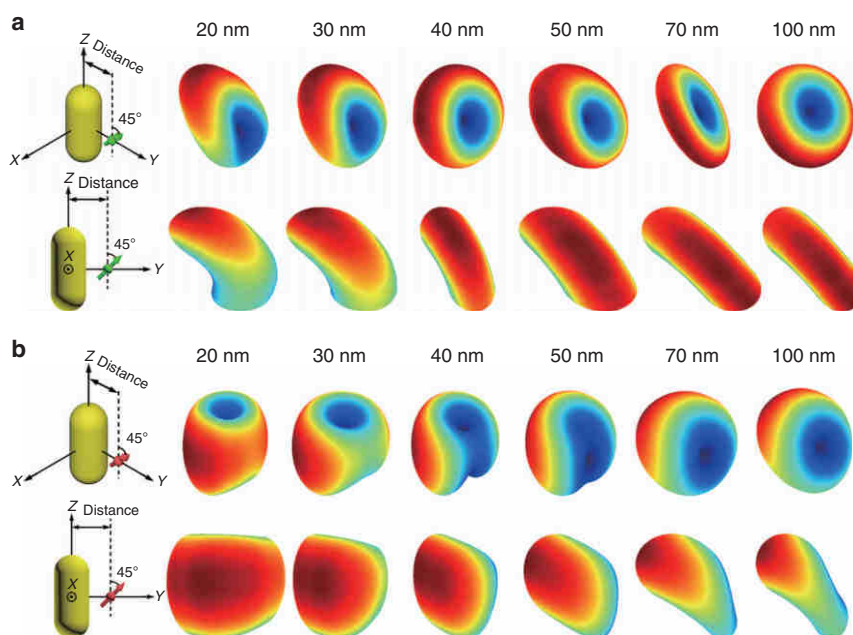


Figure 8 3D far-field-emission patterns of a dipole source in the vicinity of a bare GNR (diameter 32 nm, length 82 nm). The dipole is located in the Y–Z plane, and it is aligned at a 45° angle from the Z axis. The distance between the dipole and the center of the GNR is varied from 20 to 100 nm. The emission wavelength of the dipole was set to (a) 540 nm and (b) 660 nm. The first frame of each row indicates how the far-field-emission patterns are viewed.

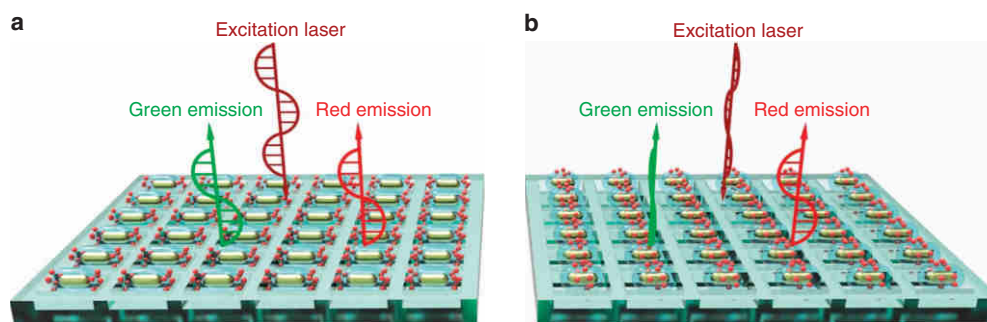


Figure 9 Schematic of ordered arrays of GNR@SiO₂@CaF₂:Yb³⁺,Er³⁺ hybrid nanostructure assembled on patterned templates. (a) When the polarization of the excitation laser (deep-red arrow) is parallel to the long axis of the hybrid nanostructures, both the enhanced green and red UC emissions (dictated by green and red arrows, respectively) would have the same polarization as the excitation laser. (b) In the case of the excitation laser with a perpendicular polarization, the resulting green UC emission would have the same polarization as the excitation laser, whereas the polarization of the red emission would be perpendicular to that of the green emission.

CONFLICT OF INTEREST

The authors declare no conflict of interest.

ACKNOWLEDGEMENTS

We acknowledge the financial support by the Hong Kong Research Grants Council (GRF Grant No. 15301414). FL acknowledges the support by the Ministry of Education, Youth and Sports of the Czech Republic under project CEITEC 2020 (LQ1601) and by the Hong Kong Polytechnic University. XC and WZ acknowledge the financial support by the NSFC (Nos. U1305244, 21325104, 11304314) and the CAS/SAFEA International Partnership Program for Creative Research Teams. JH thanks Mr. Gongxun Bai and Mr Ming-Kiu Tsang for assistance in using the Edinburgh FLS920 Fluorescence Spectrometer. JH also thanks Zijian Zheng and Xiaoling Wei for assistance in the zeta-potential measurements.

- Wang F, Banerjee D, Liu YS, Chen XY, Liu XQ. Upconversion nanoparticles in biological labeling, imaging, and therapy. *Analyst* 2010; **135**: 1839–1854.
- Liu YS, Tu DT, Zhu HM, Chen XY. Lanthanide-doped luminescent nanoprobes: controlled synthesis, optical spectroscopy, and bioapplications. *Chem Soc Rev* 2013; **42**: 6924–6958.
- Chen GY, Qiu HL, Prasad PN, Chen XY. Upconversion nanoparticles: design, nanochemistry, and applications in theranostics. *Chem Rev* 2014; **114**: 5161–5214.
- Zheng W, Tu DT, Huang P, Zhou SY, Chen Z *et al*. Time-resolved luminescent biosensing based on inorganic lanthanide-doped nanoprobes. *Chem Commun* 2015; **51**: 4129–4143.
- Liu Q, Sun Y, Yang TS, Feng W, Li CG *et al*. Sub-10 nm hexagonal lanthanide-doped NaLuF₄ upconversion nanocrystals for sensitive bioimaging *in vivo*. *J Am Chem Soc* 2011; **133**: 17122–17125.
- Cheng L, Yang K, Li YG, Chen JH, Wang C *et al*. Facile preparation of multifunctional upconversion nanoprobes for multimodal imaging and dual-targeted photothermal therapy. *Angew Chem Int Ed* 2011; **50**: 7385–7390.
- Yang JP, Shen DK, Zhou L, Li W, Fan JW *et al*. Mesoporous silica-coated plasmonic nanostructures for surface-enhanced Raman scattering detection and photothermal therapy. *Adv Healthc Mater* 2014; **3**: 1620–1628.

- 8 Wang HQ, Batentschuk M, Osvet A, Pinna L, Brabec CJ. Rare-earth ion doped up-conversion materials for photovoltaic applications. *Adv Mater* 2011; **23**: 2675–2680.
- 9 Yu DC, Martin-Rodríguez R, Zhang QY, Meijerink A, Rabouw FT. Multi-photon quantum cutting in $\text{Gd}_2\text{O}_3\text{:Tm}^{3+}$ to enhance the photo-response of solar cells. *Light Sci Appl* 2015; **4**: e344, doi:10.1038/lsa.2015.117.
- 10 Auzel F. Upconversion and anti-stokes processes with f and d ions in solids. *Chem Rev* 2004; **104**: 139–174.
- 11 Boyer JC, van Veggel FCM. Absolute quantum yield measurements of colloidal $\text{NaYF}_4\text{:Er}^{3+}, \text{Yb}^{3+}$ upconverting nanoparticles. *Nanoscale* 2010; **2**: 1417–1419.
- 12 Hao JH, Zhang Y, Wei XH. Electric-induced enhancement and modulation of upconversion photoluminescence in epitaxial $\text{BaTiO}_3\text{:Yb/Er}$ thin films. *Angew Chem Int Ed* 2011; **50**: 6876–6880.
- 13 Wang HQ, Nann T. Monodisperse upconverting nanocrystals by microwave-assisted synthesis. *ACS Nano* 2009; **3**: 3804–3808.
- 14 Liu YS, Tu DT, Zhu HM, Li RF, Luo WQ *et al*. A strategy to achieve efficient dual-mode luminescence of Eu^{3+} in lanthanides doped multifunctional NaGdF_4 nanocrystals. *Adv Mater* 2010; **22**: 3266–3271.
- 15 Chen GY, Ohulchanskyy TY, Liu S, Law WC, Wu F *et al*. Core/shell $\text{NaGdF}_4\text{:Nd}^{3+}/\text{NaGdF}_4$ nanocrystals with efficient near-infrared to near-infrared downconversion photoluminescence for bioimaging applications. *ACS Nano* 2012; **6**: 2969–2977.
- 16 Zhou B, Tao LL, Tsang YH, Jin W. Core-shell nanoarchitecture: a strategy to significantly enhance white-light upconversion of lanthanide-doped nanoparticles. *J Mater Chem C* 2013; **1**: 4313–4318.
- 17 Wang F, Wang J, Liu XG. Direct evidence of a surface quenching effect on size-dependent luminescence of upconversion nanoparticles. *Angew Chem Int Ed* 2010; **49**: 7456–7460.
- 18 Zhao JB, Jin DY, Scharfner EP, Lu YQ, Liu YJ *et al*. Single-nanocrystal sensitivity achieved by enhanced upconversion luminescence. *Nat Nanotechnol* 2013; **8**: 729–734.
- 19 Wang F, Deng RR, Wang J, Wang QX, Han Y *et al*. Tuning upconversion through energy migration in core-shell nanoparticles. *Nat Mater* 2011; **10**: 968–973.
- 20 Wang J, Wang F, Wang C, Liu Z, Liu XG. Single-band upconversion emission in lanthanide-doped KMnF_3 nanocrystals. *Angew Chem Int Ed* 2011; **50**: 10369–10372.
- 21 Han SY, Deng RR, Xie XJ, Liu XG. Enhancing luminescence in lanthanide-doped upconversion nanoparticles. *Angew Chem Int Ed* 2014; **53**: 11702–11715.
- 22 Zhang H, Li YJ, Ivanov IA, Qu YQ, Huang Y *et al*. Plasmonic modulation of the upconversion fluorescence in $\text{NaYF}_4\text{:Yb/Tm}$ hexaplate nanocrystals using gold nanoparticles or nanoshells. *Angew Chem Int Ed* 2010; **49**: 2865–2868.
- 23 Zhang F, Braun GB, Shi YF, Zhang YC, Sun XH *et al*. Fabrication of $\text{Ag}@\text{SiO}_2\text{:Y}_2\text{O}_3\text{:Er}$ nanostructures for bioimaging: tuning of the upconversion fluorescence with silver nanoparticles. *J Am Chem Soc* 2010; **132**: 2850–2851.
- 24 Schietinger S, Aichele T, Wang HQ, Nann T, Benson O. Plasmon-enhanced upconversion in single $\text{NaYF}_4\text{:Yb}^{3+}/\text{Er}^{3+}$ codoped nanocrystals. *Nano Lett* 2010; **10**: 134–138.
- 25 Saboktakin M, Ye XC, Chettiar UK, Engheta N, Murray CB *et al*. Plasmonic enhancement of nanophosphor upconversion luminescence in Au nanohole arrays. *ACS Nano* 2013; **7**: 7186–7192.
- 26 Wu DM, García-Etxarri A, Salleo A, Dionne JA. Plasmon-enhanced upconversion. *J Phys Chem Lett* 2014; **5**: 4020–4031.
- 27 Lu DW, Cho SK, Ahn S, Brun L, Summers CJ *et al*. Plasmon enhancement mechanism for the upconversion processes in $\text{NaYF}_4\text{:Yb}^{3+}, \text{Er}^{3+}$ nanoparticles: Maxwell versus Förster. *ACS Nano* 2014; **8**: 7780–7792.
- 28 Sun QC, Mundoor H, Ribot JC, Singh V, Smalyukh II *et al*. Plasmon-enhanced energy transfer for improved upconversion of infrared radiation in doped-lanthanide nanocrystals. *Nano Lett* 2014; **14**: 101–106.
- 29 Liu N, Qin WP, Qin GS, Jiang T, Zhao D. Highly plasmon-enhanced upconversion emissions from $\text{Au}@\text{p-NaYF}_4\text{:Yb}$, Tm hybrid nanostructures. *Chem Commun* 2011; **47**: 7671–7673.
- 30 Priyam A, Idris NM, Zhang Y. Gold nanoshell coated NaYF_4 nanoparticles for simultaneously enhanced upconversion fluorescence and darkfield imaging. *J Mater Chem* 2012; **22**: 960–965.
- 31 Greybush NJ, Saboktakin M, Ye XC, Della Giovampaola C, Oh SJ *et al*. Plasmon-enhanced upconversion luminescence in single nanophosphor-nanorod heterodimers formed through template-assisted self-assembly. *ACS Nano* 2014; **8**: 9482–9491.
- 32 Ge W, Zhang XR, Liu M, Lei ZW, Knize RJ *et al*. Distance dependence of gold-enhanced upconversion luminescence in $\text{Au/SiO}_2\text{:Y}_2\text{O}_3\text{:Yb}^{3+}, \text{Er}^{3+}$ nanoparticles. *Theranostics* 2013; **3**: 282–288.
- 33 Xu W, Min XL, Chen X, Zhu YS, Zhou PW *et al*. $\text{Ag-SiO}_2\text{-Er}_2\text{O}_3$ nanocomposites: highly effective upconversion luminescence at high power excitation and high temperature. *Sci Rep* 2014; **4**: 5087.
- 34 Chen GY, Ågren H, Ohulchanskyy TY, Prasad PN. Light upconverting core-shell nanostructures: nanophotonic control for emerging applications. *Chem Soc Rev* 2015; **44**: 1680–1713.
- 35 Ming T, Chen HJ, Jiang RB, Li Q, Wang JF. Plasmon-controlled fluorescence: beyond the intensity enhancement. *J Phys Chem Lett* 2012; **3**: 191–202.
- 36 Yuan PY, Lee YH, Gnanasammandhan MK, Guan ZP, Zhang Y *et al*. Plasmon enhanced upconversion luminescence of $\text{NaYF}_4\text{:Yb, Er}@\text{SiO}_2\text{:Ag}$ core-shell nanocomposites for cell imaging. *Nanoscale* 2012; **4**: 5132–5137.
- 37 Liu X, Lei DY. Simultaneous excitation and emission enhancements in upconversion luminescence using plasmonic double-resonant gold nanorods. *Sci Rep* 2015; **5**: 15235.
- 38 Taminiau TH, Stefani FD, Segerink FB, van Hulst NF. Optical antennas direct single-molecule emission. *Nat Photonics* 2008; **2**: 234–237.
- 39 Chen P, Song M, Wu E, Wu BT, Zhou JJ *et al*. Polarization modulated upconversion luminescence: single particle vs. few-particle aggregates. *Nanoscale* 2015; **7**: 6462–6466.
- 40 Zhou JJ, Chen GX, Wu E, Bi G, Wu BT *et al*. Ultrasensitive polarized up-conversion of $\text{Tm}^{3+}\text{-Yb}^{3+}$ doped $\beta\text{-NaYF}_4$ single nanorod. *Nano Lett* 2013; **13**: 2241–2246.
- 41 Singh A, Calbris G, van Hulst NF. Vectorial nanoscale mapping of optical antenna fields by single molecule dipoles. *Nano Lett* 2014; **14**: 4715–4723.
- 42 Tuchin VV, Wang LH, Zimnyakov DA. *Optical Polarization in Biomedical Applications*. Berlin/Heidelberg: Springer; 2006.
- 43 Tuchin V. *Tissue Optics: Light Scattering Methods and Instruments for Medical Diagnosis*, 2nd edn. Bellingham, WA, USA: SPIE Publications; 2007.
- 44 Ming T, Zhao L, Yang Z, Chen HJ, Sun LD *et al*. Strong polarization dependence of plasmon-enhanced fluorescence on single gold nanorods. *Nano Lett* 2009; **9**: 3896–3903.
- 45 Gorelikov I, Matsuura N. Single-step coating of mesoporous silica on cetyltrimethyl ammonium bromide-capped nanoparticles. *Nano Lett* 2008; **8**: 369–373.
- 46 He JJ, Zheng W, Chen XY, Lei DY. Plasmon-modulated polarized upconversion emissions from single gold nanorod-nanophosphors hybrid nanostructures. In: *International Photonics and Optoelectronics*. Washington, DC, USA: OSA; 2015.
- 47 Zheng W, Zhou SY, Chen Z, Hu P, Liu YS *et al*. Sub-10 nm lanthanide-doped CaF_2 nanoprobe for time-resolved luminescent biodetection. *Angew Chem Int Ed* 2013; **52**: 6671–6676.
- 48 Bogdan N, Zheng W, Zhou SY, Tu DT, Chen Z *et al*. Lanthanide-doped LiLuF_4 upconversion nanoprobe for the detection of disease biomarkers. *Angew Chem Int Ed* 2014; **53**: 1252–1257.
- 49 Bao ZY, Lei DY, Jiang RB, Liu X, Dai JY *et al*. Bifunctional $\text{Au}@\text{Pt}$ core-shell nanostructures for in situ monitoring of catalytic reactions by surface-enhanced Raman scattering spectroscopy. *Nanoscale* 2014; **6**: 9063–9070.
- 50 Li N, Tittl A, Yue S, Giessen H, Song C *et al*. DNA-assembled bimetallic plasmonic nanosensors. *Light Sci Appl* 2014; **3**: e226, doi:10.1038/lsa.2014.107.
- 51 Chen HJ, Shao L, Li Q, Wang JF. Gold nanorods and their plasmonic properties. *Chem Soc Rev* 2013; **42**: 2679–2724.
- 52 Bogdan N, Vetrone F, Ozin GA, Capobianco JA. Synthesis of ligand-free colloidal stable water dispersible brightly luminescent lanthanide-doped upconverting nanoparticles. *Nano Lett* 2011; **11**: 835–840.
- 53 Zhang ZJ, Wang LM, Wang J, Jiang XM, Li XH *et al*. Mesoporous silica-coated gold nanorods as a light-mediated multifunctional theranostic platform for cancer treatment. *Adv Mater* 2012; **24**: 1418–1423.
- 54 Li ZQ, Wang LM, Wang ZY, Liu XH, Xiong YJ. Modification of $\text{NaYF}_4\text{:Yb, Er}@\text{SiO}_2$ nanoparticles with gold nanocrystals for tunable green-to-red upconversion emissions. *J Phys Chem C* 2011; **115**: 3291–3296.
- 55 Abadeer NS, Brennan MR, Wilson WL, Murphy CJ. Distance and plasmon wavelength dependence of fluorescence of molecules bound to silica-coated gold nanorods. *ACS Nano* 2014; **8**: 8392–8406.
- 56 Huang YJ, Kim DH. Dark-field microscopy studies of polarization-dependent plasmonic resonance of single gold nanorods: rainbow nanoparticles. *Nanoscale* 2011; **3**: 3228–3232.
- 57 Li GC, Zhang YL, Lei DY. Hybrid plasmonic gap modes in metal film-coupled dimers and their physical origins revealed by polarization resolved dark field spectroscopy. *Nanoscale* 2016; **8**: 7119–7126.
- 58 Ming T, Zhao L, Chen HJ, Woo KC, Wang JF *et al*. Experimental evidence of plasmon-induced polarized emission from gold nanorod-fluorophore hybrid nanostructures. *Nano Lett* 2011; **11**: 2296–2303.
- 59 Reifemberger JG, Snyder GE, Baym G, Selvin PR. Emission polarization of europium and terbium chelates. *J Phys Chem B* 2003; **107**: 12862–12873.
- 60 Curto AG, Taminiau TH, Volpe G, Kreuzer MP, Quidat R *et al*. Multipolar radiation of quantum emitters with nanowire optical antennas. *Nat Commun* 2013; **4**: 1750.
- 61 Sugimoto H, Chen TH, Wang R, Fujii M, Reinhard BM *et al*. Plasmon-enhanced emission rate of silicon nanocrystals in gold nanorod composites. *ACS Photonics* 2015; **2**: 1298–1305.
- 62 Fischer S, Hallermann F, Eichelkraut T, von Plessen G, Krämer KW *et al*. Plasmon enhanced upconversion luminescence near gold nanoparticles—simulation and analysis of the interactions: errata. *Opt Express* 2013; **21**: 10606–10611.
- 63 Ren MX, Chen M, Wu W, Zhang LH, Liu JK *et al*. Linearly polarized light emission from quantum dots with plasmonic nanoantenna arrays. *Nano Lett* 2015; **15**: 2951–2957.



This work is licensed under a Creative Commons Attribution-NonCommercial-ShareAlike 4.0 International License. The images or other third party material in this article are included in the article's Creative Commons license, unless indicated otherwise in the credit line; if the material is not included under the Creative Commons license, users will need to obtain permission from the license holder to reproduce the material. To view a copy of this license, visit <http://creativecommons.org/licenses/by-nc-sa/4.0/>

© The Author(s) 2017

Supplementary Information for this article can be found on the *Light: Science & Applications* website (<http://www.nature.com/lsa>).

Epitaxial VO₂ Nanostructures: A Route to Large-Scale, Switchable Dielectric Metasurfaces

Filip Ligmajer,^{†,‡,§} Lukáš Kejík,^{†,§} Uddhab Tiwari,^{||} Meng Qiu,[⊥] Joyeeta Nag,[#] Martin Konečný,[‡] Tomáš Šikola,^{†,‡} Wei Jin,[⊥] Richard F. Haglund, Jr.,[#] Kannatassen Appavoo,^{*,||} and Dang Yuan Lei^{*,§,||}

[†]Central European Institute of Technology, Brno University of Technology, Purkyňova 123, Brno, 612 00, Czech Republic

[‡]Institute of Physical Engineering, Brno University of Technology, Technická 2896/2, Brno, 616 69, Czech Republic

[§]Department of Applied Physics, The Hong Kong Polytechnic University, Hong Kong, China

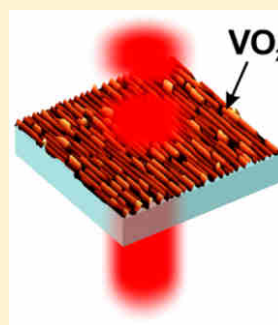
^{||}Department of Physics, The University of Alabama at Birmingham, Birmingham, Alabama 35294, United States

[⊥]Department of Electrical Engineering, The Hong Kong Polytechnic University, Hong Kong, China

[#]Department of Physics and Astronomy, Vanderbilt University, Nashville, Tennessee 37235-1807, United States

ABSTRACT: Metasurfaces offer unparalleled functionalities for controlling the propagation and properties of electromagnetic waves. But to transfer these functions to technological applications, it is critical to render them tunable and to enable fast control by external stimuli. In most cases, this has been realized by utilizing tunable materials combined with a top-down nanostructuring process, which is often complicated and time intensive. Here we present a novel strategy for fabricating a tunable metasurface comprising epitaxially grown nanobeams of a phase transition material, vanadium dioxide. Without the need for extensive nanolithographic fabrication, we prepared a large-area (>1 cm²), deep-subwavelength (thickness of $\sim\lambda/40$) nanostructured thin film that can control light transmission with large modulation depth, exceeding 9 dB across all telecommunication wavelength bands. Furthermore, the transmission in the “on” state remains higher than 80% from near- to mid-infrared region. This renders our metasurface useful also as a phase-shifting element, which we demonstrate by carrying out cross-polarized transmission measurements. To provide insights about the relationship between metasurface morphology and its resulting optical properties, we perform full-field three-dimensional numerical simulations as a function of width, height, and edge-to-edge separation of the epitaxial VO₂ nanobeams.

KEYWORDS: vanadium dioxide, plasmonics, phase transition, near-infrared modulation, metasurfaces, metamaterials



The ability to effectively control the propagation and properties of light using layers of nanostructured materials with subwavelength dimensions has become central to the emerging field of metasurfaces and metamaterials.¹ Artificially structured layers of materials have provided unprecedented optical functionalities^{2–5} and facilitated miniaturization of conventional optical elements and devices like lenses^{6–8} and polarimeters.^{9,10} Although metasurfaces were originally based on noble metal plasmonics,¹¹ an effort to increase their efficiency and bring new applications has led to utilization of new materials with reduced losses,¹² especially dielectrics,^{13–15} and materials with tunable optical properties.¹⁶ The latter class of materials is represented mainly by doped transparent conductive oxides (typically indium tin oxide),¹⁷ which can be readily controlled via electrostatic gating, and by phase transition materials (typically vanadium dioxide or germanium antimony telluride),^{18–21} which can undergo a profound change of optical properties upon external stimuli (thermal, electrical, optical).

Phase transition materials have been utilized in the development of metamaterials with on-demand reflection and transmission resonances,^{22,23} tunable perfect absorbers^{24–26} and tunable polarizing elements,^{27,28} or optical modulators.^{20,29}

Yet to produce a tunable, large-area metasurface still remains a challenge, as documented by the fact that reports in literature describe almost exclusively designs made by advanced nanofabrication techniques: either via nanostructuring plasmonic metals on top of a tunable substrate that then indirectly influences the optical response of nanoantennas on the substrate^{25–27,30–36} or via nanostructuring the tunable material itself through a top-down nanofabrication process.^{23,28,29,37–40}

Here we present a new class of tunable plasmonic-dielectric metasurfaces composed of epitaxial vanadium dioxide (VO₂) nanobeams. The main benefit of our design is that we circumvent the time-consuming, serial process of top-down metasurface fabrication, instead producing the nanostructured films by a one-step epitaxial-growth process using pulsed laser deposition. Thus, a large area of the substrate can be covered with anisotropic nanostructures of VO₂ that act as a plasmonic-dielectric tunable metasurface, as characterized by using optical measurements and numerical simulations. VO₂ provides

Special Issue: Recent Developments and Applications of Plasmonics

Received: November 16, 2017

Published: May 7, 2018

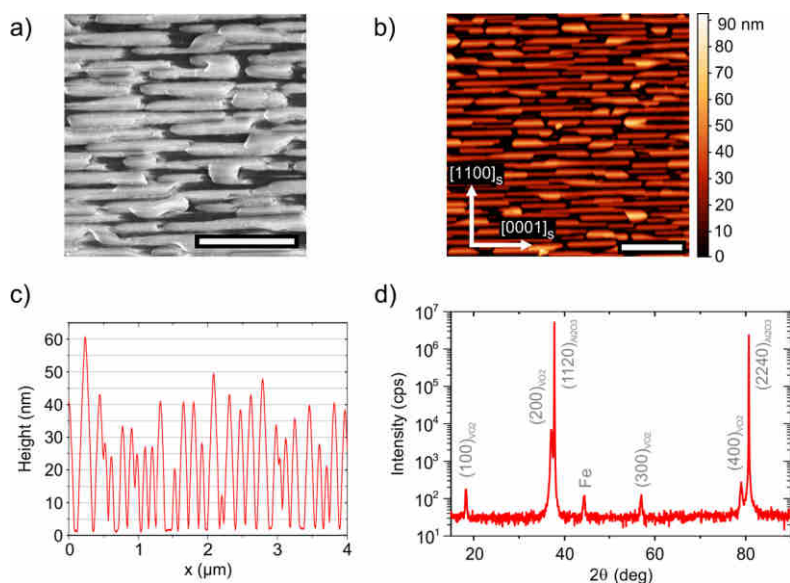


Figure 1. (a) SEM and (b) AFM images of the epitaxial VO_2 metasurface. Scale bars are 0.5 and 1 μm , respectively. Labels denote the crystallographic directions of the substrate surface. (c) Typical AFM height profile measured across the VO_2 nanobeams in (b). (d) Room-temperature XRD spectrum of the same sample of VO_2 on a-cut sapphire substrate with diffraction maxima labeled in gray. Note the iron peak comes from a small part of the beam hitting the sample stage.

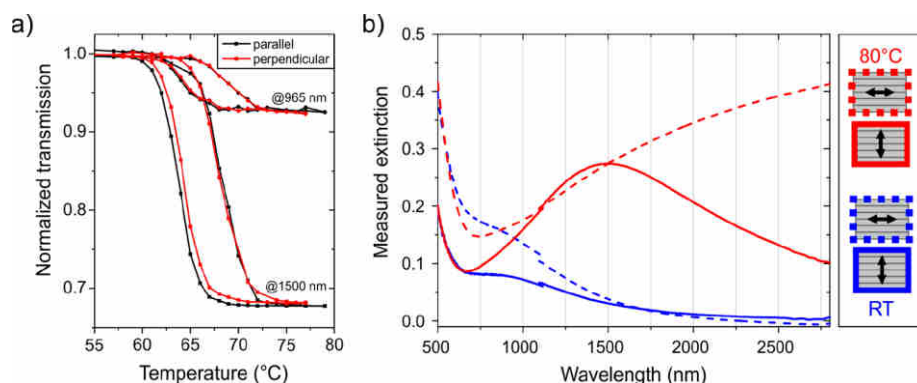


Figure 2. (a) Transmission hysteresis at two representative wavelengths for light polarized parallel (black) and perpendicular (red) with VO_2 nanobeams. The data are normalized to transmission at room temperature. (b) Measured extinction spectra of the epitaxial VO_2 metasurface for incident-light polarization parallel (dashed lines) or perpendicular (solid lines) with the nanobeams. Spectra were acquired and calculated for both insulating state of VO_2 (room temperature, RT, blue lines) and the metallic state (80 $^{\circ}\text{C}$, red lines).

inherent switching functionality at telecommunication wavelengths due to the changes in the dielectric properties as it undergoes an insulator-to-metal phase transition. Moreover, because the phase transition material itself forms the metasurface building blocks, the optical properties can be controlled in a direct manner, reducing potential interfacial effects caused by heterostructuring. Our measurements with crossed polarizers also help to visualize the phase-shifting properties of our metasurface, and our extensive analysis establishes the relationship between electronic and structural properties of the fabricated thin films and resulting optical properties. In detail, our numerical simulations match the observed transmission spectra and reveal how optical properties of the metasurface can be tuned based on the lateral size and height of the individual nanobeams and also on their intrinsic separation.

The properties and surface morphology of VO_2 films strongly depend on the growth technique, pressure, temperature, and substrate.^{41,42} The growth of separated laterally confined VO_2

nanobeams was demonstrated on various substrates^{43–46} and their formation was associated with minimization of surface energy during vapor–solid growth process that leads to preferential formation of thermodynamically favorable nanobeam facets.^{47,48} Here, our strategy is to use the a-cut (11 $\bar{2}$ 0) sapphire substrate to facilitate the anisotropic growth pattern of the VO_2 and to create a dense layer of VO_2 nanobeams,^{49–51} in contrast to what is usually seen on its c-cut, m-cut, or r-cut counterparts.^{52–54} Typical deposition of a polycrystalline VO_2 film on a glass substrate is performed at room temperature and low background oxygen pressure, followed by annealing at high pressure of oxygen. For this work, we perform a single-step direct deposition by sputtering high-purity vanadium metal target by pulsed laser excitation at a background oxygen gas pressure of 50 mTorr onto the a-cut face of a sapphire substrate held at 500 $^{\circ}\text{C}$ (see [Methods](#) for more details). We employ a similar mechanism that enforces an unusual growth pattern on the VO_2 , different from what is typically seen on c-cut or r-cut

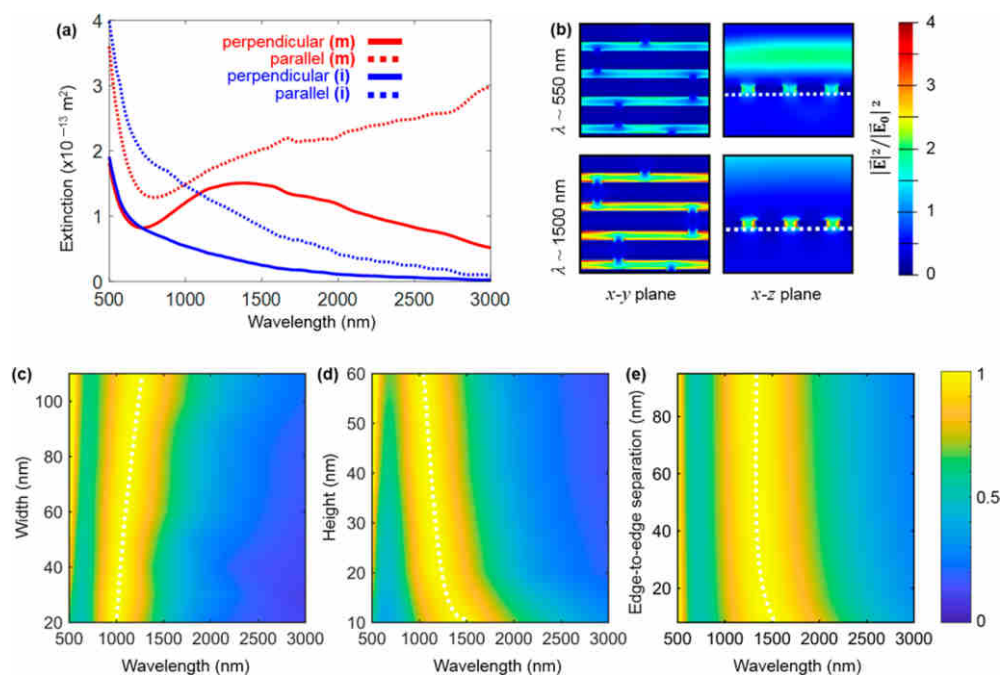


Figure 3. (a) Simulated extinction spectra for VO_2 nanobeams with an insulating (i) and metallic (m) dielectric function for incident polarization parallel and perpendicular to their longitudinal anisotropy axis. The nanobeams were 96 nm in width, 28 nm in height, $1.3 \mu\text{m}$ in length, and were arranged into a lattice with constant inter-rod spacing in both x - and y -directions (48 nm) and random offset along the anisotropic y -axis. (b) In-plane and out-of-plane maps of electric field intensity enhancement in the metallic VO_2 metasurface extracted from the calculations at two representative wavelengths. (c–e) Calculated extinction spectral maps for an individual infinitely long metallic VO_2 nanobeam (on top of a sapphire substrate) with (c) constant height of 30 nm and varied width, (d) constant width of 60 nm and varied height, (e) similar results for two nanobeams with constant width of 100 nm and height of 30 nm, and varied separation between them. Incident light polarization was perpendicular to the nanobeam. The data were normalized to the NIR resonance peak (dashed white line).

sapphire, to create a dense layer of anisotropic VO_2 nanobeams.^{47,48} This enhances the kinetics at the surface during growth process and facilitates epitaxial growth, while at the same time the preferential growth along one direction is caused by in-plane lattice strains.^{47,55} While VO_2 is initially mismatched with a -cut sapphire (35% along the x axis and only $\sim 5\%$ along the y axis), during epitaxial growth, the composite unit cell has a very low amount of mismatch and we thus get a certain integral number of unit cells to grow on the substrate with a good match. As the deposition proceeds, relaxation occurs through dislocations and leads to formation of separate nanobeams that form our anisotropic VO_2 metasurface.

The morphology of the resulting thin film was evaluated using scanning electron microscopy (SEM, FEI Verios) and atomic force microscopy (AFM, Bruker Dimension Icon), both of which revealed a strongly anisotropic polycrystalline structure with grains about 100–200 nm wide, 1000–2000 nm long, and 40 nm high (see Figure 1). The AFM measurements also provided evidence for a close-packed nature of the nanobeams, highlighting this self-limiting growth. The crystal orientation of the VO_2 nanobeams was then identified by room-temperature (RT) X-ray diffraction (XRD, Rigaku SmartLab) with respect to the substrate. From a standard θ – 2θ scan (Figure 1d), it is evident that the VO_2 nanobeams have a preferential orientation of (200) on the a -cut sapphire, which confirms their epitaxial nature.

To assess the phase-transition behavior of our metasurface films, we first performed a classic transmission measurement with the light polarized both parallel and perpendicular to the VO_2 nanobeams (see Figure 2a). The epitaxial VO_2 metasur-

face exhibits a sharp optical transmission hysteresis centered around 65°C for both polarizations, with a hysteresis width ΔT of only 4°C . This suggests that the structural anisotropy does not translate into the hysteresis anisotropy. The narrow hysteresis width for the epitaxial nanostructures is suggestive of increased structural homogeneity, with little variation in size, crystallographic domain orientations, and strain.^{41,56} Optical properties of the fabricated VO_2 metasurface were fully investigated using polarized Fourier-transform infrared spectroscopy. In Figure 2b, the measured extinction spectra are presented for both insulating (RT) and metallic (80°C) state of the VO_2 (see the experimental details in Methods). At the RT, the dielectric nature of VO_2 nanobeams assures high transmittance ($>80\%$) across the whole near-infrared spectral range (from 700 nm to $3 \mu\text{m}$) and their elongated shape manifests itself in the anisotropy of the measured extinction mainly at the wavelengths in the visible range.

A particularly useful variation in optical properties can be observed for a VO_2 metasurface that has undergone the insulator-to-metal transition (IMT): For the incident light polarized along the nanobeams, we observe a typical monotonic increase of infrared extinction, similar to that observed in conventional isotropic thin films of metallic VO_2 .^{57–59} However, for light polarized perpendicular to the nanobeams, we observe a broad extinction peak centered at 1480 nm that we ascribe to excitation of a localized surface plasmon resonance. This is a direct consequence of the lateral confinement of conduction electrons in the metallic nanostructures that are achieved conventionally only by top-down nanofabrication. The self-limiting epitaxial growth of the

crystalline VO₂ along the [0001] direction of the sapphire substrate gives rise to the nanobeam morphology of the produced thin film. Due to the confined lateral size of the nanobeams, the spectral region of the largest extinction contrast between the insulating and metallic phase is located at the telecommunication wavelengths. Moreover, the measured reversible modulation depth⁶⁰ is greater than 9 dB across the whole set of standard telecommunication wavelength bands. Although structurally anisotropic, our metasurface also shows only weak polarization dependence in this spectral region, and around the telecommunication wavelength of 1.5 μm it is virtually isotropic. A device with such a high extinction contrast and broad bandwidth is highly desirable for many applications in optical modulation, as these attributes are crucial for high signal-transmission capacity, better resistance to noise, and longer achievable distances.⁶¹ Although the modulation is performed using inherently slow external heating in our experiment, it has been demonstrated that the phase transition in VO₂ can be induced by optical pulses on ultrafast time scales.^{62,63}

Apart from the IMT, there is an additional light-modulating capacity of our metasurface that stems from the optical anisotropy at the IR wavelengths beyond 1.5 μm . While the insulating phase provides almost perfectly isotropic response in this spectral region, the measured extinction contrast between light polarized across (perpendicular) and along (parallel) the metallic VO₂ nanobeams gradually increases (cf. Figure 2b). This behavior lays the groundwork for an extra degree of freedom, that is, polarization of incident light, that can be superimposed on top of the IMT-based switching and thus enable two separated modulation channels for the optical signals. For example, at wavelengths between 2 and 2.8 μm , two transmission modulation levels, well separated by at least 2.4 dB, can be controlled by varying the VO₂ phase and incident light polarization. Additionally, this approach can be used not only to modulate the intensity of light, but also to control the amplitudes of its orthogonal polarizations. Extra information could thus be encoded into the intensity difference between the two polarizations, which is not easily achievable in conventional bulk optics,⁶⁴ and efficient polarization modulator between the circular and linear polarization would be created.⁶⁵ If an electric field instead of temperature was used,^{66,67} this modulation could be much faster and therefore more useful for applications in communication technologies.

To confirm the plasmonic nature of the demonstrated functionality and to also provide a deeper physical insight into the relationship between metasurface morphology and optical properties, we performed three-dimensional full-wave numerical simulations using a commercial finite-difference time-domain (FDTD) solver (see Methods for more details). First, we aimed to reproduce the measured experimental spectra. To this end, we created a model corresponding to the measured morphology of the sample: VO₂ nanobeams of constant width (96 nm), height (28 nm), and length (1.3 μm) were arranged into a lattice with a constant inter-rod spacing (48 nm) in both directions and random offset along the anisotropy axis (see inset of Figure 2b). The dielectric function of VO₂ was obtained from ref 48, and the nanobeam length was extended further than the nominal simulation volume to avoid any residual scattering effect. Following the experiment, the calculated extinction spectra for both phases of VO₂ and for two principal polarizations are plotted in Figure 3a. Although small discrepancies appear, the agreement between measured

and calculated spectra is remarkable. Both the anisotropy of the dielectric metasurface in its insulating state and the resonant extinction observed in its metallic state are well reproduced. Moreover, we see from the electric field plots in Figure 3b that perpendicular polarization with respect to the nanobeam long axis generates around 4-fold increase in electric field strength. The nature of this resonance, an electric dipole, is similar to a previous work by Appavoo et al., where VO₂ nanodisks of comparable height were fabricated by top-down electron-beam lithography for small array size (100 \times 100 μm^2).⁶⁸ We note that, contrary to the typical situation, the plasmonic resonances in our experiments are of better quality (i.e., larger *Q*-factors) than those in simulations. We ascribe this to the high quality of the fabricated epitaxial nanobeams while using polycrystalline VO₂ dielectric function in the simulations.

To assess how the dimensions of VO₂ nanobeams influence the resulting optical properties of the metasurface, we performed another set of FDTD simulations, featuring only a single infinitely long metallic VO₂ nanobeam. First, the effect of nanobeam width was calculated while its height was fixed at 30 nm. The resulting extinction spectral map for incident light polarized across the nanobeam is shown in Figure 3c. A characteristic red-shift of the localized surface plasmon resonance with increasing the beam width is clearly visible. The situation is quite opposite in the extinction map calculated for a nanobeam with fixed width (60 nm) and varied height (Figure 3d). The blue-shift of the resonance stems from the fact that the height increase leads to less confinement of conduction electrons in the width direction (effectively reducing the induced surface charge density). Note that the extinction spectra for light polarized along the nanobeam are naturally insensitive to changes in the nanobeam width and height. The last effect investigated was the edge-to-edge separation between nanobeams (Figure 3e). A small red-shift can be observed when the separation decreases into the near-field regime (below 20 nm), suggesting the appearance of weak dipolar coupling.⁶⁹ Together, our simulations reveal the strong effect of structural parameters on the shape and position of the metasurface resonance. Translating this knowledge into technological applications, albeit still a significant challenge in terms of epitaxial fabrication, will only require tuning the parameters of the VO₂ growth.

Metasurface building blocks play an important role as subwavelength phase-shifting elements. Likewise, the VO₂ metasurface studied here can demonstrate its potential not only by the control of light transmission via absorption (related to the imaginary part of the complex refractive index) but also via its phase-shifting properties (related to its real part). The enhanced light absorption contrast between the insulating and metallic phases of VO₂ is in fact accompanied by the similar contrast in terms of the transmitted light phase.^{57–59} Although retrieving the anisotropic complex refractive index of our metasurfaces is not possible at present, we can qualitatively test this hypothesis. To visualize the phase-shifting properties, we set the incident polarization at 45° with respect to the nanobeams and we incorporated another polarizer (herein referred to as analyzer) into the detection branch of our infrared microscope. Thus, an equal amount of light with the two principal polarizations (parallel and perpendicular to the VO₂ nanobeams) will interact with our nanobeam sample. Due to anisotropic material dispersion, the two polarizations will acquire a nontrivial phase during propagation through the metasurface, the light polarization will be converted from linear

to elliptical, and the transmission will then be a function of the analyzer angle. And if the light transmission without analyzer is equal for the two principal polarizations (as it is around 1500 nm for our sample at both RT and 80 °C, cf. Figure 2a), the pure phase-shifting effect will be observed. We performed such an experiment and the results are presented in Figure 4. Our

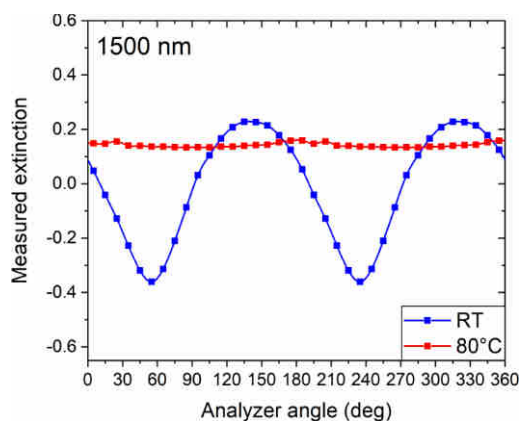


Figure 4. Measured extinction of the epitaxial VO₂ metasurface for incident-light polarization 45° to the nanobeams as a function of the analyzer angle (0° is parallel to the nanobeams). Results are shown for the insulating (RT, in blue) and metallic (80 °C, in red) state at 1500 nm. Note that the right half of the data is a copy of data from 0° to 180° and the extinction, as defined in this work, can be negative or larger than one when measured with the combined polarizer and analyzer.

metasurface in its insulating state at RT behaves like a simple attenuator at 1500 nm (with the intensity oscillations according to Malus's law). But when turned into its metallic phase at 80 °C, the metasurface behaves like a quarter-wave plate, turning the linearly polarized incident wave into a circularly polarized one with the transmission characteristically insensitive to the analyzer angle. Together with the polarization-modulating function described above (intensity modulation), this second degree of freedom (phase modulation) makes it possible for our samples to work as multifunctional devices at various wavelengths, controlling both the intensity and the phase of the transmitted light.

In conclusion, we have demonstrated a facile fabrication route to a tunable dielectric-plasmonic metasurface on centimeter scale. The foundation of the method is epitaxial growth of VO₂ on a (11 $\bar{2}$ 0) face of sapphire substrate that leads to formation of a thin layer of parallel, closely spaced VO₂ nanobeams due to the substrate–film interaction. Although transparent in the room-temperature insulating state, the nanobeams support localized surface plasmon resonances in the metallic state, which can be reached at elevated temperature by Joule heating or assisted by electric field or laser excitation. As we show, this effect can be used for perfect transmission control with very large modulation depth exceeding 9 dB across the entire telecommunication wavelength bands. This renders our metasurface comparable or even better than similar designs recently reported,⁷⁰ while being fabricated in a more facile way. Moreover, combining the switching functionality with polarization-based control, we put forward a two-level modulation scheme in the mid-infrared range. Subsequent numerical simulations not only reproduced the measured spectra but provided also deeper insight into relationship between

morphology of the nanobeams and optical characteristics of the resulting metasurface. The opposing effects of increasing nanorod width (red-shift) and height (blue-shift) were observed together with the influence of the sapphire substrate on the resonance and also of the edge-to-edge separation between nanobeams. Apart from the transmission control based solely on the absorption in the nanobeams, we also considered their phase-shifting properties stemming from the changes in their refractive index. With transmission experiments employing two polarizers crossed at variable angles, we demonstrate how such an effect can be also used for an effective control of light flow. Our results establish epitaxially grown VO₂ nanobeams as promising metasurface building blocks with deeply subwavelength thickness that can be easily switched from the isotropic transparent dielectric state to the anisotropic opaque metallic state and thus effectively control the flow of light. We envision that other types of tunable metasurfaces can be fabricated by similar methods. For example, isolated hemispherical VO₂ nanoparticles, acting as nanoantennas, can be created by simple annealing of a VO₂ thin film.^{18,52,71} A more sophisticated approach would reside in utilization of the epitaxial growth on a 3-fold symmetric surface of c-cut sapphire.^{46,72} That way, 3-fold symmetric nanostructures which resemble V-shaped nanoantennas, a prototypical metasurface building block, could be fabricated.⁷³

METHODS

VO₂ Nanobeam Growth. High-purity vanadium metal target was sputtered by a pulsed KrF excimer laser beam ($\lambda = 248$ nm) at a background oxygen gas pressure of 50 mTorr onto the a-cut (11 $\bar{2}$ 0) face of a sapphire substrate held at 500 °C during the entire growth process. The pulse energy was 385 mJ and the optical pulses were focused onto 0.3 cm² of the vanadium metal target. The repetition rate of the laser was 10 Hz and the target–substrate distance was 5 cm.

Extinction Measurements. Extinction spectra are calculated from the transmission data as $1 - T/T_{\text{REF}}$, where T is transmission through the VO₂ nanobeams and T_{REF} is transmission through the bare sapphire substrate. Transmission hysteresis was measured with a fiber-coupled halogen lamp that acted as an unpolarized white-light source, two optical fiber collimators that illuminated the sample and collected the transmitted light, respectively, a polarizer placed in front of the sample, and a fiber-coupled spectrometer (Ocean Optics Jaz Series). Transmission spectra were acquired using an infrared microscope (Bruker Hyperion 3000) coupled to a Fourier-transform infrared spectrometer (Bruker Vertex 80 V). A Global light source, a KBr beamsplitter and an MCT detector were used for the MIR region; tungsten lamp, CaF₂ beamsplitter and silicon detector were used for the visible and NIR region. A couple of ultrabroadband polarizers were used to control incident and detected light polarization and a 36 \times objective (NA: 0.5) was used to collect the transmitted light. The small discontinuity of the measured spectra around 1.1 μm stems from the use of the two measurement configurations. The slightly negative values of extinction (that are of course unphysical) can be ascribed to irregularities within the substrate.

Numerical Simulations. Three-dimensional, full-field electromagnetic simulations were carried out using the Lumerical FDTD Solutions software. The simulation volume was 1600 nm in each dimension with a nonuniform mesh type ($n = 3$). The boundary conditions were set as periodic in the

sample plane and perfectly matched layers were used for top and bottom face of the unit cell (i.e., in the direction of light propagation). The dielectric constant used for sapphire was acquired from Palik. The extinction spectra were calculated by utilizing a built-in total-field scattered-field source and related analysis groups.

AUTHOR INFORMATION

Corresponding Authors

*E-mail: danyuan.lei@polyu.edu.hk.

*E-mail: appavoo@uab.edu.

ORCID

Filip Ligmajer: 0000-0003-0346-4110

Dang Yuan Lei: 0000-0002-8963-0193

Author Contributions

J.N. and K.A. fabricated and characterized (XRD, hysteresis) the sample. F.L., L.K., and M.K. performed the additional sample characterization (SEM, AFM, XRD). F.L., L.K., and D.Y.L. performed the NIR optical measurements. U.T., M.Q., and K.A. performed the simulations. All authors contributed to preparing the manuscript. K.A., R.F.H., and D.Y.L. oversaw the overall research project.

Notes

The authors declare no competing financial interest.

ACKNOWLEDGMENTS

The authors thank Ondřej Čaha for his assistance with XRD measurements. This work was supported by the MEYS CR (Project No. LQ1601 – CEITEC 2020) and it was also carried out with the support of CEITEC Nano Research Infrastructure (ID LM2015041, MEYS CR, 2016–2019). J.N. and K.A. were supported for the fabrication and characterization of the sample by the National Science Foundation (EECS-0801985) and the Office of Science, United States Department of Energy (DE-FG02-01ER45916), respectively. K.A. thanks the Department of Physics at UAB for support through startup funds. F.L. and L.K. thank the support by the Hong Kong Polytechnic University under the Research Student Attachment Programme for Incoming Visiting Ph.D. students. W.J. and D.Y.L. acknowledge the financial support by the Hong Kong Polytechnic University (Project No. I-YW1R).

REFERENCES

- (1) Kildishev, A. V.; Boltasseva, A.; Shalaev, V. M. Planar Photonics with Metasurfaces. *Science* **2013**, *339*, 1232009.
- (2) Shalaev, V. M. Optical negative-index metamaterials. *Nat. Photonics* **2007**, *1*, 41–48.
- (3) Moitra, P.; et al. Realization of an all-dielectric zero-index optical metamaterial. *Nat. Photonics* **2013**, *7*, 791–795.
- (4) Zheng, G.; et al. Metasurface holograms reaching 80% efficiency. *Nat. Nanotechnol.* **2015**, *10*, 308–12.
- (5) Balthasar Mueller, J. P.; Rubin, N. A.; Devlin, R. C.; Grover, B.; Capasso, F. Metasurface Polarization Optics: Independent Phase Control of Arbitrary Orthogonal States of Polarization. *Phys. Rev. Lett.* **2017**, *118*, 113901.
- (6) Khorasaninejad, M.; et al. Achromatic Metalens over 60 nm Bandwidth in the Visible and Metalens with Reverse Chromatic Dispersion. *Nano Lett.* **2017**, *17*, 1819–1824.
- (7) Lalanne, P.; Chavel, P. Metalenses at visible wavelengths: past, present, perspectives. *Laser Photonics Rev.* **2017**, *11*, 1600295.
- (8) Yuan, G. H.; Rogers, E. T.; Zheludev, N. I. Achromatic super-oscillatory lenses with sub-wavelength focusing. *Light: Sci. Appl.* **2017**, *6*, e17036.
- (9) Ding, F.; Pors, A.; Chen, Y.; Zenin, V. A.; Bozhevolnyi, S. I. Beam-Size-Invariant Spectropolarimeters Using Gap-Plasmon Metasurfaces. *ACS Photonics* **2017**, *4*, 943–949.
- (10) Maguid, E.; et al. Multifunctional interleaved geometric-phase dielectric metasurfaces. *Light: Sci. Appl.* **2017**, *6*, e17027.
- (11) Bomzon, Z.; Kleiner, V.; Hasman, E. Pancharatnam–Berry phase in space-variant polarization-state manipulations with sub-wavelength gratings. *Opt. Lett.* **2001**, *26*, 1424–1426.
- (12) Boltasseva, A.; Atwater, H. A. Low-Loss Plasmonic Metamaterials. *Science* **2011**, *331*, 290–291.
- (13) Chong, K. E.; et al. Efficient Polarization-Insensitive Complex Wavefront Control Using Huygens' Metasurfaces Based on Dielectric Resonant Meta-atoms. *ACS Photonics* **2016**, *3*, 514–519.
- (14) Kuznetsov, A. I.; Miroshnichenko, A. E.; Brongersma, M. L.; Kivshar, Y. S.; Luk'yanchuk, B. Optically resonant dielectric nanostructures. *Science* **2016**, *354*, aag2472.
- (15) Genevet, P.; Capasso, F.; Aieta, F.; Khorasaninejad, M.; Devlin, R. Recent advances in planar optics: From plasmonic to dielectric metasurfaces. *Optica* **2017**, *4*, 139.
- (16) Shaltout, A. M.; Kildishev, A. V.; Shalaev, V. M. Evolution of photonic metasurfaces: From static to dynamic. *J. Opt. Soc. Am. B* **2016**, *33*, 501.
- (17) Gregory, S. A.; Wang, Y.; de Groot, C. H.; Muskens, O. L. Extreme Subwavelength Metal Oxide Direct and Complementary Metamaterials. *ACS Photonics* **2015**, *2*, 606–614.
- (18) Suh, J. Y.; Lopez, R.; Feldman, L. C.; Haglund, R. F. Semiconductor to metal phase transition in the nucleation and growth of VO₂ nanoparticles and thin films. *J. Appl. Phys.* **2004**, *96*, 1209–1213.
- (19) Markov, P.; et al. Optically Monitored Electrical Switching in VO₂. *ACS Photonics* **2015**, *2*, 1175–1182.
- (20) Gholipour, B.; Zhang, J.; MacDonald, K. F.; Hewak, D. W.; Zheludev, N. I. An All-Optical, Non-volatile, Bidirectional, Phase-Change Meta-Switch. *Adv. Mater.* **2013**, *25*, 3050–3054.
- (21) Tan, Y.; et al. Tunable Picosecond Laser Pulses via the Contrast of Two Reverse Saturable Absorption Phases in a Waveguide Platform. *Sci. Rep.* **2016**, *6*, 26176.
- (22) Dicken, M. J.; et al. Frequency tunable near-infrared metamaterials based on VO₂ phase transition. *Opt. Express* **2009**, *17*, 18330–18339.
- (23) Wang, Q.; et al. Optically reconfigurable metasurfaces and photonic devices based on phase change materials. *Nat. Photonics* **2016**, *10*, 60–65.
- (24) Kats, M. A.; et al. Ultra-thin perfect absorber employing a tunable phase change material. *Appl. Phys. Lett.* **2012**, *101*, 221101.
- (25) Yao, Y.; et al. Electrically Tunable Metasurface Perfect Absorbers for Ultrathin Mid-Infrared Optical Modulators. *Nano Lett.* **2014**, *14*, 6526–6532.
- (26) Tittel, A.; et al. A Switchable Mid-Infrared Plasmonic Perfect Absorber with Multispectral Thermal Imaging Capability. *Adv. Mater.* **2015**, *27*, 4597–4603.
- (27) Earl, S. K.; et al. Switchable polarization rotation of visible light using a plasmonic metasurface. *APL Photonics* **2017**, *2*, 16103.
- (28) Rensberg, J.; et al. Active Optical Metasurfaces Based on Defect-Engineered Phase-Transition Materials. *Nano Lett.* **2016**, *16*, 1050–1055.
- (29) Karvounis, A.; Gholipour, B.; MacDonald, K. F.; Zheludev, N. I. All-dielectric phase-change reconfigurable metasurface. *Appl. Phys. Lett.* **2016**, *109*, 1–5.
- (30) Michel, A.-K. U.; et al. Using Low-Loss Phase-Change Materials for Mid-Infrared Antenna Resonance Tuning. *Nano Lett.* **2013**, *13*, 3470–3475.
- (31) Earl, S. K.; et al. Tunable optical antennas enabled by the phase transition in vanadium dioxide. *Opt. Express* **2013**, *21*, 27503.
- (32) Kaplan, G.; Aydin, K.; Scheuer, J. Dynamically controlled plasmonic nano-antenna phased array utilizing vanadium dioxide [Invited]. *Opt. Mater. Express* **2015**, *5*, 2513.

- (33) Muskens, O. L.; et al. Antenna-assisted picosecond control of nanoscale phase transition in vanadium dioxide. *Light: Sci. Appl.* **2016**, *5*, e16173.
- (34) Yin, X.; et al. Beam switching and bifocal zoom lensing using active plasmonic metasurfaces. *Light: Sci. Appl.* **2017**, *6*, e17016.
- (35) Park, J.; Kang, J.; Kim, S. J.; Liu, X.; Brongersma, M. L. Dynamic Reflection Phase and Polarization Control in Metasurfaces. *Nano Lett.* **2017**, *17*, 407–413.
- (36) Chen, Y. G.; et al. Hybrid phase-change plasmonic crystals for active tuning of lattice resonances. *Opt. Express* **2013**, *21*, 13691.
- (37) Chen, Y.; et al. Engineering the Phase Front of Light with Phase-Change Material Based Planar lenses. *Sci. Rep.* **2015**, *5*, 8660.
- (38) Chu, C. H.; et al. Active dielectric metasurface based on phase-change medium. *Laser Photonics Rev.* **2016**, *10*, 986–994.
- (39) Ke, Y.; et al. Controllable Fabrication of Two-Dimensional Patterned VO₂ Nanoparticle, Nanodome, and Nanonet Arrays with Tunable Temperature-Dependent Localized Surface Plasmon Resonance. *ACS Nano* **2017**, *11*, 7542–7551.
- (40) Wang, D.; et al. Switchable Ultrathin Quarter-wave Plate in Terahertz Using Active Phase-change Metasurface. *Sci. Rep.* **2015**, *5*, 15020.
- (41) Marvel, R. E.; Harl, R. R.; Craciun, V.; Rogers, B. R.; Haglund, R. F. Influence of deposition process and substrate on the phase transition of vanadium dioxide thin films. *Acta Mater.* **2015**, *91*, 217–226.
- (42) Lopez, R.; Haynes, T. E.; Boatner, L. A.; Feldman, L. C.; Haglund, R. F. Temperature-controlled surface plasmon resonance in VO₂ nanorods. *Opt. Lett.* **2002**, *27*, 1327.
- (43) Guiton, B. S.; Gu, Q.; Prieto, A. L.; Gudiksen, M. S.; Park, H. Single-crystalline vanadium dioxide nanowires with rectangular cross sections. *J. Am. Chem. Soc.* **2005**, *127*, 498–499.
- (44) Sohn, J. I.; et al. Direct observation of the structural component of the metal-insulator phase transition and growth habits of epitaxially grown VO₂ nanowires. *Nano Lett.* **2007**, *7*, 1570–1574.
- (45) Strelcov, E.; Davydov, A. V.; Lanke, U.; Watts, C.; Kolmakov, A. In situ monitoring of the growth, intermediate phase transformations and templating of single crystal VO₂ nanowires and nanoplatelets. *ACS Nano* **2011**, *5*, 3373–3384.
- (46) Zhang, J.; et al. Self-Assembling VO₂ Nanonet with High Switching Performance at Wafer-Scale. *Chem. Mater.* **2015**, *27*, 7419–7424.
- (47) Narayan, J.; Larson, B. C. Domain epitaxy: A unified paradigm for thin film growth. *J. Appl. Phys.* **2003**, *93*, 278–285.
- (48) Cheng, Y.; Wong, T. L.; Ho, K. M.; Wang, N. The structure and growth mechanism of VO₂ nanowires. *J. Cryst. Growth* **2009**, *311*, 1571–1575.
- (49) Cheng, C.; et al. Self-Assembly and Horizontal Orientation Growth of VO₂ Nanowires. *Sci. Rep.* **2015**, *4*, 5456.
- (50) Nag, J.; Haglund, R. F., Jr Synthesis of vanadium dioxide thin films and nanoparticles. *J. Phys.: Condens. Matter* **2008**, *20*, 264016.
- (51) Nag, J. *The Solid-Solid Phase Transition in Vanadium Dioxide Thin Films: Synthesis, Physics and Application*; Vanderbilt University, 2011.
- (52) Zhao, Y.; et al. Structural, electrical, and terahertz transmission properties of VO₂ thin films grown on c-, r-, and m-plane sapphire substrates. *J. Appl. Phys.* **2012**, *111*, 53533.
- (53) Kittiwatanakul, S.; Wolf, S. A.; Lu, J. Large epitaxial bi-axial strain induces a Mott-like phase transition in VO₂. *Appl. Phys. Lett.* **2014**, *105*, 73112.
- (54) Makarevich, A. M.; et al. Chemical synthesis of high quality epitaxial vanadium dioxide films with sharp electrical and optical switch properties. *J. Mater. Chem. C* **2015**, *3*, 9197–9205.
- (55) Brady, N. F.; et al. Heterogeneous nucleation and growth dynamics in the light-induced phase transition in vanadium dioxide. *J. Phys.: Condens. Matter* **2016**, *28*, 125603.
- (56) Appavoo, K.; Haglund, R. F. Detecting Nanoscale Size Dependence in VO₂ Phase Transition Using a Split-Ring Resonator Metamaterial. *Nano Lett.* **2011**, *11*, 1025–1031.
- (57) Verleur, H. W.; Barker, A. S.; Berglund, C. N. Optical properties of VO₂ between 0.25 and 5 eV. *Rev. Mod. Phys.* **1968**, *40*, 737.
- (58) Kakiuchida, H.; Jin, P.; Nakao, S.; Tazawa, M. Optical Properties of Vanadium Dioxide Film during Semiconductive–Metallic Phase Transition. *Jpn. J. Appl. Phys.* **2007**, *46*, L113–L116.
- (59) Kana Kana, J. B.; Ndjaka, J. M.; Vignaud, G.; Gibaud, A.; Maaza, M. Thermally tunable optical constants of vanadium dioxide thin films measured by spectroscopic ellipsometry. *Opt. Commun.* **2011**, *284*, 807–812.
- (60) Lei, D. Y.; et al. Optically-Triggered Nanoscale Memory Effect in a Hybrid Plasmonic-Phase Changing Nanostructure. *ACS Photonics* **2015**, *2*, 1306–1313.
- (61) Reed, G. T.; Mashanovich, G.; Gardes, F. Y.; Thomson, D. J. Silicon optical modulators. *Nat. Photonics* **2010**, *4*, 518–526.
- (62) Cavalleri, A.; Dekorsy, T.; Chong, H. H. W.; Kieffer, J. C.; Schoenlein, R. W. Evidence for a structurally-driven insulator-to-metal transition in VO₂: A view from the ultrafast timescale. *Phys. Rev. B: Condens. Matter Mater. Phys.* **2004**, *70*, 161102.
- (63) Wegkamp, D.; Stähler, J. Ultrafast dynamics during the photoinduced phase transition in VO₂. *Prog. Surf. Sci.* **2015**, *90*, 464–502.
- (64) Liu, Q.; Liu, M. Circular-polarization modulator. *Nat. Photonics* **2017**, *11*, 614–616.
- (65) Bull, J. D. 40-GHz electro-optic polarization modulator for fiber optic communications systems. *Proc. SPIE* **2004**, 133.
- (66) Gopalakrishnan, G.; Ruzmetov, D.; Ramanathan, S. On the triggering mechanism for the metal–insulator transition in thin film VO₂ devices: electric field versus thermal effects. *J. Mater. Sci.* **2009**, *44*, 5345–5353.
- (67) Jeong, J.; et al. Suppression of Metal-Insulator Transition in VO₂ by Electric Field-Induced Oxygen Vacancy Formation. *Science* **2013**, *339*, 1402–1405.
- (68) Appavoo, K.; et al. Role of Defects in the Phase Transition of VO₂ Nanoparticles Probed by Plasmon Resonance Spectroscopy. *Nano Lett.* **2012**, *12*, 780–786.
- (69) Rechberger, W.; et al. Optical properties of two interacting gold nanoparticles. *Opt. Commun.* **2003**, *220*, 137–141.
- (70) Butakov, N. A.; et al. Switchable Plasmonic-Dielectric Resonators with Metal-Insulator Transitions. *ACS Photonics* **2018**, *5*, 371.
- (71) Pauli, S. A.; et al. X-ray diffraction studies of the growth of vanadium dioxide nanoparticles. *J. Appl. Phys.* **2007**, *102*, 1–6.
- (72) Huber, M. A.; et al. Ultrafast Mid-Infrared Nanoscopy of Strained Vanadium Dioxide Nanobeams. *Nano Lett.* **2016**, *16*, 1421–1427.
- (73) Yu, N.; et al. Light Propagation with Phase Discontinuities: Generalized Laws of Reflection and Refraction. *Science* **2011**, *334*, 333–337.